NATIONAL TECHNICAL UNIVERSITY OF ATHENS
SCHOOL OF NAVAL ARCHITECTURE AND MARINE ENGINEERING
DIVISION OF SHIP AND MARINE HYDRODYNAMICS

Hydrodynamic Effects of Marine Environment on the Analysis and Optimization of Solar and Wave Energy Systems with Application to Floating Units and Solar Ships

Dissertation Submitted in Fulfillment of the Requirements for the Degree of
Doctor of Engineering

Ph.D. Dissertation

Alexandros A. Magkouris

Advisory Committee:

K. Belibassakis, Professor NTUA (Supervisor)
T. Soukissian, Research Director, Institute of Oceanography, HCMR
E. Kaplani, Associate Professor, UEA

Athens, January 2025

NATIONAL TECHNICAL UNIVERSITY OF ATHENS
SCHOOL OF NAVAL ARCHITECTURE AND MARINE ENGINEERING
DIVISION OF SHIP AND MARINE HYDRODYNAMICS

Hydrodynamic Effects of Marine Environment on the Analysis and Optimization of Solar and Wave Energy Systems with Application to Floating Units and Solar Ships

Author: **Alexandros A. Magkouris**
School of Naval Architecture & Marine Engineering
National Technical University of Athens
Heroon Polytechniou 9, 15780, Athens, Greece
E–mail: alexmagouris@gmail.com
Phone: (+30) 698 310 7351

Advisory Committee

- **Prof. Konstantinos A. Belibassakis (Supervisor)**
  Division of Ship and Marine Hydrodynamics
  School of Naval Architecture & Marine Engineering
  National Technical University of Athens
  Heroon Polytechniou 9, 15780, Athens, Greece
  E–mail: kbel@fluid.mech.ntua.gr
- **Dr. Takvor Soukissian**
  Institute of Oceanography
  HCMR Hellenic Centre for Marine Research
  46.7 km Athens–Sounio Ave., 19013, Anavyssos, Greece
  E–mail: tsouki@hcmr.gr
- **Assoc. Prof. Eleni Kaplani**
  Engineering Division, Faculty of Science
  University of East Anglia
  Norwich Research Park, Norwich, Norfolk, NR4 7TJ, UK
  E–mail: E.Kaplani@uea.ac.uk

Athens, 07 / 01 / 2025

NATIONAL TECHNICAL UNIVERSITY OF ATHENS
SCHOOL OF NAVAL ARCHITECTURE AND MARINE ENGINEERING
DIVISION OF SHIP AND MARINE HYDRODYNAMICS

Hydrodynamic Effects of Marine Environment on the Analysis and Optimization of Solar and Wave Energy Systems with Application to Floating Units and Solar Ships

Ph.D. Dissertation

Alexandros A. Magkouris

Examination Committee

1. K. Belibassakis*, Professor NTUA (Supervisor),
   School of Naval Architecture and Marine Engineering
2. T. Soukissian*, Research Director HCMR,
   Institute of Oceanography
3. E. Kaplani*, Associate Professor UEA,
   School of Engineering
4. M. Angelou, Assistant Professor NTUA,
   School of Naval Architecture and Marine Engineering
5. G. Papadakis, Associate Professor NTUA,
   School of Naval Architecture & Marine Engineering
6. J. Prousalidis, Professor NTUA,
   School of Naval Architecture & Marine Engineering
7. Th. Gerostathis, Associate Professor UNIWA,
   School of Engineering, Department of Naval Architecture

**Member of the Advisory Committee*

Athens, 07 / 01 / 2025

ABSTRACT

The present dissertation investigates the innovative utilization of renewable energy from the sea, focusing on contemporary technologies such as floating photovoltaics (FPV), wave energy converters (WEC), and solar ships. Additionally, it explores hybridization concepts as potential future work, proposing ideas to enhance energy efficiency and performance. The research conducted is mainly focused on the investigation of marine environment effects on power output, which is accomplished by developing appropriate hydrodynamic models. The research is structured into several critical areas, each addressing different aspects of marine renewable energy technologies and their interaction with the dynamic marine conditions.

The introductory section provides a brief overview of the marine renewable energy potential. It delves into the concepts of FPV systems, solar ships, wave energy parks, as well as the possibilities of hybrid systems combining these technologies. This section discusses the importance of harnessing marine energy to sustainably meet global energy demands, highlighting the need for innovative approaches to harness and utilize the abundant energy resources available in the marine environment. In Part I, simplified hydrodynamic models are developed and applied to analyze the behaviour and performance of FPV systems. The models leverage detailed hydrodynamic data, and combine the results with a simple PV model, to quantify the effects of wave–induced motions on the power output of FPV systems. By examining how various hydrodynamic conditions, such as wave height and frequency as well as the local seabed topography, impact the efficiency of FPV installations, the models provide valuable insights into optimizing both the design and deployment of these systems for maximum energy efficiency. The research identifies a range of key factors that influence FPV system performance, including the amplitude and frequency of platform oscillations and the interaction between wavefields and FPV structures. By understanding these dynamics, the studies offer strategies to mitigate adverse effects, such as energy losses due to excessive motion, and to enhance overall energy production, ensuring that FPV systems can operate more reliably and efficiently in diverse marine conditions. Case studies using real solar radiation and sea state data from specific locations in the Mediterranean region are also discussed.

The next part delves into the innovative concept of solar powered ships, focusing on the integration of photovoltaic panels into existing marine vessels. In particular, it presents a multifaceted assessment of several critical aspects associated with solar–powered ships, such as the autonomy range and the potential energy savings. The modelling is based on three dimensional models, appropriately developed to support hydrodynamic analysis with the added complexity of forward speed. By investigating the potential of solar ships, this section aims to investigate the development of more sustainable and energy–efficient maritime transport solutions. The findings and proposals presented are intended to contribute to the maturation of

new technologies through which renewable energy will play a crucial role in reducing the carbon footprint of the shipping sector.

The final part of the present work focuses on the modelling and performance evaluation of point absorber wave energy converter (WEC) arrays, considering the effects of bathymetry variability. This section investigates how bathymetry profiles, as well as hydrodynamic interactions among multiple floating bodies, affect the energy capturing capacity and performance of WEC arrays operating nearshore. Case studies are conducted to demonstrate the applicability of the developed models, indicating that they serve as valuable supporting tools for optimization studies. Subsequently, the deployment of WEC arrays on the exposed side of breakwaters is examined. Hydrodynamic interactions between waves, wave energy converters and breakwater structures are modelled and quantified, assessing how they influence the performance and energy output of such systems. A case study in this context also illustrates the utility of the model, providing insights into the design and placement of WEC arrays alongside coastal defence structures, highlighting opportunities to enhance energy production by exploiting existing infrastructure, while simultaneously augmenting the provided coastal protection, by attenuating the incoming wave energy. Finally, the potential for hybridization is discussed, combining technologies for harnessing wave, solar and other forms of energy in the marine environment.

By addressing these diverse aspects of marine renewable energy technologies, the present work aims to contribute to the advancement and practical implementation of sustainable energy solutions from the sea, providing valuable insights for engineers, policymakers and researchers working towards a sustainable and energy–efficient future. Through detailed modelling, case studies, and performance evaluations, the work aims to provide an overview of the opportunities and challenges associated with marine renewable energy, paving the way for innovative applications and increased adoption of these technologies.

The computational methods employed involve the development of algorithms based on the application of the Boundary Element Method (BEM). These algorithms are utilized to calculate the dynamic behaviour of floating bodies of general geometry, as well as ships moving at forward speed. The Boundary Element Method is a numerical technique, widely used in engineering and physics, that addresses problems involving flow fields and wave phenomena by enabling dimensionality reduction through the use of boundary integral representations. This method proves particularly advantageous for analysing the hydrodynamic characteristics of floating bodies and ships. However, to exploit the computational efficiency that dimensionality reduction provides, the models must be simplified based on certain assumptions, such as non-viscous, irrotational flows, and incompressible media, that define the linearized theory for floating bodies. The latter is briefly described in Appendix A, for completeness purposes. While these assumptions facilitate more efficient calculations, they do not fully capture the complexities of real–world fluid dynamics where viscosity, rotationality, and compressibility are significant factors under certain flow conditions.

Within the context of the present dissertation, the BEM algorithms are combined with various supplementary techniques to improve their effectiveness and accuracy. Firstly, Perfectly Matched Layers (PML) are utilized to absorb wave–like behaviour at infinity, preventing numerical reflections from contaminating the evaluated solutions. This ensures that a finite computational domain can accurately simulate an infinite medium without the complications introduced by boundary numerical reflections. Additionally, mirroring techniques are employed to decrease the computational mesh size while preserving the integrity of the problems' physical aspects. By leveraging the symmetrical properties of the geometry, these techniques allow for a more efficient representation of hydrodynamic problems, many of which inherently exhibit symmetrical properties. Furthermore, a Coupled Mode Model is incorporated to analyze wave propagation across general seabed bathymetry, enabling the simulation of hydrodynamic phenomena in more realistic environments. Finally, parallel programming methods are adopted to accelerate the calculations by distributing the computational workload across multiple processors. This results in a significant reduction in simulation time, facilitating the analysis of more complex scenarios within practical time constraints. These approaches ensure that the developed computational algorithms not only yield accurate results, but also operate with enhanced computational efficiency.

ΠΕΡΙΛΗΨΗ

Η παρούσα διατριβή διερευνά καινοτόμες μεθόδους αξιοποίησης της ανανεώσιμης ενέργειας από τη θάλασσα, εστιάζοντας σε σύγχρονες τεχνολογίες όπως τα πλωτά φωτοβολταϊκά (FPV), τα ηλιακά πλοία και οι μετατροπείς κυματικής ενέργειας (Wave Energy Converters – WECs). Επιπλέον, εξετάζει ιδέες υβριδοποίησης ως προτάσεις για μελλοντική έρευνα, προτείνοντας λύσεις για την ενίσχυση της ενεργειακής απόδοσης. Η έρευνα εστιάζεται στον προσδιορισμό των επιπτώσεων του θαλάσσιου περιβάλλοντος στην παραγωγή ενέργειας, που επιτυγχάνεται με την ανάπτυξη κατάλληλων υδροδυναμικών μοντέλων, και είναι δομημένη σε διάφορους κρίσιμους τομείς, καθένας από τους οποίους αναφέρεται σε διαφορετικές πτυχές των τεχνολογιών ανανεώσιμης ενέργειας από τη θάλασσα και την αλληλεπίδρασή τους με τις δυναμικές θαλάσσιες συνθήκες.

Η εισαγωγική ενότητα παρέχει μια επισκόπηση του δυναμικού της θαλάσσιας ανανεώσιμης ενέργειας. Εξετάζει τις έννοιες των πλωτών φωτοβολταϊκών, των ηλιακών πλοίων και των ενεργειακών πάρκων κυματικής ενέργειας, καθώς και δυνατότητες υβριδικών συστημάτων που συνδυάζουν αυτές τις τεχνολογίες. Η ενότητα αυτή θέτει το πλαίσιο για την κατανόηση της σημασίας της εκμετάλλευσης της θαλάσσιας ενέργειας για την ικανοποίηση των παγκόσμιων ενεργειακών αναγκών με βιώσιμο τρόπο, επισημαίνοντας την ανάγκη για καινοτόμες προσεγγίσεις όσον αφορά την απομάστευση και τη χρήση των πλούσιων ενεργειακών πόρων που διατίθενται στο θαλάσσιο περιβάλλον. Στο πρώτο μέρος της εργασίας, αναπτύσσονται απλοποιημένα υδροδυναμικά μοντέλα, τα οποία εφαρμόζονται για την ανάλυση της συμπεριφοράς και απόδοσης των συστημάτων πλωτών φωτοβολταϊκών μονάδων. Τα μοντέλα αυτά παρέχουν λεπτομερή υδροδυναμικά δεδομένα, τα οποία σε συνδυασμό με ένα μοντέλο υπολογισμού της παραγόμενης ισχύος από ηλιακούς συλλέκτες, ποσοτικοποιούν την επίδραση της δυναμικής στην παραγωγή ενέργειας. Εξετάζοντας τον τρόπο με τον οποίο διάφορες υδροδυναμικές παράμετροι, όπως το ύψος κύματος και η συχνότητα αλλά και η τοπική τοπογραφία του θαλασσίου πυθμένα, επηρεάζουν την απόδοση των εγκαταστάσεων, τα μοντέλα παρέχουν πολύτιμες πληροφορίες για τη βελτιστοποίηση τόσο του σχεδιασμού όσο και της ανάπτυξης αυτών των συστημάτων με γνώμονα την μέγιστη ενεργειακή απόδοση. Εξετάζεται μια σειρά βασικών παραγόντων που επηρεάζουν την απόδοση των συστημάτων, συμπεριλαμβανομένων του πλάτους και της συχνότητας των κινήσεων των κατασκευών καθώς και των αλληλεπιδράσεων μεταξύ κυματικών πεδίων και πλωτών σωμάτων. Μέσω της κατανόησης των παραπάνω, η μελέτη προσφέρει δεδομένα για τη μείωση των αρνητικών επιπτώσεων, όπως οι απώλειες ενέργειας λόγω υπερβολικών κινήσεων, και για την ενίσχυση της συνολικής παραγωγής ενέργειας, διασφαλίζοντας ότι τα πλωτά φωτοβολταϊκά συστήματα λειτουργούν με μεγαλύτερη αξιοπιστία και αποτελεσματικότητα σε διάφορα θαλάσσια περιβάλλοντα. Επίσης, παρουσιάζονται αποτελέσματα βασισμένα σε πραγματικά δεδομένα

ηλιακής ακτινοβολίας και θαλάσσιων συνθηκών από συγκεκριμένες τοποθεσίες στην περιοχή της Μεσογείου.

Στη συνέχεια της διατριβής εξετάζεται το καινοτόμο αντικείμενο των ηλιακών πλοίων, εστιάζοντας στην ενσωμάτωση φωτοβολταϊκών συλλεκτών σε υπάρχοντα πλοία. Η συγκεκριμένη ενότητα αναλύει εκτενώς αρκετές κρίσιμες πτυχές που σχετίζονται με τα ηλιακά πλοία, όπως η αυτονομία και οι πιθανοί τρόποι εξοικονόμησης ενέργειας. Η μοντελοποίηση βασίζεται σε τριδιάστατα μοντέλα, κατάλληλα δομημένα ώστε να υποστηρίζουν την υδροδυναμική ανάλυση με την πρόσθετη πολυπλοκότητα της πρόσω ταχύτητας. Μέσω της διερεύνησης της προοπτικής των ηλιακών πλοίων, η ενότητα στοχεύει στο να συνεισφέρει στην ανάπτυξη βιώσιμων και ενεργειακά αποδοτικών λύσεων για τις θαλάσσιες μεταφορές. Τα αποτελέσματα και οι προτάσεις που παρουσιάζονται σκοπό έχουν να συμβάλλουν στην ωρίμανση νέων τεχνολογιών, μέσω των οποίων η ανανεώσιμη ενέργεια θα αναλάβει κομβικό ρόλο στη μείωση του αποτυπώματος άνθρακα του τομέα της ναυτιλίας.

Το τελευταίο μέρος της εργασίας επικεντρώνεται στη μοντελοποίηση και αξιολόγηση της απόδοσης συστοιχιών αποτελούμενων από σημειακούς απορροφητές κυματικής ενέργειας, λαμβάνοντας υπ’ όψιν τη μεταβλητότητα της βαθυμετρίας. Εξετάζονται οι επιπτώσεις τόσο του προφίλ βαθμομετρίας όσο και των αλληλεπιδράσεων μεταξύ πολλαπλών πλωτών σωμάτων, στην απομάστευση ενέργειας και την απόδοση κυματικών πάρκων που λειτουργούν σε παράκτιες περιοχές. Επιπλέον, διεξάγονται περιπτωσιολογικές μελέτες με στόχο την ανάδειξη της εφαρμοσιμότητας των προτεινόμενων μοντέλων, υποδεικνύοντας ότι αυτά λειτουργούν ως πολύτιμα υποστηρικτικά εργαλεία για μελέτες βελτιστοποίησης. Στη συνέχεια, εξετάζεται η τοποθέτηση σημειακών απορροφητών στην εκτεθειμένη πλευρά κυματοθραυστών. Συγκεκριμένα, μελετώνται οι υδροδυναμικές αλληλεπιδράσεις μεταξύ κυματικών πεδίων, μονάδων απομάστευσης ενέργειας και κυματοθραυστών, αξιολογώντας πώς αυτές οι αλληλεπιδράσεις επηρεάζουν την απόδοση και την παραγωγή ενέργειας. Μια μελέτη περίπτωσης σε αυτό το πλαίσιο επίσης επιδεικνύει τη χρησιμότητα του μοντέλου, παρέχοντας πληροφορίες για το σχεδιασμό και την τοποθέτηση μονάδων κυματικής ενέργειας σε προϋπάρχουσες δομές, όπως οι λιμένες, επισημαίνοντας τη δυνατότητα ενίσχυσης της παραγωγής ενέργειας παρέχοντας παράλληλα πρόσθετα οφέλη, όπως η προστασία των ακτών. Τέλος, αναφέρονται δυνατότητες υβριδοποίησης, που συνδυάζουν τεχνολογίες για την απομάστευση κυματικής, ηλιακής καθώς και άλλων μορφών ενέργειας, στο θαλάσσιο περιβάλλον.

Αναλύοντας τις παραπάνω πτυχές των τεχνολογιών της θαλάσσιας ανανεώσιμης ενέργειας, η παρούσα εργασία στοχεύει να συμβάλλει στην προαγωγή και την πρακτική εφαρμογή βιώσιμων λύσεων παραγωγής ενέργειας από τη θάλασσα, παρέχοντας πολύτιμα δεδομένα για μηχανικούς, πολιτικούς και ερευνητές που εργάζονται για ένα βιώσιμο και ενεργειακά αποδοτικό μέλλον. Μέσω λεπτομερούς μοντελοποίησης, περιπτωσιολογικών μελετών και αξιολογήσεων απόδοσης, η εργασία έχει στόχο να παράσχει μία πλήρη επισκόπηση των ευκαιριών και προκλήσεων που σχετίζονται με τη θαλάσσια ανανεώσιμη ενέργεια, διευκολύνοντας την εφαρμογή καινοτομιών και την υιοθέτηση αυτών των τεχνολογιών σε επίπεδο βιομηχανίας.

Οι υπολογιστικές μέθοδοι που χρησιμοποιούνται περιλαμβάνουν την ανάπτυξη αλγορίθμων βασισμένων στην εφαρμογή της μεθόδου συνοριακών στοιχείων (Boundary Element Method – BEM). Οι αλγόριθμοι αυτοί χρησιμοποιούνται για τον υπολογισμό της δυναμικής συμπεριφοράς πλωτών σωμάτων γενικής γεωμετρίας, καθώς και πλοίων που κινούνται με πρόσω ταχύτητα. Η μέθοδος συνοριακών στοιχείων είναι μια αριθμητική μέθοδος που χρησιμοποιείται ευρέως στη μηχανική και τη φυσική για την επίλυση προβλημάτων που σχετίζονται με πεδία ροής και κυματικά φαινόμενα, επιτρέποντας τη μείωση της χωρικής διαστατικότητας των προβλημάτων μέσω χρήσης ολοκληρωτικών συνοριακών αναπαραστάσεων των εμπλεκομένων πεδίων. Η μέθοδος αποδεικνύεται ιδιαίτερα χρήσιμη για την ανάλυση των υδροδυναμικών χαρακτηριστικών πλωτών σωμάτων και πλοίων. Ωστόσο, η εκμετάλλευση της υπολογιστικής αποδοτικότητας που παρέχει η μέθοδος συνοριακών στοιχείων απαιτεί την απλοποίηση της μοντελοποίησης βάσει ορισμένων υποθέσεων. Συγκεκριμένα οι ροές θεωρούνται ατριβείς και αστρόβιλες, ενώ αγνοούνται οι επιδράσεις της συμπιεστότητας. Βάσει των παραπάνω καθορίζεται η γραμμικοποιημένη υδροδυναμική θεωρία πλωτών σωμάτων, η οποία περιγράφεται εν συντομία στο Παράρτημα A, για λόγους πληρότητας. Παρόλο που αυτές οι υποθέσεις διευκολύνουν τους υπολογισμούς, δεν αντικατοπτρίζουν πλήρως την πολυπλοκότητα ρεαλιστικών ροών, όπου το ιξώδες, η στροβιλότητα και η συμπιεστότητα αποτελούν, υπό ορισμένες συνθήκες, σημαντικούς παράγοντες.

Εντός του πλαισίου της παρούσας διατριβής, η μέθοδος συνοριακών στοιχείων συνδυάζεται με διάφορες επιπλέον τεχνικές για τη βελτίωση της αποτελεσματικότητας και της ακρίβειας. Αρχικά, χρησιμοποιούνται στρώματα απορρόφησης (Perfectly matched layers – PML) για την απόσβεση της κυματικής συμπεριφοράς των λύσεων στο άπειρο, εμποδίζοντας τις αριθμητικές ανακλάσεις στο εκάστοτε υπολογιστικό χωρίο. Έτσι διασφαλίζεται ότι ένα πεπερασμένο υπολογιστικό πλέγμα μπορεί να προσομοιώσει φαινόμενα που εκτυλίσσονται στον άπειρο χώρο. Επιπλέον, εφαρμόζονται τεχνικές κατοπτρισμού για τη μείωση του μεγέθους του υπολογιστικού πλέγματος, διατηρώντας την ακεραιότητα των φυσικών πτυχών των προβλημάτων. Αξιοποιώντας συμμετρίες της γεωμετρίας, αυτές οι τεχνικές επιτρέπουν μια πιο αποδοτική και ακριβή αναπαράσταση των υδροδυναμικών προβλημάτων, πολλά εκ των οποίων εμπεριέχουν εγγενείς ιδιότητες συμμετρίας. Επιπλέον, ο υπολογισμός κυματικής διάδοσης σε περιοχές μεταβαλλόμενου βάθους επιτυγχάνεται με χρήση του μοντέλου συζευγμένων ιδιομορφών, επιτρέποντας την προσομοίωση υδροδυναμικών φαινομένων σε πιο ρεαλιστικά περιβάλλοντα. Τέλος, χρησιμοποιούνται μέθοδοι παράλληλου προγραμματισμού για την επιτάχυνση των υπολογισμών μέσω της διανομής του υπολογιστικού φόρτου σε πολλαπλούς επεξεργαστές. Αυτό οδηγεί σε σημαντική μείωση του χρόνου προσομοίωσης, διευκολύνοντας την ανάλυση πιο πολύπλοκων καταστάσεων εντός λογικών χρονικών πλαισίων. Αυτές οι προσεγγίσεις εξασφαλίζουν ότι οι υπολογιστικοί αλγόριθμοι που χρησιμοποιούνται όχι μόνο παρέχουν ακριβή αποτελέσματα, αλλά επιπρόσθετα λειτουργούν με βελτιωμένη υπολογιστική απόδοση.

ACKNOWLEDGMENTS

Profound gratitude is extended to the supervisor, Prof. K. Belibassakis, for his invaluable advice and continuous support throughout the development of the present dissertation. His accumulated knowledge and abundant experience have been a source of great encouragement during the academic research conducted in the framework of the thesis. The author also wishes to express sincere appreciation to Dr. T. Soukissian and Prof. E. Kaplani, members of the advisory committee, for their insightful feedback and guidance, which have greatly enriched the quality of the research. Sincere thanks are also due to Associate Prof. Th. Gerostathis for his valuable technical assistance and helpful comments, which have significantly contributed to the advancement of the present thesis. Moreover, sincere appreciation is expressed to Prof. E. Rusu and Prof. L. Rusu for their invaluable contribution of data and insights, which significantly contributed to the completion of this work.

The author would further like to acknowledge the honour of receiving support from the Special Account for Research Funding (E.L.K.E.) of the National Technical University of Athens, which has been essential for the completion of the present dissertation, covering the entire duration of the doctoral studies from 2021 to early 2025.

Finally, sincere gratitude is extended to my family for their unwavering encouragement and understanding throughout the course of this work. Their constant presence and support have been a source of invaluable motivation and inspiration.

TABLE OF CONTENTS

Abstract vii

Περίληψη xi

Acknowledgments xv

Table of Contents xvii

1. Introduction 1

- 1.1. Renewable energy from the sea 1
- 1.2. Solar energy status and potential 3
- 1.3. Solar Ships 7
- 1.4. Wave energy technologies and hybridization 10
- 1.5. Methods 12
- 1.6. Thesis outline and original contributions 14

Part I. Analysis of Floating PV Units 19

2. PV Systems and the Effects of Hydrodynamics 21

- 2.1. Photovoltaic cell operation 21
- 2.2. Basic performance factors 22
- 2.3. PV model 24
  - 2.3.1. Hydrodynamic Effects on Floating PV 28

3. Simplified 2D Model of Twin–Hull FPV Unit 31

- 3.1. Mathematical Formulation of the 2D Problem 31
- 3.2. BEM formulation for 2D floating structures 37
  - 3.2.1. The Incidence, Diffraction and Radiation fields 37
  - 3.2.2. Equations of Motion 38
- 3.3. Model Verification 40
- 3.4. Numerical Results 42
  - 3.4.1. Effects of dynamic motions on FPV performance 45

4. Simplified 3D model of Pontoon–type FPV and Case Studies 51

4.1. Extension of 2D Hydrodynamic Model via strip theory 52
4.1.1. Mathematical formulation.... 54

4.2. Numerical Results and Verification 56

4.3. Offshore–to–Nearshore Transformation of Wave Conditions 58

4.4. Responses of the FPV Structure 61

4.5. Effects of Dynamics on FPV Module Power Performance 63

Part II. Solar Ship 69

5. Hydrodynamics of Twin–Hull Vessels with Application to Solar Ships....71

5.1. Problem Formulation.... 72
5.1.1. Formulation of the steady problem.... 75
5.1.2. 3D BEM for the steady flow problem.... 76
5.1.3. Formulation of the unsteady problem 82
5.1.4. Estimation of Added Wave Resistance 87

5.2. Model Verification 88

5.3. Case study in the Saronic Gulf 89
5.3.1. Selected Results of Dynamic Responses and Added Resistance.... 91
5.3.2. Estimation of Energy Needs and PV Contribution 93

5.4. Discussion and model extensions 95

Part III. Hydrodynamic Analysis and Performance of Wave Energy Parks....99

6. Modelling of Nearshore Wave Energy Parks 101

6.1. Mathematical Formulation....103
6.1.1. Formulation of the Incident Field....104
6.1.2. BEM Formulation for the Diffraction and Radiation Problems 106
6.1.3. Mesh Generation and Evaluation of Power Output....108

6.2. Case Study in the Eastern Aegean region 109
6.2.1. Application of the BEM–CMS Model 112
6.2.2. Q–factor of the WEC park 119
6.2.3. Estimation of Absorbed Power....122

6.3. Discussion and future extensions....124

7. Integration of Point Absorber WECs on Breakwaters 127

7.1. Mathematical Formulation and 3D BEM 129
7.1.1. Mesh Generation and Power Output....132
7.1.2. Model Verification 134
7.1.3. Numerical Results 135

7.2. Case Study in the port of Heraklion 142
  7.2.1. Estimation of absorbed power 145
7.3. Discussion and Optimization Considerations 147

8. Conclusions and Suggestions for Future Work 151

Appendices 155

A. Hydrodynamic Theory for Floating Bodies 157

A.1. Reference Frames (Coordinate Systems) 159

A.2. Degrees of Freedom 159

A.3. Equations of motion of a floating solid body 160
  A.3.1. Linearization 162
  A.3.2. Linearization in the case of a floating body with forward speed 165
  A.3.3. Hydrostatic Loads 166
  A.3.4. Hydrodynamic Loads 167

A.4. The General Hydrodynamic Problem 168
  A.4.1. Decomposition of the flow field 170
  A.4.2. Decomposition of the hydrodynamic loads 171
  A.4.3. Hydrodynamic coefficients 172

A.5. Numerical Implementation 173

B. The Quadrilateral Element 175

C. Evaluation of Induced Potential and Velocity 179

C.1. Potential and velocity induced from doublet element 179

C.2. Potential and velocity induced from source element 182

D. Estimation of Wind Loads and Cooling Effect 185

References 191

1

INTRODUCTION

1.1. *Renewable energy from the sea*

Energy consumption and its environmental consequences are deeply embedded in every aspect of our personal and public existence, to such an extent that they are often overlooked [1]. With the global energy consumption on the rise and under the climate change pressure, European policy makers have promoted a series of renewable energy action plans to achieve energy security for the European Union (EU), while simultaneously abating social and environmental impacts. The European Green Deal [2] places paramount importance on the energy transition, as part of the EU's efforts to achieve climate neutrality and minimize biodiversity loss and pollution by 2050. As part of this effort, interim targets have been set for 2030 that aim to boost the use of renewable energy sources [3]. For instance, the 2018 revision of the Renewable Energy Directive [4] had set the target of at least 32% of the total EU consumption to be derived from renewable energy sources by 2030, while the revised Renewable Energy Directive EU/2023/2413 [5] raised this percentage to a minimum of 42.5%, with the aspiration to reach 45%, reflecting a stronger commitment to sustainability and combating climate change in the EU. The result of these action plans and other supporting policies (e.g., Energy Roadmap 2050 [6]), naturally led to a direct increase in renewable energy production. However, only a small portion of that energy is generated offshore.

Moving renewable energy production offshore offers significant advantages, primarily due to abundant resources and virtually unlimited available space. Offshore areas have stronger and more consistent wind speeds, ideal for wind power generation, while ample space is a critical advantage for solar farms, considering the land constraints often faced in densely populated areas. Moreover, offshore facilities enable the development of larger, more efficient energy plants by mitigating visual and noise impacts, which are often pointed out as the reason for local communities' objection to the installation of renewable power plants [7]. Beyond the environmental benefits, offshore renewable energy projects boost local economies and drive technological innovation, thus playing a key role in the transition towards a sustainable energy future.

Oceans hold a great variety of energy forms that can be harnessed, presenting a wide range of renewable energy opportunities with the potential to revolutionize global energy production. These among others, include floating and bottom fixed wind turbines, floating solar farms, wave energy conversion technologies and tidal energy units (see Figure 1-1).

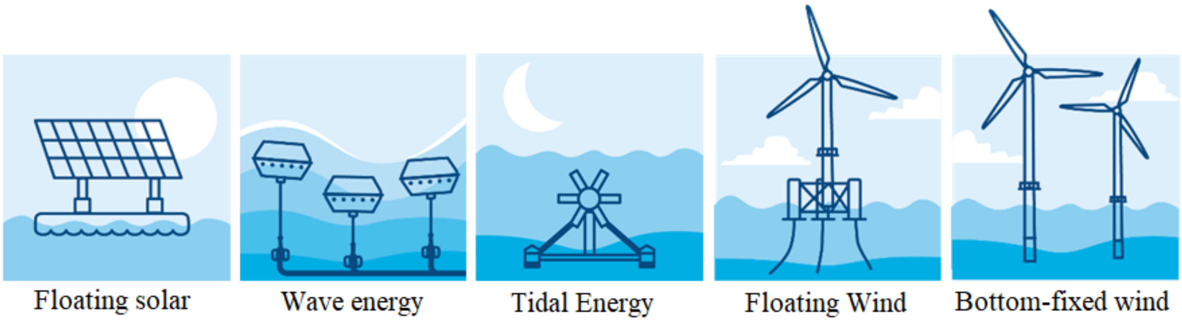

Figure 1-1. Basic Pillars of offshore Renewable energy technologies. (Adapted from [3]).

The above technologies harness various forms of energy from the ocean, such as wind, waves, tides, and solar radiation to generate electricity. Currently, the leading offshore renewable energy source in Europe is wind, with offshore wind farms being launched at the GW scale. By 2020, Europe had a total installed offshore wind capacity of 25 GW [8]. It is thus evident that any novel, offshore energy application must rival the viability of wind farms. The European marine renewable energy mix also includes a tidal barrage in France [9], tidal current turbines and wave energy converters. However, the latter technologies are still under development and large–scale commercialization has not yet been achieved.

Beyond the more well–known forms of wind, wave, solar and tidal energy, ocean energy includes a wide range of renewable resources. For instance, Ocean Thermal Energy Conversion (OTEC) technology utilizes the temperature difference between warm surface waters and colder deep waters to generate energy, see e.g., [10]. Salinity gradients – resulting from the difference in salt concentrations between freshwater and seawater – also represent a promising energy source. Another form of energy derived from the sea is ocean biomass, which involves cultivating marine plants for biofuel production [11]. In addition, ocean current energy technology harnesses the kinetic energy of underwater currents, while underwater geothermal energy utilizes heat generated by volcanic activity beneath the ocean floor. The commercialization of ocean energy is progressing at a much slower pace compared to other renewable energy sources. This lag can be attributed to the fact that the technology for harnessing ocean energy is still largely in development and several challenges must be addressed before achieving commercial viability [12]. Despite many alternative ocean energy sources being in their early developmental stages and needing additional funding and research for broader implementation, they nonetheless present promising opportunities for facilitating the transition towards a more sustainable global energy portfolio.

In the present dissertation's context, the focus is narrowed to two particularly promising ocean energy sources, namely floating solar energy systems and wave energy technologies. Floating solar energy systems are innovative installations that harness sunlight while being positioned on bodies of water, thereby minimizing land usage and providing additional benefits such as reduced evaporation and improved water quality [13]. Meanwhile, wave energy technologies harness the kinetic energy generated by ocean waves, which makes them a virtually inexhaustible source. The present work specifically investigates the potential impacts of marine environments on these technologies, with an emphasis on hydrodynamic modelling. This includes examining interactions among multiple floating structures in close proximity, effects of forward velocity in the hydrodynamic analysis of solar powered vessels and assessment of the impact on solar energy production, as well as the effects of wave fields' interactions with floating installations along with variable seabed profiles, commonly encountered in nearshore and coastal regions.

1.2. *Solar energy status and potential*

Solar radiation is the most widely accessible and abundant source of energy. Additionally, while wind availability is intermittent, solar energy is cyclic and diurnal. Moreover, solar radiation is the main cause that drives ocean and atmospheric circulation [14], inducing the ocean wave motion, winds and currents that are currently harnessed offshore. The global solar market noted unprecedented growth in 2022, with China alone expanding its total solar capacity by almost 100 GW [15], based on photovoltaics (often abbreviated as PVs). Since 2012, China has been expanding its solar capacity through extensive and substantial subsidies, in an attempt to secure its energy future away from fossil fuels. In early 2018, a world record was achieved in Saudi Arabia, where a solar project tender was won at the lowest price ever recorded; less than \$0.02/kWh. In 2022, TotalEnergies [16] announced the startup of the Al Kharsaah 800 MWp solar power plant, which constitutes one of the largest plants in the Middle East, comprising two million bifacial modules mounted on single–axis trackers. The Al Kharsaah power plant is anticipated to supply 10% of Qatar's peak power demand and is projected to prevent 26 million tons of carbon dioxide (CO_2) emissions throughout its operational lifespan [16], providing power for QAR 0.0571/kWh, the lowest winning bid ever registered in an auction for large scale renewable energy, as of 2020 [17].

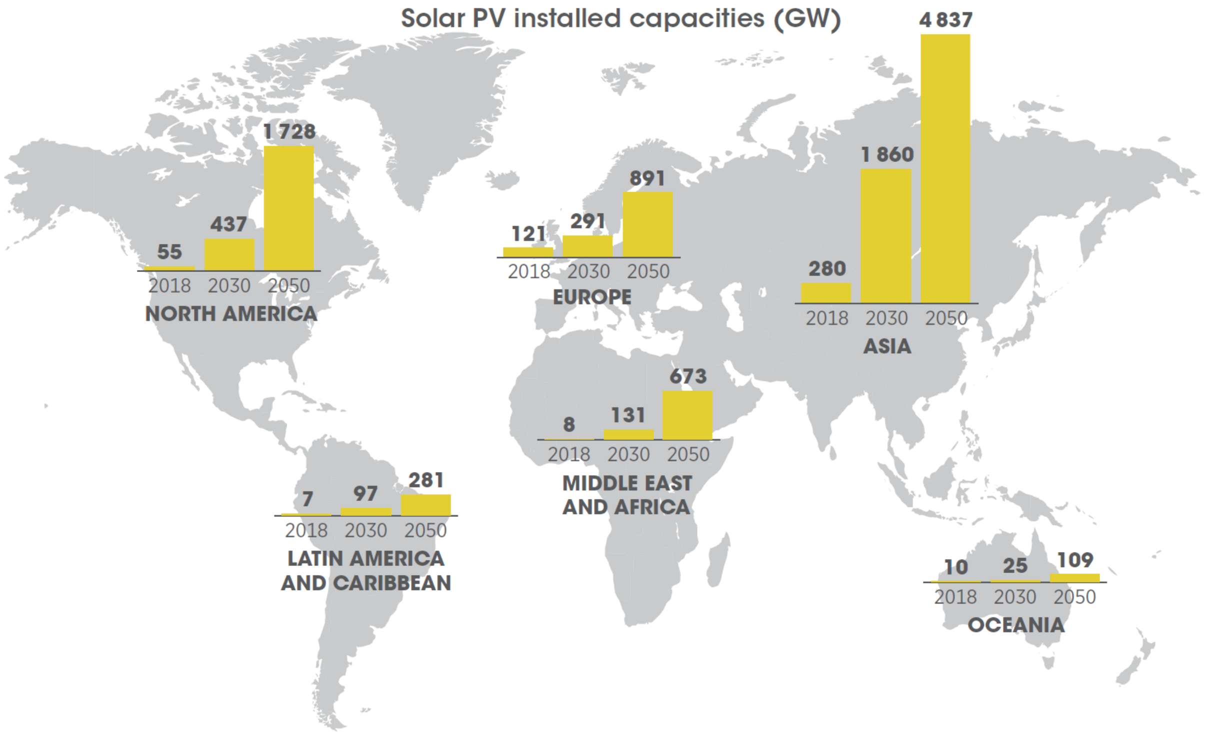

Figure 1-2. Projected World solar PV installed capacity by 2050 (source: [18]).

Figure 1-2 illustrates the proportional contribution of each continent to the global solar PV installed capacity in the year 2018, along with projections for the years 2030 and 2050, as per the analysis conducted by the International Renewable Energy Agency (IRENA) through the REmap programme, 2019 [18]. As compared to the PV installations recorded in 2018, which totalled 481 gigawatts (GW), the projections indicate a nearly sixfold increase in the world's PV installed capacity by 2030, reaching 2,841 GW. Furthermore, this capacity is forecasted to expand even more by 2050, reaching 8,519 GW. It is noteworthy that within this projection, distributed scale installations, such as rooftop solar, are anticipated to constitute 40%, with the remaining 60% being utility–scale installations [19].

However, in order for the goals set by the aforementioned projections to be accomplished, it is imperative to address the limiting factor of land conservation. While the renewable energy industry rapidly expands in an unprecedented scale, utility–scale PV plants are increasingly occupying agricultural land. This fact inevitably leads to raising concerns about the land requirements and associated impacts on land use, related to PV installations [20]. Floating solar farms have emerged as a promising option to address this matter. Furthermore, high temperatures can detrimentally impact the efficiency of PV systems, typically resulting in a reduction of power output by 5–25% from the nominal value for incident irradiance of $1000\ \mathrm{W/m^2}$, solely due to cell temperature [21]. Thus, with water and wind near the surface acting as coolants, floating PV systems operate at lower temperatures, thereby mitigating the temperature–caused efficiency reduction.

Installations in closed basins and reservoirs, such as irrigation ponds, wastewater treatment plants etc., have already been deployed in the US, Europe and Asia. During the last decade floating PV installations have experienced exponential growth, with the global cumulative installed FPV capacity being 3.8 GW in 2021 [22]. This capacity is projected to reach 4.8 GW in 2026 [23]. A 6.3MW floating PV installation of very large horizontal dimensions (approximately $57000\ \mathrm{m^2}$) was deployed in 2020 in Queen Elizabeth II Reservoir by LightsourceBP [24]. The installation covers less than 10% of the reservoir, and is able to generate 5.8 GWh worth of energy on an annual basis [25]. Similar installations have been reported in bays. In those applications, PV panels are mounted on floating structures that provide buoyancy, with the whole arrangement benefiting from the positioning on a flat surface; see, e.g., Figure 1-3(a). In the context of the aforementioned applications, floating PV installations prevented water evaporation, which significantly contributes to the depletion of global water supply [26]; (estimates suggest that up to 40% of global water loss can be attributed to evaporation [27]). Furthermore, due to the shading supplied to the water body, the algae growth rate dropped as a consequence of the reduction in photosynthesis processes [13].

Extrapolating on the above idea, the potential energy yield of offshore (or nearshore) floating PV (also known as Floatovoltaics, or FPV) installations has recently been brought to the spotlight. Offshore regions offer ample surface, necessary for the successful commercialization of floating solar farms as well as the potential of creating hybrid renewable energy units, via exploitation of existing facilities serving the operation of offshore wind or wave farms.

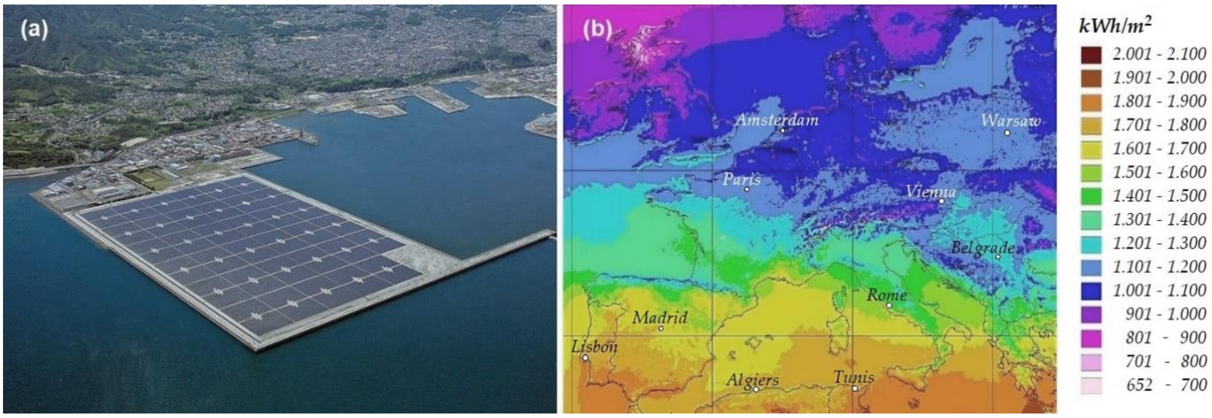

Figure 1-3. (**a**) Floatovoltaic installation in Kagoshima Bay, Japan (Adapted from [28]). (**b**) Annual solar surface irradiance for Europe (from CM-SAF data [29]).

Furthermore, the cooling effect of water and wind along with direct solar exposure, raises floating PV systems to a rather appealing renewable energy production solution. The importance of the aforementioned characteristics is reinforced, considering the high potential of solar radiation encountered in southern latitudes and especially the Mediterranean Sea, in contrast to the relatively lower wind and wave potential, see Figure 1-3 (b). (Detailed solar irradiance data for the Mediterranean Sea are also available in Ref. [30]).

Most interestingly, a recent techno–economic survey comparing renewable offshore technologies [31], suggested that a potential offshore PV plant would feature a higher yield per footprint area than the market protagonist; wind farms. However promising, it must be considered that the analysis compared existing and proven technologies hence it could not accurately account for the cost of a supporting, offshore floating structure and the durability of the otherwise well–established PV cell technology in the saline and volatile marine environment. It is evident that the successful deployment of floating PV farms at sea requires a suitable supporting ballast structure that will ensure safe operation. The optimal design of such structure heavily depends on the expected prevailing sea states, under operation conditions, and the mechanical characteristics (i.e., bending stiffness) of the employed PV technology. In order to pave the way towards the successful commercialization of nearshore and offshore floating PV farms, issues concerning structural robustness, operational safety, power yield in the marine environment and optimal grid integration need to be addressed. The highly complex nature of this venture requires multidisciplinary cooperation in order to establish an integrated design approach for floating PV parks.

Several studies have been conducted towards the general direction of comparing floating photovoltaic units to land–based ones of corresponding expected power output. Such studies are a key pillar for the further development of floating solar technology, since they reveal key similarities and differences compared to a relatively mature form of green energy technology. FPV installations do not occupy land and thus provide a direct solution to avoid disputes regarding the usage of agricultural zones, protecting their characteristics, flora and fauna. In addition, the supporting floating (moored) structures provide the unit with the ability to be transported in a fully reversible manner, in contrast to land–based plants, which are fully ground–fixed [32]. This flexibility of floating units allows for the integration of solar tracking techniques in a much more cost–effective way, compared to corresponding land–based units [33].

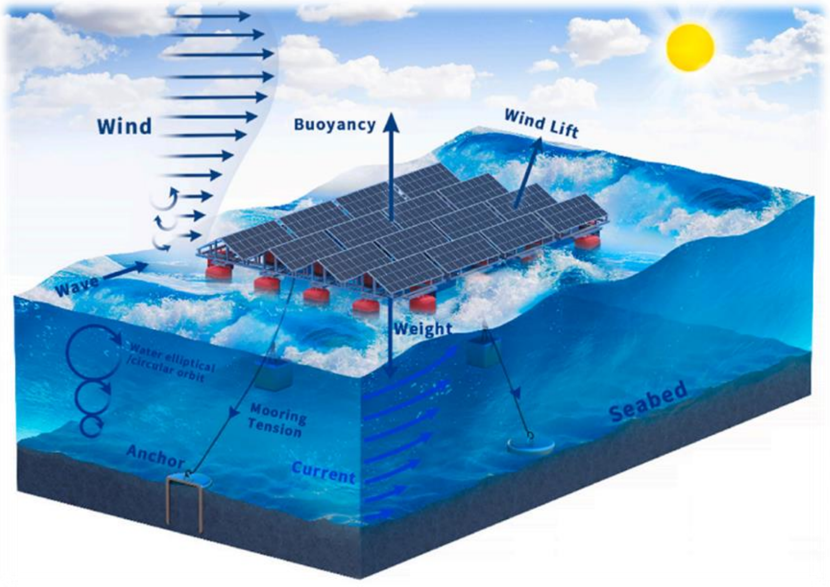

Figure 1-4. Schematic representation of parameters involved in the operation of floating FPV systems in open water. Adapted from [34].

According to case studies, the implementation of simple tracking mechanisms can increase the produced energy output of the panels by a factor of 25% [32]. However, the marine environment also introduces a wide range of new parameters that must be carefully considered in the design and operation of floating photovoltaic (FPV) systems (see Figure 1-4). Primarily, as concerns offshore floating PV systems, defining the hydrostatic forces acting on the supporting structures is crucial in the preliminary design stages to ensure they remain buoyant and stable. Furthermore, the dynamic movement of floating platforms supporting PV systems, due to loads by waves and wind, can impose varying stresses on the structures, while also dynamically altering the azimuth and tilt angles of mounted PV systems. Therefore, the above parameters can affect stability and orientation, influencing the efficiency and lifespan of PV units. On the other hand, the cooling effects provided by the surrounding water and wind can enhance the performance of solar panels by reducing the heat buildup [35]. In harsh marine conditions, the potential for “green water” effects arises as well, where waves splash over the platform and onto the panels, possibly causing damage or reducing performance. Proper anchoring systems are also essential to prevent drift and ensure the long–term reliability of the FPV installation. The above environmental factors require a multidisciplinary approach to design, incorporating elements of marine engineering, structural analysis, and environmental science to optimize the performance and resilience of floating PV systems.

The energy yield of floating photovoltaics (FPVs) is in the spotlight, as offshore photovoltaic (PV) installations present significant advantages over corresponding land–based ones. These, among others, include the ample surface available for arrangements in farms, as well as the potential of hybridization with offshore wind / wave energy installations. The development of offshore FPV parks is particularly important for southern European regions, e.g., in the Mediterranean Sea, since solar radiation in southern latitudes is nearly 150–200% greater than that of the Atlantic Ocean, the North Sea and Baltic Sea regions [30], while wind and wave potentials are comparatively low. It is worth mentioning that, according to a recent report from DNV GL, it is expected that offshore FPVs will reach maturity by 2030 (see also DNVGL–RP–

0584–Edition 2021–03 [36]). On the other hand, although several solar farms have been built on closed water basins, transitioning to open sea is a challenging task as their interaction with several environmental factors is not yet fully understood [37].

Floating PV market in the East is already appreciable. A recent survey [38] indicates that offshore solar plants have a high potential of becoming the new standard for solar energy production, after the technological challenges are mastered, based on the general guideline which suggests that floating arrays are 50% more cost-effective than solar rooftops and 20% more cost–effective than land–based solar farms. As the floating solar market continues to evolve, innovative applications are emerging. These include the development of energy efficient ships, that are partially or fully powered by solar technology.

1.3. *Solar Ships*

Maritime transportation services expand at an increasing pace, which unavoidably contributes to a significant increase in the number of vessels worldwide. The latter has risen from 2,605 in 1970 to 5984 in 2000 and 11,071 in 2019 [39]. The whole spectrum of shipping, from short-distance local transport to international operations, remains heavily reliant on fossil fuels [40]. Shipping is considered a relatively climate–friendly mode of transport due to significantly lower amounts of CO_2 emitted per ton–kilometer, particularly for large vessels [41]. Indicative data of CO_2 emissions by mode of transport are provided in Figure 1-5, where it can be observed that shipping (and particularly large vessels) is characterized by significantly lower carbon footprint as compared to other modes of transport, due to the ability of loading substantial volumes of cargo. Nonetheless, the combined greenhouse gas emissions from maritime operations worldwide remain significant, since they account for about 3% of total annual anthropogenic CO_2 emissions and are projected to undergo a remarkable increase, should mitigation measures not be enforced [42]. As of 2019, transportation accounted for approximately 28.5% of total emissions in the EU, (with road transport alone being responsible for 20.5% [43]). The goal of reducing shipping emissions has led to a growing shift towards electric and hybrid vessels.

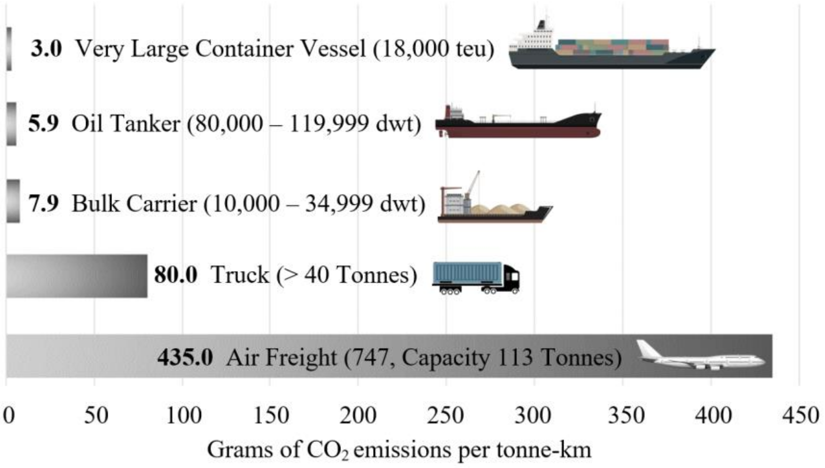

Figure 1-5. CO_2 emissions per tonne–km by mode of transport. Data adapted from [41].

The latter’s success and commercialization, however, is highly dependent on several parameters, such as technological innovations, the development of operational and regulatory frameworks, as well as cost–related issues [40].

Integration of solar technology into ship design presents a promising path towards environmentally friendly maritime operations, while also introducing numerous other substantial advantages. These include lower noise levels and reduced maintenance costs [44]. Furthermore, solar–augmented vessels provide enhanced safety by minimizing fuel–related risks [45]. In recent years, significant efforts have been made towards the direction of building vessels equipped with hybrid engines, utilizing the incident solar radiation by using mounted PV modules. The power collected from PVs is stored and utilized when the vessel enters or exits a port, while in open water, propulsion is still based on diesel. Such hybrid technologies will not only reduce fuel costs, but also assist shipowners in meeting the continuously growing demands in the Emission Control Areas (ECA) and marine parks, in the near future [46]. The potential benefits of integrating solar technology for covering the hotel loads of recreational boats are discussed in Ref. [47]. Moreover, Ref. [48], provides financial and technical analyses of solar vessels, including estimated investment costs. The latter work also concludes that a sufficient energy storage system is required, as the real–time solar power generated is inadequate for achieving sufficient propulsion speed. Meeting the total energy demands of a vessel (including propulsion) solely through solar power is a challenging objective, given the current technological constraints. However, there have been research studies and projects that address this concept.

The MS Tûranor Planet Solar, which was launched in March 2010 and sailed from its headquarters in September of the same year, became the first solar ship ever to circumnavigate the globe in 2012, completing the journey in 548 days [49]. It is a 31–meter–long catamaran-type vessel, designed by LOMOcean Design and built by Kneierim Yachtbau, with solar modules occupying an area of 537 m^2 when fully developed (see Figure 1-6.). The ship's lithium batteries are capable of storing enough energy to allow three days of autonomy, in the event of a complete absence of sunshine and the propulsion system is able to generate a maximum of 93.5 kW from the arrays of installed solar panels [50].

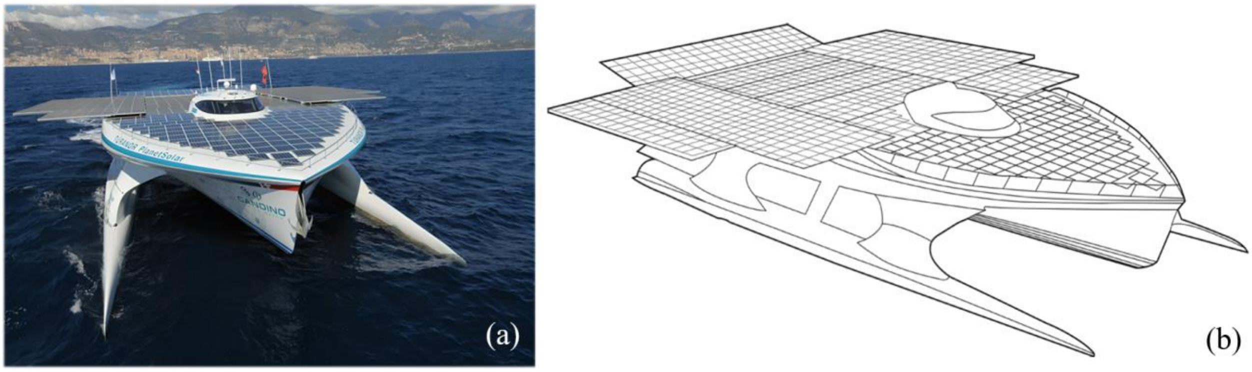

Figure 1-6. (**a**) SolarPlanet Tûranor, with developed photovoltaic installation. Adapted from [51]. (**b**) 3D sketch of the vessel. Adapted from [49].

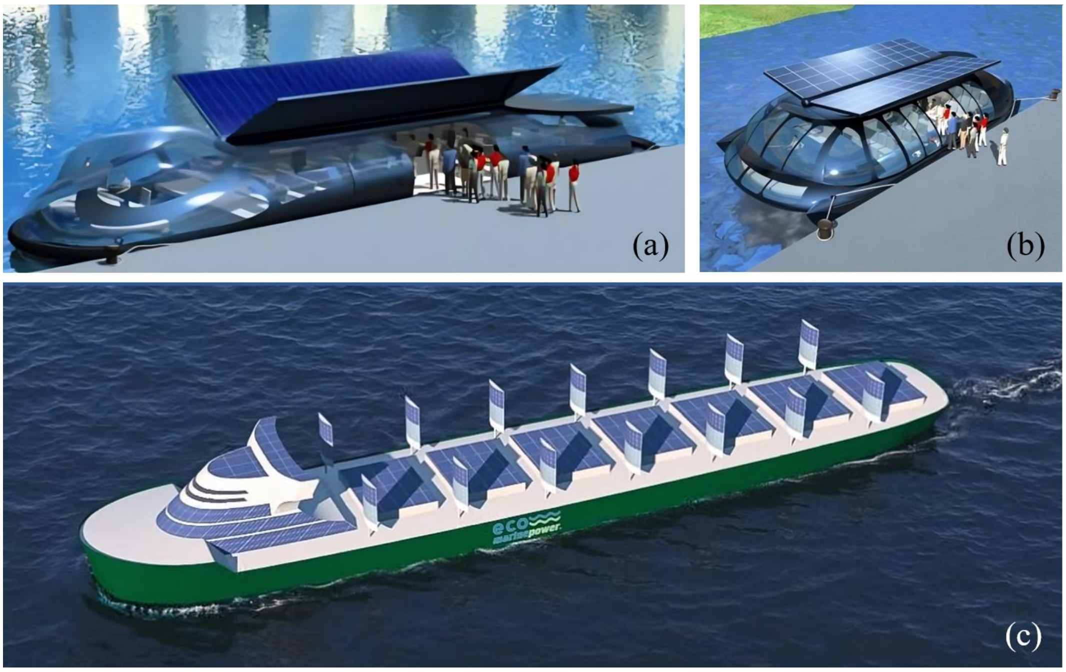

Figure 1-7. (**a**) Tonbo Solar Hybrid Ferry, (**b**) Medaka Eco Commuter Ferry and (**c**) Aquarius Eco Ship. Adapted from [46].

Standalone PV systems for small ships are also examined in Ref. [52], aiming to the development of a design strategy for solar–electric boats for river transportation. Studies on fully electric solar ships usually focus on catamaran vessels operating at low speeds; see e.g. [53]. This approach seeks to maximize the available surface area for PV array installations while simultaneously minimizing resistance.

Due to the exponential relationship between speed and ship resistance, vessels that operate using fully electric propulsion systems can achieve limited cruising speeds. This is evidenced in several ongoing projects, such as the Tonbo Solar Hybrid Ferry by Eco Marine Power [see Figure 1-7(b)], which is a 30–m–long vessel, designed to operate in urban waterways. In particular, based on ongoing research [46], this vessel will be able to operate in fully electric mode using the on–board batteries, when cruising at around 8 knots or less ($Fn \leq 0.24$). Another project by the same company involves a shorter, 22–m–long vessel, namely the Medaka Eco Commuter Ferry, designed to operate as an urban commuter ferry but also as a sightseeing vessel or tourist cruiser. Within the framework of this project, research is also being conducted on improving the operation of commuter ferries and reducing maintenance costs by incorporating advanced monitoring systems [46]. Other concepts that the latter company investigates include the deployment of solar panels on rigid sails that automatically adjust to wind conditions [see Figure 1-7(c)], aiming to provide a more consistent power source, that exploits the available combined solar and wind power.

In addition to harnessing solar and wind energy, wave energy presents a promising avenue for enhancing the sustainability of shipping, as well as the global energy portfolio in general. For instance, flapping–foil thrusters, arranged at the bow of the vessel, can effectively exploit the energy generated by wave–induced motions, converting it directly into useful propulsive power.

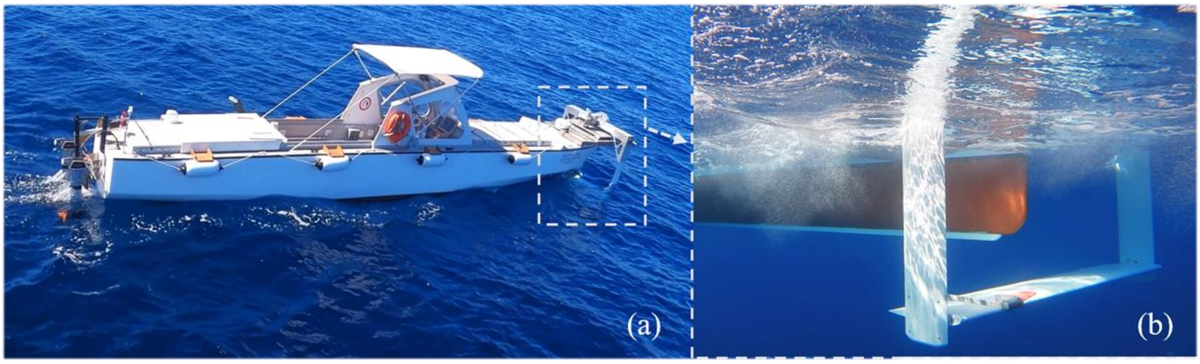

Figure 1-8. (**a**) 10–meter–long model during sea tests, featuring an attached hydrodynamic wing. (**b**) Underwater perspective of the hydrodynamic wing in operation. Adapted from [54].

This concept has been numerically investigated in Ref. [55]. Furthermore, it has been experimentally tested using both tank–scale experimental analysis and a large–scale 10–m–long model tested at sea (see Figure 1-8), in the framework of the EU funded "SeaTech" project [54]. The complete analysis and results can be found in Ref. [56]. This approach not only facilitates energy generation but also contributes to dynamic stability, thereby improving the vessel's overall performance. Furthermore, the implementation of flapping–foils can mitigate added wave resistance [55], and thus reduce fuel consumption and operational costs. By integrating such systems, the maritime industry can significantly bolster its efforts toward renewable energy utilization, promoting a more sustainable and environmentally responsible future for shipping.

1.4. *Wave energy technologies and hybridization*

Water is significantly denser than air, allowing water currents and waves to transport much greater energy per volume of medium. Consequently, developing ocean energy–capturing technologies to match the current capabilities of other renewables could position oceans as a prominent player in national renewable energy markets. Specifically, sea waves are regarded as a high–quality renewable energy source due to their superior energy density compared to other renewables [57]. Additionally, considering the inherent uncertainties associated with various phenomena affecting renewable energy production, diversifying energy resources within the grid is bound to contribute to a more balanced and stable green energy supply. "Wave power" specifically describes the utilization of energy extracted from wind–generated waves for various applications, including electricity generation, water desalination and water pumping, while Wave Energy Converters (WECs) are specialized devices designed to harness this type of energy. It is essential to differentiate wave power from tidal power, which relates to the energy derived from water movement caused by the gravitational forces of the Sun and Moon. Furthermore, waves and tides are distinct from ocean currents, which arise from other influences, such as the Coriolis Effect and differences in temperature or salinity.

Wave power generation has not yet reached commercial maturity, despite efforts to harness it dating back centuries [58]. Interestingly, current estimates suggest that the global wave power resource totals around 2.11 TW, which could potentially cover up to 90% of the average global electricity demand [59]. Therefore, advancements in wave energy harnessing could significantly contribute to the pursuit of clean energy. However, existing WEC technologies are unable to fully exploit this potential. Key challenges include high maintenance costs, insufficient infrastructure, and the general immature state of such concepts, all of which must be addressed before global adoption can occur (see e.g. [60]). The obstacles that wave energy development faces are considerable, particularly given its current underdevelopment compared to other renewable and conventional energy sources. As a result, it is perceived as less reliable and competitive than other renewable energy sources, which directly impacts, along with the aforementioned factors, the resulting Levelized Cost of Energy (LCOE); see e.g., [61].

Wave energy conversion technologies can be classified in several different ways, based on their working principle [62], geometry or primary location [63,64]. The number of existing wave energy harvesting concepts is immense. However, almost every device falls into one of three categories, namely point absorbers, attenuators and terminators. Point absorbers are devices with small dimensions, compared to the wavelength of the incident waves and are usually axisymmetric about a vertical axis [65]. Attenuators have one dominant horizontal dimension and are designed such that their principal axis is parallel to the dominant wave propagation direction, while terminators are devices whose dominant direction coincides with the wavefront, resulting in wave interception (see e.g., [62]). A review of wave energy technologies can be found in Ref. [66].

In this work's framework, point absorber WEC parks are studied as part of the broader objective of developing computational tools for modelling hybrid wave–solar offshore energy systems. While the primary focus is not on the direct modelling of these hybrid systems, the discussed methodologies and models provide a foundational framework for studying and evaluating various hybridization concepts. By combining the numerical techniques developed throughout this study, future research can extend these models to simulate and optimize the performance of hybrid energy systems that incorporate point absorber WEC parks alongside PV systems (and wind turbines). Interestingly, studies on wind–wave hybrid energy units, indicate that the "shadow effect" caused by WECs reduces the local wave heights and improves the operational conditions for co–located wind turbines [67].

The symmetry of point absorber WECs, combined with their compact dimensions, ensures that the direction of wave propagation has minimal impact on their overall efficiency [68]. However, this characteristic no longer holds when WECs are deployed in arrays or in regions characterized by bathymetric inhomogeneities. In the latter cases, the interactions between multiple devices, including diffraction and reflection phenomena, along with potential refraction effects induced by nearshore shoaling bathymetric profiles, can significantly amplify or diminish power absorption depending on propagation direction (see e.g., [69]). Additionally, hydrodynamic interactions between closely spaced floating bodies introduce complex effects, such as wave interference and energy redistribution, which can further alter the power absorption characteristics of each individual unit within an array. These factors must be carefully accounted for in the modelling of large–scale WEC installations to accurately predict their collective performance. The above phenomena are modelled and studied in the present work, aiming to provide the foundation and computational tools necessary for analyzing hybrid energy units.

1.5. *Methods*

The interaction of free surface gravity waves with floating bodies at intermediate depths, in areas possibly characterized by non–uniform seabed topographies, is a mathematically interesting problem which can be used to analyze a wide range of applications, such as the design and performance evaluation of ships and other floating structures operating in coastal regions. Theoretical aspects of the problem of small–amplitude water waves propagating over finite depth areas and their interaction with floating and / or submerged bodies have been presented under various geometric assumptions by many authors; see e.g. [70,71]. Furthermore, shallow–water conditions are commonly encountered in marine applications, particularly when floating structures or docks are anchored in areas with limited water depth. Precise predictions of the motions induced by prevailing sea states are paramount. These forecasts serve to optimize mooring systems based on stability requirements, as well as to ensure that the under–keel clearance remains adequate to prevent the structure from grounding in extreme weather and sea conditions specific to the area under examination. Accurate predictions are crucial not only for operational efficiency but also for mitigating the risk of structural damage or accidents due to insufficient clearance.

In many applications, the water depth is assumed to be constant. This assumption holds practical validity under circumstances where depth fluctuations are minor or where the dimensions of the floating body are significantly smaller than the variations in bottom topography. However, in scenarios involving the deployment of floating structures in coastal waters, variations in bathymetry can exert significant influences on the dynamic responses of these structures to wave–induced forces and moments. Under the premise of slowly varying bathymetry, mild–slope models have been developed to analyze the dynamic motions induced by waves on floating bodies. Nevertheless, to address environments characterized by abrupt changes in bathymetry – such as those encountered near coastlines or at the entrances of ports and harbours – more comprehensive models are requisite. These extended models are indispensable for accurately assessing and predicting the dynamic behaviour of floating structures in such complex and dynamic coastal environments. For instance, Ohyama and Tsuchida [72], used expanded mild–slope equations incorporating evanescent modes to study wave induced ship motion in a harbour. Their model accounts for incoming waves being diffracted and refracted before they reach the floating body. In addition, it accounts for re–reflection by breakwaters of diffracted and radiated waves propagating from the body, causing them to return to it. The study indicates that waves diffracted and radiated by a floating body can significantly influence the wave–height distribution in harbours [72].

The computational methods employed in this study are centered around the development of algorithms based on the application of the Boundary Element Method (BEM). These algorithms are specifically designed to calculate the dynamic behaviour of floating bodies with arbitrary geometries, as well as the hydrodynamics of ships moving at forward speed. Quantities of interest, such as power extraction, are computed either directly through the BEM models in the case of wave energy systems, or by coupling the hydrodynamic results with a photovoltaic model for floating PV systems and solar ships.

The Boundary Element Method is a powerful numerical technique that is widely used in engineering and physics to address problems related to potential flow, wave propagation, and other fluid–structure interaction scenarios. The core advantage of BEM models lies in the method's ability to reduce the dimensionality of the studied problems (from a volume integral to a boundary integral), which is achieved by using boundary integral representations of the studied flow fields (see e.g., [73]). Due to this property, the method is also called boundary integral equation method (BIEM) in the literature [74]. Direct Boundary Integral Equation (BIE) formulations and their modern numerical boundary element solutions were developed in the 1960s [75], leading to extensive research into BIE formulations and numerical methods throughout the next decades. The term "Boundary Element Method" was introduced in the mid–1970s, as an analogy to the Finite Element Method (FEM) [74].

The dimensionality reduction drastically limits the computational requirements, especially when dealing with complex domains. The method is particularly effective for modelling the hydrodynamic characteristics of floating bodies, as it accurately captures the effects of wave scattering, diffraction, and radiation, which are critical for analysing the behaviour of offshore structures, such as floating platforms [76], wave energy converters [68,77] and ships [78,79]. As regards the latter case, the BEM can account for the added complexities of ship motions due to both wave interactions and forward motion.

In the present dissertation, the BEM algorithms are integrated with several complementary techniques to enhance both their accuracy and computational efficiency. One of the key strategies employed is the use of Perfectly Matched Layers (PMLs), which are incorporated to absorb wave–like behaviour at the boundaries of the computational domain [80]. PMLs act as an artificial extension of the domain that prevents numerical reflections from the outer boundary, ensuring that wave propagation can be simulated as if the domain were infinite. This way, PMLs eliminate the need to model additional boundary parts, serving as radiation boundaries, thus reducing the total computational requirements. Mirroring techniques are also employed to further optimize computational efficiency. The latter techniques take advantage of inherent symmetries in many hydrodynamic problems, allowing for a significant reduction in the size of the required computational mesh without reducing the physical accuracy of the developed models. By reflecting the geometry across certain planes of symmetry, mirroring approaches ensure that only a portion of the problem domain needs to be modelled (see e.g. [77,79]), thereby also reducing the overall computational cost. In order to simulate more complex seabed topographies, a Coupled Mode Model is also incorporated [81,82], enabling the analysis of wave propagation over general seabed bathymetry, which is essential for simulating realistic environmental conditions.

Finally, to address the computational demands of the above models, parallel programming techniques are utilized to distribute the workload across multiple processors. This significantly accelerates the simulation process, allowing for the analysis of more complex and larger–scale problems, such as floating offshore structures subjected to complex environmental conditions, within feasible timeframes.

1.6. *Thesis outline and original contributions*

The investigation of offshore solar energy represents a collaborative convergence of solar energy technology and marine engineering. The rapidly expanding body of knowledge in both these fields creates a promising environment for advancing the development of floating solar solutions, facilitating their transition along the technology readiness level (TRL) spectrum [83]. The present work aims to bridge knowledge gaps between these diverse fields by proposing models and techniques for simulating and assessing the power output of floating solar platforms, solar–augmented vessels, and wave energy parks. Wave parks are modelled in standalone configurations. However, the developed models can be integrated for the study of hybrid systems. The results and findings aim to accelerate the utilization of marine renewable energy in EU countries, thus contributing to maintaining Europe's leadership in the development of innovative green energy technologies in both science and engineering.

Gaps in the current body of knowledge regarding floating solar technologies include the need for effective transformation of offshore environmental data for use in nearshore applications. Additionally, there is limited research on FPV performance in harsh marine conditions, particularly regarding the long–term effects on panel efficiency and the degradation mechanisms in these environments [84]. Another area that requires further investigation is the development of coupling methods for FPV marine applications, given that current models do not fully integrate hydrodynamics and structural motion. By addressing the above issues, the present work aims to provide insights that could support the development of guidelines and standardization efforts by the EU, helping to establish a technological framework for the deployment of nearshore / offshore FPV systems in EU waters and beyond, raising international interest and paving the way for market growth in offshore FPV.

Offshore PV installations require a supporting resilient ballast structure. In the offshore and nearshore region, safety and viability require the design and construction of resilient FPV structures that can withstand the harsh marine environment. Regarding the deployment of floating structures of relatively large dimensions in nearshore and coastal areas, it is also expected that bathymetric variations may significantly affect their responses under wave loads, which in turn alter the performance of the power output, due to oscillatory motions of the structure and the panels arranged on deck. Stability requirements, in conjunction with the need for a lightweight structure with the center of gravity located at a relatively increased height above the keel, prompted the adoption of a twin–hull design [see Figure 1-9(a)].

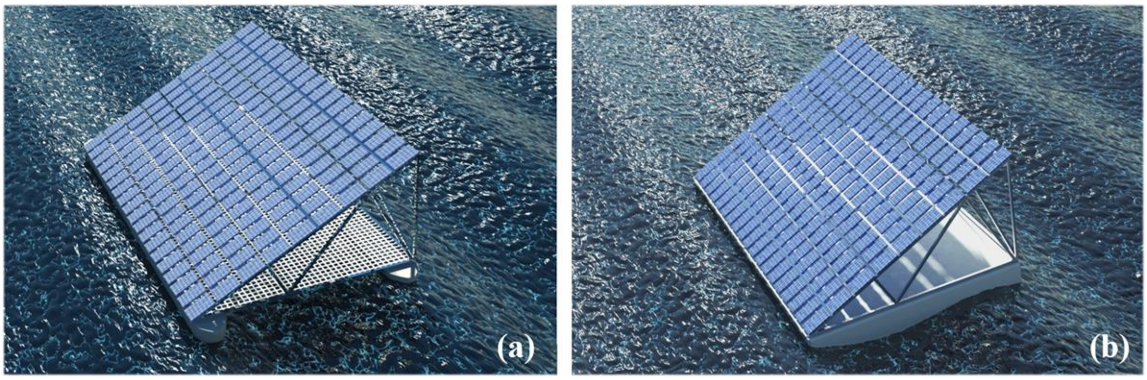

Figure 1-9. Photorealistic illustration of (**a**) Twin–Hull FPV and (**b**) pontoon–type FPV.

Twin–hull structures can be designed so as to present increased freeboard height offering protection of PV panels on deck from splashing and green water. In that case, there is also sufficient space below the main deck for arrangement of required ballast tanks, machinery and electrical systems (switchboards, inverters, cables, transmission, connection to grid etc.) and battery rooms for storage. Finally, they are characterized by very low towing resistance, facilitating mobility from production to deployment as well as the possibility of usage as a supplementary or emergency energy station for small islands and isolated touristic and other coastal industry facilities.

As concerns the Mediterranean Sea, several islands are not yet connected to the main electricity grid and rely on independent local grids to meet their power needs. The latter grids primarily use imported fossil fuels [85]. Consequently, the discussed systems offer a promising solution to mitigate this issue by providing a renewable and local energy source, reducing reliance on costly and environmentally damaging fossil fuels. On the other hand, twin–hulls introduce more complex response patterns and resonance characteristics into the analysis since the interactions between the two hulls generate additional hydrodynamic forces, leading to varying motions and wave patterns which in turn result in amplified or reduced responses under certain conditions.

Pontoon–type platforms are also modelled and investigated as an alternative scenario for floating PV installations [see Figure 1-9(b)]. These structures typically offer a simpler and more cost–effective design compared to twin–hulls, with a wide and stable surface area that provides sufficient space for accommodating PV panels and associated equipment. They enable easy scalability and adaptability to different deployment sizes and site–specific conditions. However, their low freeboard height makes them more susceptible to wave overtopping and splashing, which could compromise the durability of PV systems and other onboard components. Furthermore, pontoons generally have higher hydrodynamic resistance, which can increase towing and installation challenges. Despite these drawbacks, their straightforward design and lower construction costs make them an appealing option for certain applications.

The solar ship concept is examined via a 33–meter–long catamaran vessel (see Figure 1-10), utilizing optimized hull lines derived from the literature [86]. To assess the vessel's performance, BEM models are developed, focusing on evaluating the resistance, dynamic responses and added resistance of the vessel under various conditions. The modelling aims to quantify how effectively a mounted PV system can meet the vessel's energy demands, helping to determine the feasibility of solar–powered maritime solutions.

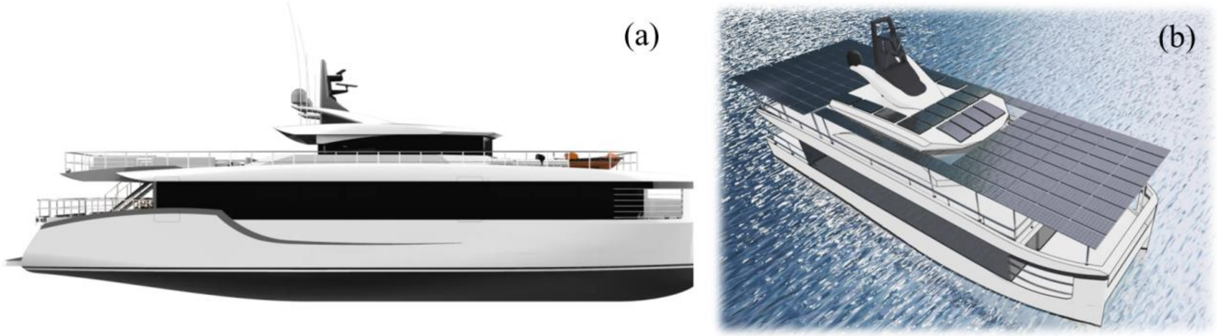

Figure 1-10. (**a**) 33–m–long catamaran vessel (source: https://elcatproject.gr/). (**b**) 3D model of the vessel with integrated PV system.

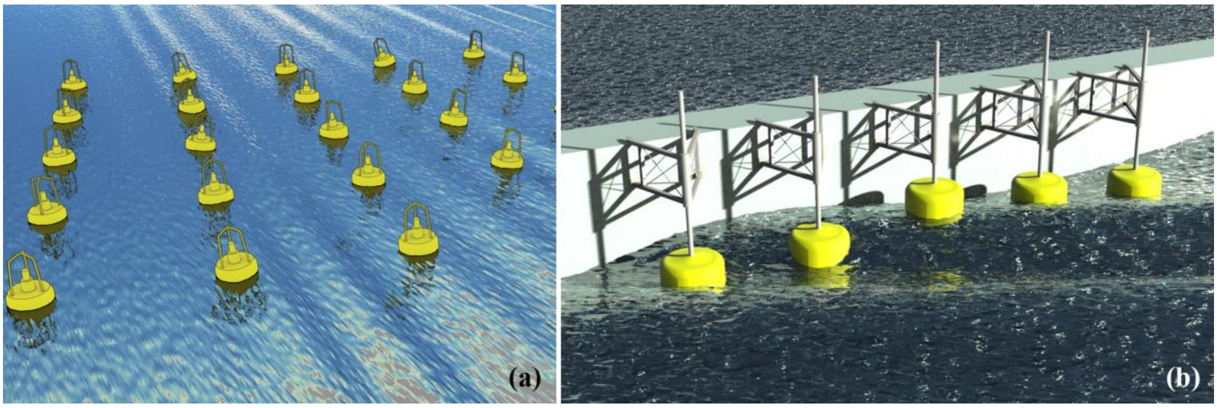

Figure 1-11. (**a**) Wave park comprising multiple point absorber WECs. (**b**) WEC array attached to a breakwater.

The final section of the work focuses on the operation of wave energy parks consisting of multiple point absorber devices (see Figure 1-11). It examines how the performance of such energy parks is influenced by several key factors, based on specific assumptions regarding the geometry and positioning of the floaters. The analysis explores the impact of varying water depths, intra–array hydrodynamic interactions between multiple floating devices, as well as the effects that breakwaters pose on the operation of such systems [see Figure 1-11(b)]. The above factors are critical in understanding how efficiency can be optimized, highlighting the complex dynamics involved in the design and operation of such systems.

The author's contributions in terms of scientific peer–reviewed publications, including works directly derived from the research conducted in the context of the present thesis, as well as works addressing other relevant aspects developed during the doctoral studies, are listed below:

P1. Magkouris, A.; Bonovas, M.; Belibassakis, K. Hydrodynamic Analysis of Surge-Type Wave Energy Devices in Variable Bathymetry by Means of BEM. *Fluids* **2020**, *5*, doi:10.3390/fluids5020099.

P2. Belibassakis, K.; Magkouris, A.; Rusu, E. A BEM for the Hydrodynamic Analysis of Oscillating Water Column Systems in Variable Bathymetry. *Energies* **2020**, *13*, doi:10.3390/en13133403.

P3. Magkouris, A.; Belibassakis, K.; Rusu, E. Hydrodynamic Analysis of Twin-Hull Structures Supporting Floating PV Systems in Offshore and Coastal Regions. *Energies* **2021**, *14*, doi:10.3390/en14185979.

P4. Bonovas, M.; Magkouris, A.; Belibassakis, K. A Modified Mild-Slope Model for the Hydrodynamic Analysis of Arrays of Heaving WECs in Variable Bathymetry Regions. *Fluids* **2022**, *7*, doi:10.3390/fluids7060183.

P5. Magkouris, A.; Belibassakis, K. A Novel BEM–FEM Scheme for the Interaction of Water Waves with Multiple Vertical Cylinders in the Presence of Currents. *Fluids* **2022**, *7*, doi:10.3390/fluids7120378.

P6. Magkouris, A.; Rusu, E.; Rusu, L.; Belibassakis, K. Floating Solar Systems with Application to Nearshore Sites in the Greek Sea Region. *Journal of Marine Science and Engineering* **2023**, *11*, doi:10.3390/jmse11040722.

P7. Magkouris, A.; Bonovas, M.; Gerostathis, T.; Belibassakis, K. A 3D BEM Model for the Hydrodynamic Analysis and Design of Heaving WEC Arrays Attached to a Breakwater. *Sustainability* **2023**, *15*, doi:10.3390/su151712777.

P8. Gerostathis, T.; Magkouris, A.; Belibassakis, K. A 3D BEM-Coupled Mode Model for the Performance Analysis of Wave Energy Converter Parks in Nearshore-Coastal Regions. *Journal of Marine Science and Engineering* **2024**, *12*, doi:10.3390/jmse12020212.

P9. Magkouris, A ; Belibassakis, K. A Novel BEM for the Hydrodynamic Analysis of Twin-Hull Vessels with Application to Solar Ships. *Journal of Marine Science and Engineering* **2024**, *12*, doi:10.3390/jmse12101776.

P10. Malara, G.; Arena, F.; Magkouris, A.; Belibassakis, K. Response and power output of U-oscillating water column operating in variable bathymetry regions. Journal of Ocean Engineering and Marine Energy 2024, doi:10.1007/s40722-024-00367-5.

Works have also been presented at the following international conferences and published in the corresponding proceedings:

C1. Belibassakis, K.; Magkouris, A. A BEM for the performance of surge-type wave energy devices in variable bathymetry. In Proceedings of the *5th International Conference on Maritime Technology and Engineering* (*MARTECH 2020*), Lisbon, Portugal, 2020.

C2. Magkouris, A.; Belibassakis, K.A.; Filippas, E. A 3D BEM for the propagation of water waves scattered by arrays of vertical cylinders in the presence of currents. In Proceedings of the *6th International Conference on Maritime Technology and Engineering* (*MARTECH 2022*), Lisbon, Portugal, 2022.

C3. Belibassakis, K.; Bonovas, M.; Magkouris, A. Hydrodynamic analysis of WEC array in variable bathymetry regions by a simplified mild-slope model. In Proceedings of the *5th International Conference on Renewable Energies Offshore* (*RENEW 2022*), Lisbon, Portugal, 2022.

C4. Magkouris, A.; Belibassakis, K. A 3D BEM-CMS scheme for the hydrodynamic analysis of floating structures supporting PV systems in general seabed topography. In Proceedings of the *5th International Conference on Renewable Energies Offshore* (*RENEW 2022*), Lisbon, Portugal, 2022.

C5. Magkouris, A.; Karperaki, A.; Belibassakis, K. A coupled BEM-FEM scheme for the interaction of water waves with multiple vertical cylinders in the presence of currents. In Proceedings of the *19th International Congress of the International Maritime Association of the Mediterranean* (*IMAM 2022*), Istanbul, Turkey, 2022.

C6 Bonovas, M.; Magkouris, A.; Belibassakis, K. Effects of control strategies on the performance of floating WEC point absorbers operating attached to a breakwater by time-domain simulator. In Proceedings of the *15th European Wave and Tidal Energy Conference* (*EWTEC 2023*), 2023.

C7. Magkouris, A.; Belibassakis, K. Performance of photovoltaic systems supported by twin-hull floating structures in offshore and coastal regions. In Proceedings of the *XII International Conference on Structural Dynamics* (*EURODYN 2023*), Delft, The Netherlands, 2023.

C8. Gerostathis, T.; Magkouris, A.; Belibassakis, K. Wave energy converter arrays performance in variable water depth regions. In Proceedings of the *7th International Conference on Maritime Technology and Engineering* (*MARTECH 2024*), Lisbon, Portugal, 2024.

C9. Belibassakis, K.; Magkouris, A.; Malara, G.; Arena, F. Response of U-Oscillating Water Column installed in a variable bathymetry region In Proceedings of the *34th International Ocean and Polar Engineering Conference* (*ISOPE 2024*), Rhodes, Greece, 2024.

Part I

ANALYSIS OF FLOATING PV UNITS

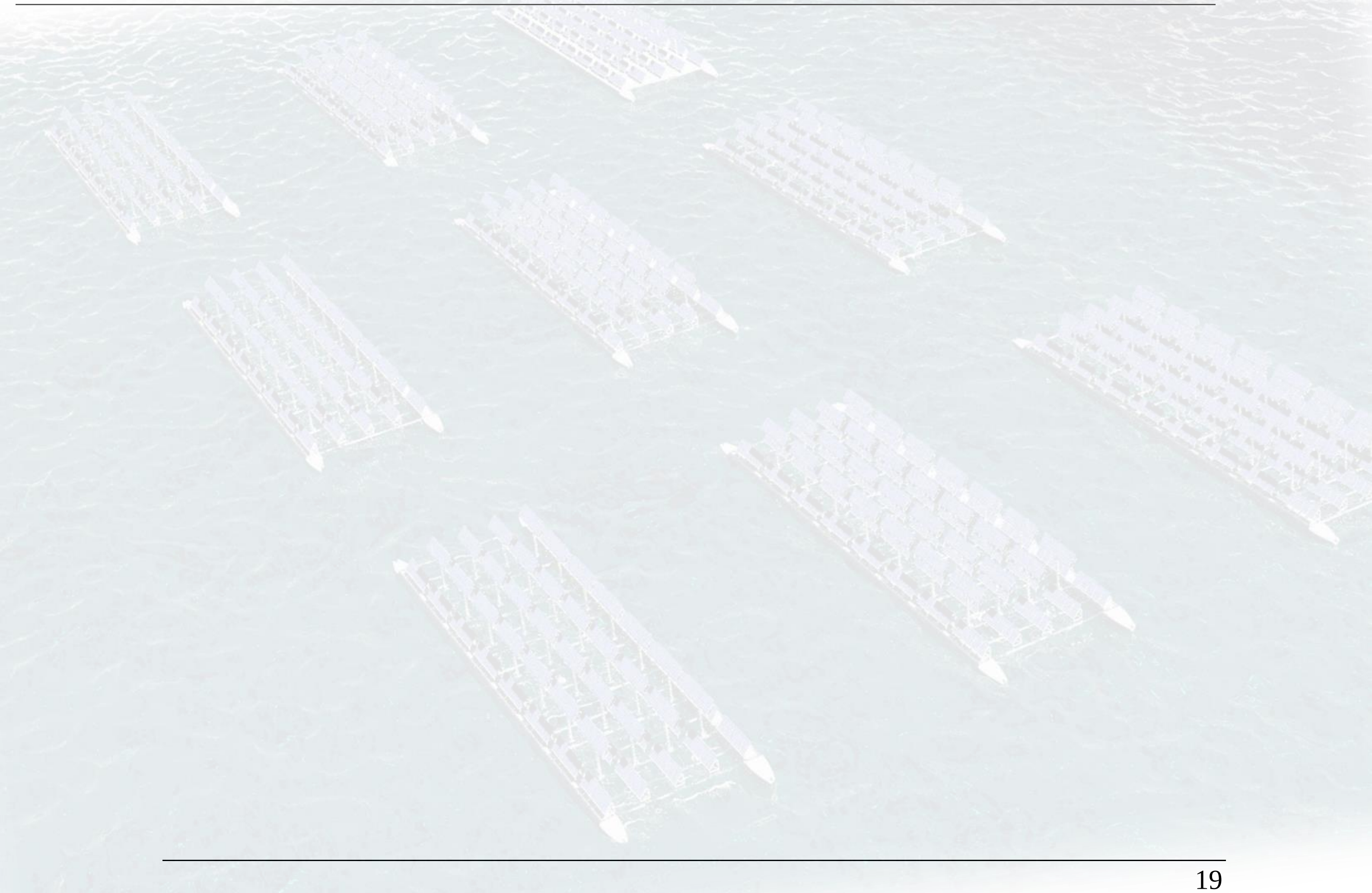

2

PV SYSTEMS AND THE EFFECTS OF HYDRODYNAMICS

Photovoltaic systems have gained widespread attention as a sustainable solution for renewable energy generation [87]. These systems typically consist of solar panels, inverters, and associated components that convert sunlight into electrical power, via the photovoltaic effect. The latter phenomenon – first observed by the French physicist Alexandre Edmond in 1839 and later described by Albert Einstein in 1904 [88] – refers to the process by which certain materials (typically semiconductors like silicon [89]) generate an electric current when exposed to electromagnetic radiation. Semiconductors are materials whose electrical conductivity lies between that of conductors and insulators [90]. The energy difference between the valence band, where electrons are bound, and the conduction band, where electrons are free to move (band gap) in semiconductors is small enough so that electrons can be excited into the conduction band with the addition of sufficient energy, such as heat or light, allowing the material to conduct electricity under certain conditions.

2.1. *Photovoltaic cell operation*

When sunlight photons strike a semiconductor material, their energy can excite electrons. In case the photon energy is sufficient, it promotes electrons from the valence band to the conduction band, overcoming the band gap. Silicon, which has four (4) valence electrons, forms the basis of most solar cells [91]. To modify its conductivity, silicon undergoes a process called doping, where pentavalent atoms (such as phosphorus) are introduced to create n–type material, which has an excess of electrons, while trivalent atoms (like boron) are used to create p–type material, which has an excess of holes (electron deficiencies) [92]. When silicon is doped with pentavalent atoms in one part and trivalent atoms in another, a material is formed with both p–type and n–type portions, creating a p–n junction. At the junction, electrons from the n–type region are diffused into the p–type region, while holes from the p–type region are diffused into the n–type region. As a result, a depletion region is created, where no free charge carriers are present due to the recombination of electrons and holes; see Figure 2-1(b). An electric field is established across the depletion region, which acts to separate the electron–hole pairs generated by incoming light. This electric field drives the free electrons toward the n–type region and the holes toward the p–type region, creating a flow of electric current when the solar cell is connected to an external circuit.

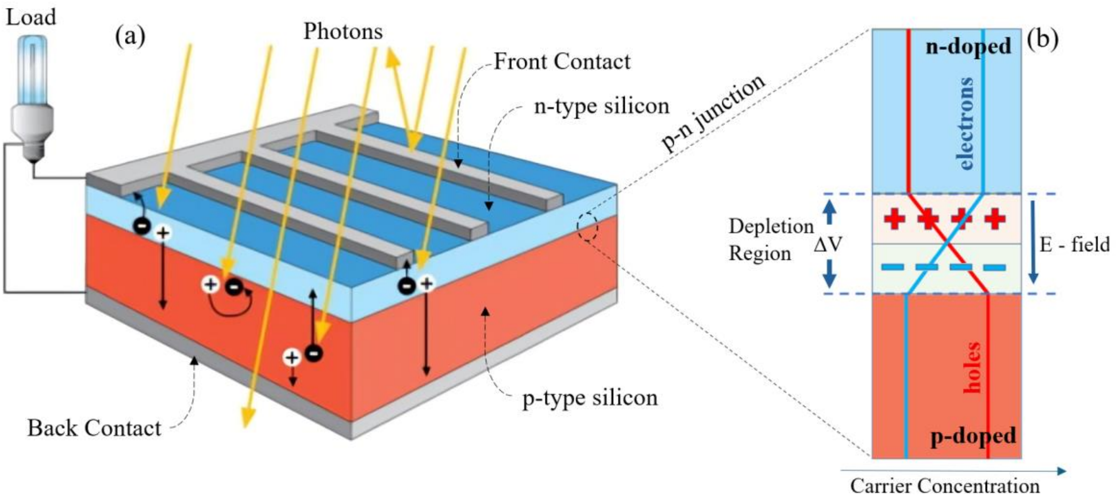

Figure 2-1. (**a**) Essential interfaces and surfaces of a solar cell. Adapted from [87]. (**b**) p–n junction and depletion region. Adapted from [93].

Basic solar cell structure also comprises metal contacts, which are crucial for extracting current [see Figure 2-1(a)]. The front contact – typically a metal grid on the n–type layer – collects free electrons while minimizing sunlight blockage. The back contact on the p–type layer provides a path for holes, thus completing the circuit. Together, these contacts enable current flow through external loads, supplying usable power.

Solar cells are the basic building blocks of solar energy systems. Multiple solar cells, connected in series and parallel, comprise a solar panel which produces a certain power output [94]. Panels are then combined into larger arrays to increase power output. Inverters convert the generated variable direct current (DC) output of a photovoltaic panel into alternating 220V current (AC) for grid compatibility [95]. When scaled up and deployed across large areas, along with monitoring and control systems, these interconnected arrays form a solar farm, capable of supplying renewable energy to meet regional demands.

2.2. *Basic performance factors*

The performance of PV systems is influenced by several factors, including solar irradiance, panel efficiency, temperature and orientation. Solar irradiance, or the amount of sunlight reaching the panels' surface, directly impacts energy generation, varying with the time of day, the seasons and the weather conditions. This irradiance comprises three primary components, namely beam irradiance, diffuse irradiance and reflected irradiance (see Figure 2-2).

Beam irradiance refers to the direct sunlight that reaches the panel's surface, when the sun rays are unobstructed by clouds or other atmospheric conditions. Diffuse irradiance is the sunlight scattered in the atmosphere, which reaches the panels from all directions. Finally, reflected irradiance refers to the sunlight that is reflected by nearby surfaces, such as the ground or surrounding structures, which also contributes to the total energy available to the PV system.

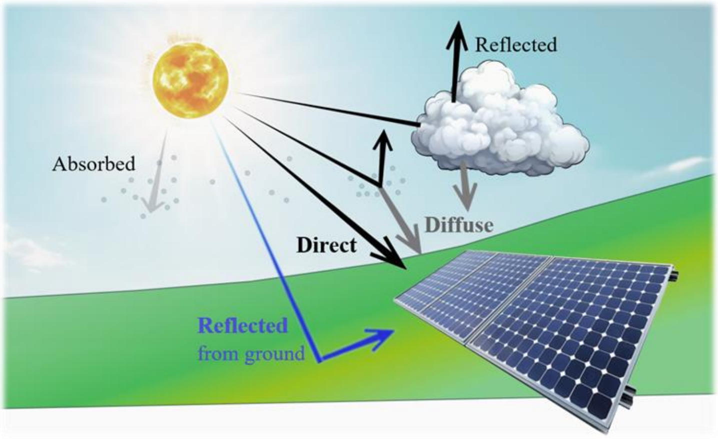

Figure 2-2. Main components of irradiance reaching a solar panel.

Cell temperature plays a significant role, as higher temperatures typically cause the efficiency of PV modules to decrease [96]. This is mainly caused by the increased rate at which charge carriers (electrons and holes) recombine inside the cell, due to increased carrier concentrations resulting from thermal excitation [97]. As more carriers are generated, the likelihood of them recombining before they can contribute to electricity production increases, leading to a decrease in the overall efficiency of the solar cell.

The tilt angle (β – angle between the solar panel and the horizontal plane) and azimuth angle (ψ – direction the panel faces, measured clockwise from true north) are also crucial parameters for maximizing sunlight capture. It is widely acknowledged that in the northern hemisphere, optimum azimuth angle for tilted surfaces is facing due South [98,99], while the optimum tilt angle varies depending on the latitude (φ) and the time of year. A commonly accepted approach is using $\beta = \varphi$ as a yearly optimal value for the tilt angle [100]. However, numerous studies have been conducted to determine seasonal (as well as daily) adjustments regarding optimal tilt angles. For instance, Stanciu C. and Stanciu D. [101] determined the optimal tilt angle for a flat plate collector across latitudes ranging from 0° to 80° as $\beta = \varphi - \delta$, considering the latitude (φ) as well as the Earth's declination angle δ. The latter quantity (also called solar declination) refers to the angle between the sun rays and the Earth's equatorial plane [102]. It represents how far north or south the Sun is relative to the celestial equator at any given time (see Figure 2-3), thus directly impacting the beam irradiance received by a specific location on Earth. The declination angle can be evaluated as [103]; [see Figure 2-3(d)],

$$\delta = -23.45\cos\left[\frac{360}{365}\left(d+10\right)\right], \tag{2.1}$$

where d denotes the day of the year with January 1 as $d = 1$. Eq. (2.1) is based on the assumption that the sun's orbit is a perfect circle, while the adjustment of ten (10) days in the argument of the cosine function reflects the fact that the winter solstice ($\delta = -23.45°$) occurs approximately ten days before the start of the calendar year [104]. A more accurate estimation for solar declination, accounting for additional factors, is discussed in Ref. [105]. Moreover Ref. [106] reviews several studies and optimization techniques developed to derive more accurate formulae for determining the optimal tilt angles of solar systems, taking into account various geographical locations and solar technologies.

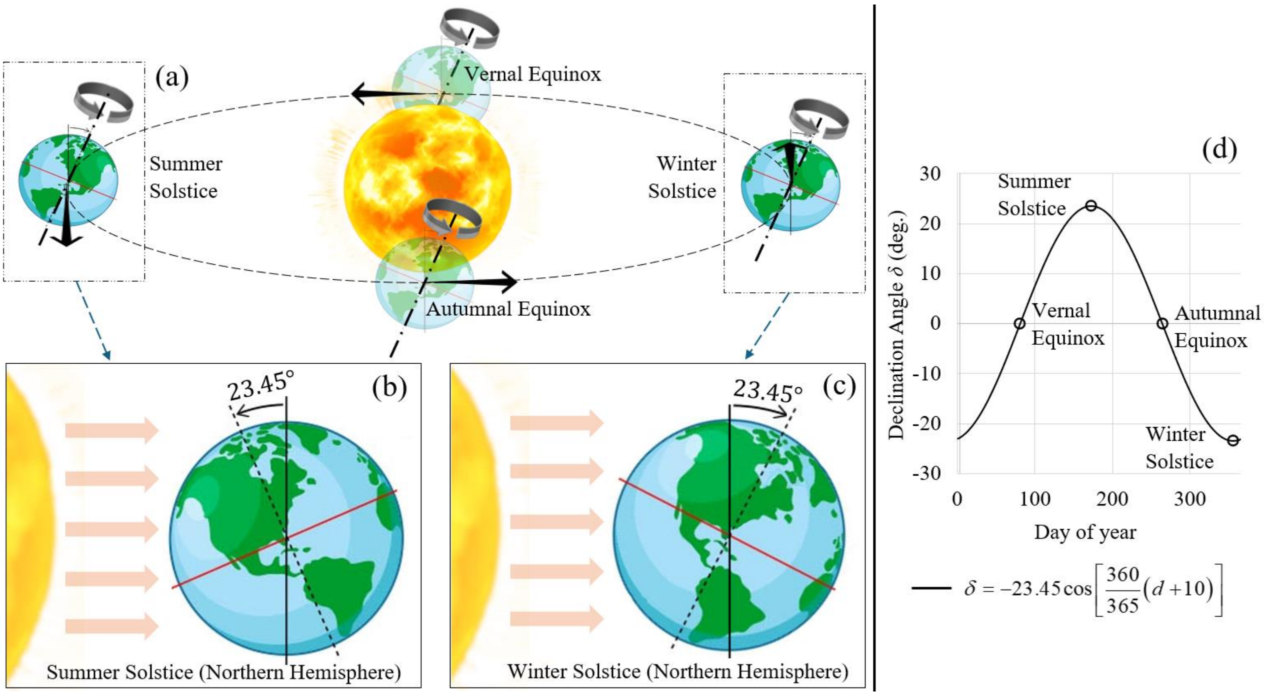

Figure 2-3. (**a**) Earth's orbit, indicating the positions of equinoxes and solstices. Earth's position during (**b**) the summer solstice and (**c**) the winter solstice. (**d**) Solar declination (δ) throughout the year.

Finally, electrical performance is influenced by several factors such as the voltage, current, power output, as well as inverter design [107]. An extended review of the factors affecting solar performance can be found in Ref. [108].

2.3. *PV model*

As global demand for renewable energy continues to rise, new opportunities are emerging to expand the use of photovoltaic (PV) systems, including innovative floating PV systems deployed on floating platforms in water bodies such as lakes, reservoirs, or the open sea. As regards the latter case, it integrates the established principles of photovoltaic energy conversion with the distinct challenges and advantages presented by marine environments. Notably, the dynamic behaviour of floating platforms introduces hydrodynamic effects that can influence the performance of PV modules in ways that differ from those encountered in conventional land–based systems. These effects include platform angular motions, such as roll, pitch and yaw, which can induce dynamic variations in the tilt and azimuth angles of the photovoltaic modules relative to the sun, leading to fundamentally different operational conditions from the stable ones encountered in land–based applications. These dynamic conditions must be accounted for in the modelling, design and operation of FPV systems.

While certain factors that influence the energy efficiency of FPV are also found in corresponding land–based units, with comparable power output levels, others are not present in land installations. In open water, there is generally a higher level of humidity than inland, as well as lower ambient temperatures. Several factors contribute to the temperature drop, including the transparency of water (which leads incoming solar radiation to exceed the surface layer and be transmitted to the inner layers of the medium) [109], as well as the fraction of incident irradiation that is used for evaporation. Furthermore, wind speed is typically higher than on land due to longer fetch distances. The above parameters contribute to maintaining a lower operating temperature of the solar cells, which in turn leads to increased efficiency. In the context of the present work, the following equation is used to evaluate the instantaneous power generation by floating PV units [104],

$$P(t)=\eta_{pv}A_{pv}G\left(1-k_p\left(T_c-T_{\mathrm{STC}}\right)\right),\ \text{ where } G=B+D+R, \tag{2.2}$$

also accounting for the effects of dynamics induced by hydrodynamic loads, as discussed in more detail in the sequel. In Eq. (2.2), P is the power generated by the solar panels, η_{pv} is the efficiency of the panels on standard test conditions (STCs), A_{pv} is the panel surface area, G is the global irradiance on the panels, k_p is the temperature coefficient, T_c is the cell's temperature in a specific time and T_{STC} is the standard test temperature (25°C). The beam and diffuse components are computed as follows (see, e.g., [104]),

$$B=DNI\left[\ell_1+\ell_2\cos(HRA)+\ell_3\sin(HRA)\right],\ \text{ where} \tag{2.3}$$

$$\ell_1=\sin(\delta)\sin(\varphi)\cos(\beta)-\sin(\delta)\cos(\varphi)\sin(\beta)\cos(\psi), \tag{2.4}$$

$$\ell_2=\cos(\delta)\cos(\varphi)\cos(\beta)+\cos(\delta)\sin(\varphi)\sin(\beta)\cos(\psi), \tag{2.5}$$

$$\ell_3=\cos(\delta)\sin(\psi)\sin(\beta)\ \text{ and} \tag{2.6}$$

$$D=DHI\,(\pi-\beta)/\pi\,. \tag{2.7}$$

In the above equations, DNI is the Direct Normal Irradiance on a plane always normal to the sun rays and DHI is the diffuse horizontal irradiance, which quantifies the amount of solar radiation received by a horizontal surface from sunlight that has been scattered by atmospheric particles or clouds [110]; see Figure 2-2. DNI is often not directly measured due to practical limitations and is instead estimated from global and diffuse horizontal irradiance measurements or satellite–based models [105]. In the framework of the present work, DNI and DHI are derived from databases that incorporate such models. Furthermore, in Eqs. (2.3)–(2.7), φ is the latitude of the studied location, ψ is the module azimuth (measured from South to West) and β is the panel tilt. The Hour Angle (HRA) is a critical parameter in solar position calculations, which determines the angle between the meridian plane that passes through the Sun's center and the local meridian at the observer's location [102]; see Figure 2-4. The Hour Angle can be evaluated as,

$$HRA=15^{\circ}(LST-12)\,, \tag{2.8}$$

where LST is the Local Solar time with $LST = 12$ corresponding to solar noon ($HRA = 0°$). Eq. (2.8) is based on the fact that the Earth rotates 15° every hour. The basis for defining Local Solar Time is the Local Standard Time Meridian ($LSTM$) which defines an angle, measured in degrees of longitude, representing the central meridian of a time zone, spaced at 15° intervals that correspond to each hour of the Earth's rotation relative to Coordinated Universal Time (UTC),

$$LSTM=15^{\circ}\times\Delta T_{\mathrm{UTC}}. \tag{2.9}$$

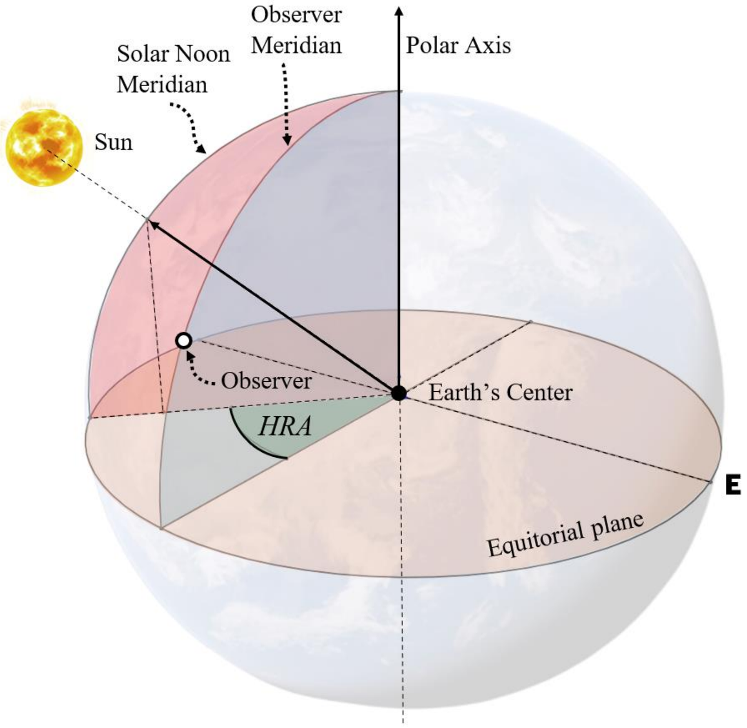

Figure 2-4. Hour Angle (HRA) with respect to an observer's meridian.

In Eq. (2.9), ΔT_{UTC} is the Time Zone Offset from UTC. More specifically, the Local Solar Time can be evaluated by means of the local time (LT) as

$$LST = LT + \frac{C}{60}, \tag{2.10}$$

where C is a correction factor expressed in minutes [111].

In particular, the latter correction factor accounts for the differences between an observer's local solar time and the standard time in the specified time zone. It is calculated as,

$$C = 4(\lambda - LCTM) + EoT, \tag{2.11}$$

where the first term adjusts for the observer's longitude (λ) relative to the time zone's central meridian ($LSTM$), with each degree of longitude corresponding to four (4) minutes. EoT is the Equation of Time, measured in minutes, which can be computed as [112],

$$EoT = 9.87\sin(2Q) - 7.35\cos(Q) - 1.5\sin(Q), \text{ where } Q = \frac{360}{365}(284 + d). \tag{2.12}$$

The latter term is used to account for the difference between solar time (measured by a sundial) and mean time (measured by a clock); see Figure 2-5. This difference arises from two main factors [113], namely the Earth's elliptical orbit – causing its speed to vary throughout the year – and the tilt of the Earth's axis with respect to the ecliptic plane (see Figure 2-3), which causes a second sinusoidal variation with double the frequency. Finally, as concerns the evaluation of Beam Irradiance, the varying distance between the Earth and the Sun is not explicitly factored into the calculations, as it is assumed that the DNI data already account for this variation.

Regarding the reflected irradiance component R, it is approximated in the present model by [114],

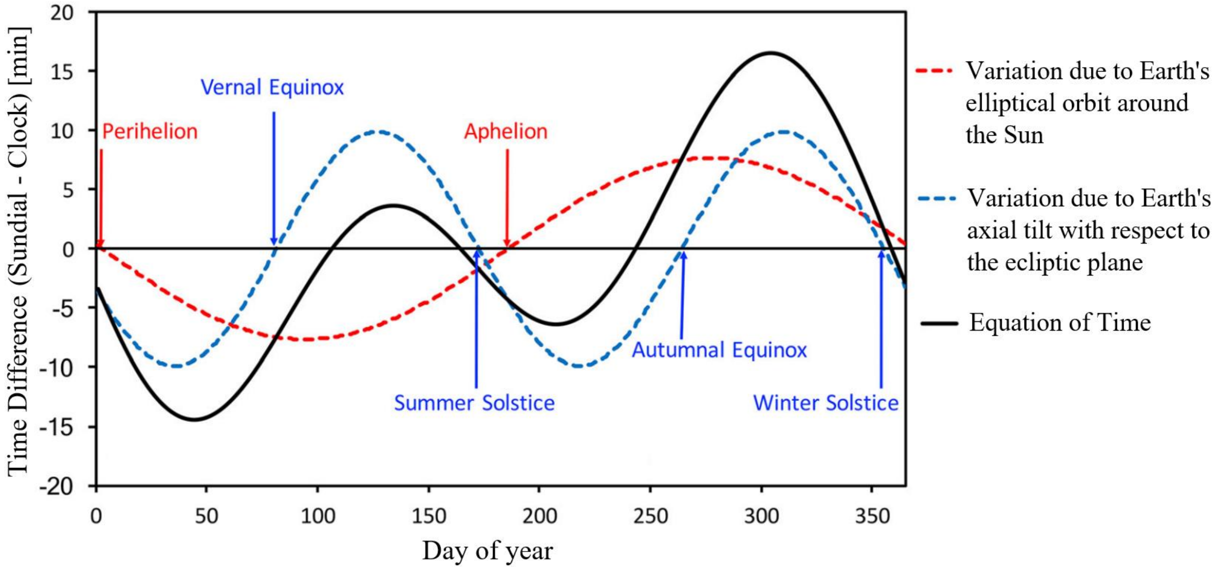

Figure 2-5. The Equation–of–Time (*EoT*) and its two components. Adapted from [113].

$$R = c \cdot GHI \frac{1-\cos(\beta)}{2}, \tag{2.13}$$

where GHI is the global horizontal irradiance (see e.g., [115]), evaluated as the sum of the Direct Normal Irradiance, projected onto a horizontal surface, and the Diffuse Horizontal Irradiance [116],

$$GHI = DNI\cos(\theta_z) + DHI, \tag{2.14}$$

and θ_z denotes the solar zenith angle, defined as the angle between the vertical direction (zenith) and the line connecting an observer to the sun's position. The latter angle can be evaluated based on the previous analysis as [117],

$$\cos(\theta_z) = \sin(\varphi)\sin(\delta) + \cos(\varphi)\cos(\delta)\cos(HRA). \tag{2.15}$$

In Eq. (2.13), the coefficient c models the albedo effect. For water bodies this coefficient is approximately $c = 0.1$, while in rural areas it typically ranges from 0.2 to 0.4; see e.g., [118]. In the present work's context, data concerning the direct normal irradiance (DNI), diffuse horizontal irradiance (DHI) and environmental conditions concerning the temperature and wind for specific sites are obtained from the PVGIS SARAH2 database in the form of a typical meteorological year (TMY) data set with a 1–hour temporal resolution, provided by PVG tools (https://re.jrc.ec.europa.eu/pvg_tools/en/). The latter data set provides information concerning the dry–bulb temperature, relative humidity and wind speed, from which the ambient temperature is calculated as [119],

$$T_A = T_{DB} + 0.33p_V - 0.7U - 4, \tag{2.16}$$

where T_A is the apparent temperature, T_{DB} is the dry–bulb temperature at 2 m height, U is the wind speed and p_V is the vapor pressure in hPa, which is calculated using the following equation,

$$p_V = \exp\left[1.8096 + 17.69D_T / \left(273.3 + D_T\right)\right]. \tag{2.17}$$

In Eq.(2.15), D_T is the dew point temperature and it is estimated based on the relative humidity (RH), using the approximate formula $D_T = 100 - 0.2(100 - RH)$, that is valid for $RH > 50\%$ (which is expected in coastal and nearshore regions). The values of RH included in the TMY data set are used for calculations regarding land–based configurations, while at sea it is assumed that $RH = 80\%$ [120]. After calculating the ambient temperature, the panel cell temperature can be estimated using the following correlation, provided by Sandia National Laboratories [121],

$$T_C = G\exp\left(a + bU\right) + T_A\,, \tag{2.18}$$

where G is the incident solar irradiance on the panels and a, b are parameters depending on the module construction, which for glass / cell / polymer sheet panels are defined as $a = -3.56, b = -0.075$ [121]. In the present work's framework, the analyses discussed are restricted to the latter type of panels to shift the focus toward the effects of hydrodynamics on FPV systems and narrow down the influence of additional variables. The aforementioned values of the parameters a and b constitute empirically derived constants, based on land–based PV systems, and their use in the analysis of floating PV systems is based on the assumption that the fundamental mechanisms of heat transfer are similar in both environments. In particular, while floating systems may experience some additional cooling from the water surface, it is assumed the primary factors affecting cell temperature (irradiance and wind speed) behave similarly in both settings.

2.3.1. Hydrodynamic Effects on Floating PV

In the first two Parts of the present thesis, the above PV model is applied alongside results derived from various hydrodynamic models to investigate the influence of dynamics on floating photovoltaic (FPV) systems and solar ships. The general framework and hydrodynamic theory applied is included in Appendix A, for completeness purposes. The different utilized hydrodynamic models include both two–dimensional (2D) and three–dimensional (3D) frameworks, each addressing specific aspects. Certain models incorporate the effects of local bathymetry and shallow water conditions, which are critical for accurately computing the hydrodynamic loads acting on floating structures in nearshore areas. Additionally, §5 investigates twin–hull vessels, operating as solar augmented travelling ships, studying the dynamic interactions between hydrodynamic forces and forward motion under varying operational conditions. The above approaches enable the analysis and understanding of hydrodynamic influences on PV systems across a range of applications and environments. The focus is specifically placed on the dynamic changes in instantaneous orientation of mounted PV systems, which are influenced by the movement of floating platforms / moving ships. The variations in orientation, induced by the hydrodynamic loads, can significantly affect the system's energy yield, efficiency, and overall performance and thus it is crucial to incorporate these dynamic factors into the modelling and performance analysis of FPV systems to ensure more accurate predictions.

The angular motions (roll, pitch and yaw) impose significant implications regarding the orientation of mounted PV systems. Yaw, which refers to the rotational motion around the vertical axis of a floating structure, dynamically alters the azimuth angle of the mounted panels. In cases where the panels are aligned with the longitudinal axis of a floating platform, the rolling motion, (representing rotation around the longitudinal axis), directly influences the tilt angle of the modules, as any variations in roll induce corresponding changes in tilt. Conversely, the pitching motion (rotation about the lateral axis), does not affect the tilt or azimuth angles, as its impact does not align with the panel orientation. However, in case the panels are not aligned with the longitudinal or the lateral axis of a supporting structure, both rolling and pitching motions affect the tilt in the short time scale. The translational degrees of freedom (DoFs) of any supporting structure (surge, sway and heave) do not directly impact the PV model. Nonetheless, the overall hydrodynamic behaviour of any structure placed on a water body is affected by all DoFs, since the equations of motion form coupled systems (refer to Appendix A).

Solar tracking is significantly easier to implement in FPV, as compared to traditional land–based installations, as the platforms can be dynamically oriented without the constraints of rigid foundations (see e.g., [122]). Although the latter aspect is not addressed in the present work's framework, recent studies have indicated that single–axis and dual–axis tracking PV systems with appropriate control systems can increase electrical energy production by 22–56% [33].

Floating platforms also offer the potential for hybrid systems when integrated with wave energy converters (WECs), such as point absorbers (see e.g., [123]). This synergy allows for the coupling of solar and wave energy generation, optimizing the use of marine space. The hydrodynamic modelling of wave parks based on point absorber WECs is explored in §6 and §7. The study of hybrid FPV–WEC systems remains a promising area for future investigation, offering opportunities for more efficient renewable energy solutions in marine environments. WEC arrays are already being studied in the context of wind–wave hybrid energy units, with results indicating that the "shadow effect" created by WECs can locally reduce the values of the wave height distribution within the array, enhancing operational conditions for co–located wind turbines [67]. The latter effect opens up new opportunities for integrating floating photovoltaic systems in these same spaces. The study of such hybrid systems can be achieved by extending and unifying the modelling techniques discussed in the present work, which remains an open topic for future research.

3

SIMPLIFIED 2D MODEL OF TWIN–HULL FPV UNIT

In this chapter, preliminary results are derived, regarding a twin–hull floating PV Module's wave induced dynamic responses, via a two–dimensional simplified Boundary Element Method (BEM) model. The simulations aim towards the investigation of the marine environment's effects on the floating photovoltaic module, as concerns the dynamics of the structure, using a low–order boundary element method, based on linear wave theory. Following the hybrid formulation by Yeung [124], the present method utilizes the simplicity of Rankine sources, in conjunction with appropriate representations of the wave field in the exterior semi–infinite domain, as presented by Nestegard & Sclavounos [125] for 2D radiation problems in deep water and by Drimer & Agnon [126] in the case of finite water depth. Subsequently, results are extracted using systematic applications in selected examples, illustrating the effect of dynamic motions on the energy efficiency of the floating unit.

The interactions of the wavefield, both with the floating structure and the seabed are taken into account. The numerical formulation allows for the seabed profile to be inhomogeneous, exhibiting mild or steep depth variations, as well as corrugations. This allows for the investigation of potential effects on the module, triggered by the interaction of the wave field with the local seabed topography. Furthermore, the model is capable of simulating the interaction of the field with twin–hull structures, which are inevitably characterized by complicated resonance characteristics.

A boundary integral representation is applied for the near–field in the vicinity of the floating body, involving simple (Rankine) sources, while the far–field is modelled by complete (normal–mode) series expansions derived by separation of variables in the constant depth half strips, in either side of the middle, non–uniform domain, where the depth exhibits a general variation, overcoming mild bottom–slope assumptions (see Figure 3-1). Numerical results are presented concerning floating bodies of simple geometry lying over uniform and sloping seabeds. With the aid of systematic comparisons, the effects of bottom slope on the hydrodynamic characteristics (hydrodynamic coefficients and responses) as well as the floating PV performance, are presented and discussed.

3.1. *Mathematical Formulation of the 2D Problem*

The 2D problem is considered, concerning the hydrodynamic behaviour of a twin–hull floating body of arbitrary cross section in a coastal–marine environment, as illustrated in Figure 3-1. The Cartesian coordinate system $\mathbf{x} = (x_1, x_2, x_3)$ is used, with the origin placed on the mean water level, coinciding with the structure's center of flotation, and the x_3–axis pointing upwards. The configuration is considered unchanged in the x_1–direction and therefore the analysis is limited to the x_2, x_3–plane, modelling a two–dimensional cross section. Consequently, surge, pitch and yaw motions are set to zero as they are not supported by the modelled 2D geometry. The module is thus free to move along the DoFs corresponding to sway $(k = 2)$, heave $(k = 3)$ and roll $(k = 4)$.

The environment comprises a water layer bounded by the free surface at $x_3 = 0$ and the rigid bottom at depth $h = h(x_2)$. It is assumed that $h(x_2)$ exhibits a general variation, i.e., the corresponding bathymetry is defined by parallel, straight contours lying between two regions of constant but possibly different water depths: $h = h_a$ at the region of wave incidence and $h = h_b$ at the region of transmission. The fluid is assumed to be homogeneous, inviscid and incompressible and its motion irrotational and of small width. The wave field in the region is excited by a harmonic incident field, with propagation direction normal to the depth contours (along the x_2–axis). Without loss of generality, a left–incident wave field is assumed; see Figure 3-1. In the context of linearized wave theory, the fluid motion is fully described by the 2D wave potential $\Phi(x_1, x_2; t)$ with the velocity field being equal to $\mathbf{v}(\mathbf{x}; \mathrm{t}) = \nabla\Phi(\mathbf{x}; \mathrm{t})$. Assuming that the free surface elevation as well as the wave velocities are small, the potential function $\Phi(x_1, x_2; t)$ satisfies the linearized wave equations (see, e.g., [127,128] or refer to Appendix A). Under these assumptions, the wave field is time–harmonic and its potential function can be represented by the time–independent (normalized) complex potential $\varphi(\mathbf{x})$,

$$\Phi(x_2, x_3; t) = \mathrm{Re}\left\{-\frac{igA}{\omega}\varphi(x_2, x_3; \mu)\cdot\exp(-i\omega t)\right\}. \tag{3.1}$$

In the above expression, $H = 2A$ is the incident wave height, g is the acceleration of gravity, $\mu = \omega^2/g$ is the frequency parameter and $i = \sqrt{-1}$ is the imaginary unit. The free surface elevation is obtained in terms of the wave potential at $x_3 = 0$ as follows,

$$\eta(x_2; t) = -\frac{1}{g}\frac{\partial\Phi(x_2, 0; t)}{\partial t}. \tag{3.2}$$

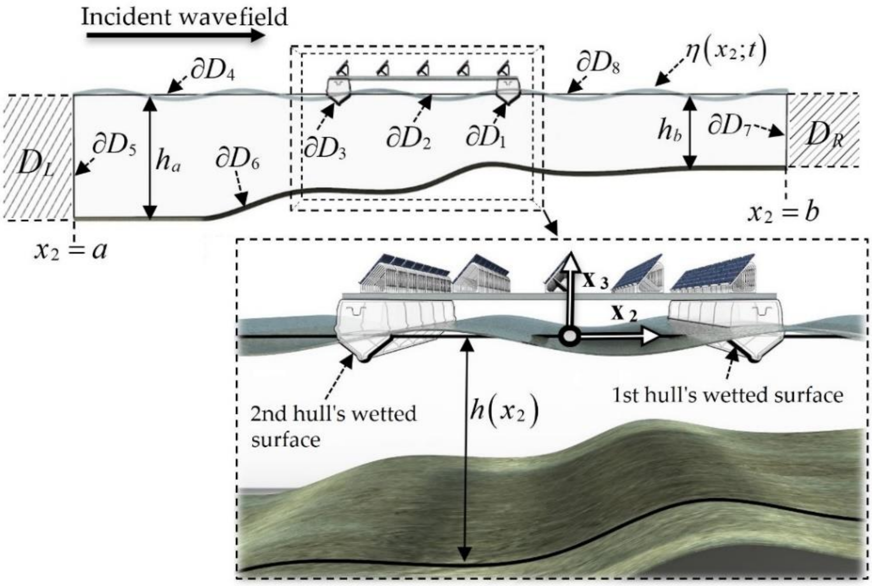

Figure 3-1. Geometrical configuration of the 2D problem.

In addition to the physical boundaries (floating body, free surface, seabed), two vertical interfaces (on either side of the domain) are further introduced, serving as incidence / radiation / transmission boundaries. Therefore, the boundary ∂D of the two–dimensional domain D, occupied by the fluid, is decomposed in eight subsections, $(\partial D_i, i = 1,2, \ldots ,8)$ as depicted in Figure 3-1, so that D is enclosed by the curve,

$$\partial D = \bigcup_{i=1}^{8} \partial D_i \, , \tag{3.3}$$

with ∂D_1 and ∂D_3 respectively being the right and left–hand sides of the twin–hull's wetted surface. Following a counterclockwise numbering, starting from the right–hand side wetted surface, the sections of ∂D numbered as $2, 4$ and 8 correspond to the water free surface, while ∂D_6 is the impermeable seabed. Finally, the wave incidence occurs via ∂D_5, which also serves – along with ∂D_7 – as a radiation interface for the diffracted field, due to the presence of the (fixed) body, as well as the radiation fields that develop due to the wave–induced body motions.

As illustrated in Figure 3-1, apart from the non–uniform bounded domain D, containing the floating structure, the total flow field is considered to be of infinite length and – therefore – also comprises the uniform semi–infinite subdomains D_L and D_R, where the depth is constant and equal to $h = h_a$ and $h = h_b$, respectively. Hence, the function $h = h(x_2)$ is of the form

$$h(x_2) = \begin{cases} h_a, & x_2 \le a \\ h(x_2), & a < x_2 < b \\ h_b, & x_2 \ge b. \end{cases} \tag{3.4}$$

The frequency dependent function $\varphi(x_2, x_3; \mu)$, appearing in Eq. (3.1), is the normalized potential in the frequency domain, which will be hereafter simply written as $\varphi(x_2, x_3)$. Using standard floating body hydrodynamic theory [129], as described earlier in this chapter, the total velocity potential $\varphi(x_2, x_3)$ is decomposed and represented by (refer to Appendix A),

$$\varphi(x_2, x_3) = \varphi_p(x_2, x_3) + \frac{\mu}{A} \sum_{k=2}^{4} \xi_k \varphi_k(x_2, x_3), \tag{3.5}$$

where $\varphi_p(x_2, x_3) = \varphi_0(x_2, x_3) + \varphi_D(x_2, x_3)$ is the propagating field, with $\varphi_0(x_2, x_3)$ denoting the incident field, (which corresponds to the solution of the wave propagation problem across the non–uniform subdomain in the absence of the floating structure) and $\varphi_D(x_2, x_3)$ being the diffraction potential, which accounts for the presence of the structure, fixed at its mean position (refer to Appendix A for more details). Moreover, the functions $\varphi_k(x_2, x_3),\ k = 2,3,4$, denote the radiation potentials, associated with the motion of the twin–hull structure, corresponding to its three (3) degrees of freedom (DoFs), i.e., the linear transverse motion (sway – $k = 2$), the linear vertical motion (heave – $k = 3$) and the rotation about the longitudinal (x_1) axis (roll – $k = 4$). Finally, $\xi_k,\ k = 2,3,4$ stand for the complex amplitudes of the corresponding wave–induced motions. As stated earlier, the remaining linear longitudinal motion, i.e., the oscillation of the structure along the x_1–direction (surge – $k = 1$), cannot be taken into account by the present reduced, two–dimensional model, since the modelled configuration is considered unchanged in this direction. This assumption implies that the simulations concern the dynamic behaviour of an infinite–length structure, and the relevant results refer to unit length in the x_1–direction. The same holds for the rotations about the transverse (x_2) and vertical (x_3) axes, namely the pitch ($k = 5$) and yaw ($k = 6$) motions, since any motion in these degrees of freedom is not in line with the above assumption.

The sub–problems, whose solutions determine the potential functions $\varphi_k(x_2, x_3)$, $k = p, 2,3,4$ in the general bathymetry region, can be formulated as radiation–type problems in the bounded subdomain D, with the aid of the following general representations of the wave potential $\varphi(x_2, x_3)$ in the left and right side semi–infinite strips D_L and D_R which are obtained by separation of variables; see, e.g. [130],

$$\begin{aligned}\varphi_p^{(L)}(\mathbf{x}) = {} & \left[\exp\left(ik_0^{(L)}x_2\right) + C_0^{(L)}\exp\left(-ik_0^{(L)}x_2\right)\right] Z_0^{(L)}(x_3) \\ & + \sum_{n=1}^{\infty} C_n^{(L)}\exp\left[k_n^{(L)}(x_2-a)\right] Z_n^{(L)}(x_3), \quad \mathbf{x}\in D_L,\end{aligned} \tag{3.6}$$

$$\begin{aligned}\varphi_k^{(L)}(\mathbf{x}) = {} & C_0^{(L)}\exp\left(-ik_0^{(L)}x_2\right) Z_0^{(L)}(x_3) \\ & + \sum_{n=1}^{\infty} C_n^{(L)}\exp\left[k_n^{(L)}(x_2-a)\right] Z_n^{(L)}(x_3), \quad \mathbf{x}\in D_L, \quad k=2,3,4,\end{aligned} \tag{3.7}$$

$$\begin{aligned}\varphi_k^{(R)}(\mathbf{x}) = {} & C_0^{(R)}\exp\left(ik_0^{(R)}x_2\right) Z_0^{(R)}(x_3) \\ & + \sum_{n=1}^{\infty} C_n^{(R)} Z_n^{(R)}(x_3)\exp\left[k_n^{(R)}(b-x_2)\right], \ \mathbf{x}\in D_R, \ k=p,2,3,4.\end{aligned} \tag{3.8}$$

The first term ($n = 0$) in the above equations [(3.6)–(3.8)] is the propagating mode, while the remaining ones ($n > 0$) are the evanescent modes, with $C_n = 0,1,2,\ldots$ being the corresponding coefficients. The first term of $\varphi_p{}^{(L)}(\mathbf{x})$ is further separated to a unit–amplitude mode propagating towards D – playing the role of the incident field – and the additional mode $C_0{}^{(L)}\exp(-ik_0{}^{(L)}x_2)Z_0{}^{(L)}(x_3)$, propagating towards the negative x_2–direction, which is the reflected field, coming from the diffraction potential $\varphi_D(\mathbf{x})$. In the above expansions, the functions $[Z_n^{(i)}]_{n=0}^{\infty}, i = L, R$ are defined as $Z_n^{(i)} = \cosh[\, k_n^{(i)}(x_3 + h^{(i)})\,]/\cosh(k_n^{(i)} h^{(i)})$ and are obtained by separation of variables, via the vertical Sturm–Liouville problem, to which the Laplace equation reduces in the constant depth strips $[D_L\,|-h_a < x_3 < 0, x_2 < a]$ and $[D_R\,|-h_b < x_3 < 0, x_2 > b]$. The corresponding eigenvalues $k_0{}^{(i)}$ and $[k_n^{(i)}]_{n=0}^{\infty}, i = L, R$ are respectively obtained as the real root and the imaginary roots of the dispersion relation: $\omega^2 = k^{(i)} g \tanh\left(k^{(i)} h^{(i)}\right)$, $i = L, R$, where g denotes the acceleration of gravity. The completeness of the expansions derives from the standard theory of regular eigenvalue problems; see, e.g., [131]. Based on the above representations, the hydrodynamic problems concerning the propagating and radiation potentials $\varphi_k(x_2, x_3), k = p, 2,3,4$ can be formulated as radiation–type problems, satisfying the following systems of equations, boundary conditions and matching conditions for $k = p, 2,3,4$,

$$\frac{\partial^2\varphi_k(x_2,x_3)}{\partial x_2{}^2} + \frac{\partial^2\varphi_k(x_2,x_3)}{\partial x_3{}^2} = 0, \ \mathbf{x}\in D\Big|_{(Domain\ of\ Transmission)}, \tag{3.9}$$

$$\frac{\partial\varphi_k(\mathbf{x})}{\partial n} - \mu\varphi_k(\mathbf{x}) = 0, \ \mu = \frac{\omega^2}{g}, \ \mathbf{x}\in\left(\partial D_2 \cup \partial D_4 \cup \partial D_8\right)\Big|_{(Free\ Surface)}, \tag{3.10}$$

$$\frac{\partial \varphi_k(\mathbf{x})}{\partial n} = 0,\ \mathbf{x} \in \partial D_6\big|_{(Seabed)}, \tag{3.11}$$

$$\frac{\partial \varphi_k(\mathbf{x})}{\partial n} = N_k(\mathbf{x}),\quad \mathbf{x} \in \left(\partial D_1 \cup \partial D_3\right)\big|_{(Wetted\ Surface)}, \tag{3.12}$$

$$\frac{\partial \varphi_k(\mathbf{x})}{\partial n} - T_L\left[\varphi_k^{(L)}(\mathbf{x})\right] = Q_k,\ \mathbf{x} \in \partial D_5\big|_{(\text{Incidence /Reflection /Radiation})}, \tag{3.13}$$

$$\frac{\partial \varphi_k(\mathbf{x})}{\partial n} - T_R\left[\varphi_k^{(R)}(\mathbf{x})\right] = 0,\ \mathbf{x} \in \partial D_7\big|_{(\text{Radiation})}. \tag{3.14}$$

The boundary sections to which Eqs. (3.10)–(3.14) refer are also illustrated in Figure 3-1. Moreover, in the above equations, $\mathbf{n} = (0, n_2, n_3)$ denotes the unit normal vector to the boundary ∂D, directed toward the exterior of D. The boundary data $N_k = 2,3,4$ involved in the right–hand side of Eq. (3.12), are defined by the components of the generalized normal vector on the wetted surface boundary section $(\partial D_1 \cup \partial D_3)$: $N_2 = n_2,\ N_3 = n_3,\ N_4 = x_2 n_3 - x_3 n_2$ (refer to Eq. (A.60) in Appendix A), and constitute the (unit–amplitude) excitations of the systems for each k. N_p is set to 0, so that the solution of the propagating field is obtained by treating the floating body as an impermeable, immobile solid boundary. Finally, the operators T_L and T_R are appropriate Dirichlet–to–Neumann (DtN) maps, see e.g., [132], ensuring the complete matching of the fields $\varphi_k(x_2, x_3)$ on the vertical interfaces ∂D_5 and ∂D_7, respectively. These operators are derived from Eqs. (3.6)–(3.8), exploiting the completeness properties of the vertical bases $[Z_n^{(i)}(x_3), n = 0,1,2, \dots.], i = L, R$. Specifically, projection of the terms of Eq. (3.6) on the orthonormal basis, spanned by the normalized eigenfunctions $\tilde{Z}_n^{(i)}(x_3) = Z_n^{(i)}(x_3) / \left\| Z_n^{(i)} \right\|$, with $\left\| Z_n^{(i)} \right\|$ standing for the L_2–norm of each vertical function,

$$\left\| Z_n^{(i)} \right\| = \left\{ \int_{z=-h_i}^{0} \left[Z_n^{(i)}(x_3) \right]^2 dx_3 \right\}^{1/2}, i = L,\ R, \tag{3.15}$$

yields,

$$\left\langle \varphi_p^{(L)}(\mathbf{x}) \cdot \tilde{Z}_n^{(L)}(x_3) \right\rangle = \begin{cases} \exp\left(ik_0^{(L)} x_2\right) + C_0^{(L)} \exp\left(-ik_0^{(L)} x_2\right), & n = 0 \\ C_n^{(L)} \exp\left[k_n^{(L)}(x_2 - a)\right], & n \geq 1 \end{cases} \text{, where} \tag{3.16}$$

$$\left\langle f(x_3), g(x_3) \right\rangle = \int_{x_3=-h_a}^{x_3=0} \left[f(x_3) \cdot g(x_3) \right] dx_3 . \tag{3.17}$$

Therefore, the reflection coefficient in the left half–strip D_L equals

$$C_0^{(L)} = \frac{-\exp\left(ik_0^{(L)} x_2\right) + \left\langle \varphi_p^{(L)}(\mathbf{x}) \cdot \tilde{Z}_0^{(L)}(x_3) \right\rangle}{\exp\left(-ik_0^{(L)} x_2\right)},\ (x_2, x_3) \in D_L. \tag{3.18}$$

Moreover, calculating the derivative of Eq. (3.6) with respect to the unit normal vector $\mathbf{n}$ (which is directed opposite to the x_2–direction on ∂D_5) and substituting in Eq. (3.13) yields,

$$\begin{aligned}-\frac{\partial\varphi_p^{(L)}(\mathbf{x})}{\partial n}&=ik_0^{(L)}\left[\exp\left(ik_0^{(L)}x_2\right)-C_0^{(L)}\exp\left(-ik_0^{(L)}x_2\right)\right]Z_0^{(L)}(x_3)\\&+\sum_{n=1}^{\infty}k_n^{(L)}C_n^{(L)}\exp\left[k_n^{(L)}(x_2-a)\right]Z_n^{(L)}(x_3)=-T_L\left[\varphi_p^{(L)}(\mathbf{x})\right]-Q_p,\ \ \mathbf{x}\in D_L.\end{aligned}\tag{3.19}$$

Finally, substitution of the modes' projections [Eq. (3.16)], results in,

$$\begin{aligned}T_L\left[\varphi_p^{(L)}(\mathbf{x})\right]&=ik_0^{(L)}\tilde{Z}_0^{(L)}(x_3)\left\langle\varphi_p^{(L)}(\mathbf{x})\cdot\tilde{Z}_0^{(L)}(x_3)\right\rangle\\&-\sum_{n=1}^{\infty}k_n^{(L)}\tilde{Z}_n^{(L)}(x_3)\left\langle\varphi_p^{(L)}(\mathbf{x})\cdot\tilde{Z}_n^{(L)}(x_3)\right\rangle,\end{aligned}\tag{3.20}$$

and

$$Q_p=-2ik_0^{(L)}\exp\left(ik_0^{(L)}x_2\right)\tilde{Z}_0^{(L)}(x_3).\tag{3.21}$$

For $k = 2,3,4$,

$$\left\langle\varphi_k^{(L)}(\mathbf{x})\cdot\tilde{Z}_n^{(L)}(x_3)\right\rangle=\left\{\begin{matrix}C_0^{(L)}\exp\left(-ik_0^{(L)}x_2\right), & n=0.\\ C_n^{(L)}\exp\left[k_n^{(L)}(x_2-a)\right], & n\geq 1.\end{matrix}\right\},\ k=2,3,4.\tag{3.22}$$

Similarly, the calculation of the derivative of Eq. (3.7) with respect to the unit normal vector **n** yields,

$$\begin{aligned}-\frac{\partial\varphi_k^{(L)}(\mathbf{x})}{\partial n}&=-ik_0^{(L)}C_0^{(L)}\exp\left(-ik_0^{(L)}x_2\right)Z_0^{(L)}(x_3)\\&+\sum_{n=1}^{\infty}k_n^{(L)}C_n^{(L)}\exp\left[k_n^{(L)}(x_2-a)\right]Z_n^{(L)}(x_3)=-T_L\left[\varphi_k^{(L)}(\mathbf{x})\right]-Q_k,\ \ \mathbf{x}\in D_L.\end{aligned}\tag{3.23}$$

Next, by substituting the modes' projections [Eq. (3.22)] in the derivative's expression [Eq. (3.23)] it is concluded that $T_L\left[\varphi_k^{(L)}(\mathbf{x})\right] = T_L\left[\varphi_p^{(L)}(\mathbf{x})\right], k = 2,3,4$; [see Eq. (3.20)], and $Q_k = 0, k = 2,3,4$.

For the wave field in the domain D_R it holds that,

$$\left\langle\varphi_k^{(R)}(\mathbf{x})\cdot\tilde{Z}_n^{(R)}(x_3)\right\rangle=\left\{\begin{matrix}C_0^{(R)}\exp\left(ik_0^{(R)}x_2\right), & n=0.\\ C_n^{(R)}\exp\left[k_n^{(R)}(x_2-a)\right], & n\geq 1.\end{matrix}\right\},\ k=p,2,3,4\ ,\tag{3.24}$$

$$\begin{aligned}\frac{\partial\varphi_p^{(R)}(\mathbf{x})}{\partial n}&=ik_0^{(R)}C_0^{(R)}\exp\left(ik_0^{(R)}x_2\right)Z_0^{(R)}(x_3)\\&+\sum_{n=1}^{\infty}k_n^{(R)}C_n^{(R)}\exp\left[k_n^{(R)}(b-x_2)\right]Z_n^{(R)}(x_3)=T_R\left[\varphi_p^{(R)}(\mathbf{x})\right],\ \ \mathbf{x}\in D_R,\end{aligned}\tag{3.25}$$

and therefore,

$$\begin{aligned}T_R\left[\varphi_p^{(R)}(\mathbf{x})\right]&=ik_0^{(R)}Z_0^{(R)}(x_3)\left\langle\varphi_k^{(R)}(\mathbf{x})\cdot\tilde{Z}_0^{(R)}(x_3)\right\rangle\\&+\sum_{n=1}^{\infty}k_n^{(R)}Z_n^{(R)}(x_3)\left\langle\varphi_k^{(R)}(\mathbf{x})\cdot\tilde{Z}_n^{(R)}(x_3)\right\rangle.\end{aligned}\tag{3.26}$$

3.2. *BEM formulation for 2D floating structures*

3.2.1. The Incidence, Diffraction and Radiation fields

The sub–problems concerning the propagating and radiation potentials $\varphi_k(x_2,x_3),\ k=p,2,3,4$, [Eqs. (3.9)–(3.14)] are treated by means of boundary integral equation formulations, based on the single layer potential; see, e.g., [133]. The following integral formulations are used for the representation of $\varphi_k(\mathbf{x}),\ k=p,2,3,4$, in the bounded subdomain D.

$$\varphi_k(\mathbf{x})=\int_{\partial D}\sigma_k(\mathbf{x}')G(\mathbf{x}',\mathbf{x})\,d\ell(\mathbf{x}'),\ \ \mathbf{x}=(x_2,x_3)\in D,\ \ \mathbf{x}'\in\partial D,\ k=p,2,3,4, \tag{3.27}$$

where $G(\mathbf{x}',\mathbf{x})=\ln|\mathbf{x}'-\mathbf{x}|/2\pi$ is the Green's function of the Laplace equation in 2D free–space, $\sigma_k(\mathbf{x}'),\ k=p,2,3,4$ is a source / sink strength distribution, defined on the boundary of the bounded subdomain D (for each of the four subproblems) and $d\ell(\mathbf{x}')$ denotes the differential distance along the boundary ∂D; see, e.g., [134]. Based on the properties of single–layer distributions, the derivatives of the functions $\varphi_k(\mathbf{x}),\ k=p,2,3,4$, normal to the ∂D boundary's geometry, are given by (see, e.g., [135]),

$$\frac{\partial\varphi_k(\mathbf{x})}{\partial n}=-\frac{\sigma_k(\mathbf{x})}{2}+\int_{\partial D}\sigma_k(\mathbf{x}')\frac{\partial G(\mathbf{x}',\mathbf{x})}{\partial n}\,d\ell(\mathbf{x}'),\ \ (\mathbf{x},\mathbf{x}')\in\partial D,k=p,2,3,4. \tag{3.28}$$

Using the above representations of the potential functions and their normal derivatives in the system of Equations (3.9)–(3.14), results in a system of boundary integral equations with support on the different sections of ∂D, for the determination of the corresponding unknown source distributions $\sigma_k(\mathbf{x}),\ \mathbf{x}\in\partial D, k=p,2,3,4$, for each of the potential functions $\varphi_k(\mathbf{x}),\ k=p,2,3,4$. The final system for $k=p,2,3,4$, reads as follows,

$$\begin{aligned}&-\frac{\sigma_k(\mathbf{x})}{2}+\int_{\partial D}\sigma_k(\mathbf{x}')\frac{\partial G(\mathbf{x}',\mathbf{x})}{\partial n}\,d\ell(\mathbf{x}')\\&\qquad-\mu\int_{\partial D}\sigma_k(\mathbf{x}')G(\mathbf{x}',\mathbf{x})\,d\ell(\mathbf{x}')=0,\ \ \mathbf{x}\in(\partial D_2\cup\partial D_4\cup\partial D_8),\ \ \mathbf{x}'\in\partial D,\end{aligned} \tag{3.29}$$

$$-\frac{\sigma_k(\mathbf{x})}{2}+\int_{\partial D}\sigma_k(\mathbf{x}')\frac{\partial G(\mathbf{x}',\mathbf{x})}{\partial n}\,d\ell(\mathbf{x}')=0,\ \ \mathbf{x}\in\partial D_6,\ \ \mathbf{x}'\in\partial D, \tag{3.30}$$

$$-\frac{\sigma_k(\mathbf{x})}{2}+\int_{\partial D}\sigma_k(\mathbf{x}')\frac{\partial G(\mathbf{x}',\mathbf{x})}{\partial n}\,d\ell(\mathbf{x}')=N_k(\mathbf{x}),\ \ \mathbf{x}\in(\partial D_1\cup\partial D_3),\ \ \mathbf{x}'\in\partial D, \tag{3.31}$$

$$\begin{aligned}&-\frac{\sigma_k(\mathbf{x})}{2}+\int_{\partial D}\sigma_k(\mathbf{x}')\frac{\partial G(\mathbf{x}',\mathbf{x})}{\partial n}\,d\ell(\mathbf{x}')\\&\qquad-T_L\left[\int_{\partial D}\sigma_k(\mathbf{x}')G(\mathbf{x}',\mathbf{x})\,d\ell(\mathbf{x}')\right]=Q_k,\ \ \mathbf{x}\in\partial D_5,\ \ \mathbf{x}'\in\partial D,\end{aligned} \tag{3.32}$$

$$-\frac{\sigma_k(\mathbf{x})}{2}+\int_{\partial D}\sigma_k(\mathbf{x}')\frac{\partial G(\mathbf{x}',\mathbf{x})}{\partial n}d\ell(\mathbf{x}')$$
$$-T_R\left[\int_{\partial D}\sigma_k(\mathbf{x}')G(\mathbf{x}',\mathbf{x})d\ell(\mathbf{x}')\right]=0,\ \mathbf{x}\in\partial D_7,\ \mathbf{x}'\in\partial D. \tag{3.33}$$

From the above systems' solutions $\sigma_k(\mathbf{x}), k=p,2,3,4$ the corresponding potential functions $\varphi_k(\mathbf{x}),\ k=p,2,3,4$ and all other quantities associated to them, can be calculated in the bounded subdomain D, using Eqs. (3.27) and (3.28).

The solutions of the system consisting of Eqs. (3.29)–(3.33) are obtained numerically, by means of a low–order Boundary Element Method based on simple (Rankine) sources; see also Ref. [135]. The geometry of the different sections of the domain's boundary is approximated by linear segments on which the source distribution is taken to be piecewise constant. Under this assumption, the boundary integrals in Eqs. (3.29)–(3.33) associated with each linear segment's contribution can be analytically calculated; see, e.g., [136]. As a result, the systems of boundary integral equations reduce to an equal number of algebraic systems, whose unknowns are the vectors $[\sigma_{kj}]_{j=1}^{M},\ k=p,2,3,4$, with M being the number of linear boundary elements used to approximate the geometry of ∂D.

3.2.2. Equations of Motion

The total hydrodynamic loads (forces and moment) on the twin–hull structure consist of the Froude–Krylov loads, which are solely due to the undisturbed incident field $\varphi_0(\mathbf{x})$, the diffraction loads (that are caused by the pressure field generated by the presence of the floating fixed at its mean position), and the radiation loads due to the wave fields "radiated" by the body's oscillatory motions. Based on the calculated propagating potential (comprising the incident and diffraction potentials), the summation of the Froude–Krylov and the diffraction–induced hydrodynamic forces, as well as the corresponding moment $F_k, k=2,3,4$ are calculated using surface integration as follows,

$$F_k=i\omega\rho\int_{\partial D_1\cup\partial D_3}\varphi_P(\mathbf{x})\cdot\mathbf{N}_k(\mathbf{x})d\ell(\mathbf{x}),\ \ k=2,3,4,\ \mathbf{x}\in(\partial D_1\cup\partial D_3), \tag{3.34}$$

where ρ denotes the fluid (water) density and $N_k, k=2,3,4$ represent the components of the generalized normal vector on the wetted surface (also defined in §3.1). Moreover, the hydrodynamic coefficients (added mass and hydrodynamic damping) are calculated by integration of the pressure induced by the radiation potentials $\varphi_k(\mathbf{x}),\ k=2,3,4$, on the wetted surface as (see also Eqs. (A.89)–(A.91) in Appendix A),

$$\omega^2A_{kl}+i\omega B_{kl}=i\omega\rho\Pi_{kl},\ \ l,k=2,3,4,\ \text{where} \tag{3.35}$$

$$\Pi_{kl}=\int_{\partial D_1\cup\partial D_3}\varphi_l(\mathbf{x})\mathbf{N}_k(\mathbf{x})d\ell(\mathbf{x}),\ \ l,k=2,3,4,\ \mathbf{x}\in(\partial D_1\cup\partial D_3). \tag{3.36}$$

In the above expressions, $\mathbf{A}_{(3\times3)}$ is the (symmetric) matrix of added inertial coefficients, which – for each frequency – correspond to the proportion of the radiation loads in phase with the structure's acceleration (in the frequency domain). $\mathbf{B}_{(3\times3)}$ is the corresponding matrix of hydrodynamic damping coefficients, which consists of the portion of radiation loads in phase with the structure's velocity, as more adequately analyzed in Appendix A. More details about the definitions of the hydrodynamic forces and coefficients, as well as the system of equations of motion, can be found in Ref. [128] or in ship hydrodynamics textbooks; see e.g.,[129,137]. The latter quantities allow for the formulation and solution of the equations of motion of the floating body in the inhomogeneous domain. The general form of equations of motion, in the frequency domain, for the 2D twin–hull structure considered is,

$$\left\{-\omega^2\left[\mathbf{M}+\mathbf{A}(\omega)\right]-i\omega\mathbf{B}(\omega)+\mathbf{C}\right\}\boldsymbol{\xi}=\mathbf{F}. \tag{3.37}$$

Due to the symmetry of the body with respect to the vertical axis (x_3), the component N_3 of the generalized normal vector is symmetric, while the components $N_{k,}\ k=2{,}4$ are antisymmetric. Assuming that the seabed profile variations do not significantly alter the radiation potentials $\varphi_k(\mathbf{x}),\ k=2{,}3{,}4$ near the floating structure, the potential function $\varphi_3(\mathbf{x})$ is also symmetric and the functions $\varphi_k(\mathbf{x}), k=2{,}4$ are antisymmetric. This fact implies that $\Pi_{32}=\Pi_{34}=0$ and $\Pi_{23}=\Pi_{42}=0$. Therefore, the dynamic equations of motion related to the oscillations of the structure are simplified in the following form, in which the heaving motion (ξ_3) is decoupled from the sway and roll motions $(\xi_{2,}\xi_4)$ of the twin–hull,

$$\left[-\omega^2\left(M+A_{22}\right)-i\omega B_{22}\right]\xi_2-\left(\omega^2A_{24}+i\omega B_{24}\right)\xi_4=F_2, \tag{3.38}$$

$$\left[-\omega^2\left(M+A_{33}\right)-i\omega B_{33}+2\rho gB_{(H)}\right]\xi_3=F_3, \tag{3.39}$$

$$\left(-\omega^2A_{42}-i\omega B_{42}\right)\xi_2+\left[-\omega^2\left(I_{44}+A_{44}\right)-i\omega B_{44}+Mg\cdot GM\right]\xi_4=F_4. \tag{3.40}$$

In Eqs. (3.38)–(3.40) $B_{(H)}$ is the breadth of each individual hull and GM denotes the metacentric height. The total mass equals $M=\rho\nabla$, referring to unit length in the transverse direction (kg/m), where ρ denotes the fluid's density and ∇ is the displacement volume of the structure. Moreover, due to symmetry of the floating structure, the center of buoyancy (B) is located on the vertical line $x_2=0$ and its x_3 coordinate is calculated as the center of area of the submerged volume's cross section. The center of gravity (G) is also located at $x_2=0$ due to symmetry of the configuration and its x_3 coordinate is considered to be located at the waterplane $(x_3=0)$. A total radius of gyration, per unit length in the transverse direction, of $R_G=0.5(B_{(T)}-B_{(H)})$ is considered, about the longitudinal axis (x_1), where $B_{(T)}$ is the total Breadth of the twin–hull structure and therefore, $I_{44}=M(R_G)^2$. The metacentric Radius is evaluated as $BM=I/\nabla$ where I is the second moment of area of the waterplane, calculated by applying Steiner's theorem as,

$$I=2\left[\left(\frac{B_{(H)}{}^3}{12}\right)+B_{(H)}\cdot\left(\frac{B_{(T)}-B_{(H)}}{2}\right)^2\right], \tag{3.41}$$

also referring to unit length in the transverse direction (x_1). Finally, the metacentric height is calculated as $GM=KB+BM-KG$, where K is any reference point with coordinates $(0,x_3)$. The above equations can also be modified to include other external forces, as e.g., mooring forces or spring terms; see, e.g. Sec. 3.5 of Ref. [138]. The solution of the above system of equations [(3.38)–(3.40)] provides the complex amplitudes of the corresponding motions of the twin–hull: $\xi_k, k=2{,}3{,}4$. Then, the total wave potential is obtained by Eq. (3.5) from which the hydrodynamic pressure is obtained using Bernoulli's theorem. Finally, the wave loads acting on the floating structure are calculated by pressure integration on the wetted surface $\partial D_1\cup\partial D_3$.

3.3. *Model Verification*

Results obtained by the numerical model described in the previous subsections, are here compared to results from the literature for verification purposes. The results concern a twin–hull floating structure whose individual hulls are cylindrical, with draft equal to the radius, which results in wetted surfaces whose cross section shapes a semicircle. Numerical results regarding the above configuration have been presented by Ohcusu M. [139] in 1969 and Rhee K.P. [140] in 1982 concerning the amplitude ratio of the radiated fields' wave height, away from the body, divided by the amplitude of the forced oscillation which excites the field itself, in calm water.

Figure 3-2 illustrates the aforementioned ratio regarding the heave and sway motions of the twin–hull structure. The wetted surface of each individual hull has a cross section which shapes a semicircle of radius R in the x_2x_3–plane, while each of the two semicircles' centers is at distance P from the origin, following the notation established in Ref. [140]. Therefore, the two centers are $2P$ units apart and the configuration is defined so that $2P/R = 3$. The results concern the radiation fields that propagate in deep water, which is achieved in the present numerical model by setting the depth as constant and equal to half the wavelength for each simulated frequency. This distance can be easily calculated considering the dispersion relation for deep water propagation ($\lambda = 2\pi g/\omega^2$). The domain is set to extend to three (3) wavelengths away from the floating body in both directions and the far–field free surface elevation is evaluated by the discrete BEM model at the last free surface boundary element away from the structure (adjacent to the first boundary element of the radiation boundary). The amplitude ratios of Figure 3-2 are presented as functions of the non–dimensional frequency parameter ω^2R/g.

Indicative results are illustrated in Figure 3-3, concerning wave fields generated by unit–amplitude forced oscillations of the twin–hull in sway and heave, with the non–dimensional frequency parameter ω^2R/g set to 1. The configuration has been dimensionalized by setting $R = 2$. The amplitude ratios are equal to 0.992 and 0.520, for sway and heave respectively, as also shown by the diagrams of Figure 3-2.

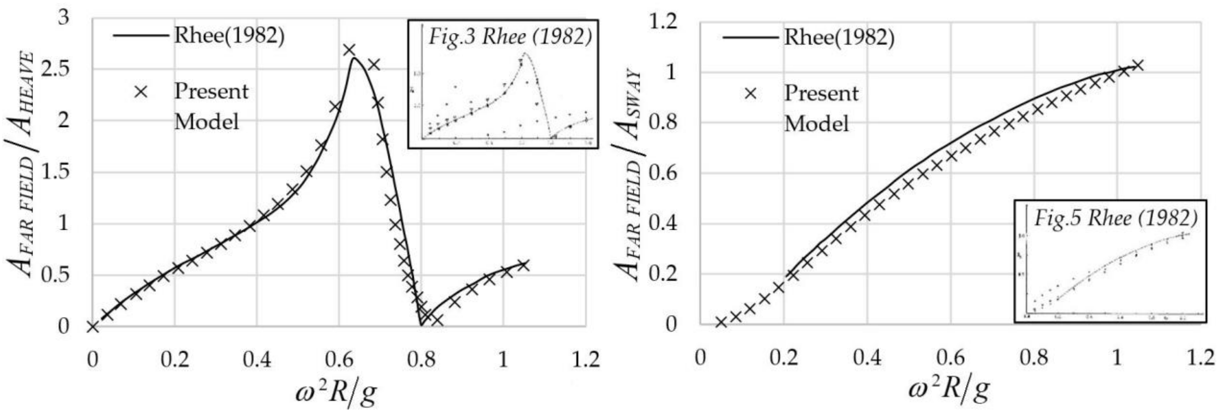

Figure 3-2. Amplitude ratios for heave and sway, for a twin–hull floating structure of semicircle hull cross sections $2P/R = 3, h/R = \infty$. (Data adapted from [140]).

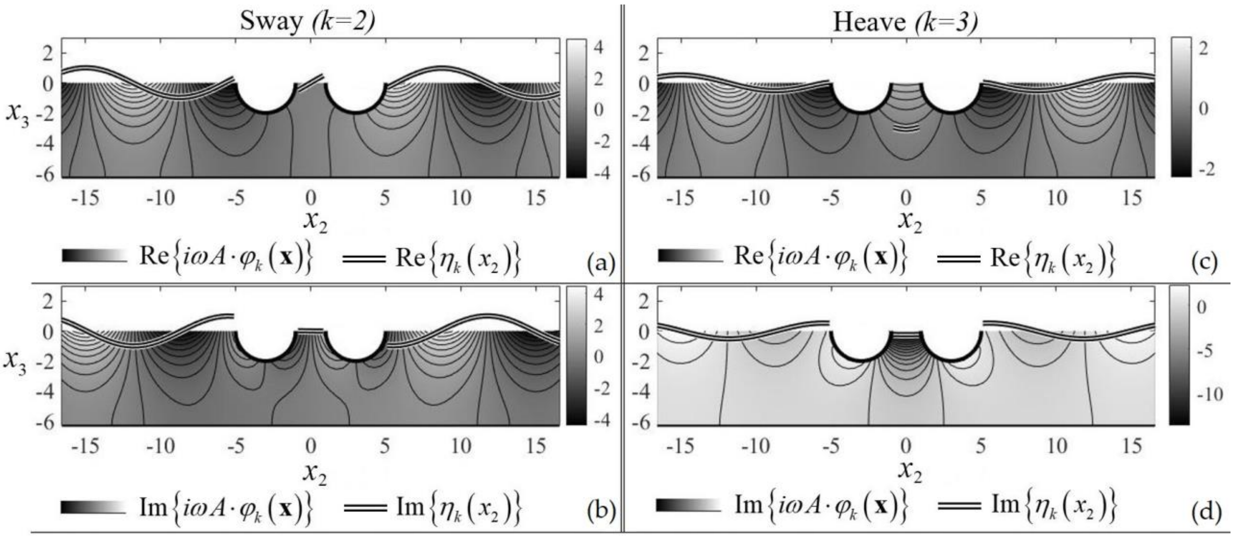

Figure 3-3. Sway and heave radiation fields for $2P/R = 3$, $h/R = \lambda/2$ and $\omega^2 R/g = 1$. Real (**a**, **c**) and imaginary (**b**, **d**) parts of the normalized sway (**a**, **b**) and heave (**c**, **d**) fields and corresponding free-surface elevation.

An identical twin–hull structure was studied by Dabssi et al. [141] in 2008 regarding its hydrodynamic coefficients. Figure 3-4 illustrates the added mass and damping of the floating structure in heave (ξ_3). The added mass (A_{33}) has been normalized by the structure's mass, while the damping coefficient for heave (B_{33}) has been normalized by the mass times the angular frequency ω so that all presented quantities are non–dimensional. It is noted that the displacement in this case does not need to be numerically calculated since it is equal to the sum of volumes of two half–cylinders of radius R that are considered to extend to unit length in the transverse direction and therefore is equal to πR^2. The results of Figure 3-4 concern the heaving motion of the twin–hull in a finite water depth h, where $h/R = 2$. The calculated data sets are presented as functions of the non–dimensional wavenumber kR.

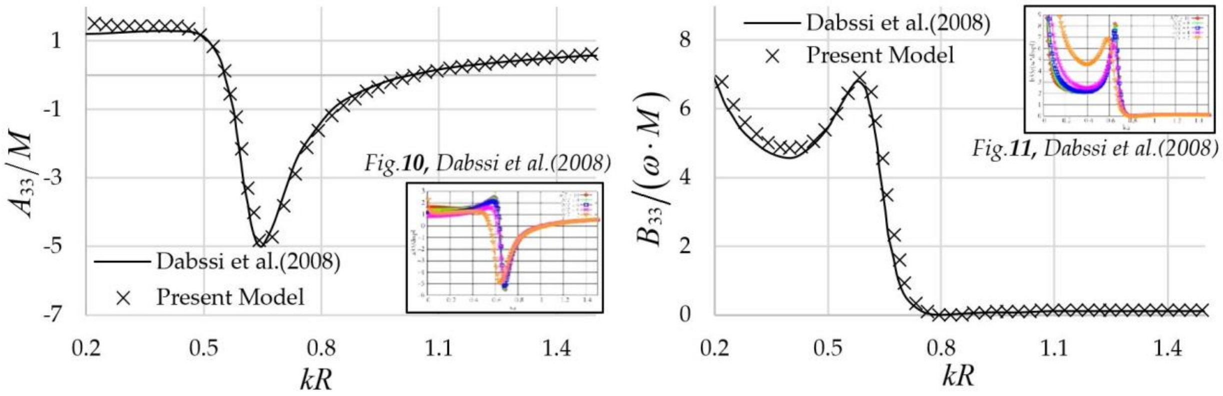

Figure 3-4. Added mass and damping coefficient of heave, for a twin–hull floating structure of semicircle hull cross sections for $2P/R = 3$, $h/R = 2$.

3.4. *Numerical Results*

In this section numerical results are derived, concerning a twin–hull structure of non–dimensional total breadth equal to $B_{(T)}/h = 2/3$, with the non–dimensional breadth and draft of each individual hull set to $B_{(H)}/h = T/h = 1/10$, where h denotes the mean water depth of the inhomogeneous domain, while also accounting for the effect of sloping seabed environments on the hydrodynamic characteristics. The individual hulls, that make up the twin–hull layout, are modelled via the cross section of a Wigley hull at $x_1 = 0$, which is given by the analytical relation,

$$x_2 = \mp \frac{B_{(H)}}{2} \cdot \left[1 - \left(\frac{x_3}{T} \right)^2 \right]. \tag{3.42}$$

The configuration is considered to be located at an inhomogeneous region; see Figure 3-6(a). The center of gravity coincides with the center of flotation and the center of buoyancy (B), which is calculated as the center of area of the submerged volume's cross section, is located at $(x_2 = 0,\ x_3 = -0.375\,T)$; see Figure 3-5. Thus, the non–dimensional metacentric height of this layout is $GM/h = 1.179$.

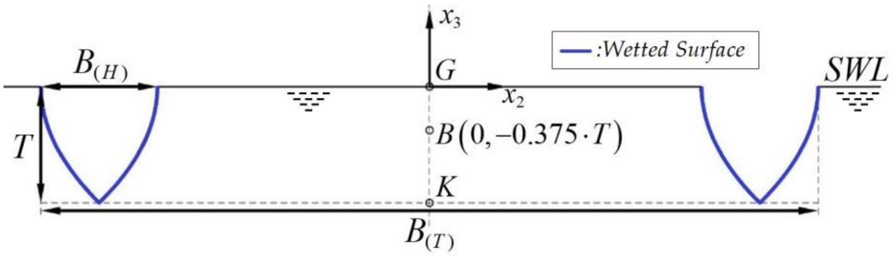

Figure 3-5. Outline of the modelled configuration and basic dimensions.

Numerical results are presented in Figure 3-6 and Figure 3-7 concerning the hydrodynamic behaviour of this floating structure in constant depth and over two linear shoals characterized by (constant) bottom slopes of 10% and 20%, respectively; see Figure 3-6(a). The shoaling environments are achieved by a linear depth reduction of $2h/3$ and $4h/3$, respectively, over a depth variation distance of $10B_{(T)}$, with the mean water depth of all three domains of transmission being equal to h. Results concerning the homogeneous domain are plotted using solid lines, while the results concerning the inhomogeneous transmission domains with bottom slopes of 10% and 20% are plotted using dashed lines and dotted lines, respectively.

In particular, subplot (b) of Figure 3-6 illustrates the normalized hydrodynamic forces as functions of the non–dimensional wavelength λ/h for all three considered domains of transmission, where $\lambda = 2\pi/k_0$ is the wavelength corresponding to the mean water depth, as obtained through application of the dispersion relation, $\omega^2 = k_0 g \tanh(k_0 h)$.

The normalization used for the hydrodynamic forces is,

$$\tilde{F}_k = F_k / \rho g h A,\ k = 2,3, \tag{3.43}$$

where A is the incident wave amplitude.

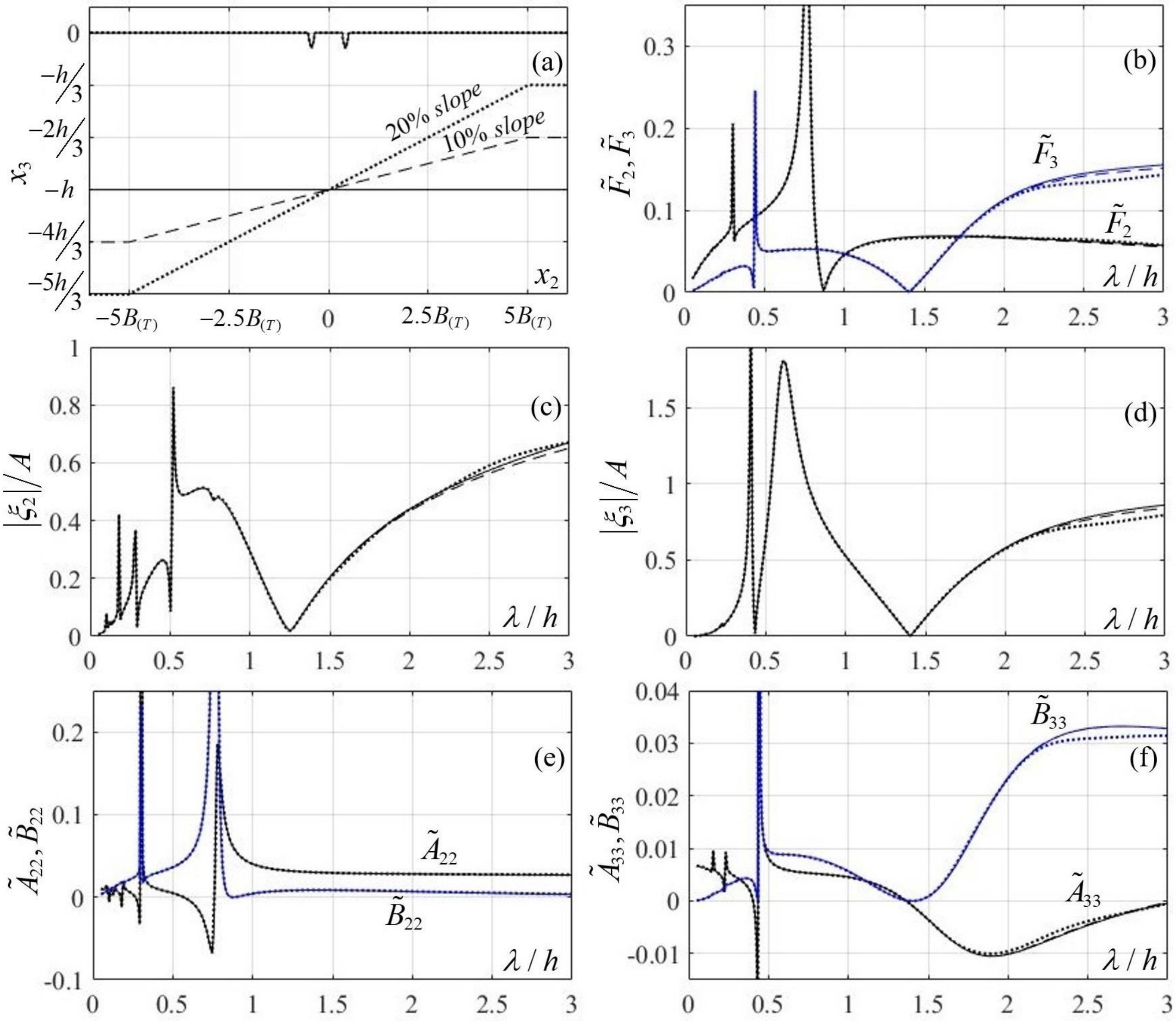

Figure 3-6. (**a**) Floating body and domains of transmission ($B_{(T)}/h = 2/3,\ B_{(H)}/h = T/h = 1/10$) (b) Hydrodynamic forces $\tilde{F}_k, k = 2,3$, (**c**, **d**) RAOs in sway and heave motion, respectively (**e**, **f**) Hydrodynamic coefficients A_{22}, B_{22} and A_{33}, B_{33}, respectively. All quantities are plotted vs. the non–dimensional wavelength λ/h, where h denotes the average water depth.

Subplots (c) and (d) of Figure 3-6 depict the twin–hull's RAOs, associated with its two linear motions i.e., sway (ξ_2) and heave (ξ_3). The body's linear responses are normalized as,

$$RAO_k = \tilde{\xi}_k = |\xi_k|/A,\ k = 2,3. \tag{3.44}$$

Finally, in subplots (e) and (f), corresponding results concerning the hydrodynamic coefficients are presented. The matrix $\mathbf{A}_{(3\times3)}$ of added inertial coefficients and the matrix $\mathbf{B}_{(3\times3)}$ of hydrodynamic damping coefficients are normalized as,

$$\tilde{\mathbf{A}} = \frac{\mathbf{A}}{\rho}\begin{pmatrix} h^{-2} & h^{-2} & h^{-3} \\ h^{-2} & h^{-2} & h^{-3} \\ h^{-3} & h^{-3} & h^{-4} \end{pmatrix},\ \tilde{\mathbf{B}} = \sqrt{\frac{h}{g}} \cdot \frac{\mathbf{B}}{\rho}\begin{pmatrix} h^{-2} & h^{-2} & h^{-3} \\ h^{-2} & h^{-2} & h^{-3} \\ h^{-3} & h^{-3} & h^{-4} \end{pmatrix}. \tag{3.45}$$

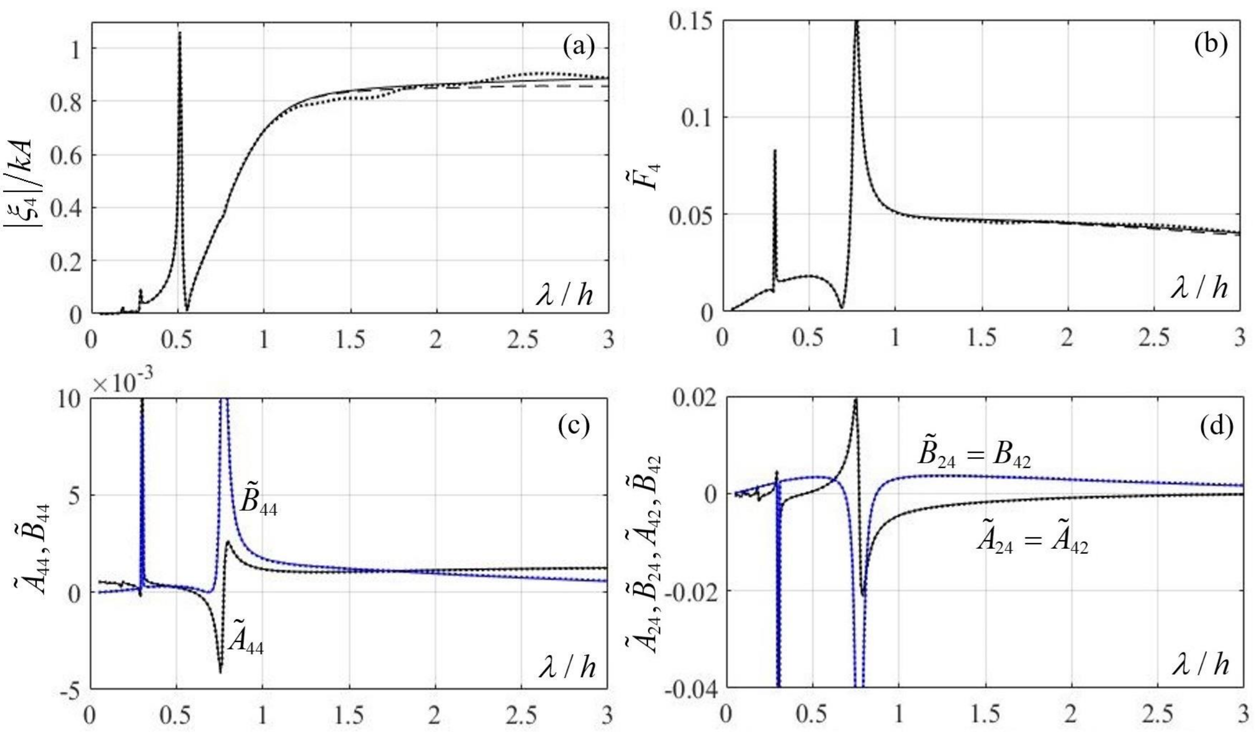

Figure 3-7. (**a**) RAO in roll motion, (**b**) Hydrodynamic moment $\tilde{F}_4$, (**c**, **d**) Hydrodynamic coefficients A_{44}, B_{44} and A_{24}, B_{24}, respectively. All quantities are plotted vs. the non–dimensional wavelength λ/h, where h denotes the average water depth.

Figure 3-7(a) illustrates the twin–hull's RAO, associated with the angular motion i.e., roll (ξ_4). The angular response is normalized as

$$RAO_4 = \tilde{\xi}_4 = |\xi_4|/kA, \tag{3.46}$$

with k being the wavenumber evaluated at the mean water depth h.

The corresponding normalized hydrodynamic moment,

$$\tilde{F}_4 = F_4 / \rho g h^2 A, \tag{3.47}$$

is shown in subplot (b). Figure 3-7(c) depicts the corresponding diagonal elements (A_{44}, B_{44}) of the added inertia and damping matrices. Finally, the non–diagonal elements A_{24}, B_{24} of the (symmetric) added inertia and hydrodynamic damping matrices are shown in subplot (d). All results are plotted as functions of the non–dimensional wavelength λ/h.

Indicative results regarding the total induced wave fields are depicted in Figure 3-8 for non–dimensional wavelength equal to $\lambda/h = 2.4$. In particular Figure 3-8(a) illustrates the real part of the total potential $\varphi(\mathbf{x})$; [see Eq. (3.5)], for the three considered cases of 0%, 10% and 20% bottom slope; [see Figure 3-6(a)], in the general vicinity of the twin–hull structure. Figure 3-8 (b) depicts the imaginary parts of the corresponding potential functions. The configurations have been made dimensional by setting $h = 30$m and an incident field of amplitude $A = 1.5$ m has been considered.

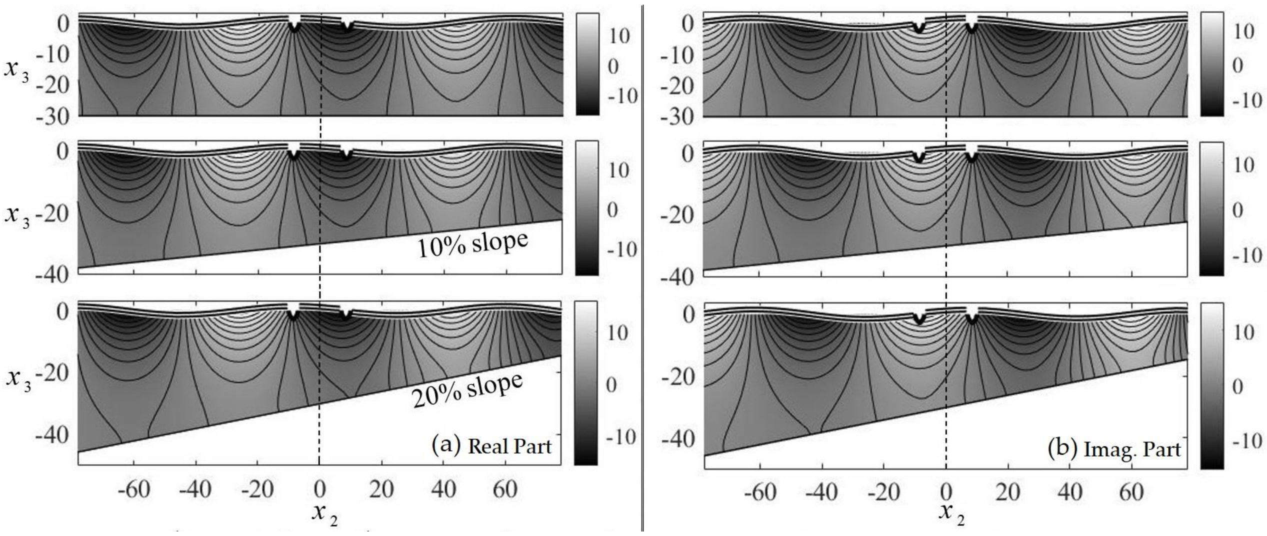

Figure 3-8. (**a**) Real and (**b**) Imaginary part of the total complex wave potential and corresponding free surface elevation, for a twin–hull floating structure of breadth $B_{(T)} = 20\text{m}$ and three considered cases of bottom slope (0%, 10% and 20%) in environment of mean water depth $h = 30\text{m}$ in the case of incident waves of wavelength $\lambda/h = 2.4$ and amplitude $A = 1.5\text{m}$.

In the considered wavelength case, the interaction of the field with the local topography becomes significant. Specifically, in Figure 3-8, it is evident that the equipotential lines normally intersect the non–horizontal parts of the seabed profile, resulting from the application of the homogeneous Neumann boundary condition [Eq. (3.11)]. Furthermore, the wavelength appears elongated in the deeper part of the domain and shortened in the shallower regions, attributable to the dissimilar phase velocities caused by dispersion, inherent in water wave dynamics.

3.4.1. Effects of dynamic motions on FPV performance

The energy efficiency of a floating photovoltaic (FPV) unit relies on various parameters, many of which are triggered by the surrounding marine environment. Some of the factors that affect energy efficiency of FPV are also found in corresponding land–based units, with equal or different impact on the power output, while others are completely absent on land. The panel tilt is explicitly involved in computing the power generation, as analyzed in §2.3, which implies that efficiency is directly dependent on the angle of incidence (AOI) of solar irradiation. The latter is directly affected by the dynamic wave–induced angular motions.

In this section’s context, a preliminary assessment of a floating photovoltaic system’s energy efficiency is made, taking into account data regarding the dynamic motions of the floating unit carrying the panels, as derived by the hydrodynamic model presented and discussed in §3.1 and §3.2. All other effects, including the impacts of temperature and humidity are intentionally disregarded at this stage. This deliberate simplification enables a clearer examination of the influence of motions on the system's performance, providing a deeper understanding of the influence of dynamics on power output. The linear motions, i.e., sway ($k = 2$) and heave ($k = 3$), are considered to have no effect on the tilt angle of the panels and therefore the angle of incidence. Hence the effect of the unit’s mobility is limited to the angular oscillation i.e., roll

($k = 4$). The power output of photovoltaic cells is strongly affected by the angle of incidence (AOI) of solar irradiation and the Plane of Array Irradiance (G_{POA}), which is approximated, in the framework of the discussed 2D methodology, by the following equation [142],

$$G_{POA} = DNI\cos\left(AOI\right) + D + R, \tag{3.48}$$

where DNI is the direct normal irradiance and D, R denote diffuse and reflected irradiance components on a tilted surface, respectively. In the simplified 2D framework, the term $DNI\cos(AOI)$ quantifies the beam irradiance component (B), defined in §2.3, without accounting for 3D phenomena such as solar declination, azimuth, or Hour Angle. This simplification is made to isolate the effects of hydrodynamics in an otherwise fully controlled environment, at a preliminary analysis level, as analyzed in more detail in the sequel. In order to provide indicative results, as regards the effect of wave–induced motions of the floating structure on the power output, an offshore installation is considered in the geographical sea area of the southern Aegean Sea. For the latter area, the optimized values for tilt and azimuth angles of photovoltaic installations respectively are $\beta = \varphi \approx 35°$ and $\psi = 0°$ (refer to §2.2). In the simplified 2D approach discussed, the sun's rays are assumed to be coplanar with the cross–sectional plane of the modelled panels. Consequently, the azimuth angle is not explicitly incorporated in the computations. Instead, this approach models a scenario resembling an experimental setup, where the sun's rays are directed at a specific angle relative to the panel's plane, bypassing the need for explicit consideration of panel orientation. The aim of this simplification is to isolate and quantify the effects induced solely by the dynamics, with all other parameters held constant.

Response data, simulated by assuming specific sea conditions characterized by a frequency spectrum, are considered to describe the incident waves interacting with a floating twin–hull structure of total breadth $B_{(T)} = 20$ m, identical to the structure presented in the previous sections, at water depth $h = 30$ m. The sea state is described by a Brettschneider spectrum model (see §2.3 of Ref. [143]) as follows,

$$S\left(\omega; H_s, T_p\right) = \frac{5}{16} H_s^2 \frac{\omega_p^4}{\omega^5} \exp\left[-\frac{5}{4}\left(\frac{\omega}{\omega_p}\right)^{-4}\right], \tag{3.49}$$

where H_S is the significant wave height, $\omega_p = 2\pi/T_p$ is the peak frequency and T_p is the corresponding peak period.

The roll responses calculated by the 2D numerical model, as discussed in §3.1 and §3.2, are used to evaluate the fluctuations of the AOI and the effect on the power output performance of a PV system consisting of panels, with the aforementioned value of tilt (relative to the horizontal deck of the structure). Specifically, the roll spectrum is evaluated using the RAO in roll motion [see Figure 3-7(a)] of the twin–hull structure using, the following relation,

$$S_4\left(\omega\right) = RAO^2\left(\omega\right) k^2 S\left(\omega\right), \tag{3.50}$$

where the wavenumber k is given by the dispersion relation of water waves for the water depth considered. Based on the calculated roll spectrum, time series of roll motion $\xi_4(t; H_S, T_p)$ of the above floating twin–hull structure are simulated, for the considered configuration (structure and coastal environment) and incident waves, characterized by the parameters (H_S, T_p) using the random–phase model [143,144].

In the discussed simplified model, fluctuations in the tilt angle are directly transferred to the Angle of Incidence, since the model assumes the sun rays to be coplanar with the panels' section. Therefore, any fluctuations in the tilt angle are mirrored in the AOI, as the two quantities are intrinsically linked in the 2D framework, making them effectively equivalent. The results are normalized using the value corresponding to calm water (flat horizontal deck of the structure) in the same environment, which defines the following performance index,

$$PI(t) = \frac{a\cos\left(\alpha_m + \xi_4(t)\right) + b}{a\cos\left(\alpha_m\right) + b}, \tag{3.51}$$

where $a = DNI$, $b = D + R$ and a_m is a representative value for the angle of incidence, with $a_m = 0°$ representing the ideal case where the sun rays are normal to the panel surface.

Numerical results concerning (a) the calculated roll response of the floating twin–hull structure of breadth $B_{(T)} = 20$ m at depth $h = 30$ m and (b) incident wave spectrum (dashed line) and roll angle spectrum (solid line) of the structure in the case of incident waves of significant wave height $H_S = 0.5$ m and peak period $T_P = 4$ s, corresponding to the Beaufort scale levels $BF = 1 - 2$, are presented in Figure 3-9. Based on the calculated roll spectrum, simulated time series of roll motion of the above floating twin–hull structure in the considered marine–coastal environment and incident spectrum, are presented in Figure 3-10. The time series refer to an interval of one hour and a small representative interval of three minutes, respectively, and have been generated using the random–phase model; see e.g. [143,144].

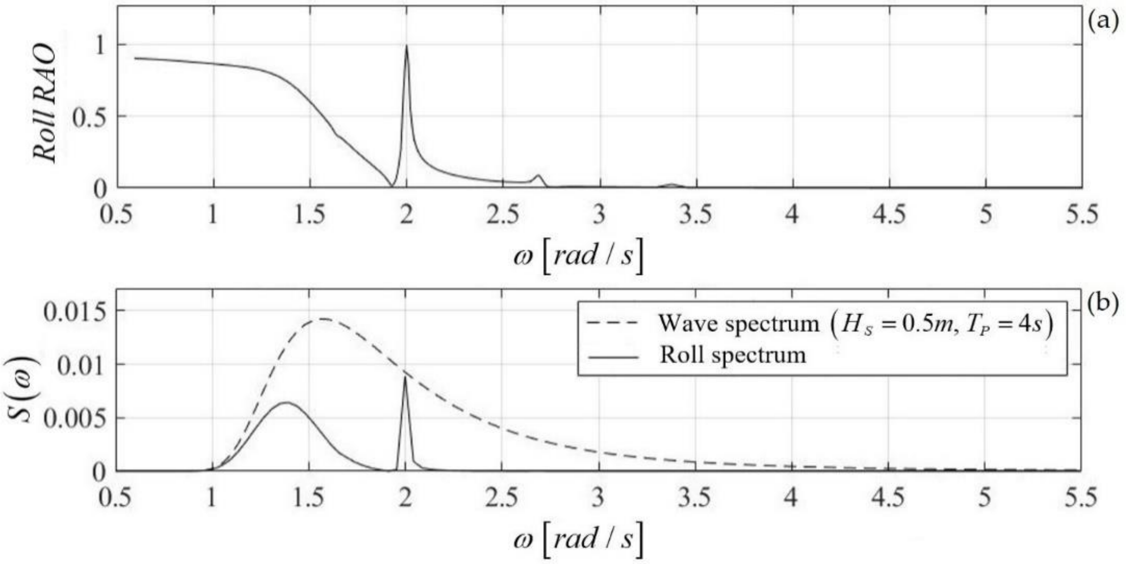

Figure 3-9. (**a**) Roll response of floating twin–hull structure of breadth $B_{(T)} = 20$ m at depth $h = 30$ m and (**b**) Incident wave spectrum (dashed line) and roll angle spectrum (solid line) of the structure in the case of incident waves of significant wave height $H_S = 0.5$ m and peak period $T_P = 4$ s.

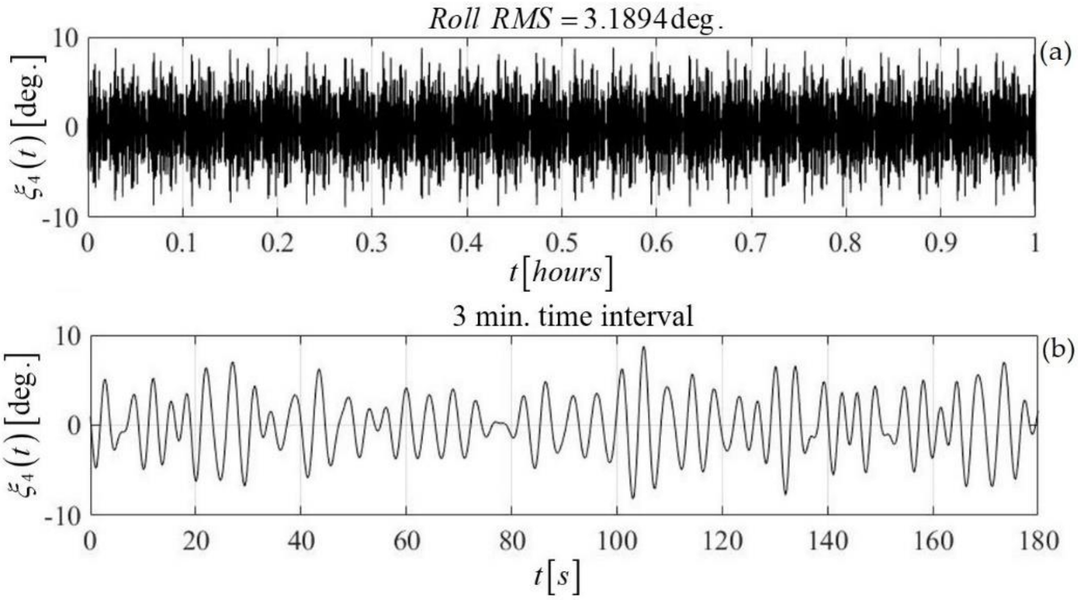

Figure 3-10. Simulated time series of the floating twin–hull structure's roll motion. Total Breadth $B_{(T)} = 20$ m at depth $h = 30$ m. Incident waves of significant wave height equal to $H_S = 0.5$ m and peak period $T_P = 4$ s. (**a**) 1–hour–long time series and (**b**) indicative roll motion in a 3–minute–long time interval.

For the case considered ($H_S = 0.5$ m, $T_P = 4$ s), indicative results concerning the effect of waves and roll responses of the structure on the performance index [Eq. (3.51)] are presented in Figure 3-11, using a representative value of the mean angle of incidence equal to $a_m = 5°$ and omitting, as a first approximation, the effect of diffuse and reflected irradiance components ($b \approx 0$). For the considered incident spectrum, which is characterized by a very low energy content, the RMS value of the estimated performance index drops to $PI_{RMS} = 0.9947$. An indicative one–hour–long time series of $PI(t)$ is depicted in Figure 3-11, where the mean value is denoted by using a cyan line. The PI is normalized relative to a land–based PV unit, providing insight into the performance fluctuations of the FPV system in the considered maritime environment.

Aggregated results are presented in Table 3-1, reporting the evaluated mean value of the performance index for different sea states corresponding to the Beaufort scale from $BF = 1$ (relatively calm sea) to $BF = 5 - 6$ conditions. It can be observed that the system's dynamics can cause a significant drop in the performance index since the fluctuations in AOI are particularly pronounced as sea conditions transition from calm to moderate and subsequently to more severe states. This variability underscores the importance of considering dynamic sea conditions when evaluating the performance of offshore PV units. A more complete picture of the sea states' effect on the FPV module's power output, as estimated using the present method, is shown in Figure 3-12, indicating the presented model's supportive role in the systematic analysis and design of FPV systems, which include the offshore structure, as well as the electric production and storage subsystems. The value corresponding to each point of the grid illustrated in Figure 3-12 represents an average of results obtained from multiple simulations, reflecting the stochastic nature of the studied phenomenon.

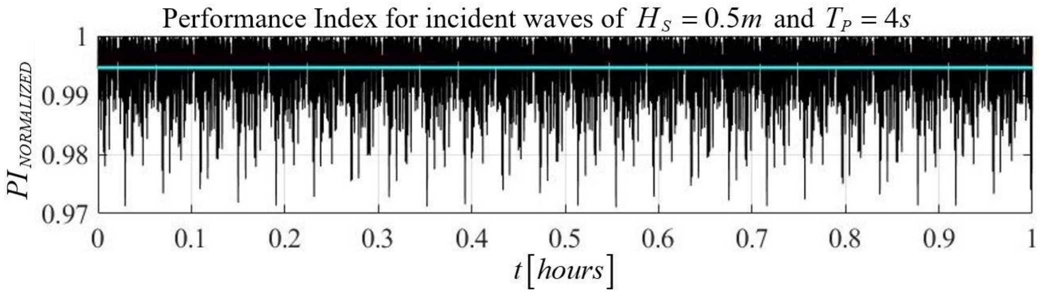

Figure 3-11. Time series of performance index (PI) of the floating photovoltaic unit over a one–hour period and mean value (cyan line). ($B_{(T)} = 20$ m, $h = 30$ m, $H_S = 0.5$ m, $T_P = 4$ s).

These simulations account for the inherent variability and randomness in sea state conditions, ensuring that the data provides reliable estimates of the FPV module's power output under various scenarios.

The dynamic wave motion of floating PV systems in the open sea is a stochastic phenomenon that can cause slight, temporary adjustments in panel orientation, which may occasionally align the panels more optimally with the sun. However, the overall effect of these fluctuations is expected to be negative, as schematically illustrated in Figure 3-12, particularly in optimized configurations where tilt and azimuth are already set for maximum performance. However, as shown in Figure 3-12, the performance drop for sea states typically encountered in nearshore areas of the Mediterranean Sea (see e.g., [145]) is of the order of a few percent, with more significant drops observed under more severe conditions, such as those typically found in the ocean or in more exposed offshore regions. Nonetheless, this negative impact could be balanced or even reversed by the cooling effect (refer to Appendix D) and other environmental factors associated with the marine environment. The latter factors could mitigate temperature–induced power losses, offering a compensatory benefit that helps offset the power reduction caused by fluctuations in instantaneous orientation. In fact, several experimental studies have indicated that FPVs outperform corresponding land–based units by factors of the order of 5% [146], with specific reports indicating performance increases of 20% or more; see e.g. [147,148]. Experimental studies often overlook the impact of dynamics, since most floating photovoltaic (FPV) installations are currently located in confined water environments. The models developed in the present work's context primarily concentrate on the effects of dynamics, while other aspects introduced by the marine environment are only partially addressed. Consequently, combined effects and interactions between various marine environmental factors remains a topic for further investigation.

Table 3-1. Performance indices for different sea conditions.

BF	Sea Condition	H_S (m)	T_P (s)	PI_{RMS}
1–2	1–2	0.5	4	0.9947
3	3	1	6	0.9771
4–5	4	2	8	0.9203
5–6	4–5	3	9	0.8475

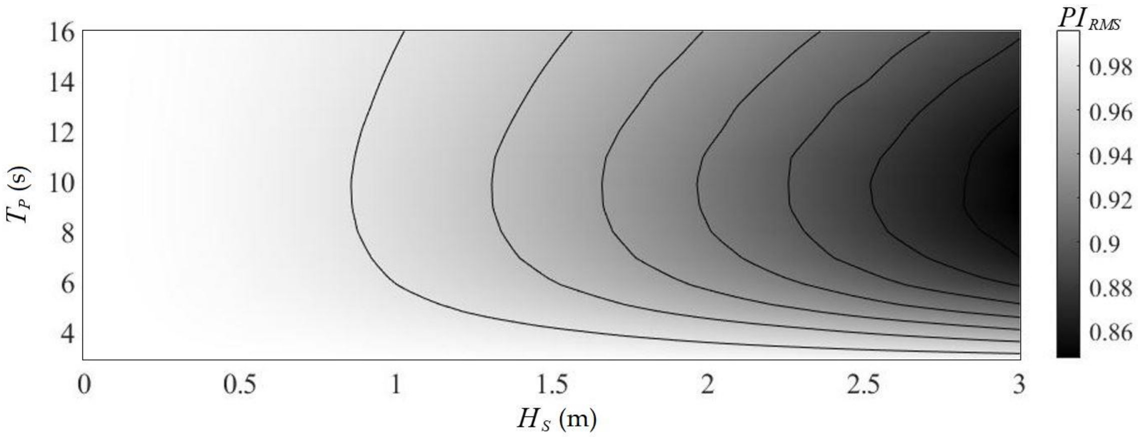

Figure 3-12. Contour map of Normalized Performance Index as a function of the prevailing sea state (Significant wave height H_S and Peak Period T_P).

4

SIMPLIFIED 3D MODEL OF PONTOON–TYPE FPV AND CASE STUDIES

The two–dimensional hydrodynamic model discussed in §3 is here extended using strip theory, to estimate the dynamic responses of 3D pontoon–type floating structures and their effects on the power performance of mounted PV systems in nearshore / coastal regions. The latter structure is examined as a simple alternative for the exploitation of solar energy with applications to nearshore and coastal regions of the Greek seas; (see Figure 4-1). On the basis of linear wave theory, the wave–structure interaction problem is first solved for harmonic incident waves and subsequently the hydrodynamic response operators, calculated in the frequency domain, are used to derive the response frequency spectra; see, e.g., [144]. Using linear system theory, the response spectrum is exploited, in conjunction with the random phase model, to generate short–term time series of the responses of wave motions and their effects on the dynamic variation in the panel tilt angle, from which the solar power performance of the pontoon FPV is derived. Using as an example a 100 kWp floating module, located in the nearshore area of the Pagasitikos Gulf and Evia Island in central Greece, the time series of environmental parameters concerning wave, wind and solar data are used, in conjunction with the hydrodynamic responses, to investigate the effects of hydrodynamics on the floating PV power performance.

In particular, a 45–m–long and 15–m–wide pontoon–type FPV module is considered. The module's deployment is studied in two distinct regions of the Greek coastal area, namely the southeastern coastal area of Evia Island and the western part of the Pagasitikos Gulf, in central Greece. Wave data are generated in the coastal regions by using the nearest offshore points from the ERA5 database [149] in conjunction with an offshore–to–nearshore transformation technique using the SWAN wave model [150,151].

Figure 4-1. Pontoon–type floating structure supporting arrays of photovoltaic panels.

Calculated long–term responses of the FPV structure under wave loads are used to evaluate the effect on the performance of the solar station. These evaluations indicate considerable fluctuations in the performance index in relation to varying sea states. The results are statistically processed for a typical meteorological year (TMY) and used in combination with the corresponding solar data provided by the photovoltaic geographical information system PVG tools (https://re.jrc.ec.europa.eu/pvg_tools/en/), in order to derive predictions of the power performance of the floating module. Additionally, the power output is compared against the corresponding land–based solar module configurations, operating in the same nearby coastal region and the results indicate significant variations in the energy production due to the sea environment and dynamic angle of solar incidence generated from the floating module's responses depending on the sea state, that need to be considered during the design process. The findings suggest that this particular concept presents a promising and techno–economically viable alternative for marine renewable energy exploitation, thereby contributing to the objectives of the European Green Deal policies [2].

In the analysis discussed in this chapter, the techniques of absorbing layers and mirroring are introduced, in the framework of a rather simplified pseudo–3D hydrodynamic model, based on strip theory. Absorbing layers are critical for accurately managing conditions at infinity and simulating physical interactions in computational models. Furthermore, they eliminate the need for additional boundary parts serving as radiation boundaries (see e.g. [152,153]), thereby reducing the overall complexity of the model and minimizing computational resource requirements. Mirroring techniques also serve as valuable tools for reducing the computational costs of BEM models, by eliminating the need to model specific components of the studied domain's boundary surface, under certain conditions. The application of the above techniques, however, is not limited to this introductory framework, since they are widely employed in the subsequent, more complex models which are discussed throughout the remainder of the present work.

4.1. *Extension of 2D Hydrodynamic Model via strip theory*

The hydrodynamic analysis of the floating module is performed using a BEM hydrodynamic model (see also [153]), based on a boundary integral formulation, involving simple singularities for the representation of the near field, in the vicinity of the floating body, in conjunction with suitable models for the treatment of radiation conditions of the considered diffraction / radiation problems. The Cartesian coordinate system $\mathbf{x} = (x_1, x_2, x_3)$ is used, where x_1, x_2 and x_3 are the longitudinal, transverse and vertical axes, respectively, in the local coordinate system of the hull.

The origin is taken to coincide with the structure's center of flotation, with the x_3–axis pointing upwards. Following linear water wave theory, the velocity field is given by the gradient of a potential function $\Phi(\mathbf{x};t)$, which in turn can be represented by a time–independent complex potential $\varphi(\mathbf{x})$, exploiting the assumption of harmonic time dependence,

$$\Phi(\mathbf{x};t) = \mathrm{Re}\left\{\varphi(\mathbf{x};\mu)\cdot\exp(-i\omega t)\right\}. \tag{4.1}$$

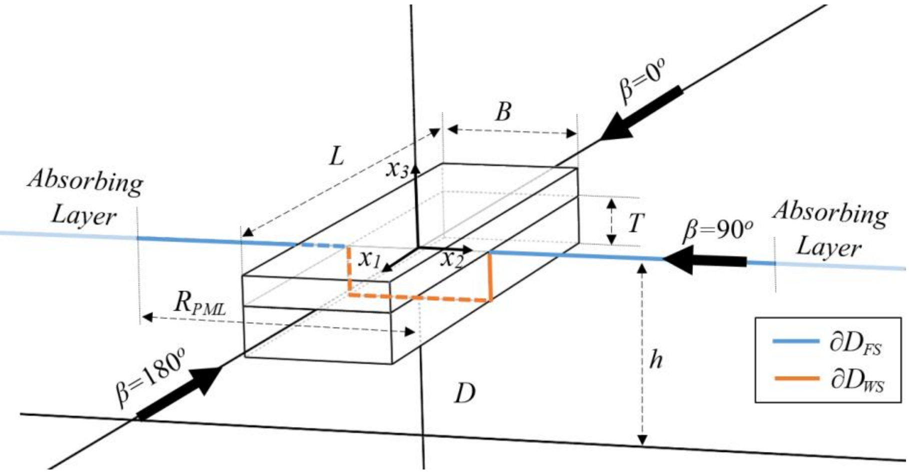

Figure 4-2. Elongated floating pontoon structure supporting photovoltaic panels and parameters of the hydrodynamic model.

In Eq. (4.1), i is the imaginary unit and $\mu = \omega^2/g$ is the frequency parameter, with ω being the angular frequency and g the acceleration due to gravity. The free surface elevation can be obtained in terms of the potential on the mean free surface level ($x_3 = 0$), as follows,

$$\eta(x_1,x_2;t) = -\frac{1}{g}\frac{\partial\Phi(x_1,x_2,0;t)}{\partial t} = \mathrm{Re}\left\{\frac{i\omega}{g}\varphi(x_1,x_2,0;\mu)\cdot\exp(-i\omega t)\right\}. \tag{4.2}$$

A simple pontoon–type floating structure of length L is considered. The hull is characterized by a rectangular cross section of breadth B and draft T, as schematically illustrated in Figure 4-2. The water depth of the domain is denoted by h. The origin is located in the middle of the floating unit on the waterplane level. The hydrodynamic modelling only accounts for the roll response (ξ_4) of the structure, which dynamically alters the tilt angle of the solar panels on deck, while the linear oscillatory motions are considered not to impact the solar irradiance received. Using standard floating body hydrodynamic theory [128,129], the complex potential can be decomposed as follows (refer to Appendix A),

$$\varphi(\mathbf{x}) = -i\omega\sum_n \xi_n\varphi_n(\mathbf{x}),\ n = 0,d,4 \tag{4.3}$$

where $-i\omega\varphi_0(\mathbf{x})$ denotes the normalized incident field of unit amplitude A, $-i\omega\varphi_d(\mathbf{x})$ is the diffracted field, $\varphi_4(\mathbf{x})$ is the radiation field induced by a (unit amplitude) angular rolling oscillation of the structure about the longitudinal axis (x_1), ξ_4 is the complex amplitude of the structure's response in roll motion and $\xi_0 = \xi_d = A$. The incident wave field is considered to be known and equal to,

$$\varphi_0(\mathbf{x}) = \frac{g}{\omega^2}\frac{\cosh(k(x_3+h))}{\cosh(kh)}\exp\left(ik\left(\cos(\beta)x_1+\sin(\beta)x_2\right)\right), \tag{4.4}$$

where β denotes the propagation direction of the incident field, as shown in Figure 4-2, and k is the wavenumber, calculated as the real root of the dispersion relation,

$$\omega^2 = kg\tanh(kh). \tag{4.5}$$

4.1.1. *Mathematical formulation*

Considering the elongated hull, in conjunction with the fact that the sections of the structure remain the same (orthogonal sections) and restricting the analysis to excitation mainly by waves incident from the transverse direction, a strip–theory approximation is used for the hydrodynamic analysis; see, e.g., [129,154]. In this context, the 2D problem is considered, which involves incident waves to the orthogonal cross section in the corresponding flow domain D of constant water depth h, which is enclosed by the free surface ∂D_{FS}, the wetted surface of the structure ∂D_{WS} and the impermeable seabed ∂D_{BS} (see Figure 4-2).

Assuming a homogeneous horizontal bathymetry profile at the vicinity of the floating module, a mirroring technique is applied to account for the interaction of the wave field with the seabed. Consequently, the potential functions that describe the diffracted and radiated fields are represented by the following integral formulation,

$$\varphi_k(\mathbf{x}) = \int_{\partial D} \sigma_k(\mathbf{x}')G(\mathbf{x}',\mathbf{x})d\ell(\mathbf{x}'),\ \mathbf{x}\in D,\ \mathbf{x}'\in\partial D,\ k=d,4, \tag{4.6}$$

where $\partial D = \partial D_{FS} \cup \partial D_{WS}$ and

$$G(\mathbf{x}',\mathbf{x}) = \frac{\ln\left(|\mathbf{x}'-\mathbf{x}|\cdot|\mathbf{x}'-\hat{\mathbf{x}}|\right)}{2\pi} \tag{4.7}$$

is Green's function for the Laplace equation in 2D. In Eq. (4.7), $\hat{\mathbf{x}} = (x_1, -2h-x_3)$ is the mirror point with respect to the bottom plane ($x_3 = -h$) and $\sigma_k(\mathbf{x}'),\ \mathbf{x}' \in \partial D, k = d, 4$ denotes source–sink strength distributions defined on ∂D, corresponding to the diffraction ($k = d$) and the roll radiation field ($k = 4$), respectively. Based on the properties of single–layer distributions, the corresponding derivatives of the functions $\varphi_k(\mathbf{x}), k = d, 4$, normal to the boundary ∂D, are given by [134],

$$\mathbf{n}\cdot\nabla\varphi_k(\mathbf{x}) = -\frac{\sigma_k(\mathbf{x})}{2} + \int_{\partial D} \sigma_k(\mathbf{x}')G(\mathbf{x}',\mathbf{x})d\ell(\mathbf{x}'),\ (\mathbf{x},\mathbf{x}')\in\partial D,\ k=d,4, \tag{4.8}$$

where $\mathbf{n} = (n_2, n_3)$ is the unit vector normal to ∂D, directed towards the exterior of the domain. Based on the above integral representation, the diffracted and radiated fields are evaluated by appropriately formulated boundary value problems (BVPs), involving the linearized free–surface–BC (FSBC) on ∂D_{FS}, as well as excitation terms on the wetted surface. Specifically, the diffracted and radiated fields are obtained as solutions to the following BVPs for $k = d, 4$,

$$\nabla^2\varphi_k(\mathbf{x}) = 0,\ \mathbf{x}\in D, k=d,4, \tag{4.9}$$

$$\mathbf{n}\cdot\nabla\varphi_k(\mathbf{x}) - \mu(x_2;\,\omega)\varphi_k(\mathbf{x}) = 0,\ \mathbf{x}\in\partial D_{FS}, k=d,4, \tag{4.10}$$

$$\mathbf{n}\cdot\nabla\varphi_k(\mathbf{x}) = N_k(\mathbf{x}),\ \mathbf{x}\in\partial D_{WS}, k=d,4, \tag{4.11}$$

where

$$N_d(\mathbf{x}) = -\mathbf{n}\cdot\nabla\varphi_0(\mathbf{x}) \text{ and } N_4(\mathbf{x}) = x_2n_3 - x_3n_2. \tag{4.12}$$

In order to eliminate the infinite extent of the domain in the x_2–direction, a perfectly matched layer (PML) technique is adopted, consisting of an absorbing layer which is used to attenuate the outgoing wave solutions in an optimal way, preventing reflections from the outer boundary; see, e.g., [80]. The thickness of the layer is of the order of one local wavelength $\lambda = 2\pi/k$ and implementation is achieved by making the frequency parameter complex inside the layer, as follows,

$$\mu(x_2) = \begin{cases} \omega^2 g^{-1}, & |x_2| < R_{PML} \\ \omega^2 g^{-1}\left(1 + ic\dfrac{\left(|x_2| - R_{PML}\right)^q}{\lambda^n}\right)^2, & |x_2| \geq R_{PML}. \end{cases} \tag{4.13}$$

In Eq. (4.13), R_{PML} denotes the absorbing layer activation "radius" which, in the simplified formulation discussed, reduces to a simple distance along the x_2–axis (from the origin to the PML activation point). The parameters c and q, as well as the effective length are defined depending on the angular wave frequency ω. Details concerning optimal values for the above parameters can be found in Table 1 of Ref. [155], which presents cumulative results of an analysis comparing numerical solutions obtained by using variously tuned layers against an analytical solution, aiming towards the minimization of the Chebyshev norm of the resulting difference.

Numerical solutions to the above BVPs are obtained by means of a low–order BEM, based on piecewise constant singularity distributions on linear panels, ensuring continuity of the boundary geometry approximation; (see also [135]). In the numerical scheme, the BCs are chosen to be satisfied at the collocation points coinciding with the panel midpoints and therefore, the BVPs expressed by Eqs. (4.9)–(4.13) reduce to two linear algebraic systems ($\mathbf{A}\boldsymbol{\sigma}_k = \mathbf{b}_k, k = d, 4$) each comprising M equations and M unknown quantities, where M denotes the number of panels used to discretize the boundary ∂D. The components A_{ij} of the influence matrix $\mathbf{A}$ are calculated in terms of the induced potential and velocity from constant unitary source–sink distribution on the panel m to the i^{th}–collocation point and constitute a discretized form of the left–hand side of Eqs. (4.10)–(4.11). Moreover, the right–hand sides of the linear systems (b_j) contain the values of $N_k, k = d, 4$ given by Eq. (4.12) evaluated at the i^{th} collocation point. The piecewise constant values of the source/sink strength distribution defined on the boundary ∂D are then used to evaluate the potential and the velocities inside the domain, as follows,

$$\varphi_k(\mathbf{x}) = \sum_{m=1}^{M} \sigma_m^{(k)} \Phi_m(\mathbf{x}), \quad \nabla\varphi_k(\mathbf{x}) = \sum_{m=1}^{M} \sigma_m^{(k)} \mathbf{U}_m(\mathbf{x}), \; k = d, 4 \tag{4.14}$$

where $\Phi_m(\mathbf{x})$ and $\mathbf{U}_m(\mathbf{x})$, respectively, denote the induced potential and velocity from the m^{th} panel carrying unitary singularity strength to the field point identified by the position vector $\mathbf{x}$; which can be calculated analytically (see, e.g., [156]). This fact ensures both speed and precision, while eliminating the potential for integration errors, making the method highly efficient and well–suited for optimization problems.

Based on the incident, diffracted and radiated wave fields, the roll response of the floating module (ξ_4) is evaluated by means of the following equation of motion,

$$\xi_4 = \frac{F_{04} + F_{d4}}{-\omega^2\left(I_{44} + A_{44}\right) - i\omega B_{44} + C_{44}}, \tag{4.15}$$

where $F_{k4}, k = 0, d$ respectively denote the Froude–Krylov ($k = 0$) and diffraction ($k = d$) roll moments. The latter moments are calculated via integration (on the wetted surface) of the pressure induced by the incident and diffracted subfields: $p_k(\mathbf{x}) = -i\omega\rho\varphi_k(\mathbf{x}), k = 0, d$, (with ρ being the water density), multiplied by the component of the generalized normal vector, corresponding to rotation about the longitudinal axis ($N_4 = x_2 n_3 - x_3 n_2$),

$$F_{k4} = \omega^2\rho \int_{-L/2}^{L/2} \int_{\partial D_{WS}} \varphi_k(\mathbf{x}) N_4(\mathbf{x}) d\ell(\mathbf{x}) dx_1 = \omega^2\rho L \int_{\partial D_{WS}} \varphi_k(\mathbf{x}) N_4(\mathbf{x}) d\ell(\mathbf{x}), k = 0, d. \tag{4.16}$$

The moment of inertia equals $I_{44} = MR_{44}$, where $M = \rho V$ is the mass of the structure, $V = LBT$ is the submerged volume and R_{44} is the radius of gyration about the longitudinal axis, considering uniform weight distribution along the x_2–direction. The parameter C_{44}, modelling the hydrostatic restoring moment, equals $C_{44} = gM \cdot GM$, where GM denotes the metacentric height, evaluated as $GM = KB + BM - KG$, where K is a reference point at the keel of the structure ($x_3 = -T$), G is the center of gravity positioned at the waterplane level, and B denotes the center of buoyancy, located at $x_3 = -T/2$. Furthermore, the metacentric radius BM is evaluated as $BM = I/\rho\nabla$, where I is the second moment of area of the waterplane with respect to the longitudinal axis (x_1), which in the case of the floating pontoon is given by $I = LB^3/12$. Finally, the added moment of inertia and hydrodynamic damping coefficients of the floating pontoon are obtained from the corresponding expression of the radiation moment as follows (see also Eq. (A.89) of Appendix A),

$$\omega^2 A_{44} + i\omega B_{44} = \Pi_{44}, \text{ where} \tag{4.17}$$

$$\Pi_{44} = \omega^2\rho \int_{-L/2}^{L/2} \left[\int_{\partial D_{WS}} \varphi_4(\mathbf{x}) \cdot N_4(\mathbf{x}) d\ell(\mathbf{x}) \right] dx_1. \tag{4.18}$$

4.2. *Numerical Results and Verification*

Results obtained via the numerical scheme, described in the previous subsection, are here compared against experimental measurements from the literature for verification purposes. The results concern a pontoon–type structure floating at depth h, with dimension ratios $L/h = 3$, $B/h = 1$, $T/h = 0.2$ and the radius of gyration about the longitudinal axis is set to $R_{44} = 0.4B$. Numerical and experimental results regarding the above configuration have been presented by Pinkster and van Oortmerssen [157]. In the latter work, model tests were conducted in the shallow water laboratory of the Netherlands Ship Model Basin, which measures 210 m in length and 15.75 m in breadth, and the water depth is equal to 1 m. The tests were carried out using a model at a scale of 1: 50. Regular waves were generated at one end of the basin using a flap–type wave maker (see e.g., [158]), while a perforated sloping beach at the other end of the basin served as a wave damper to minimize reflections. Concerning the present discrete BEM model, a minimum of 20 boundary elements per wavelength was applied to the free–surface boundary, while the number of equally distributed panels on the wetted surface of the pontoon cross section is set to 300, which was found to be sufficient for numerical convergence in the studied frequency range.

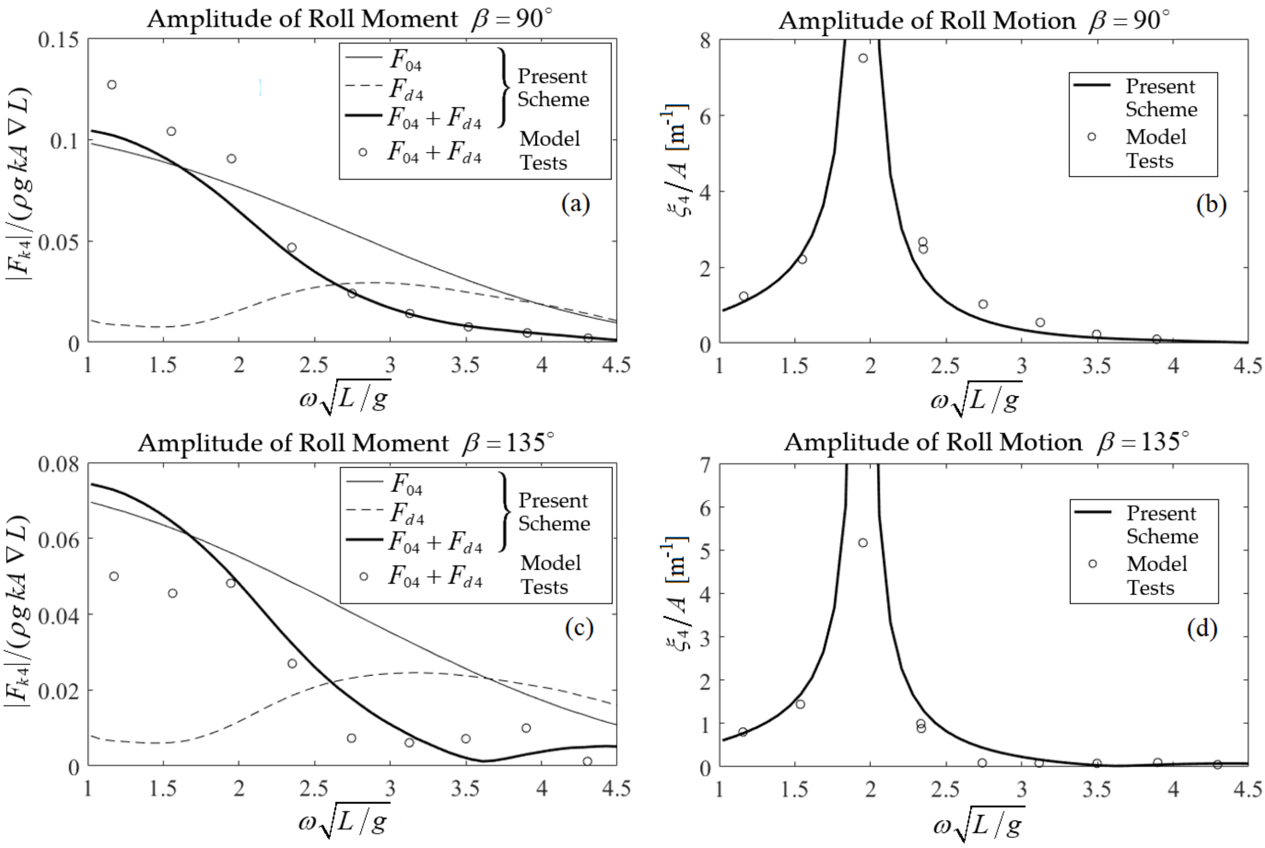

Figure 4-3. (**a**, **c**) Normalized non–dimensional roll moments and (**b**, **d**) roll motion responses, as functions of the non–dimensional frequency, as calculated via the present method and as measured using model tests [157] for incident wave fields propagating at (**a**, **b**) $\beta = 90°$ and (**c**, **d**) $\beta = 135°$. Froude–Krylov, diffraction and total roll moments, as calculated by the present BEM scheme, are plotted using thin, dashed and thick lines, respectively.

Figure 4-3(a) depicts the normalized Froude–Krylov, diffraction and total roll moments acting on the structure, as calculated by the present BEM scheme, using thin, dashed and thick lines, respectively. The total moments are compared against experimental measurements [157] for beam seas ($\beta = 90°$). Furthermore, Figure 4-3(b) shows the resulting response in roll motion for beam seas ($\beta = 90°$), as calculated via the present numerical scheme using Eq. (4.15), and as measured in the model tests. Corresponding results for quartering waves ($\beta = 135°$) are presented in Figure 4-3(c–d). It is observed that the present simplified model provides numerical predictions in good agreement with the experimental data, especially for beam seas. As concerns the quartering seas case the results exhibit certain discrepancies, which can be attributed to the limitations of strip theory.

Using the calculated responses of the aforementioned floating structure in conjunction with year–long time–series data of wave parameters from the nearshore regions proposed for deployment, the impact of wave conditions on the power performance of the floating photovoltaic system is evaluated. The power output is compared against corresponding results from a nearby land–based solar park, featuring identical components and dimensions. The analysis incorporates the dynamic variations in the angle of incidence of solar irradiance on the floating configuration, accounting for the perturbations in the tilt angle of the panels resulting from the structure’s responses to wave loads. Two nearshore coastal sites within the Greek sea region are selected as case studies for the deployment and operation of the pontoon–type structure, as further detailed in the following sections.

4.3. *Offshore–to–Nearshore Transformation of Wave Conditions*

The nearshore / coastal regions of western Pagasitikos Gulf in central Greece and southeastern coastal area of Evia Island, shown in Figure 4-4, are considered to demonstrate the applicability of the present method, as regards the evaluation of the floating solar module’s power performance. In the above regions, a simple pontoon–type platform of dimensions $L = 45$ m in length and $B = 15$ m in breadth is considered to be deployed, in salt water of depth $h = 15$ m. The water density is $\rho = 1025\ \mathrm{kg/m^3}$ and the draft of the structure is $T = 3$ m. Therefore, the total mass of the structure is $M = 2.076 \times 10^6$ kg and the moment of inertia with respect to the longitudinal axis (x_1) equals $I_{44} = 7.47 \times 10^7\ \mathrm{kgm^2}$. Moreover, the center of gravity is assumed to be located at a vertical distance of 3 m above the keel.

An Offshore–to–Nearshore (OtN) transformation technique is employed to generate wave data at the coastal locations of the floating structures, utilizing corresponding offshore wave and wind data along with geographical information, as described in more detail in the sequel. Various sources of offshore wave and wind data are available for the sea areas of interest. The most comprehensive datasets are typically derived from operational wave models maintained by meteorological and oceanographic agencies, as well as from dedicated long–term hindcast studies. In addition, satellite–based data, offering broad spatial coverage, is readily accessible for offshore regions worldwide (see e.g., [159]). To estimate nearshore wave conditions, offshore data is often transformed through nearshore wave models. This process involves integrating offshore wind and wave data with bathymetric and coastline information, specific to the areas under study (see e.g., [160]). Concerning the Pagasitikos Gulf region, the geographical area considered is $[39°14'1''\mathrm{N}, 39°21'58''\mathrm{N}] - [22°48'9''\ \mathrm{E}, 23°11'23''\ \mathrm{E}]$, as shown in Figure 4-5(a).

Figure 4-4. Nearshore areas considered for the deployment of FPV modules. (**a**) Pagasitikos Gulf area, and (**b**) southeastern coastal region of Evia Island.

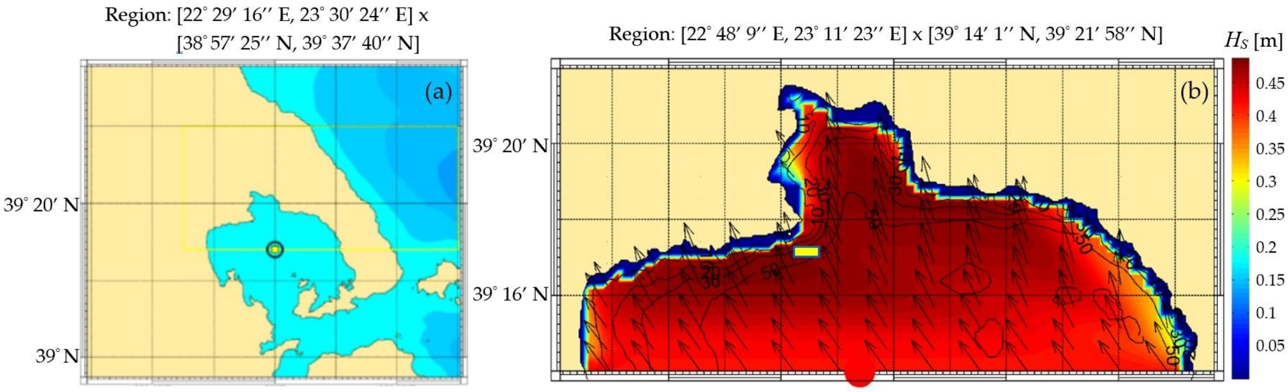

Figure 4-5. (**a**) Nearshore area considered for FPV deployment in western Pagasitikos Gulf region. (**b**) Calculated waveheight distribution using SWAN model for the offshore data, $H_S = 0.42$ m, $T_e = 4.44$ s, mean wave direction: 141°, wind speed: 6.33 m/s, wind direction: 180°. The position of the considered FPV structure is shown by using a yellow rectangle.

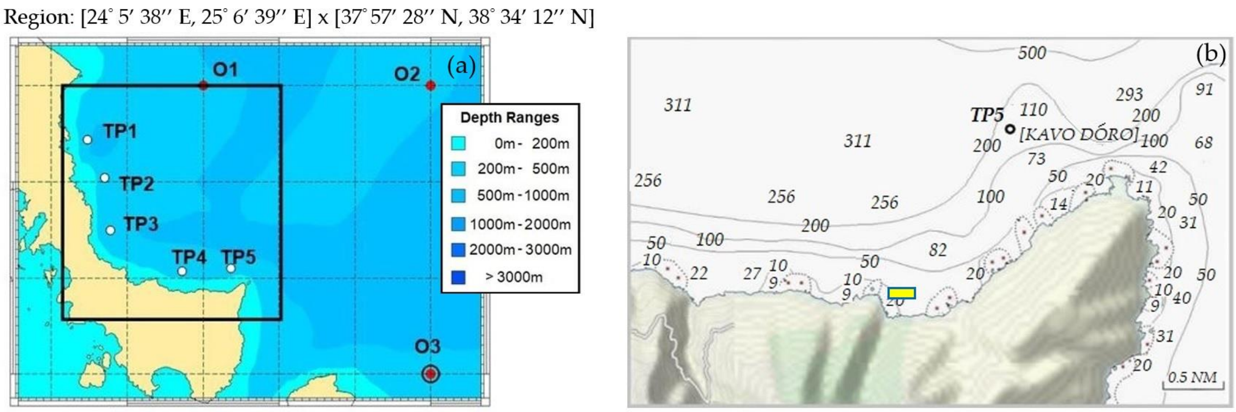

Figure 4-6. (**a**, **b**) Nearshore area considered for the FPV deployment in southeastern region of Evia Island. The position of the considered FPV structure is indicated by a yellow rectangle.

In the southeastern coastal area of Evia Island, the geographical area considered is defined by the coordinates $[24°10' \text{ E}, 24°40' \text{ E}] – [38°05' \text{ N}, 38°30' \text{ N}]$, shown in Figure 4-6. In both cases, the floating pontoon is considered to be deployed with the longitudinal axis directed eastward. In the context of the present analysis, the wave climate in the considered nearshore regions was derived from the ERA database, using an Offshore–to–Nearshore (OtN) transformation of wave conditions obtained based on SWAN wave model [150,151]. The bathymetric data in the areas of interest were used along with coastline data in order to set up the SWAN model for calculating the offshore–to–nearshore wave transformations for the nearshore target points coinciding with the deployment locations at water depth $h = 15$ m. The bathymetric data used for obtaining the OtN transformation in the extended regions were created via the combination of the EMODnet Digital Bathymetry (DTM 2016) which is based on more than 7700 bathymetric data sets from various countries near European Seas and is provided on a grid resolution of 1/8 by 1/8 arc minute of longitude and latitude [161]. The database used for the coastline is the Global, Self–Consistent, Hierarchical, High–Resolution Shoreline Database (GMT–GSHHS) provided under the GNU Lesser General Public License; see the work by Wessel and Smith, 1996 [162]. The utilized OtN methodology is described in detail in Ref. [163].

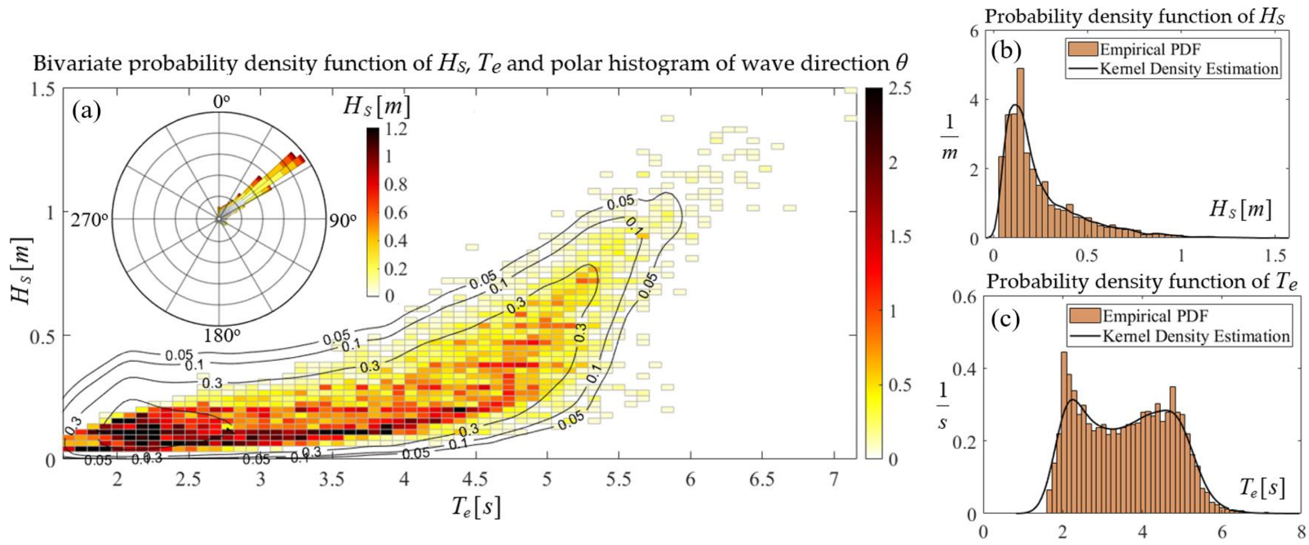

Figure 4-7. Annual distribution of wave parameters at the nearshore target point $(39°17'36''\text{N}, 22°56'40''\text{E})$ in Pagasitikos Gulf region. (**a**) Bivariate probability density function of (H_S, T_e) and corresponding polar histogram of wave direction. (**b**) Marginal probability density function of H_S and (**c**) marginal probability density function of T_e.

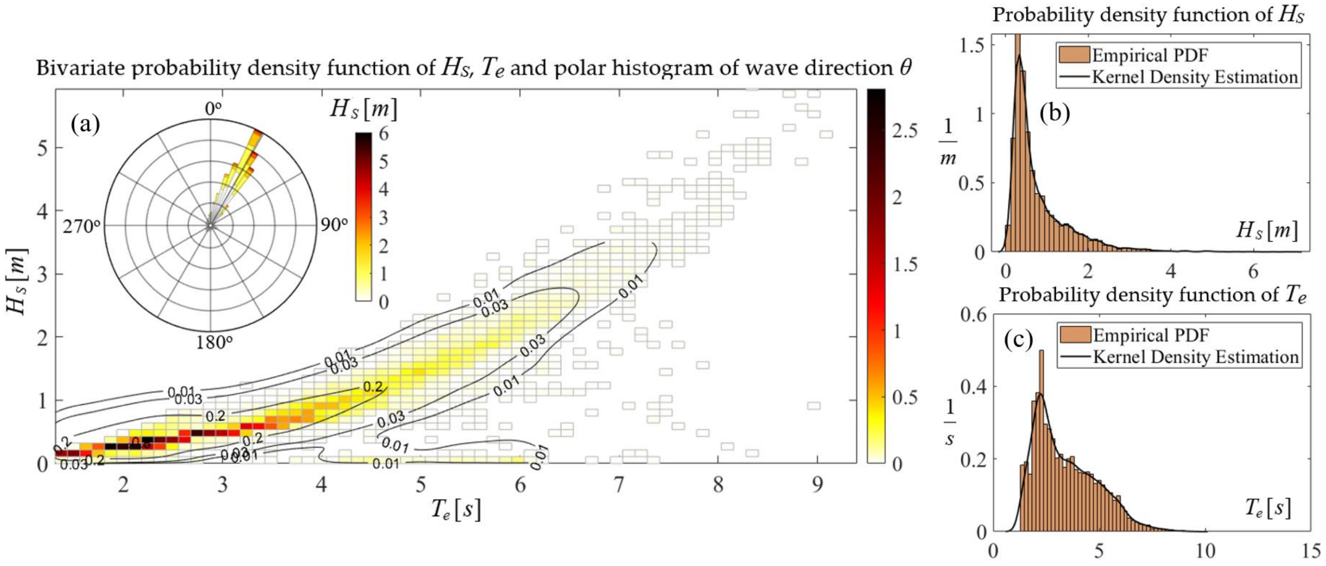

Figure 4-8. Annual distribution of wave parameters at the nearshore target point $(38°08'35''\text{N}, 24°32'52''\text{E})$ in the southeastern region of Evia Island. (**a**) Bivariate probability density function of (H_S, T_e) and corresponding polar histogram of wave direction. (**b**) Marginal probability density function of H_S and (**c**) marginal probability density function of T_e.

The derived wave climatology in the two considered nearshore regions is presented in Figure 4-7 and Figure 4-8, respectively. Moreover, the basic statistical measures concerning wave characteristics (i.e., significant wave height H_S, mean energy period T_e and mean wave direction θ_m) at the two considered locations, including standard deviation and minimum (min) – maximum (max) values, are comparatively presented in Table 4-1.

Table 4-1. Nearshore wave parameters in the considered regions.

Nearshore Point	$H_{S,mean}$	$T_{e,mean}$	$H_{S,std}$	$T_{e,std}$	H_S **min/max**	T_e **min/max**	**R (H_S,T_e)**	**θ,mean (deg)**	**θ,std (deg)**
Pagasitikos Gulf	0.25 m	3.57 s	0.20 m	1.12 s	0.03/1.50 m	1.63/7.16 s	0.796	54.04	41.07
SE Evia Island	0.79 m	3.41 s	0.73 m	1.45 s	0.01/6.98 m	1.31/9.40 s	0.877	24.37	38.73

4.4. *Responses of the FPV Structure*

The nearshore time series of wave parameters are used to define the corresponding incident wave spectra using the JONSWAP model, as presented in Figure 4-9(a) for a representative case. The spectral density, based on the latter model, is defined as [164],

$$S\left(f \mid H_S, T_e\right)=\left(\frac{a g^2}{(2\pi)^4 f^5} \exp\left[-1.25\left(\frac{f}{f_p}\right)^{-4}\right] \gamma^{\delta(f)}\right), \tag{4.19}$$

where $f = \omega/2\pi$ is the linear frequency and ω is the angular frequency; $f_p = 1/T_p$ is the peak frequency, estimated as $f_p = 0.906/T_e$ (see e.g., [165]) and $g = 9.81\ ms^{-2}$ is the acceleration due to gravity. Furthermore, a is a normalization parameter suitably defined such that $H_S = (m_0)^{1/2}$, where m_0 is the zeroth–order spectral moment [166]. Finally, the parameter γ and the function $\delta(f)$ are defined as follows,

$$\gamma = 3.3, \text{ and } \delta = \exp\left[-\frac{\left(f - f_p\right)^2}{2\sigma_0^2 f_p^2}\right] \text{ with } \sigma_0 = \begin{cases} 0.07, & \text{for } f < f_p \\ 0.09, & \text{for } f \geq f_p \end{cases}. \tag{4.20}$$

In order to combine the wave and solar data in the considered regions and evaluate the power output performance, time series for a typical meteorological year (TMY) are generated by taking mean values for each 6–hour long interval in the long–term time series of wave parameters and each date of the TMY. The derived wave data are used to reconstruct nearshore frequency spectra and are combined with the roll response amplitude operators (RAOs) of the considered pontoon–type structure, as presented in Figure 4-9(b) for two wave incidence angles ($\beta = 90°$ for beam seas, and $\beta = 135°$ for beam–quartering seas) to obtain the spectra characterizing the rolling motion of the structure. In the example presented in Figure 4-9, the FPV is located in the coastal area of Evia Island (see Figure 4-6) and the incident wave spectra correspond to the mean climatological values of $H_S (= 0.79\ \text{m})$ and $T_e (= 3.41\ \text{s})$. In particular, the incident spectrum (using the JONSWAP model) shown in Figure 4-9(a) is combined with the roll response (RAO) of the FPV, shown in Figure 4-9(b), and spectra of roll response are derived, as shown in Figure 4-9(c) for two angles of incidence. For simplicity, unidirectional incident wave spectra are considered, and the response spectra are calculated using the computed roll RAOs as follows,

$$S_4(\omega) = \int_{\theta=0}^{2\pi} RAO^2(\omega, \beta) k^2 S(\omega) d\theta, \quad \beta = \left(\theta + \frac{\pi}{2}\right) - \psi. \tag{4.21}$$

In Eq. (4.21), $S(\omega) = S(f)/2\pi$, θ is the mean wave direction – measured clockwise from the North – and the wavenumber k is evaluated using the dispersion relation [Eq. (4.5)], for each frequency of water waves at water depth $h = 15$ m. Moreover, ψ denotes the angle of the longitudinal axis of the structure with respect to the east, measured clockwise from East to South. The latter angle coincides with the azimuth of the mounted PV system, since the panels are considered to be placed parallel to the longitudinal axis of the structure (see Figure 4-1). In the considered example the azimuth is set to $\psi = 0°$, aligning with the optimal angle for solar panel placement in the northern hemisphere [99], and thus $\beta = \theta + \pi/2$. The latter relation reflects the fact that northerly (and southerly) directions of wave propagation translate to beam seas for the hydrodynamic model.

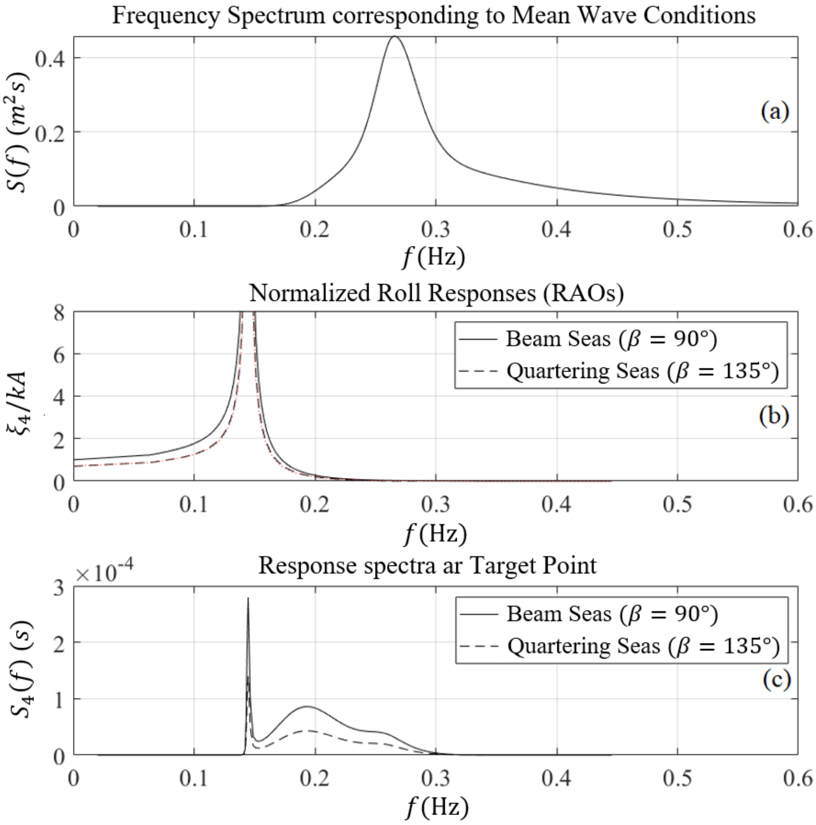

Figure 4-9. (**a**) Wave frequency spectrum corresponding to the mean climatological values, (H_S = 0.79 m, T_e = 3.41 s) at the southeastern coastal area of Evia Island (**b**) Roll response operators (RAOs) and (**c**) response frequency spectra of the floating pontoon–type FPV structure of length $L = 45$ m, breadth $B = 15$ m and draft $T = 3$ m, located at depth $h = 15$ m for beam ($\beta = 90°$) and quartering ($\beta = 135°$) seas.

Exploiting the fact that the cross sections of the structure are unchanged in the fore–aft direction, in conjunction with the transverse symmetry, the roll response for various incident wave directions, is approximated by the following relation,

$$RAO(\omega,\beta) \approx RAO_{2D}(\omega)\left|\cos(\theta)\right|, \tag{4.22}$$

where $RAO_{2D}(\omega)$ denotes the sectional response of the pontoon structure, obtained from Eq. (4.15) for various frequencies of incident waves. Based on the calculated roll response spectrum $S_4(\omega)$, simulated time series of roll motion $\xi_4(t; H_S, T_e, \theta_m)$ of the structure are constructed, for the considered configuration (structure and coastal environment) and for each data point in the time series of incident waves characterized by the parameters H_S, T_e and θ_m. The time series are obtained using the random phase model, see, e.g., [143,144]. Specifically, the response time series of the structure under spectral excitation is evaluated by the following representation,

$$\xi_4(t) = \sum_{n=1}^{N} A_n \cos(-\omega_n t + \varepsilon_n), \text{ where } A_n = \sqrt{2S_4(\omega_n)\Delta\omega_n}, \tag{4.23}$$

and $\varepsilon_n \in [0,2\pi)$ are random phases.

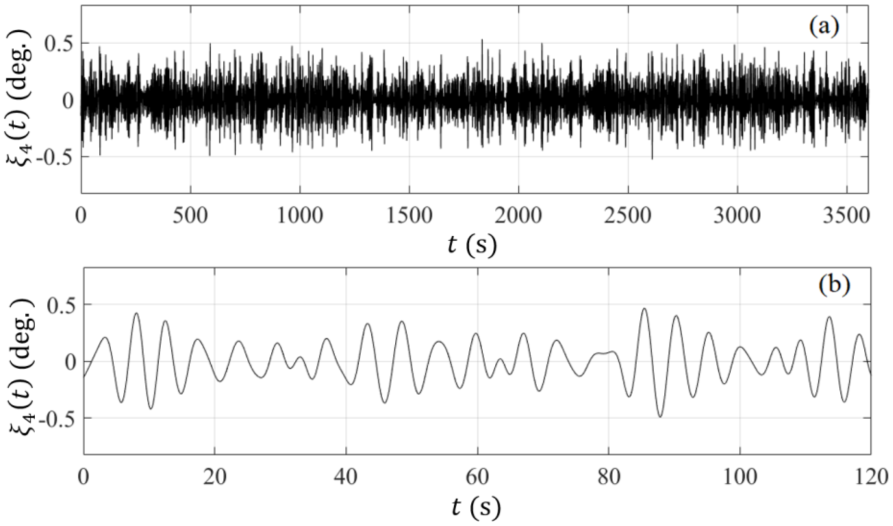

Figure 4-10. Simulated time series of the pontoon–type FPV structure's roll motion. Length $L = 45$ m, breadth $B = 15$ m, draft $T = 3$ m, depth $h = 15$ m. Incident waves of significant wave height equal to $H_S = 0.79$ m and energy period $T_e = 3.41$ s. (**a**) Simulated 1–h–long time series data and (**b**) indicative roll motion in a 2–minute–long time interval.

An indicative simulated time series of the considered pontoon FPV structure, in the case of quartering incident waves with significant wave height equal to $H_S = 0.79$ m, energy period $T_e = 3.41$ s and mean direction $\theta_m = 24.37°$ (corresponding to the climatological mean values at the FPV coastal location of the southeastern Evia Island region), is illustrated in Figure 4-10. In the sequel, the short–time roll responses $\xi_4(t; H_S, T_e, \theta_m)$ for each prevailing sea state are used to calculate the angle of incidence (AOI) at the FPV and the resulting effect on the power output of the PV system, in conjunction with other data concerning the tilt (with respect to the deck of the structure) and their orientation (azimuth angle).

4.5. *Effects of Dynamics on FPV Module Power Performance*

The power performance of a floating photovoltaic (FPV) unit is based on a variety of factors, many of which arise from the local marine environment. While certain factors that influence the energy efficiency of FPVs are also found in corresponding land–based units, with comparable power output levels, others are not present in land installations. In this section the power output of the considered FPV system is assessed, making use of the model discussed in §2.

For the examined configuration concerning the FPV platform of length 45 m and total breadth 15 m, a 100 kWp arrangement is considered, consisting of 11 parallel strings of 40 in–series modules (see Figure 4-1). In order to estimate data, the Sanyo HIP–225HDE1 panel modules of 225 Wp nominal power, with dimensions 1.6 m × 0.86 m, $V_{PM} = 33.9$ V and $I_{PM} = 6.64$ A, are considered, with module efficiency of 15% at $T_{STC} = 25$ °C. Thus, the total panel area on the FPV structure equals $A_{pv} = 605.44\, m^2$ and $k_p \approx 0.4\%/°\mathrm{C}$ is used as an approximate value of the temperature coefficient for silicon panel technology (refer to Eq. (2.2) in §2.3). The PV performance is directly affected by the angle of incidence of solar irradiance which, in the case of FPV installations, is influenced by the wave–induced responses. In order to account for the above effect, noting that the structure is oriented with its longitudinal axis directed eastward (see Figure 4-5 and Figure 4-6), the tilt angle of the present FPV panel configuration in the PV model described in §2.3, is replaced by the corresponding dynamic value obtained by the summation of the static value (β_0), which is set to $\beta_0 = 30°$, and the instantaneous roll response of the supporting structure, defined on the short time scale, as described in the previous section, for each sea state in the constructed time series of the TMY,

$$\beta_{FPV}(t) = \beta_0 + \xi_4(t). \tag{4.24}$$

Data concerning the direct normal irradiance (DNI), diffuse horizontal irradiance (DHI) and environmental conditions concerning the temperature and wind for the specific site were obtained from the PVGIS SARAH2 database in the form of a typical meteorological year (TMY) data set with 1–hour temporal resolution, provided by PVG tools (https://re.jrc.ec.europa.eu/pvg_tools/en/). The ambient and cell temperatures are computed as detailed in §2.3, based on the dry–bulb temperature, the wind speed and the relevant humidity. The albedo coefficient is set to $c = 0.1$ for the floating configuration and $c = 0.3$ for a corresponding land–based configuration [118].

Numerical results, concerning the performance and energy production of the considered 100 kWp system, are presented comparatively in Figure 4-11 and Figure 4-12 for a land–based module and the considered FPV configuration, located at the geographical nearshore / coastal locations of Pagasitikos Gulf and the southeastern region of Evia Island, respectively.

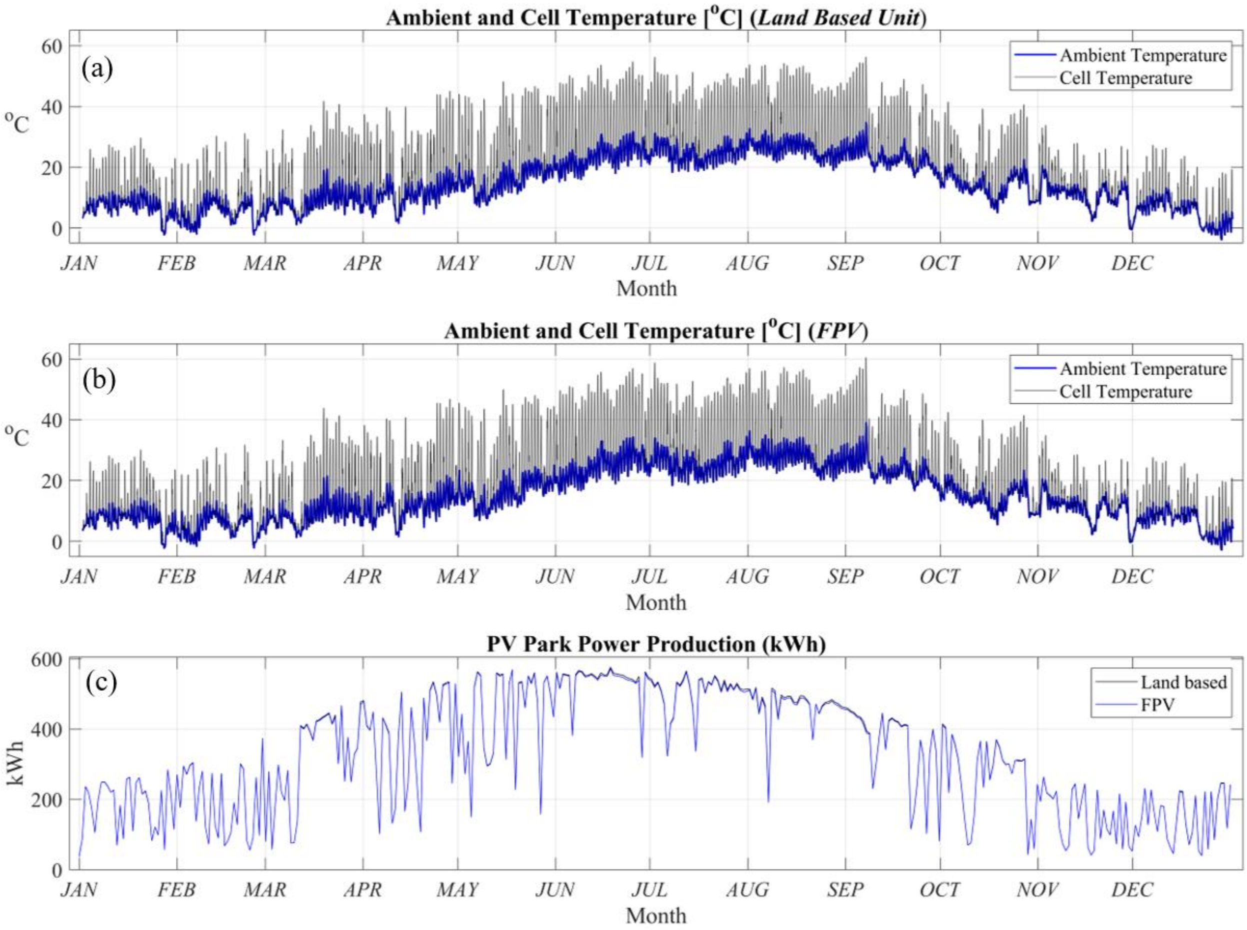

Figure 4-11. Simulated time series of temperature and power performance for land–based and FPV 100 kWp configuration at Pagasitikos Gulf region. Ambient and cell temperature of (**a**) land–based unit and (**b**) FPV. (**c**) Comparative daily power production in a TMY.

In particular, the ambient and cell temperatures of the land–based and the floating configurations are presented in subplots (a, b) of each figure, respectively. Moreover, the daily energy production in a TMY is shown in subplots (c). In the latter plots, the results concerning the calculated daily energy production for a fixed (inland) nearby configuration and for the FPV system in a TMY are comparatively plotted, using black and blue lines, respectively. It is observed that the dynamic variation in the angle of incidence on the panels produced by the wave loads, along with the effect of the reduced albedo of open water environment, leads to a drop in the energy production. In the examples considered in this work, the calculated annual production drops by a factor of the order of 1%, from $119.96\ \mathrm{MWh}$ (nearby inland configuration) to $118.98\ \mathrm{MWh}$ (FPV) in Pagasitikos Gulf (-0.51%) and from $115.41\ \mathrm{MWh}$ (inland configuration) to $114.06\ \mathrm{MWh}$ (FPV) in the southeastern region of Evia Island (-1.23%), respectively. The differences in performance losses are mainly attributed to the varying wave and wind conditions at the two locations. In particular, the installation in Pagasitikos Gulf experiences reduced wave heights and periods, leading to smaller deviations in the orientation of the PV modules. Conversely, the installation at the southeastern coast of Evia Island is exposed to longer wind fetches and therefore is subject to more significant wave–induced motion, causing greater misalignment of the PV modules with the incoming solar irradiance.

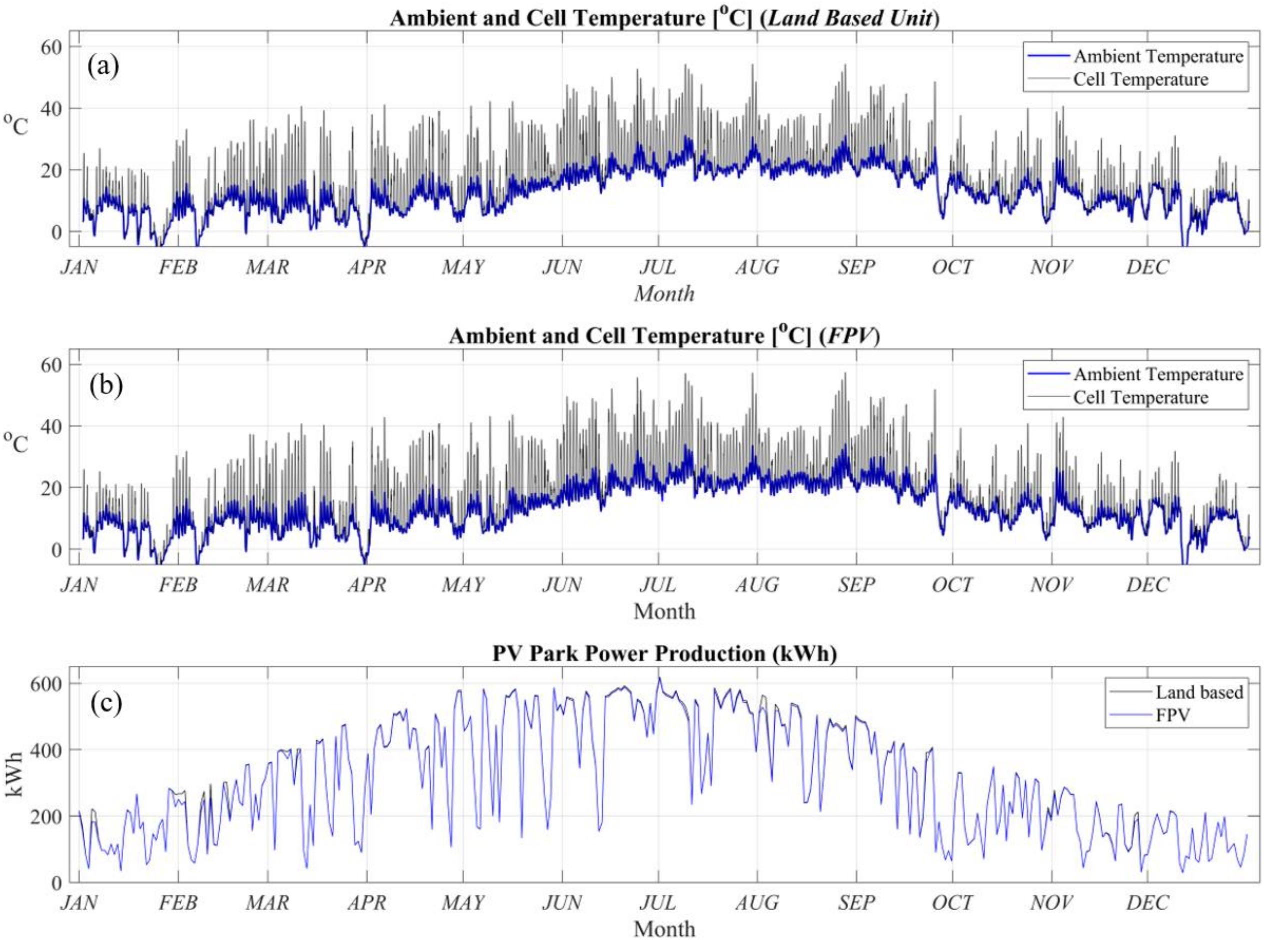

Figure 4-12. Simulated time series of temperature and power performance for land–based and FPV 100 kWp configuration at southeastern Evia Island. Ambient and cell temperature of (**a**) land–based unit and (**b**) FPV. (**c**) Comparative daily power production in a TMY.

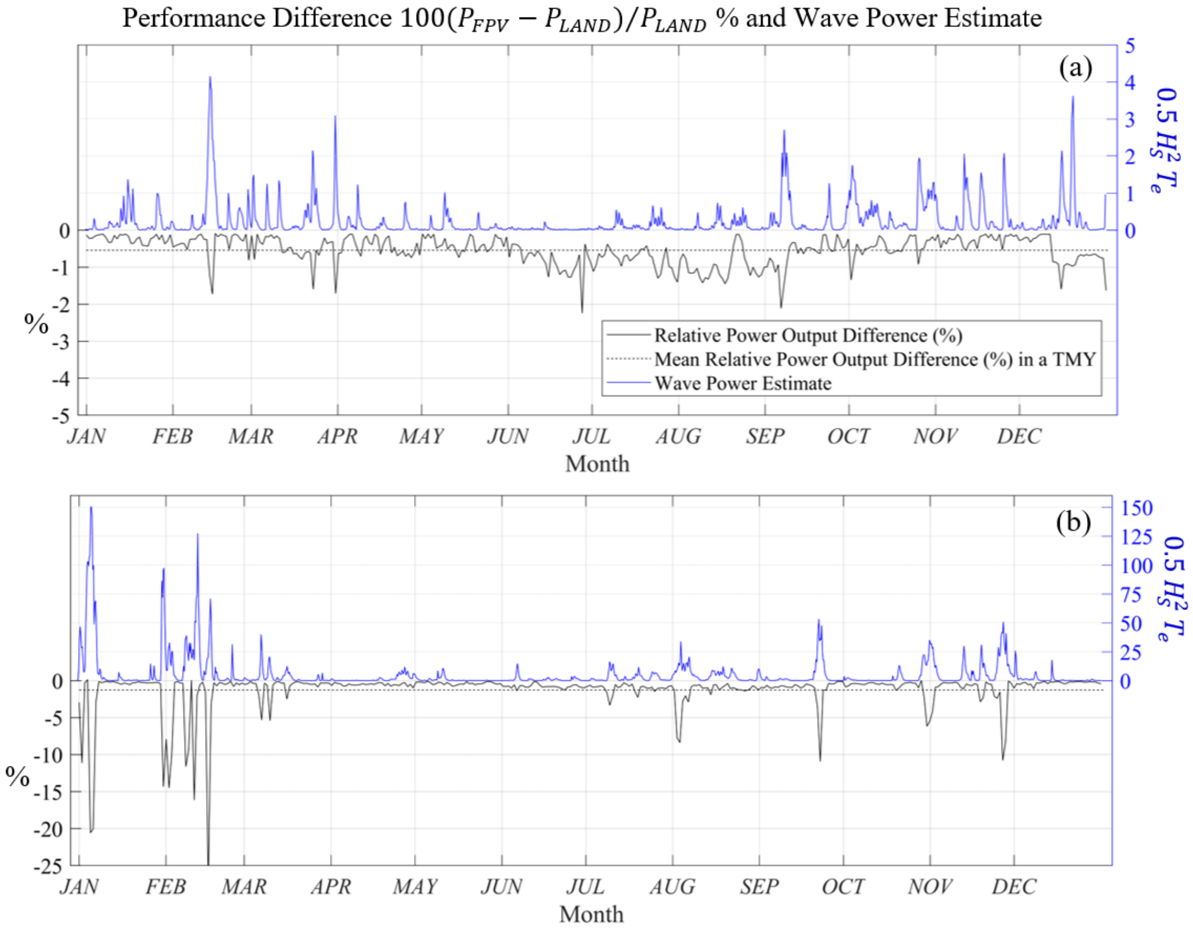

Figure 4-13. Time series and mean values of Performance Difference (%) between floating and land–based PV unit, along with time series of wave power estimates of the prevailing sea conditions. (**a**) Pagasitikos Gulf region and (**b**) southeastern coast of Evia Island.

As mentioned above, the albedo coefficient is set to $c = 0.1$ for the floating unit and $c = 0.3$ for the land–based counterpart (refer to Eq. (2.13) in §2.3). Consequently, a portion of the power output losses associated with the FPV system can be also attributed to the lower levels of reflected irradiance. Figure 4-13 illustrates simulated time series of the difference in power output (%) between the floating and the land–based units in the two considered locations, alongside time series of the wave power corresponding to the prevailing sea states. It is observed that severe sea conditions, mostly encountered during the winter months, can result in significant power losses for the floating systems, particularly in the case of the installation located on the southeastern coast of Evia Island, due to longer fetch distances.

The above result emphasizes the importance of considering site–specific environmental conditions in assessing the viability and efficiency of floating PV installations, as well as the potential need for structural damping or tracking mechanisms to mitigate performance losses in highly dynamic environments. Nevertheless, the performance reduction under sea conditions typically encountered in coastal areas of the Mediterranean Sea is not particularly severe, as also noted in §3.4.

It is worth mentioning here that the water surface acts as an imperfect reflector that affects the panels' temperature. In addition, water vapor above the water surface absorbs part of the near–infrared radiation that is highly effective for photovoltaic energy conversion in crystalline silicon–based PV panels [167], which is an adverse effect. Additionally, a salty and humid sea environment constitutes an important additional parameter concerning the degradation of PV panels (see, e.g., [168]). On the contrary, the presence of water, in conjunction with airflow due to wind, contributes to cooling. Moreover, the improvement in the performance of the system by means of the cleaning of the solar panels due to rainfall and other parameters could be taken into account. Although the modelling of the above factors (e.g., wind loads, cooling effect, etc.) should ideally be addressed using a high–fidelity simulator, such as those based on computational fluid dynamics (CFD) or methods of equivalent fidelity (e.g., FEA, SPH), simplified approaches are presented in Appendix D. The latter approaches enable the inclusion of specific key parameters in the modelling process through the use of more accessible, simplified models, thereby maintaining computational costs at reasonable levels. Based on the preliminary results presented in the Appendix D, the cooling effect over water bodies can provide a significant boost to energy production, potentially allowing floating configurations to outperform their land–based counterparts. A complete analysis of FPV operation should also incorporate wind loads and currents. However, as discussed in Ref. [169], concerning a case study in a nearshore region, wave loads account for 99% of the relevant forces in such environments, suggesting that the impact of wind and current loads may be relatively minor in this context. It should be noted, however, that increased tilt angles could result in a more pronounced impact from wind loads. Therefore, in configurations where the tilt angle is significantly elevated (e.g., in the range of 30–40 degrees), the effect of wind loads may become a critical factor and should be thoroughly accounted for in the design and structural analysis to ensure the stability and viability of the system.

The increased availability of solar energy potential, particularly in southern latitudes such as the Mediterranean and the Aegean Sea regions, provides a strong motivation for the design and development of floating offshore solar energy platforms suitable for deployment and operation in the marine environment. In this chapter, a Boundary Element Method (BEM) was employed for the hydrodynamic analysis of floating pontoon–type structures carrying photovoltaic panels on deck. The method facilitates the investigation of wave responses and their impact on solar power performance. A boundary integral formulation, incorporating simple singularities, was applied in the vicinity of the floating structure to represent the near field, while a mirroring technique was used to account for the interaction of the wavefields with the seabed, in conjunction with appropriate techniques for handling radiation conditions in the diffraction / radiation problems. Case studies involving a 100 kWp module located in the western Pagasitikos Gulf and the southeastern region of Evia Island were conducted, showing that the effects of dynamics on floating PV performance may lead to significant variations in energy production. In the framework discussed in the present chapter, these variations are mainly caused by dynamic changes in the angle of solar incidence, which results from the floating module's roll responses, dependent on the prevailing sea states.

A complete analysis of FPV systems’ performance would require consideration of various additional environmental and operational factors. These include the loads by wind and currents loads, as well as water and wind cooling mechanisms. As discussed in Appendix D, wind can effectively reduce cell temperature and thus enhance the overall efficiency of the system. The cooling effect can be particularly efficient over water bodies due to the presence of faster wind speeds, which enhance convective heat transfer, combined with the process of evaporative cooling (see e.g. [170]). These factors contribute to forming a cooler microclimate for the PV modules.

In addition, grid connection considerations are vital for assessing the potential integration of floating PV systems into the existing electrical grid [171]. This involves evaluating how the fluctuating power output, due to both environmental and system dynamics, may impact grid stability and operation. Furthermore, issues such as voltage regulation and frequency control must be addressed to ensure compliance with grid standards. However, these considerations, while essential for a complete assessment of FPV systems, are beyond the scope of the present work, which focuses on the effects of hydrodynamics.

Part II

SOLAR SHIP

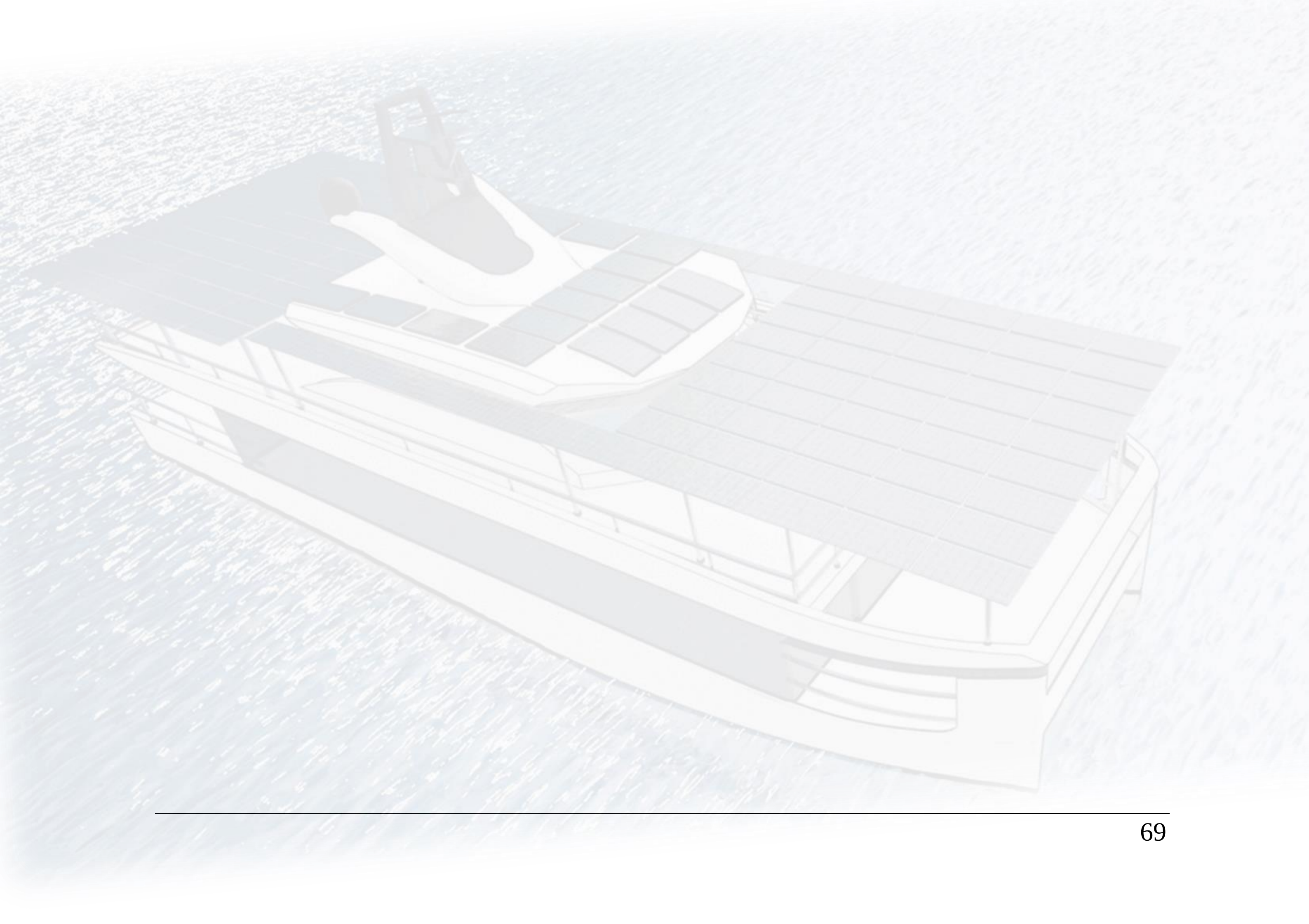

5

HYDRODYNAMICS OF TWIN–HULL VESSELS WITH APPLICATION TO SOLAR SHIPS

In recent years, the maritime industry has been increasingly exploring sustainable alternatives to traditional fossil–fuel–powered propulsion systems, driven by concerns regarding both environmental impact and rising fuel costs. A promising path is the integration of solar power into ship design, providing a renewable and environmentally friendly source of energy. This has led interest in solar–powered vessels to grow, as they offer a solution to the demand for environmentally friendly maritime transportation, while simultaneously providing several other key benefits. The latter include independence from fossil fuels, lower noise levels and reduced maintenance costs. Furthermore, solar–powered vessels provide enhanced safety by minimizing fuel–related risks [45].

This chapter focuses on assessing the feasibility and potential benefits of integrating solar panels onboard a 33–meter twin–hull vessel operating in the Greek seas. Greece, having an extensive coastline and abundant incidence of solar irradiance almost throughout the whole year, see e.g., [172], presents a promising environment for the implementation of solar–powered maritime solutions. Based on a case study approach, the analysis and results discussed in the present section aim to assess the efficacy of integrating solar energy systems in short–haul maritime operations. Estimating the extent to which solar power can partially cover the energy needs of the vessel requires a comprehensive analysis of the latter's resistance components, as well as an estimate of the energy required for service loads (lighting, navigation equipment, communication systems). For this work's scope, considering low operational speeds, the appendage and air resistance components are excluded from the analysis and the calm water resistance is approximated by the wave–making and the frictional resistance components. The wave making resistance is calculated by a Boundary Element Method (BEM), which evaluates the resulting Kelvin pattern generated by the vessel's forward motion. The stationary nature of the generated wave pattern, as observed from a body–fixed reference frame onboard the vessel, allows for the calculation of the corresponding flow field, without necessitating time–dependency considerations. It is important to note that the BEM approach relies on linear theory, which implies that flow rotation, compressibility and viscosity are not considered. However, the simplified model still provides valuable insights into the hydrodynamic behaviour of the vessel, as regards wave generation and resistance at Froude numbers corresponding to velocities well below the hull speed, where the vessel primarily operates as a displacement craft (see e.g. [173]). The frictional resistance component is incorporated based on the International Towing Tank

Conference (ITTC) 1957 recommendations [174]. Moreover, an additional hydrodynamic model is developed and applied to evaluate the Response Amplitude Operators (RAOs) of the vessel under harmonic wave excitation, depending on the prevailing sea conditions, assuming harmonic time dependence of the whole hydromechanical system. By considering the total wave field resulting from the interaction of the vessel with an incident field at a given velocity, the added wave resistance is also evaluated. The above approach allows for a thorough examination of the vessel's performance and power requirements under different sea states, laying the groundwork for assessing the feasibility and efficacy of solar panel integration for propulsion in maritime operations.

The available solar power is derived using a simple Photovoltaic (PV) model, which utilizes data provided by the SARAH2 database (https://joint-research-centre.ec.europa.eu/photovoltaic-geographical-information-system-pvgis/pvgis-data-download/sarah-2-solar-radiation-data_en), that offers information on solar irradiance levels among other parameters, enabling the estimation of the available solar energy potential. The PV model utilizes data of the vessel’s responses in the rotational degrees of freedom, to simulate instantaneous angular changes of the panels mounted on deck and accurately account for the variations in solar exposure experienced by the integrated solar system. By coupling these data with the energy requirements and the resistance components discussed earlier, the modelling aims to provide a holistic assessment of the feasibility and effectiveness of solar panel integration for sustainable maritime operations. This interdisciplinary approach combines principles from various fields, including naval architecture, renewable energy and solar technology, to address the complex challenges of transitioning towards greener maritime transportation solutions.

5.1. *Problem Formulation*

The geometry of the twin–hull vessel studied in the present chapter’s framework is based on optimized results from the literature. In particular, the dimensions and hull lines of each demi hull are used as parametrically optimized by Kanellopoulou et al. [86], in the framework of the ELCAT research project (https://elcatproject.gr/). The latter project, conducted from 2020 to 2023, was a collaboration between NTUA and Alpha Marine, focusing on designing energy–efficient electric catamarans, measuring between 19 and 33 meters in length. The project’s aim was to contribute to the reduction of greenhouse gas emissions and atmospheric pollution from the shipping industry. The design configuration employed is that of the 33–meter–long vessel developed within the aforementioned project and the configuration of the solar panels deployed on deck is adapted to the specific features of this vessel (see Figure 5-1). The hull lines are illustrated in Figure 5-2 (a, b, c), along with a 3D view of the demi hull [Figure 5-2 (d)] that offers a more detailed perspective of the demi hull’s shape. Indicative waterline levels are also depicted in the body plan [Figure 5-2 (c)] for various drafts, facilitating the visualization of the submerged geometry at different loading conditions. The main characteristics of the vessel are listed in Table 5-1.

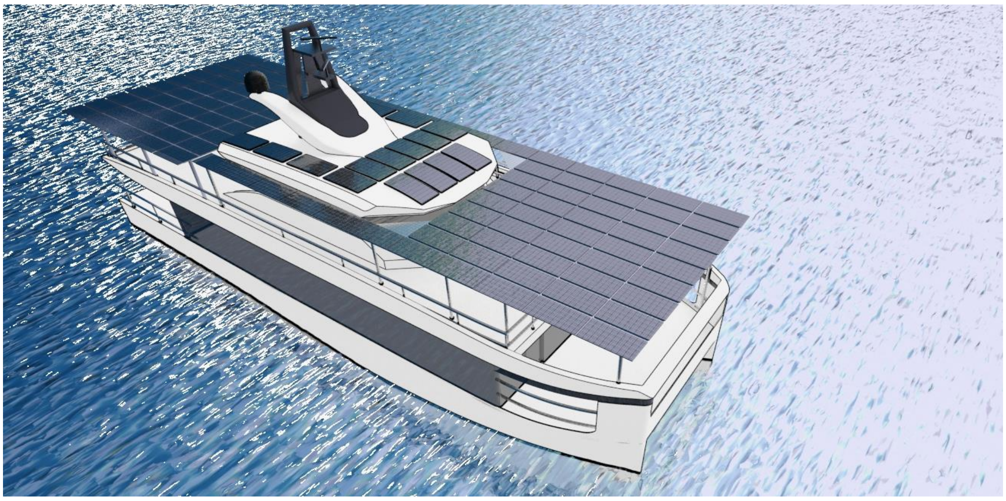

Figure 5-1. Illustration of the 33–m–long twin–hull vessel with integrated solar panels.

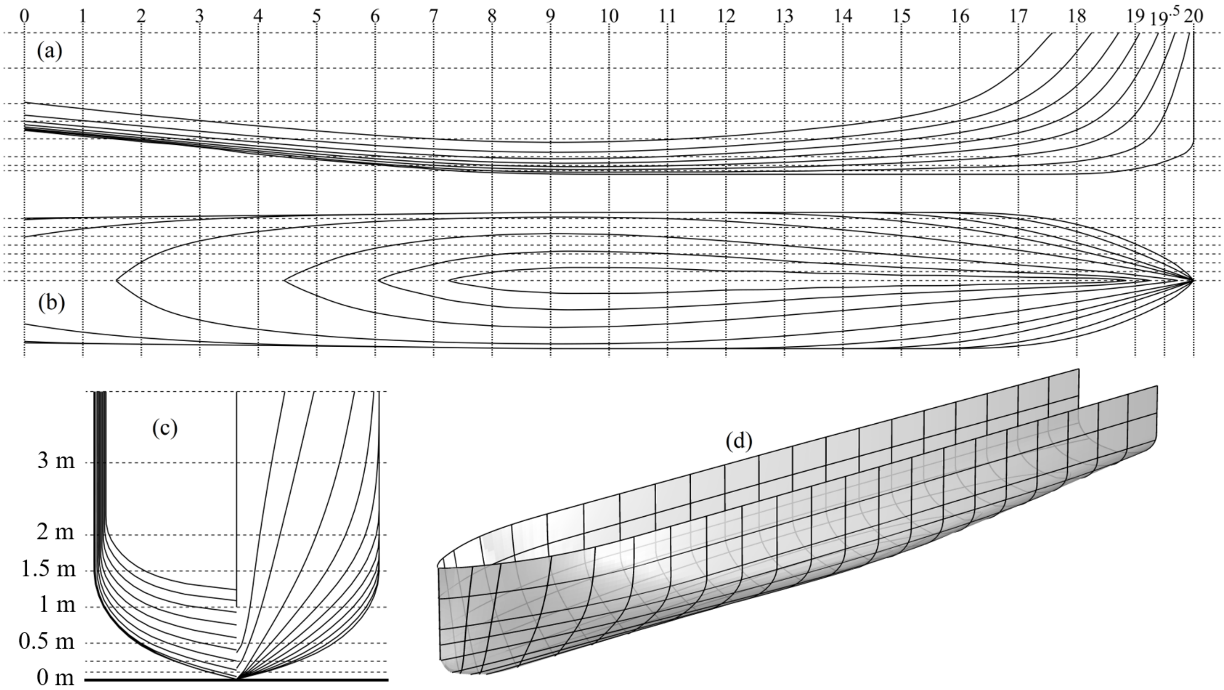

Figure 5-2. Lines plan of the demihull form (**a**) sheer plan, (**b**) breadth plan (waterlines), (**c**) body plan along with indicative waterline levels, (**d**) 3D view, incorporating the breadth and body plan lines in 3D space.

Table 5-1. Main Parameters of the fully electric version of the twin–hull vessel (source: https://elcatproject.gr/).

$L_{OA} = L_{PP}$	33.00 m	Displacement	~198 t
Beam Moulded	10.71 m	Op. Speed	12-14 kn
Demi hull Beam	3.88 m	Economy Speed	11 kn
Demi hull Depth	3.95 m	Battery Capacity	2850 kWh
T_{design}	1.64 m	Range	~40 n.m. at 13 kn

The coordinate system $\mathbf{x} = (x_1, x_2, x_3)$ is used, with the origin placed at Mean Water Level (MWL), coinciding with the center of flotation. The x_1–axis runs parallel to the vessel's length, x_2 is the transverse axis and the vertical coordinate x_3 is negative in the water body. Let $\Omega \in \mathbb{R}^3$ denote a flow domain, that extends infinitely to all azimuthal directions $\theta = atan2(x_1, x_2)$ as well as the negative x_3–direction, and is bounded by the free surface of the water at $x_3 = 0$ and the wetted surface of the twin–hull. In the body fixed coordinate system (x_1, x_2, x_3), the forward motion of the vessel at speed U along the x_1–direction, translates to the existence of a uniform water flow moving at constant speed U opposite to this direction.

The dynamic behaviour of the vessel is analyzed in the framework of linear wave theory, which allows for the flow variables to be decomposed into a steady background flow and a time–dependent wave part, which is considered to be harmonic. The velocity fields of the total flow components are described by the gradients of appropriate potential functions defined in Ω.

Given the stationary nature of both the uniform flow and the generated Kelvin pattern, as observed from the body–fixed reference frame onboard the vessel, the result of the ship's forward motion in calm water is described by steady (time–independent) potential functions, namely, the steady incident field (uniform flow) and a perturbation field, generated by the interaction of the wetted surface and the uniform water flow of velocity U. The unsteady, time dependent (wave) problem presents more complexity since the analysis involves an incident, a diffracted and – provided that the body is considered non–deformable – six radiated flow fields. The latter are a consequence of the vessel's motions in six degrees of freedom (DoFs), which include surge, sway, heave, roll, pitch, and yaw. A sketch of the studied configuration is depicted in Figure 5-3. On the basis of linear theory, each of these motions induces a distinct outgoing (radiated) wave field that contributes to the unsteady hydrodynamic responses. In the context of the present analysis, Φ is employed to denote potential functions of time–dependent flows, while (lowercase) φ is utilized to represent the potential of time–independent flows, ensuring clear differentiation between the two. Furthermore, potential functions involved in the steady problem will be annotated with the superscript (S), whereas the superscript (U) is used for potential functions corresponding to the unsteady (wave) problem. This serves to amplify the distinction between the two problems, since time–independent (complex) potential functions are also used for the wave problem, exploiting the assumption of harmonic time–dependence, as explained in more detail in the sequel.

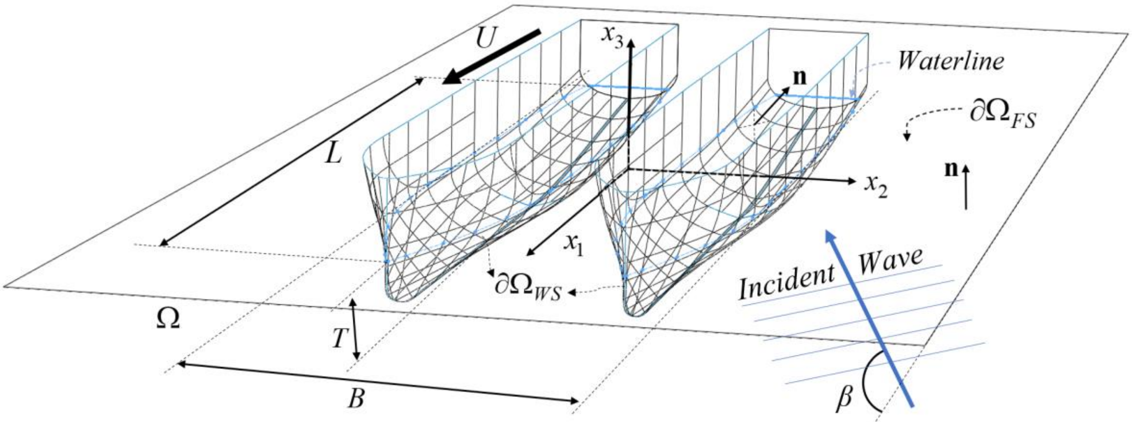

Figure 5-3. Sketch of the considered hydrodynamic model, illustrating the flow domain and its boundary parts along with basic dimensions and parameters.

5.1.1. Formulation of the steady problem

The steady flow is defined by the interaction of a uniform parallel flow $\mathbf{U}_\infty = (-U_\infty, 0,0)$ directed towards the negative x_1–axis, with the wetted surface in the domain Ω (see Figure 5-3). The perturbation field is calculated following a Neumann–Kelvin (NK) formulation (see, e.g., [73]) using the decomposition,

$$\varphi^{(S)}(\mathbf{x}) = -U_\infty x_1 + \varphi_d^{(S)}(\mathbf{x}) . \tag{5.1}$$

The potential function $\varphi_d^{(S)}(\mathbf{x})$ is used to describe the generated Kelvin pattern and is expected to exhibit wave–like behaviour downstream. The latter function is computed as solution to the Laplace equation, subjected to the free surface boundary condition and the no–entrance condition at the wetted surface. Considering the transom stern geometry of the studied vessel, a false body model is adopted (see e.g., [175]) to ensure that the flow separates smoothly from the hull's surface at the aft end. This approach is based on the addition of a virtual appendage (false body – FB) to the transom. The latter encloses the separated flow at low speeds or the created air cavity in the higher speed range [176], and excludes this region from the water body simulated by the potential flow solver. The false body naturally extends the hull geometry, initiating tangentially from the entire stern profile, ensuring a smooth geometry and thereby maintaining the integrity of the flow at the aft end of the vessel. This approach presumes the transom to remain fully ventilated at all speeds, leading to the transom stern drag, attributed to the absence of hydrostatic pressure on the stern, to be overestimated at low speeds [177]. The false body length is set to $\lambda^{(S)}/2$, where $\lambda^{(S)} = 2\pi U_\infty^2/g$ is the transverse wavelength of the Kelvin pattern. However, in cases where $\lambda^{(S)}/2$ exceeds $3B_S$, where B_S is the stern beam at mean water level (MWL), the virtual appendage length is limited to $3B_S$. This restriction is based on experimental data provided in Ref. [178], where it is shown that the boundary layer typically reattaches at a distance equivalent to six times the step height ($B_S/2$) for high Reynolds number turbulent flows. Nonetheless, relevant calculations indicated that the evaluated wave–making resistance is not severely affected by this length regardless of the precise value within these limits.

Considering the addition of the virtual boundary $\partial\Omega_{FB}$, the potential function $\varphi_d^{(S)}(\mathbf{x})$ is evaluated as solution to the following BVP,

$$\nabla^2 \varphi_d^{(S)}(\mathbf{x}) = 0, \ \mathbf{x} \in \Omega, \tag{5.2}$$

$$\frac{\partial^2 \varphi_d^{(S)}(\mathbf{x})}{\partial {x_1}^2} + \frac{g}{U_\infty^2} \frac{\partial \varphi_d^{(S)}(\mathbf{x})}{\partial x_3} = 0, \mathbf{x} \in \partial\Omega_{FS}, \tag{5.3}$$

$$\frac{\partial \varphi_d^{(S)}(\mathbf{x})}{\partial n} = -\mathbf{U}_\infty \mathbf{n} = U_\infty n_1, \ \mathbf{x} \in \partial\Omega_{WS} \cup \partial\Omega_{FB}, \tag{5.4}$$

supplemented by appropriate conditions at infinity. In the above equations, $\mathbf{n} = (n_1, n_2, n_3)$ represents the unit vector, normal to the boundary $\partial\Omega$, directed towards the exterior of Ω, as also shown in Figure 5-3. For the treatment of the above BVP, a low order panel method is adopted using a simple singularity (source) distribution on $\partial\Omega$; see, e.g., [136] in conjunction with an integral representation of $\varphi_d^{(S)}(\mathbf{x})$. Exploiting the inherent symmetry of the discussed (steady) problem with respect to the plane $x_2 = 0$, the following integral representation is employed, which utilizes a mirroring technique to amplify computational efficiency,

$$\varphi_D^{(S)}(\mathbf{x}) = \int_{\partial\tilde{\Omega}} \mu^{(S)}(\mathbf{x}')G(\mathbf{x}',\mathbf{x})dS(\mathbf{x}'), \ \mathbf{x} \in \tilde{\Omega}, \ \mathbf{x}' \in \partial\tilde{\Omega}, \text{ where} \tag{5.5}$$

$$\tilde{\Omega} = \left\{ \mathbf{x} \in \Omega \,\middle|\, x_2 \ge 0 \right\} \text{ and} \tag{5.6}$$

$$G(\mathbf{x}',\mathbf{x}) = \frac{1}{4\pi}\left(\frac{1}{|\mathbf{x}' - \mathbf{x}|} + \frac{1}{|\mathbf{x}' - \tilde{\mathbf{x}}|} \right). \tag{5.7}$$

The Green's function of the Laplace equation in 3D, described by Eq. (5.7), involves the mirror point of $\mathbf{x}$ with respect to the symmetry plane: $\tilde{\mathbf{x}} = (x_1, -x_2, x_3)$ and $\mu^{(S)}$ is a source / sink strength distribution, defined on $\partial\tilde{\Omega}$ (refer to Appendix C). The above technique introduces an artificial boundary at the symmetry plane, where a homogeneous Neumann BC is intrinsically satisfied due to the Green's function used. The above formulation is combined with an appropriate scheme to satisfy the conditions at infinity based on the discrete Dawson operator [179] as described in the sequel.

5.1.2. 3D BEM for the steady flow problem

The geometry of the different sections of $\partial\tilde{\Omega}$ is approximated using 4–node quadrilateral elements (refer to Appendix B), on which the strength of the singularity distribution is considered piecewise constant. In the discrete model, the field equation is inherently satisfied by the superposition of the fundamental fields generated by all elements, while the boundary conditions are satisfied at the centroid of each panel (collocation points). The induced potential $\varphi_{k,j}$ and velocities $(U_{k,j}, V_{k,j}, W_{k,j})$ associated with the j–element's contribution to the k–collocation point are numerically calculated and the corresponding matrices of induced potential $(\boldsymbol{\varphi})$ and velocity $(\mathbf{U}, \mathbf{V}, \mathbf{W})$ respectively, are computed. The latter square matrices have dimension $M = M_{FS} + M_{WS} + M_{FB}$ where M_{FS}, M_{WS} and M_{FB} respectively represent the number of quadrilateral elements distributed on the parts of $\partial\tilde{\Omega}$ corresponding to the free surface, the actual wetted surface and the false wetted surface, ensuring global continuity of geometry approximation. Consequently, the BVP is reduced to the algebraic system,

$$\sum_{j=1}^{M} A_{k,j}^{(S)} \mu_j^{(S)} = b_k^{(S)}, k = 1,2,\ldots,M, \tag{5.8}$$

whose solution provides with the strength of the source / sink distribution $\mu^{(S)}$ on each element. The latter, in conjunction with Eq. (5.5), fully describes the resulting function $\varphi_d^{(S)}(\mathbf{x})$ in $\tilde{\Omega}$, while for $x_2 < 0$ it holds that $\varphi_d^{(S)}(x_1, x_2, x_3) = \varphi_d^{(S)}(x_1, -x_2, x_3)$. The numerical scheme involves a streamline–like arrangement of the boundary elements on $\partial\tilde{\Omega}_{FS}$ as shown in Figure 5-4. The curvature of the potential function in the x_1–direction, that is involved in the free surface boundary condition [Eq. (5.3)], is approximated by the derivative of the velocity in the ξ–direction, as depicted in the details shown in Figure 5-4 (b, c),

$$\frac{\partial^2 \varphi_d^{(S)}(\mathbf{x})}{\partial {x_1}^2} = \frac{\partial U_d^{(S)}(\mathbf{x})}{\partial x_1} \approx -\frac{\partial U_d^{(S)}(\mathbf{x})}{\partial \xi}. \tag{5.9}$$

The present model involves a four–point upstream finite difference (FD) scheme based on the Dawson backward operator [179], that is defined as follows,

$$\left.\frac{\partial U}{\partial \xi}\right|_k \approx A_k \cdot U_k + B_k \cdot U_{k-1} + C_k \cdot U_{k-2} + D_k \cdot U_{k-3}, \tag{5.10}$$

where

$$\begin{aligned} E_k = {} & (\xi_{k-1} - \xi_k)\cdot(\xi_{k-2} - \xi_k)\cdot(\xi_{k-3} - \xi_k)\cdot(\xi_{k-3} - \xi_{k-1})\cdot(\xi_{k-2} - \xi_{k-1})\cdot \\ & (\xi_{k-3} - \xi_{k-2})\cdot(\xi_{k-3} + \xi_{k-2} + \xi_{k-1} - 3\xi_k), \end{aligned} \tag{5.11}$$

$$D_k = \frac{1}{E_k}\left[(\xi_{k-1} - \xi_k)^2 \cdot (\xi_{k-2} - \xi_k)^2 \cdot (\xi_{k-2} - \xi_{k-1}) \cdot (\xi_{k-2} + \xi_{k-1} - 2\xi_k)\right], \tag{5.12}$$

$$C_k = -\frac{1}{E_k}\left[(\xi_{k-1} - \xi_k)^2 \cdot (\xi_{k-3} - \xi_k)^2 \cdot (\xi_{k-3} - \xi_{k-1}) \cdot (\xi_{k-3} + \xi_{k-1} - 2\xi_k)\right], \tag{5.13}$$

$$B_k = \frac{1}{E_k}\left[(\xi_{k-2} - \xi_k)^2 \cdot (\xi_{k-3} - \xi_k)^2 \cdot (\xi_{k-3} - \xi_{k-2}) \cdot (\xi_{k-3} + \xi_{k-2} - 2\xi_k)\right] \text{ and} \tag{5.14}$$

$$A_k = -(B_k + C_k + D_k). \tag{5.15}$$

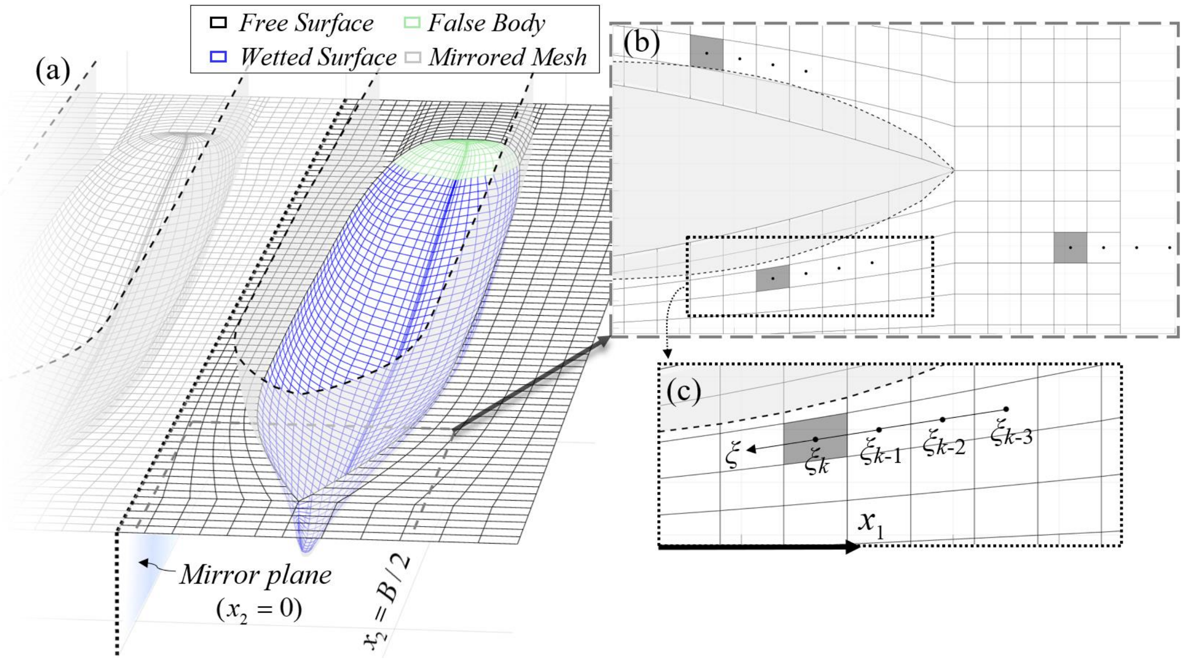

Figure 5-4. (**a**) Indicative mesh of $\partial\widetilde{\Omega}$, illustrating a sparse discretization of the various boundary parts, along with the mirror plane and the ξ–direction. (**b**, **c**) Detailed view of the mesh at the bow, also illustrating the sets of points used in the finite difference (FD) scheme for the calculation of the velocity gradient at indicative elements that appear shaded.

In the above equations, ξ denotes the distance covered in a curve defined in the ξ–direction, measured from an arbitrary point, and the velocities involved in Eq. (5.10) are equal to,

$$U_k = \sum_{j=1}^{M} \mu_j^{(S)} \cdot U_{k,j}. \tag{5.16}$$

Figure 5-4 depicts an indicative sparse boundary mesh, where it can be seen that additional grid lines are introduced behind the stern to minimize the deviation between the differentiation direction, and the actual x_1–direction. Semi–cosine spacing is employed to discretize the wetted surface in the x_3–direction, aiming to achieve increased grid resolution at the keel, where the geometry exhibits the highest gradient. Furthermore, ghost nodes are employed to assess the induced velocity gradient at the first three element rows of the grid [see Figure 5-4 (b)]. The value of induced velocity at the ghost nodes is taken to be equal to the velocity induced at the centroid of the last actual element involved in the differentiation. The same technique is also applied to compute the velocity gradient at the first three element rows behind the false body mesh.

Based on the above finite difference scheme, the (non–square) matrix $\partial\mathbf{U}$ of dimensions $M_{FS} \times M$ is defined. The elements of this matrix:

$$\partial U_{k,j} = A_k \cdot U_{k,j} + B_k \cdot U_{k-1,j} + C_k \cdot U_{k-2,j} + D_k \cdot U_{k-3,j}\,, \tag{5.17}$$

model the contribution of the j–element to $\partial U_k/\partial\xi$, at the k–collocation point on the free surface. Consequently, the discrete model of the steady flow problem, modelling the disturbance field, is defined by the linear algebraic system of Eq. (5.8) with

$$A_{k,j}^{(S)} = \begin{cases} \partial U_{k,j} + \dfrac{g}{U_\infty^2} W_{k,j}\,, & Element(k) \in \partial\Omega_{FS} \\ U_{k,j}\, n_{k,1} + V_{k,j}\, n_{k,2} + W_{k,j}\, n_{k,3}, & Element(k) \in (\partial\Omega_{WS} \cup \partial\Omega_{FB}) \end{cases} \quad \text{and} \tag{5.18}$$

$$b_k^{(S)} = \begin{cases} 0, & Element(k) \in \partial\Omega_{FS} \\ U_\infty n_{k,1}, & Element(k) \in (\partial\Omega_{WS} \cup \partial\Omega_{FB}). \end{cases} \tag{5.19}$$

Furthermore, the fact that the numerical differentiation scheme relies on information from points located upstream relative to the flow direction ensures that no numerical reflections are introduced into the solution near the edges of the computational mesh.

After obtaining the solution to the above linear system, the free surface elevation can be obtained from the dynamic boundary condition as,

$$\eta_d^{(S)}(\mathbf{x}) = \frac{U_\infty}{g} \frac{\partial \varphi_d^{(S)}(x_1, x_2, 0)}{\partial x_1}, \mathbf{x} \in \partial D_{FS}. \tag{5.20}$$

Indicative results of the field generated by the vessel, as it moves through the water at speeds of 8 and 10 knots, are provided in Figure 5-5. Specifically, subfigures (a) and (c) illustrate top views of the wave–like behaviour of the steady perturbation field trailing behind the vessel, demonstrating the characteristic wake pattern for the two selected forward speeds. Furthermore, subfigures (b) and (d) provide detailed views of the solutions on the computational grids in localized areas around the vessel, highlighting the directly computed solutions and their mirrored counterparts. The results refer to a draft of 1.55 m, ensuring the availability of experimental data for verification purposes. The latter data concerning calm water resistance can be found in Ref. [86]. The resulting dynamic pressure distributions on the wetted surface for the same velocity settings are shown in Figure 5-6, providing detailed information as concerns the pressure gradients along the submerged surface, which are crucial for understanding the hydrodynamic forces acting on the vessel. Additionally, subfigures (b), (c), (e) and (f) of Figure 5-6 illustrate how the steady free surface behaves around the wetted sections of the hull, for the two considered speed settings and draft.

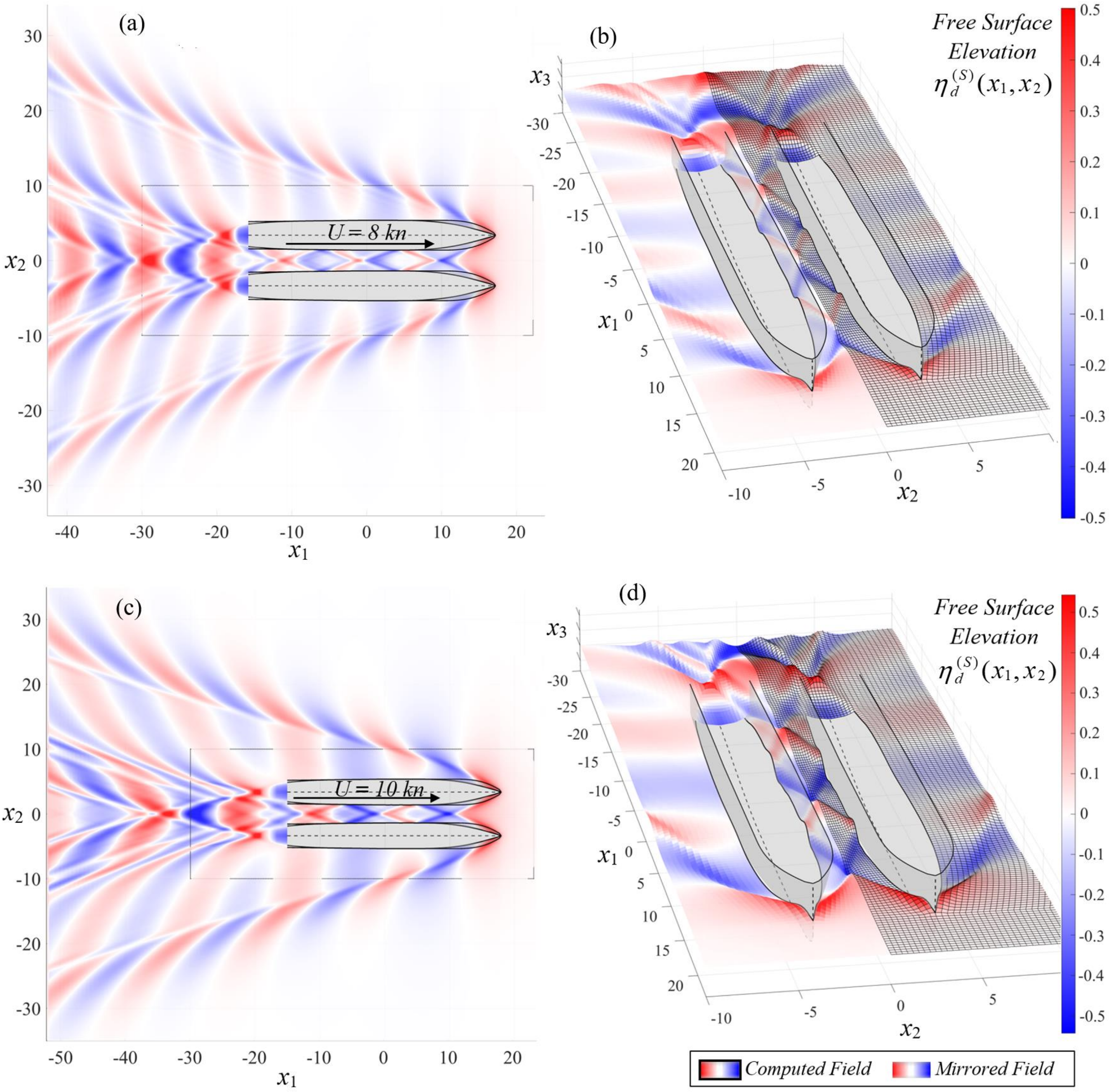

Figure 5-5. Kelvin wake pattern generated by the twin–hull vessel travelling at (**a**, **b**) $U_\infty = 8\ kn \approx 4.11\, m/s$ and (**c**, **d**) $U_\infty = 10\ kn \approx 5.14\, m/s$. (**a**, **c**) Top views and (**b**, **d**) 3D views highlighting the directly computed and the mirrored parts of the fields.

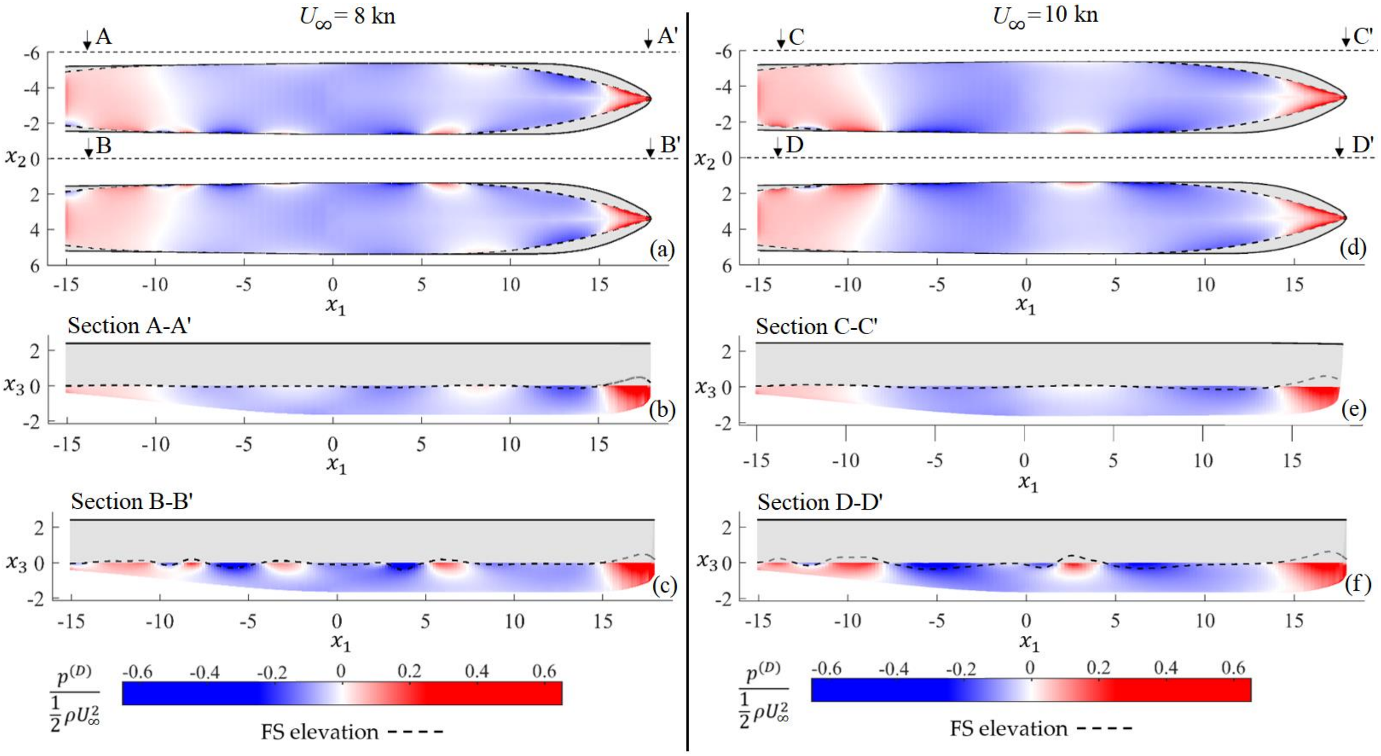

Figure 5-6. Dynamic pressure distribution on the twin–hull, for (**a** – **c**) $U_\infty = 8\ kn \approx 4.11\ m/s$ (**d** – **f**) $U_\infty = 10\ kn \approx 5.14\ m/s$. (**a**, **d**) Top views, (**b**, **e**) outer part of the demihulls and (**c**, **f**) inner part of the demihulls.

The total calm water resistance is approximated by the sum of the wave–making resistance and the frictional resistance components,

$$R_T = R_W + R_F = \left[C_W + (1+\beta k)C_F\right]\frac{1}{2}\rho U_\infty^2 A_{WS}\,, \tag{5.21}$$

where C_W and C_F respectively denote the wave–making and frictional resistance coefficients, $(1+\beta k)$ is a form factor and A_{WS} is the wetted surface area. The coefficient C_W is computed using data by the steady BEM model discussed earlier. In particular, the latter coefficient equals,

$$C_W = \frac{1}{A_{WS}}\int_{\partial\Omega_{WS}} \frac{p-p_\infty}{0.5\rho U_\infty^2}\cdot n_1 dS = \frac{1}{A_{WS}}\int_{\partial\Omega_{WS}} \left(1-\frac{V^2(\mathbf{x})-2gz}{U_\infty^2}\right)\cdot n_1 dS\,,\ \text{where} \tag{5.22}$$

$$V(\mathbf{x}) = \left[\left(-U_\infty + \frac{\partial\varphi_d^{(S)}(\mathbf{x})}{\partial x_1}\right)^2 + \left(\frac{\partial\varphi_d^{(S)}(\mathbf{x})}{\partial x_2}\right)^2 + \left(\frac{\partial\varphi_d^{(S)}(\mathbf{x})}{\partial x_2}\right)^2\right]^{1/2}. \tag{5.23}$$

The frictional resistance coefficient C_F is evaluated using the ITTC 1957 formula [174],

$$C_F = \frac{0.075}{\left(\log(\text{Re})-2\right)^2}\,, \tag{5.24}$$

and is scaled by the form factor $(1+\beta k)$ which depends on the hull form and, in the case of a twin–hull configuration, can be approximated by the following equation, based on the demihull's slenderness ratio [180],

$$1+\beta k = 3.03\left(\frac{L}{\nabla^{1/3}}\right)^{-0.4}, \tag{5.25}$$

where ∇ denotes the submerged volume of a single demihull. For the considered twin–hull geometry and draft the form factor equals $(1+\beta k) = 1.39$. The Reynolds number is evaluated, considering the dynamic viscosity of seawater at temperature $T = 20^{o}\mathrm{C}$ $(\mu = 1.09 \cdot 10^{-3}\mathrm{Nsm}^{-2})$.

Figure 5-7 depicts the calm water resistance components along with the total calm water resistance, as evaluated by the present BEM scheme, and the results are compared against experimental data. As can be observed in the Figure, the wave–making resistance is augmented by a stern drag term resulting from the absence of hydrostatic pressure at the aft end, leading to an overestimation of the total resistance at low Froude numbers, as expected from the present scheme. In the context of linearized theory this drag remains unchanged at different speeds. Apart from that, the results demonstrate good agreement with the experimental data within the range of Froude number $Fn < 0.25$. For higher values of Fn, the present model underestimates the resistance. This discrepancy arises because, at higher speeds, non–linear phenomena such as flow separation and wave breaking, which are not captured by the potential model under discussion, become more pronounced. Additionally, dynamic trim effects play a significant role in high–speed regimes. Another important factor contributing to the divergence between the model's predictions and experimental data is that the actual wetted surface area deviates from the linearized wetted surface used for integration in the model, resulting in additional errors. Moreover, the twin–hull consideration introduces hull interference phenomena, where wave interference between the two hulls lead to higher waves in the narrow water channel between them, further amplifying the deviation between the actual wetted surface and the linearized version, with this deviation becoming more prominent as the speed increases. This dependency on speed can be easily observed by comparing the resulting free surface patterns for the two selected speed regimes shown in Figure 5-6, particularly as concerns the inner part of the demihulls [Figure 5-6 (c) and (f)]. Since the resulting free surface pattern is static in the selected reference frame, the mean wetted surface over time does not converge to the linearized shape, as it would in the case of a harmonically oscillating solution.

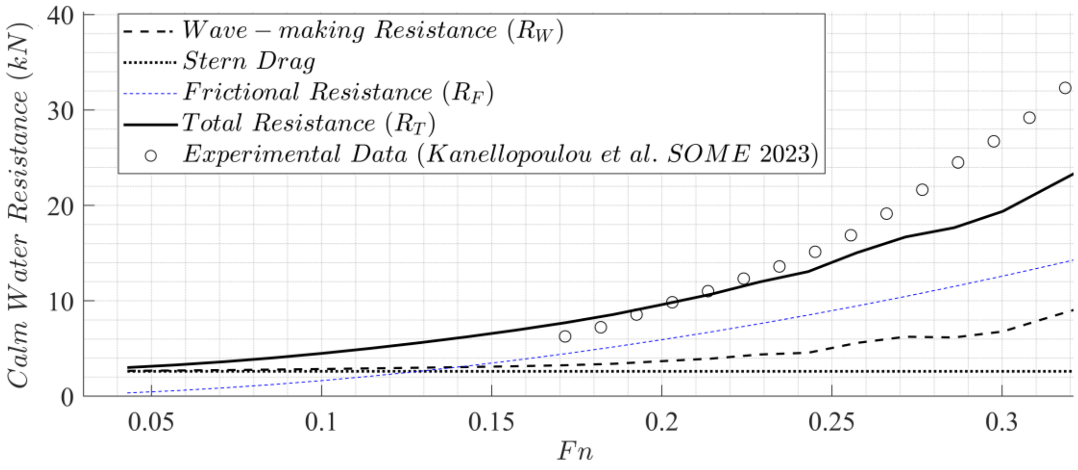

Figure 5-7. Calm water resistance components and comparison with experimental data [86].

These aspects highlight the limitations of the current approach. Based on the above observations, significantly better agreement with the experimental data can be achieved by considering the non–linear problem, including dynamic trim effects. These issues remain open for investigation in future extensions of the present work.

5.1.3. Formulation of the unsteady problem

The dynamic motions of the vessel, based on the prevailing sea conditions are derived using standard linear hydrodynamic analysis in the frequency domain. In particular, assuming that all time–dependent quantities oscillate harmonically in the form exp $(i\omega_e t)$, where ω_e denotes the encounter frequency in $[\mathrm{rad/s}]$ and $i = \sqrt{-1}$, the problem is transferred to the frequency domain using the following representation for the total unsteady potential function,

$$\Phi^{(U)}(\mathbf{x};\beta,U_\infty,t) = \Phi_0^{(U)}(\mathbf{x};\beta,U_\infty,t) + \Phi_d^{(U)}(\mathbf{x};\beta,U_\infty,t) + \sum_{m=1}^{6} \dot{\xi}_m \Phi_m^{(U)}(\mathbf{x};\beta,U_\infty,t) = \mathrm{Re}\left\{ \frac{igH}{2\omega_0} \varphi^{(U)}(\mathbf{x};\beta,U_\infty) \cdot \exp(i\omega_e t) \right\}. \tag{5.26}$$

In Eq. (5.26), $H = 2A$ denotes the incident wave height, g is the gravitational acceleration, ξ_m is the complex amplitude of the vessel's response towards the m^{th} generalized direction, β is the angle of incidence of the wave field with respect to the x_1–axis and U_∞ is the vessel's velocity in the x_1–direction. The encounter frequency ω_e is defined as,

$$\omega_e = \left| \omega_0 - U_\infty k_0 \cos(\beta) \right|, \tag{5.27}$$

where ω_0 is the absolute frequency of the incident field (as observed from a non–moving reference frame) and $k_0 = \omega_0^2/g$ is the wavenumber, considering propagation in deep water. Finally, $\varphi^{(U)}(\mathbf{x},\beta,U_\infty)$ is the total complex unsteady potential, which comprises all the unsteady subfields and is defined as,

$$\varphi^{(U)}(\mathbf{x};\beta,U_\infty) = i\omega_e \left\{ \varphi_0{}^{(U)}(\mathbf{x};\beta,U_\infty) + \varphi_d{}^{(U)}(\mathbf{x};\beta,U_\infty) + \sum_{m=1}^{6} \xi_m \varphi_m{}^{(U)}(\mathbf{x};\beta,U_\infty) \right\}. \tag{5.28}$$

In Eq. (5.28), $i\omega_e\varphi_0^{(U)}(\mathbf{x},\beta,U_\infty)$ and $i\omega_e\varphi_d^{(U)}(\mathbf{x},\beta,U_\infty)$ respectively, stand for complex amplitudes of the incident and the diffracted subfields. Furthermore, $\varphi_m^{(U)}(\mathbf{x},\beta,U_\infty), m = 1,2,..,6)$, is the complex potential of the radiation field generated by a unit–amplitude oscillation of the vessel along the m^{th} generalized direction.

The incident potential function $\varphi_0^{(U)}(\mathbf{x},\beta,U_\infty)$ is considered known and equal to,

$$\varphi_0{}^{(U)}(\mathbf{x};\beta,U_\infty) = \frac{gA}{\omega_0\omega_e} \exp(k_0 x_3) \exp\left[-ik_0(\cos(\beta)x_1 + \sin(\beta)x_2\right]. \tag{5.29}$$

The unsteady field is computed by modelling the whole domain, since it does not present symmetries, except in the special cases where β equals 0 or 180 degrees. Furthermore, the transom sterns of both demihulls are modelled as vertical boundaries, incorporated in $\partial\Omega_{WS}$, omitting the false body representation, discussed in §5.1.1. The diffraction and the six radiated fields are obtained as solutions to the following BVPs,

$$\nabla^2 \varphi_k{}^{(U)}(\mathbf{x}) = 0,\ k = d,1,2,...,6,\ \mathbf{x} \in \Omega, \tag{5.30}$$

$$\frac{\partial \varphi_k{}^{(U)}(\mathbf{x})}{\partial x_1} - \mu(\mathbf{x})\varphi_k{}^{(U)}(\mathbf{x}) + \frac{U_\infty{}^2}{g}\frac{\partial^2 \varphi_k{}^{(U)}(\mathbf{x})}{\partial x_1{}^2} - \frac{2i\omega_e U_\infty}{g}\frac{\partial \varphi_k{}^{(U)}(\mathbf{x})}{\partial x_1} = 0,\ k = d,1,2,...,6,\ \mathbf{x} \in \partial\Omega_{FS}, \tag{5.31}$$

$$\frac{\partial \varphi_d{}^{(U)}(\mathbf{x})}{\partial n} = \frac{\partial \varphi_0{}^{(U)}(\mathbf{x})}{\partial n},\ \mathbf{x} \in \partial\Omega_{WS}, \tag{5.32}$$

$$\frac{\partial \varphi_k{}^{(U)}(\mathbf{x})}{\partial n} = N_k + M_k,\ k = 1,2,....,6,\ \mathbf{x} \in \partial\Omega_{WS}. \tag{5.33}$$

In Eq. (5.33), N_k denotes the components of the generalized normal vector, defined as $N_k = n_k,\ N_{k+3} = (\mathbf{n} \times \mathbf{x})_k,\ k = 1,2,3$. Consequently, the vessel's k^{th} DoF is defined as translational motion along the k^{th} axis for $k = 1,2,3$ or rotational motion around the axis $(k-3)$ for $k = 4,5,6$. The quantities M_k, that appear in Eq. (5.33), are defined as functions of the derivatives of the relative flow velocity of the steady field at the mean position of the wetted surface. The latter quantities, mainly involve higher–order derivatives of the perturbation potential due to the motion of the ship at constant speed (see e.g., [181]) and after linearization they can be approximated by,

$$M_k \approx 0,\ k = 1,2,3,4,\quad M_5 \approx \frac{U_\infty}{i\omega_e} n_3,\quad M_6 \approx -\frac{U_\infty}{i\omega_e} n_2. \tag{5.34}$$

Numerical solutions to the above BVPs are obtained using a low order BEM, which employs piecewise constant source distributions on quadrilateral boundary elements. The seven unknown fields are represented by the following integral,

$$\varphi_k^{(U)}(\mathbf{x}) = \int_{\partial\hat{\Omega}} \mu_k{}^{(U)}(\mathbf{x}')G(\mathbf{x}',\mathbf{x})dS(\mathbf{x}'),\ \mathbf{x} \in \Omega, \mathbf{x}' \in \partial\Omega,\ k = d,1,2,...,6 \text{ where} \tag{5.35}$$

$$G(\mathbf{x}',\mathbf{x}) = |\mathbf{x}' - \mathbf{x}|^{-1} / 4\pi\,. \tag{5.36}$$

The BVPs described by Eqs. (5.30)–(5.33) are treated by a low–order panel method based on source singularity distribution on quadrilateral elements. The curvature of the potential function involved in Eq. (5.31) is treated by the FD scheme discussed in §5.1.2. It is noted that dipole singularities are ineffective in this context, since distributed constant–strength dipole singularity on planar elements fails to generate potential at co–planar points, leading to a breakdown of the employed finite difference scheme that is used to differentiate the velocity (refer to Appendix C).

The radiating behaviour of the diffraction, as well as the six radiation subfields at infinity is treated by adopting a Perfectly Matched layer (PML) technique. This technique is utilized to attenuate the evaluated solutions far from the vessel's position and prevent the occurrence of numerical reflections from the outer layers of the computational mesh. The PML is implemented by complexifying the frequency parameter $\mu = \omega_e^2/g$, involved in the Free Surface BC [Eq. (5.31)], using an appropriately defined imaginary component. More specifically, the latter parameter is redefined as,

$$\mu(\mathbf{x};\omega_e)=\begin{cases}\omega_e{}^2 g^{-1}, & |\mathbf{x}|<R_{PML}\left(\theta(x_1,x_2)\right),\\ \omega_e{}^2 g^{-1}\left(1+ic\dfrac{\left[|\mathbf{x}|-R_{PML}\left(\theta(x_1,x_2)\right)\right]^n}{\lambda_e^n}\right)^2, & |\mathbf{x}|\geq R_{PML}\left(\theta(x_1,x_2)\right).\end{cases} \tag{5.37}$$

In Eq. (5.37), λ_e represents the wavelength that propagates at frequency ω_e and is not affected by the background flow. This corresponds to the wavelength of the diffraction and radiation fields along the x_2–direction. Conversely, the wavelengths of the field components propagating along the x_1–direction are significantly affected by the background flow. In particular, the wavelengths aft of the stern are elongated while compressed wavelengths are generated ahead of the bow in the subcritical case ($\omega_0 U_\infty / g < 1/4$ for head seas). In supercritical cases, the diffraction and radiation subfields do not include components propagating along the positive x_1–axis. This can be clearly observed in Figure 5-8. The latter figure illustrates the real part of the free surface elevation generated by a unit–amplitude heaving oscillation of the vessel, for a fixed absolute frequency corresponding to $\lambda_0/L = 1$, at two different speed settings, respectively falling into the subcritical (a) and supercritical (b) regimes. Optimal values for the parameters c and n, involved in Eq. (5.37) are selected for minimizing the numerical reflections; see [155]. The PML activation curves are also depicted in Figure 5-8 using dashed lines. These curves represent the activation threshold of the PML, which is defined by the variable $R_{PML}(\theta(x_1,x_2))$ in Eq. (5.37), with $\theta(x_1,x_2)$ denoting the angle formed by the line connecting the origin to the point (x_1,x_2) with respect to the x_1–axis.

As stated earlier, the evaluation of the potential function curvature in the x_1–direction, that is involved in Eq. (5.31), is achieved by using the discrete Dawson operator, described in §5.1.2. This suggests that the boundary mesh used for evaluating the involved unsteady subfields also comprises streamline–like lines on the free surface resulting in a rectangular mesh geometry.

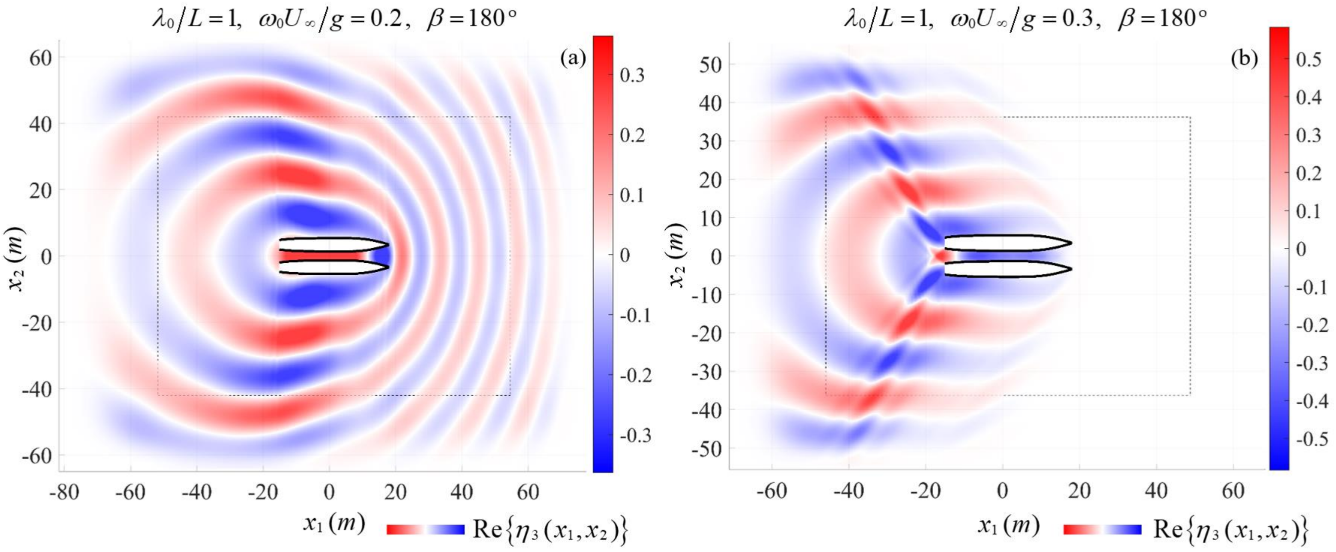

Figure 5-8. Real part of the free surface elevation induced by unit amplitude oscillation of the vessel in heave. $\lambda_0/L = 1$, $\beta = 180^0$ **(a)** $U_\infty = 0.2g/\omega_0$ – subcritical, **(b)** $U_\infty = 0.3g/\omega_0$ – supercritical. The dashed lines represent PML activation curves.

After obtaining the potential functions of all subfields, the response vector ($\boldsymbol{\xi}$) of the vessel in 6 DoF is evaluated as solution to the following system of equations,

$$\left[-\omega_e{}^2\left(\mathbf{M}+\mathbf{A}(\omega_e)\right)+i\omega_e\left(\mathbf{B}(\omega_e)+U_\infty\mathbf{N}\right)+\mathbf{C}\right]\xi=\mathbf{F}_0+\mathbf{F}_d. \tag{5.38}$$

In Eq. (5.38), the inherent inertia of the vessel is modelled via the 6 × 6 tensor **M**, which equals,

$$\mathbf{M}=\begin{pmatrix}\mathbf{M}^{tt} & \mathbf{M}^{tr}\\ \mathbf{M}^{rt} & \mathbf{M}^{rr}\end{pmatrix}, \tag{5.39}$$

where the diagonal matrix $\mathbf{M}^{tt}$ models the inertia of the translational degrees of freedom with respect to the applied forces and is defined as,

$$\mathbf{M}_{ii}^{tt}=M=\rho V=\rho\int_{\partial\Omega_{WS}}x_3\mathbf{n}\,dS,\ i=1,2,3, \tag{5.40}$$

with M denoting the vessel's mass and V the submerged volume (of both demihulls). The diagonal elements of the matrix $\mathbf{M}^{rr}$, which models the inertia of the rotational degrees of freedom with respect to the applied moments, equal the corresponding moments of inertia of the vessel with respect to the selected coordinate system, and are evaluated as,

$$\mathbf{M}_{ii}^{rr}=I_{ii}=MR_i^2, i=1,2,3, \tag{5.41}$$

where R_i represents the radius of gyration about the i^{th} axis. In the results presented and discussed in the sequel, the radii of gyration are defined as $R_1=0.2B, R_i=0.25L, i=2{,}3$ and the products of inertia I_{12} and I_{13} are assumed to be zero due to symmetry of the geometry with respect to the longitudinal axis (x_1). Additionally, due to lack of detailed information and assuming symmetry of the mass distribution relative to the beam axis (x_2) – even without explicit symmetry in the geometry – the product I_{23} is also considered negligible, making the matrix $\mathbf{M}^{rr}$ also diagonal. The submatrices $\mathbf{M}^{tr}$ and $\mathbf{M}^{rt}$ are defined as follows (see Eq. (A.22) of Appendix A),

$$M^{tr}=-M^{rt}=\begin{pmatrix}0 & J_3 & -J_2\\ -J_3 & 0 & J_1\\ J_2 & -J_1 & 0\end{pmatrix}, \tag{5.42}$$

where $\mathbf{J}=(J_1,J_2,J_3)=M\,\overrightarrow{OG}$ and $\overrightarrow{OG}$ is the position vector of the center of gravity G with respect to the origin, which is taken to be the center of flotation (refer to Appendix A). The longitudinal position of G is taken to coincide with that of the center of buoyancy, which is evaluated as the center of the submerged volume, to ensure that the vessel maintains an even keel. The vertical position of the center of gravity is placed at one third of the hull depth measured from the keel, since this positioning represents a common approximation in ship design that supports accurate stability.

The added inertia of the vessel is represented by the 6 × 6 matrix **A**, where the elements $A_{k,\ell}(\omega_e)$ correspond to the components of the radiation loads, induced by the ℓ^{th} field on the k^{th} DoF, in phase with the acceleration. The elements $B_{k,\ell}(\omega_e)$ of the 6 × 6 hydrodynamic damping matrix **B** are determined by the corresponding components in phase with the velocity. The above radiation forces and moments are computed by integrating the pressure exerted by the ℓ^{th} radiation field on $\partial\Omega_{WS}$, multiplied by the component of the generalized normal vector corresponding to the k^{th} DoF. Therefore, the hydrodynamic coefficients (added mass and hydrodynamic damping) are computed using the following equation,

$$A_{k\ell} + \frac{B_{k\ell}}{i\omega_e} = \rho \int_{\partial\Omega_{WS}} \left(\varphi_\ell^{(U)}(\mathbf{x}) - \frac{U_\infty}{i\omega_e} \frac{\partial \varphi_\ell^{(U)}(\mathbf{x})}{\partial x_1} \right) n_k \, dS(\mathbf{x}), \; k,\ell = 1,2,...,6. \tag{5.43}$$

It is noted that the above matrices are dependent on the encounter frequency, and therefore they also depend on the direction of propagation of the incident field, apart from the absolute frequency and the speed at which the vessel travels. The hydrostatic restoring forces are modelled via the Matrix **C**. As concerns the transitional DoFs, only vertical movements induce hydrostatic restoration and thus $C_{33} > 0$. Regarding the rotational DoFs, since the origin has been selected to coincide with the center of floatation (centroid of the water plane), all the first–order moments as well as the products of inertia of the waterplane are zero (refer to Eq. (A.48) in Appendix A for more details). Based on the above observations, the non–zero elements of **C** are the following,

$$C_{33} = \rho g A_{WP} \,, \tag{5.44}$$

$$C_{44} = Mg\overline{GB} + \rho g \int_{WP} {x_2}^2 dS = Mg\overline{GM}_1 \,, \tag{5.45}$$

$$C_{55} = Mg\overline{GB} + \rho g \int_{WP} {x_1}^2 dS = Mg\overline{GM}_2 \,, \tag{5.46}$$

where WP denotes the waterplane, A_{WP} is the waterplane surface area, $\overline{GB}$ is the vertical distance between the center of buoyancy and the center of gravity and $GM_k, k = 1{,}2$ is the metacentric height of the vessel with respect to the k^{th} axis. The additional 6×6 matrix **N**, defined as,

$$\mathbf{N} = \begin{pmatrix} 0 & \mathbf{N}^{tr} \\ 0 & \mathbf{N}^{rr} \end{pmatrix}, \text{ where } \mathbf{N}^{tr} = \begin{pmatrix} 0 & 0 & 0 \\ 0 & 0 & M \\ 0 & -M & 0 \end{pmatrix} \text{ and } \mathbf{N}^{rr} = \begin{pmatrix} 0 & -J_2 & -J_3 \\ 0 & J_1 & 0 \\ 0 & 0 & J_1 \end{pmatrix}, \tag{5.47}$$

models additional damping and coupling effects on the dynamic behaviour of the vessel due to forward motion. In the context of linear theory, the effect of **N** arises since products of the form $U_\infty \xi_k$ are comparable to linear terms in the equations of motion and thus cannot be neglected after linearization; see e.g., [137,181,182]. Derivation of the above result is included in Appendix A, for completeness purposes.

Finally, the forces and moments acting on the hull are evaluated by integration of the pressure induced by the incident and the diffracted subfields on the wetted surface. In particular, the components of the Froude–Krylov and the diffraction forces are computed, taking into account the vessel's forward motion, by the following equation [137,182],

$$F_{k\ell} = \rho \omega_e^2 \int_{\partial\Omega_{WS}} \left(\varphi_\ell^{(U)}(\mathbf{x}) - \frac{U_\infty}{i\omega_e} \frac{\partial \varphi_\ell^{(U)}(\mathbf{x})}{\partial x_1} \right) n_k \, dS(\mathbf{x}), \; k = 1,2,...,6, \; \ell = 0, d \,. \tag{5.48}$$

5.1.4. Estimation of Added Wave Resistance

The resistance and power demands of a ship operating in wave conditions are typically considered to increase by a factor of 20 – 40%, which is traditionally incorporated into ship design, as highlighted in Ref. [183]. However, this percentage is a rough estimate and does not accurately reflect the actual impact of the prevailing sea state in which a vessel operates. In recent years, the demand for accurate predictions of added resistance in wave conditions has been increasing, as it plays a crucial role in selecting the power that propulsion systems need to deliver [184], while it also affects the vessel's ability to maintain speed and fuel efficiency in actual weather conditions. Accurate estimation of this additional resistance is also critical for optimizing modern ship routing practices, see e.g. [185]. As stated in the latter work, added–wave resistance increases exponentially as environmental factors intensify. However, despite its significant impact, relatively little research has been conducted on this issue, highlighting the need for more precise predictions.

Added–wave resistance is a second–order force relative to the wave amplitude which opposes the ship's forward motion [183]. The mean–flow effects concerning the numerical computation of the added–wave resistance have been discussed by several authors; see, e.g., Ref. [186] and the works cited therein. In the case of the present linearized model, formulated in the frequency domain, various time–harmonic components result in zero or negligible contributions to the mean value of added–wave resistance. For the present analysis’ purpose, the mean added–wave resistance of the steady travelling vessel is estimated by the following two terms [187],

$$R_{AW}=R_{AW}^{(1)}+R_{AW}^{(2)},\ \text{where} \tag{5.49}$$

$$R_{AW}^{(1)}=-\frac{1}{2}\rho\int\limits_{\partial\Omega_{WS}}\left|\mathbf{U}(\mathbf{x})\right|^{2}n_1\,dS(\mathbf{x}),\ \text{with}\ \mathbf{U}(\mathbf{x})=\nabla\varphi^{(U)}(\mathbf{x}),\ \text{and} \tag{5.50}$$

$$R_{AW}^{(2)}=\frac{1}{4}\rho g\int\limits_{WL}\left(\left[\eta^{(U)}(x_1,x_2)-(\xi_3+\xi_4x_2-\xi_5x_1)\right]^{2}\right)\frac{n_1}{\sin\left[a(\mathbf{x})\right]}d\ell(\mathbf{x})\,. \tag{5.51}$$

In Eq. (5.51), a denotes the vertical hull slope angle at the mean draft. In the above equations, the added resistance components are evaluated as mean values of the corresponding squared time–dependent quantities over one encounter period, justifying that both right–hand sides of Eqs. (5.50) and (5.51) include a term of $1/2$ that has been factored out as the mean value of $\sin^2(i\omega_e t)$. The integral of Eq. (5.50) is defined over the mean wetted surface while the integral of Eq. (5.51) is evaluated over the calm waterline. Moreover, in the latter equation, $\eta^{(U)}(x_1,x_2)$ stands for the free surface elevation corresponding to the total unsteady problem,

$$\eta^{(U)}(\mathbf{x})=-\frac{1}{g}\left(i\omega_e\varphi^{(U)}(\mathbf{x})-U_\infty\frac{\partial\varphi^{(U)}(\mathbf{x})}{\partial x_1}\right),\ \ \mathbf{x}\in\partial\Omega_{FS}\,, \tag{5.52}$$

where $\varphi^{(U)}(\mathbf{x})$ is the total complex potential, which includes all eight subfields involved in Eq. (5.28), with the six radiated subfields scaled by the complex amplitude of the vessel’s response in the corresponding DoF, as computed by Eq. (5.38).

5.2. *Model Verification*

In this section, results from the present unsteady BEM model are compared against experimental data for verification purposes. The data are based on experimental measurements in head waves conducted in 2023 in the towing tank of the Laboratory of Ship and Marine Hydrodynamics (LSMH) of NTUA, as part of the broader objectives established within the framework of ELCAT research project; see also [86]. The tests were conducted on a $1{:}\,10$ scale and the experimental data can be found in the Technical Report No: NAL–353–F–2023. Figure 5-9 (a, b) presents the present model's predictions for the twin–hull RAOs in heave and pitch along with the corresponding experimental values. Both the numerical and experimental data refer to $Fn = 0.338$ (corresponding to $U_\infty = 11.82$kn for the prototype) and head seas with waveheight $H = 2A$ and absolute frequency corresponding to wavelength equal to λ_0. Additionally, Figure 5-9 (c) illustrates the computed RAO of added wave resistance for various incident wave frequencies where it is compared against experimental measurements at specific frequencies shown by using symbols. The latter are obtained as the difference of the total resistance in harmonic waves and the calm–water resistance of the twin–hull for the same draft and forward speed. The present BEM results show quite good agreement with the experimental data, indicating the model's reliability as concerns the prediction of the vessel's dynamic behaviour as well as the added–wave resistance. The minor differences observed are due to higher–order, non–linear effects which are not modelled by the discussed method.

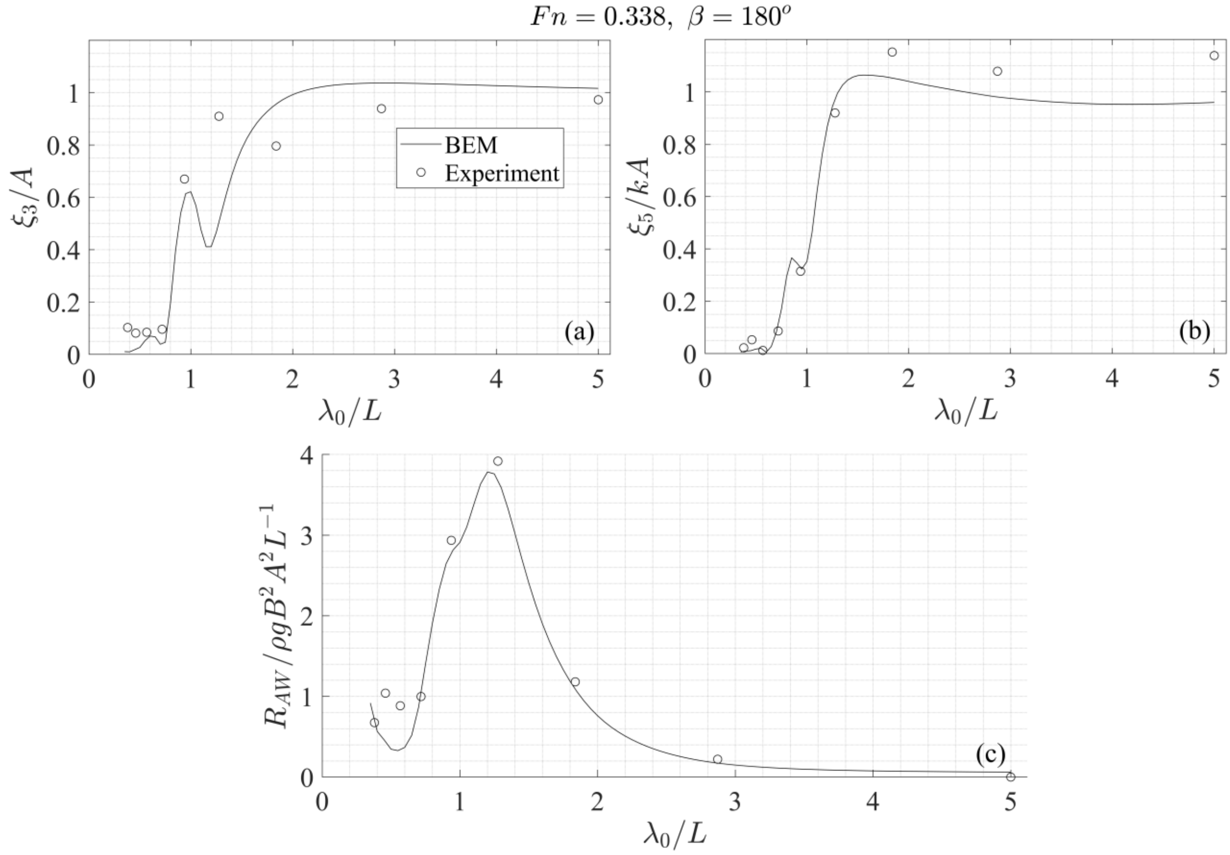

Figure 5-9. Numerical results obtained by the unsteady BEM scheme, concerning responses of the twin–hull vessel at $Fn = 0.338$ in harmonic head seas and comparison with experimental data (source: LSMH, NTUA, Technical Report No: NAL–353–F–2023). (**a**) Heave RAO, (**b**) Pitch RAO and (**c**) RAO of added–wave resistance.

5.3. *Case study in the Saronic Gulf*

As an indicative scenario, the twin–hull vessel is considered to be operating in the Saronic Gulf (central Aegean) region, concerning a line that connects Milos Island with Piraeus port, shown by the track AB in Figure 5-10. The route total distance is 82NM. The selected operating speed corresponds to $Fn = 0.25$ ($U_\infty \approx 8.74\text{kn}$) and the total travel duration is approximately 9.4 h. For the scope of this case study and in order to provide quantified results, the vessel is considered to depart at 06:00 and navigate along the route illustrated in Figure 5-10 with a bearing of –, heading northwest.

The reverse route is followed during nighttime and the trip is repeated on a daily basis. The arrangement of panels on the upper deck, consisting of 123 panels with an area of 2m^2 each, is shown in Figure 5-11. A zero–tilt configuration is employed, although it is not the optimal selection to maximize energy absorption in the considered latitude, to avoid issues concerning increased wind resistance as well as space utilization. In particular, the influence of wind resistance, which is typically proportional to the area normal to the airflow direction, is assumed to be negligible and has been omitted in the context of the present study. The selection of zero–tilt panels suggests that any arbitrary selection of azimuth angle would be equivalent as concerns the energy yield of the installed system. However, since dynamic responses are expected to provoke instantaneous changes to the tilt angle, the azimuth angle is set to 62.65° (normal to the vessel's direction).

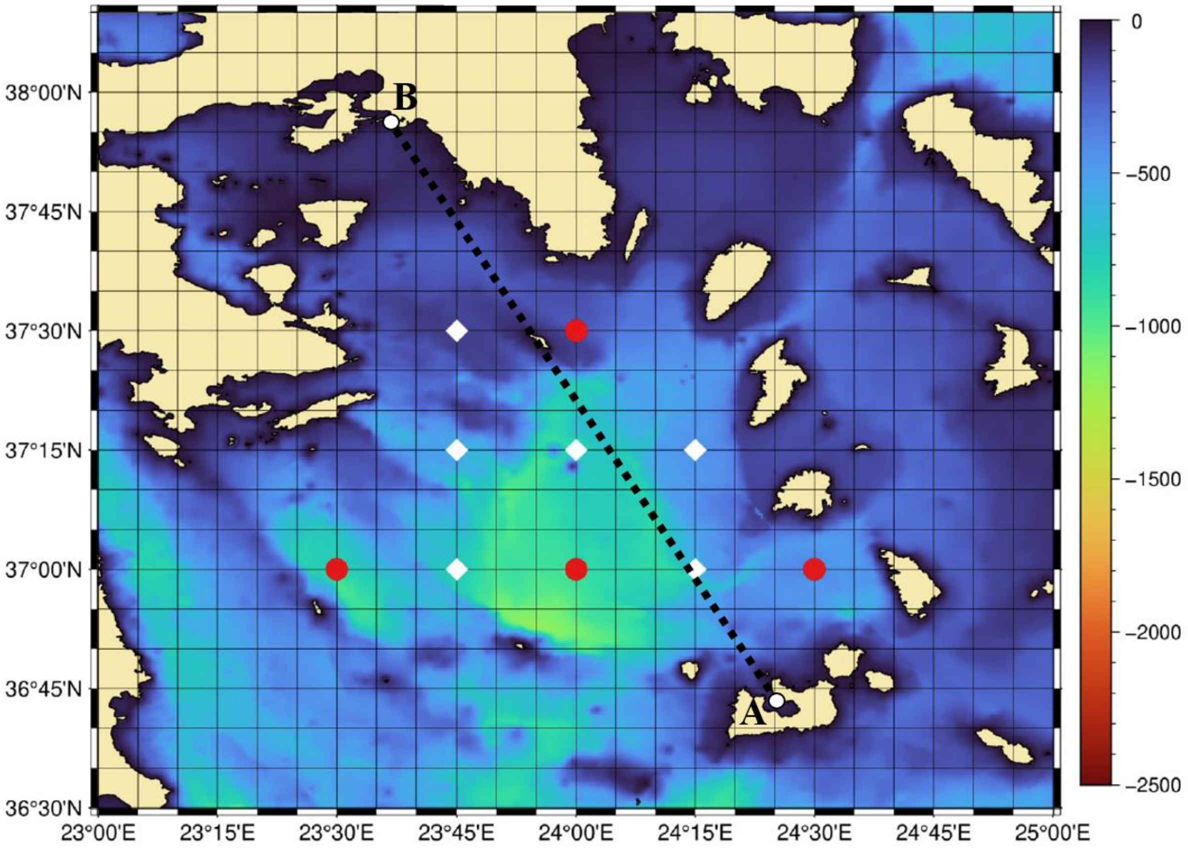

Figure 5-10. Indicative route (dotted line) from Milos Island – point A (36°43′ N, 24°25′ E) – to Piraeus port – point B (37°56′ N, 23°38′ E) – with a total distance of 82 NM.

The calm water resistance is used as evaluated from the steady BEM model discussed earlier. For simplicity, the draft of the vessel is retained unchanged as compared to the previous sections. Considering that the studied vessel's TPC is approximately $2.46\ \mathrm{tons/cm}$ at $T = 1.55\ \mathrm{m}$, the addition of the solar panels is not expected to significantly alter the draft, with an anticipated increase of about $1\ \mathrm{cm}$, assuming the panels weigh approximately $10\ \mathrm{kg/m^2}$ [188]. Furthermore, as illustrated in Figure 5-11, the arrangement of the panels ensures that the weight is distributed evenly across the vessel, thus minimizing any potential impact on the weight distribution. The mean added wave resistance as well as the spectra of dynamic responses are computed by the unsteady BEM model, in conjunction with climatological data of the considered region, acquired from Copernicus database [189].

Specifically, the wave climatology of the point $(37°\,30'\,\mathrm{N}, 24°\,\mathrm{E})$ is selected as representative of the considered route. The bivariate probability density function of significant wave height H_S and peak period T_P is depicted in Figure 5-12(a), along with a polar histogram of mean wave direction [Figure 5-12(b)]. Based on the above climatological data of the Saronic Gulf and Central Aegean Sea area, the prevailing wave directions relative to the ship track correspond to (i) head quartering seas $\beta = 115°$ and (ii) following quartering seas $\beta = 290°$. In order to illustrate the applicability of the present model, the mean values of the distribution corresponding to peak wave period equal to $T_p = 4.58\ \mathrm{s}$ and significant wave height $H_S = 0.66\ \mathrm{m}$ are considered, in conjunction with head–quartering seas corresponding to $\beta = 115°$. In this case, the resulting peak encounter frequency is $\omega_e = 1.74\ \mathrm{rad/s}$ and the parameter τ equals $\omega_e\, U/g \approx 0.8$, indicating supercritical conditions at peak frequency.

Given that rolling motion is expected to have the most significant impact, in the context of the present case study, the tilt angle of the PV configuration is substituted by the corresponding dynamic value, which is approximated by summing the static tilt angle and the instantaneous roll response of the vessel. Moreover, the vessel is considered to travel during daylight hours, exploiting solar power for the partial coverage of the power needs, and return during nighttime. The implications of simulating more realistic scenarios, based on long–term time series of wave conditions modelled by considering varying sea states and relative wave directions, including beam and following seas along the route, as well as contributions of all angular responses, are discussed in §5.4.

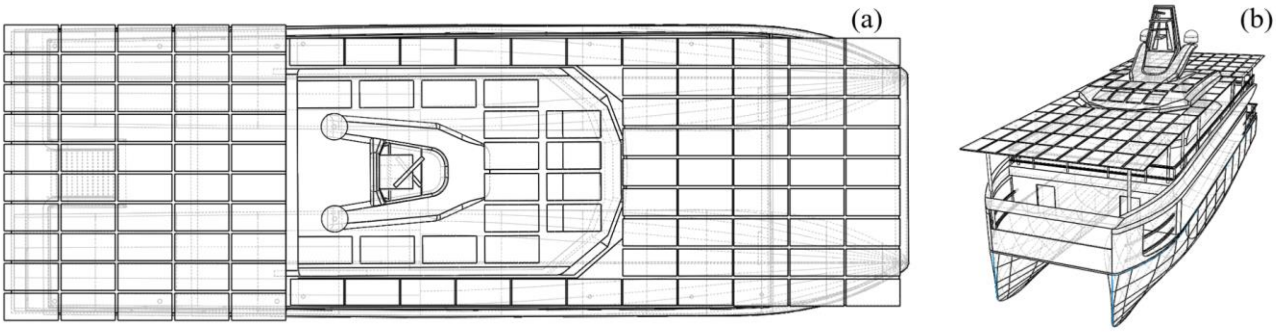

Figure 5-11. (**a**) Top view and (**b**) 3D view of the considered arrangement of 123 solar panels on the twin–hull vessel.

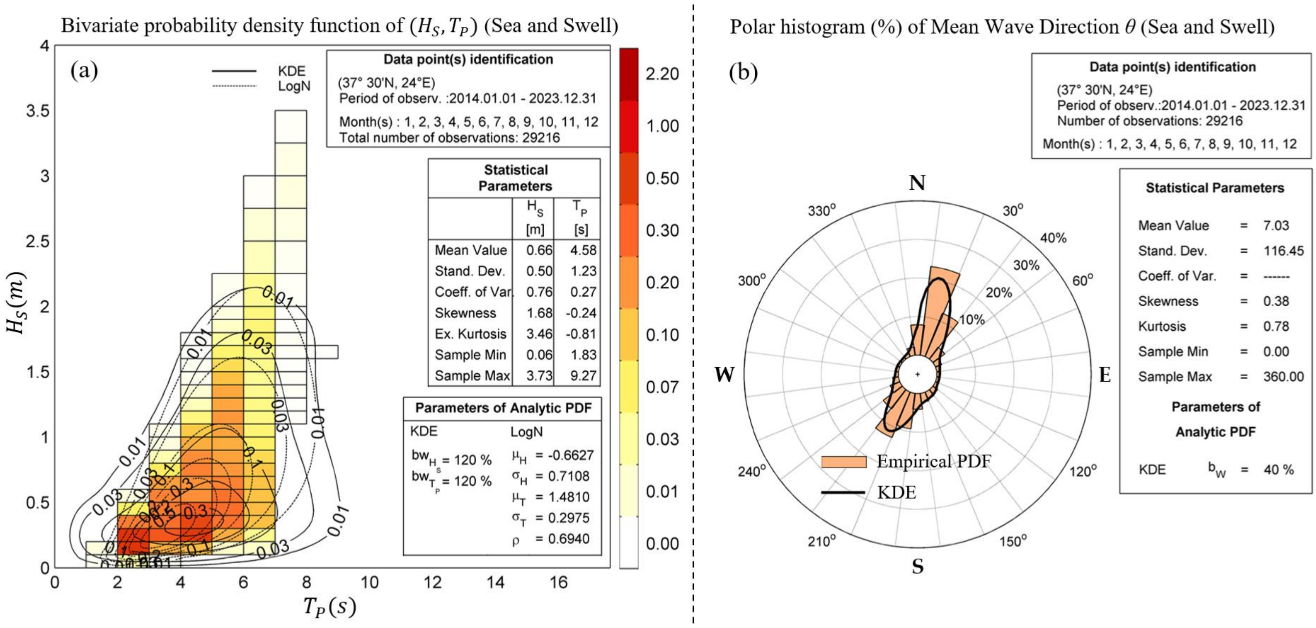

Figure 5-12. Wave climatology based on data of point (37°30′ N, 24° E) from Copernicus database. (**a**) Bivariate probability density function of (H_S, T_P) and (**b**) polar histogram (%) of mean wave direction (θ).

5.3.1. Selected Results of Dynamic Responses and Added Resistance

For the considered speed, corresponding to $Fn = 0.25$, selected results are presented in Figure 5-13, as obtained by the unsteady BEM model, discussed in subsection §5.1.3, for $\beta = 115°$ and $\beta = 290°$. The results include the vessel's response in heave, roll and pitch motions, as well as the computed normalized added–wave resistance. The RAO curves depicted in Figure 5-13(a – c) demonstrate that the limiting behaviour at low frequencies is in line with theoretical expectations. In particular, the heave response amplitudes tend to unity, while the roll and pitch response amplitudes converge to $|\sin(\beta)|$ and $|\cos(\beta)|$, respectively, confirming that the discussed model properly modulates the angular responses with respect to the angle of incidence. Furthermore, it can be observed in Figure 5-13(d) that the added–wave resistance is severely amplified in the case of head–quartering seas $(\beta = 115°)$ as compared to the following–quartering seas case $(\beta = 290°)$, primarily due to the direction of wave propagation, which causes wave loads with components that directly resist the ship's motion. As a result, the vessel must overcome the combined effect of opposing wave direction and the associated motions. Additionally, the reduced encounter periods in head or head–quartering seas lead to more frequent wave impacts, further intensifying the hydrodynamic interactions.

The sea state characterized by peak period $T_p = 4.58$ s and significant wave height $H_S = 0.66$ m is modelled using a Bretschneider spectrum [190],

$$S(\omega) = \frac{5}{16} H_s^2 \frac{\omega_p^4}{\omega^5} \exp\left(-\frac{5}{4} \left(\frac{\omega_p}{\omega} \right)^4 \right), \text{ where } \omega_p = \frac{2\pi}{T_p}. \tag{5.53}$$

Subsequently, the spectrum is redefined in terms of the encounter frequency ω_e, while maintaining the energy distribution as follows,

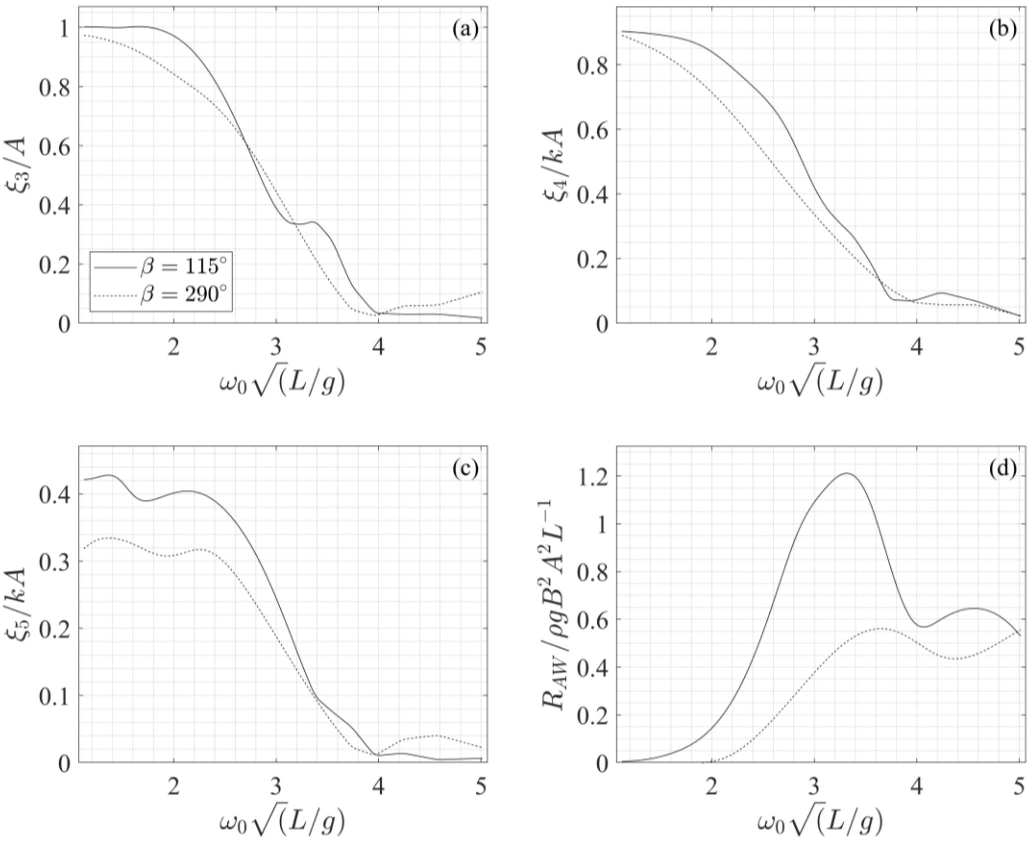

Figure 5-13. Calculated results for head quartering seas ($\beta = 115°$) and following quartering seas ($\beta = 290°$). Response Amplitude Operators (RAOs) of (**a**) heave, (**b**) roll and (**c**) pitch motions. (**d**) RAO of added–wave resistance. $Fn = 0.25$.

$$S(\omega)d\omega = S(\omega_e)d\omega_e \rightarrow S(\omega_e) = S(\omega)\left(\frac{d\omega_e}{d\omega}\right)^{-1} = \frac{S(\omega)}{1-2U\cos(\beta)\omega g^{-1}}. \tag{5.54}$$

Finally, the roll response spectrum is evaluated as

$$S_4(\omega_e) = \left|\xi_4(\omega_e)/kA\right|^2 k^2 S(\omega_e). \tag{5.55}$$

The sea spectrum and the corresponding roll response spectrum in terms of the encounter frequency ω_e are depicted in Figure 5-14(a, b). The roll RAO is plotted in Figure 5-14(a), in terms of the encounter frequency, using a distinct vertical axis, for clarity purposes. An indicative time series of rolling motion $\xi_4(t)$, obtained by applying the random–phase model, is presented in Figure 5-14(c); (see also Refs. [144,153,191] and Eq. (4.23) of §4.4). The latter quantity is used as a disturbance of the panel tilt angle due to the wave–induced motions. The results concerning the solar power output during the daily hours of the trip over a Typical Meteorological Year (TMY) are presented and discussed in the sequel.

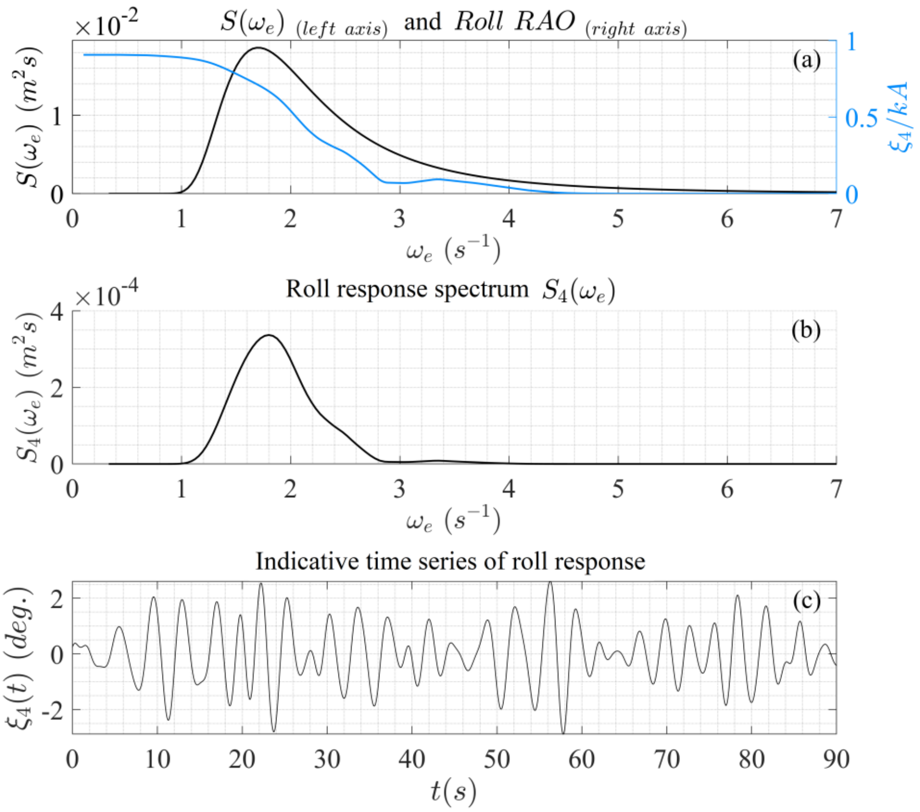

Figure 5-14. (**a**) Sea spectrum and corresponding roll RAO and (**b**) response spectrum in terms of the encounter frequency. (**c**) Indicative time series of the vessel's response in roll. $Fn = 0.25$.

5.3.2. Estimation of Energy Needs and PV Contribution

The vessel can cover a distance of 40 nautical miles at a speed of 13 kn. At the latter speed, the calm water resistance equals 49.5 kN, based on experimental measurements [86]. Moreover, the auxiliary loads (lighting, air–conditioning, equipment, etc.) for the studied vessel are estimated to be $P_{aux} = 65$ kW [192]. Considering a Depth of Discharge (DoD) of 80% for the battery and given its capacity (see Table 5-1), it is concluded that the propulsion system has a total efficiency of $\eta_{prop} = 50\%$. For the considered speed, corresponding to $Fn = 0.25$, the calm water resistance is $R_T = 14$ kN (refer to Figure 5-7). The added resistance is imported in the analysis, as obtained by integrating over the frequency spectrum, based on the considered sea state, expressed in terms of the encounter frequency. The latter parameter contributes to the total resistance by 0.25 kN. Based on the above, the total power consumption equals

$$P_{total} = U\frac{R_T + R_{AW}}{\eta_{prop}} + P_{aux} = 193.18\text{kW}. \tag{5.56}$$

The real–time contribution of the PV system is calculated based on the methodology presented and discussed in §4.5. The energy efficiency of the installed photovoltaic system is affected by several parameters such as humidity, ambient temperature, wind speed and vessel speed. Moreover, certain factors encountered in the marine environment help maintain lower operating temperatures and optimize performance. In this work, in order to proceed to a preliminary calculation of the extent to which the considered system can compensate for the energy needs of the vessel, accounting for the effect of rolling motion, as well as added–wave resistance in the specific sea state, the following equation is used to evaluate the power delivered by the solar system (refer to §2.3),

$$P(t)=\eta_{pv}A_{pv}G\left(1-k_p\left(T_c-T_{\mathrm{STC}}\right)\right), \tag{5.57}$$

where G is the global irradiance on the panels. The calculations are based on data of Direct Normal Irradiance (DNI) and Diffuse Horizontal Irradiance (DHI), along with several parameters, including the latitude and longitude of the considered location, the tilt and azimuth angles of the PV installation as well as the earth's declination angle, as detailed in §2.3.

In order to estimate energy production data, a representative value of efficiency $\eta_{pv} = 20\%$ is assumed at STC, which falls within the upper limit of the current range for solar cell efficiency; see, e.g., Ref. [193]. The total area covered is $A_{pv} = 246\ \mathrm{m}^2$ (see Figure 5-11), and the installed system's nominal power is approximately $50\ \mathrm{kWp}$. The temperature coefficient is set to $k_p = 0.4\% \,/\, {}^\circ\mathrm{C}$, based on estimates for silicon panel technology; see also [96]. For the present case study, the values of latitude and longitude used in the PV model are approximated by the values corresponding to the midpoint of the route i.e., $\varphi = 37.34°$ and $\lambda = 24.02°$. (see Figure 5-10). Furthermore, the panels' tilt and azimuth angles are set to $\beta_0 = 0°$ and $\psi = 62.65°$, as discussed earlier in the present chapter (refer to §5.3).

The effects of dynamics are incorporated in the PV model by considering the dynamic value of the tilt angle, obtained by the summation of the static value and the instant roll response of the vessel, defined on the short time scale (refer to §4). Numerical results concerning the ambient and cell temperatures as well as the daily energy production of the considered system are illustrated in Figure 5-15. It is worth noting that electrical system losses are not accounted for in the present study, The latter factor, along with the impact of all angular responses, varying sea states, and relative wave directions, remain open for further investigation.

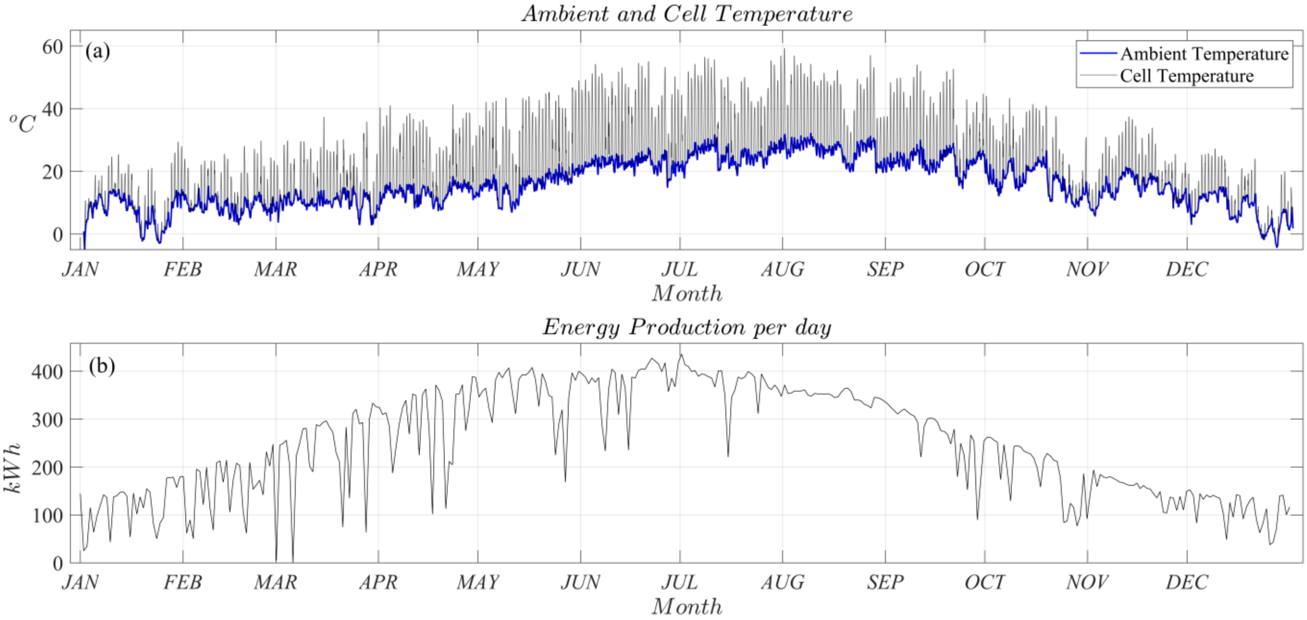

Figure 5-15. (**a**) Ambient temperature and cell temperature of the installed solar system and (**b**) daily energy production in kWh during a TMY.

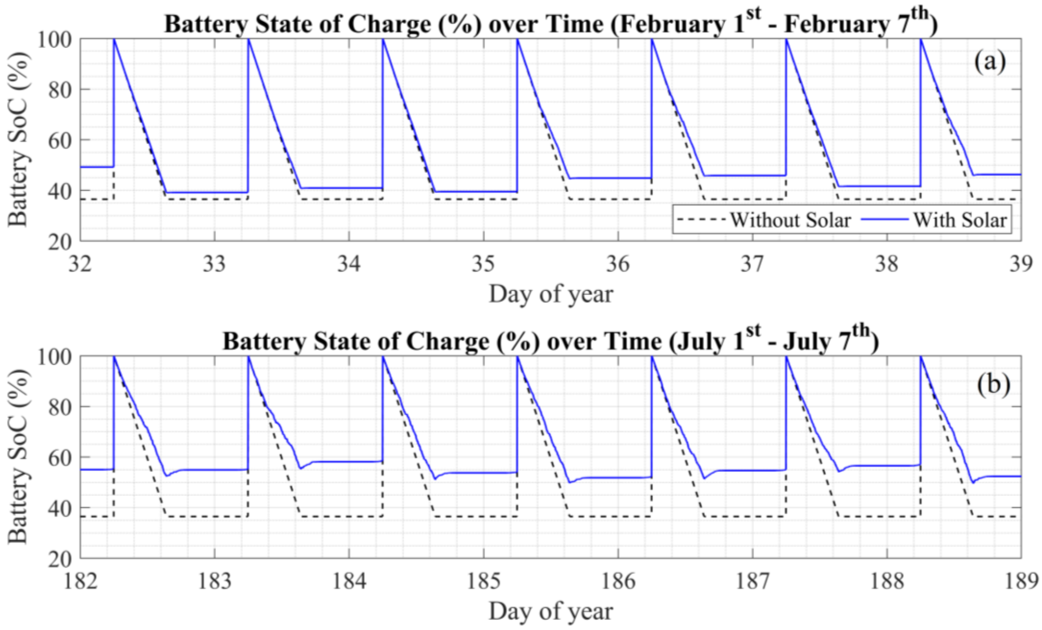

Figure 5-16. State of Charge (SoC) of battery, as it evolves with and without the auxiliary solar system, for two indicative weeks of the year, corresponding to (**a**) winter and (**b**) summer conditions.

Charging from external sources is assumed to restore the battery to fully charged before each departure. For the scope of the present case study, the charging is considered instantaneous to simplify the calculations. Figure 5-17 depicts the percentage of energy needs covered by the auxiliary solar system on a daily basis and in average monthly values. This percentage ranges from approximately 5% in winter months to a maximum of 18.3% during summer. The mean percentage of power needs covered within a TMY equals 13.6%.

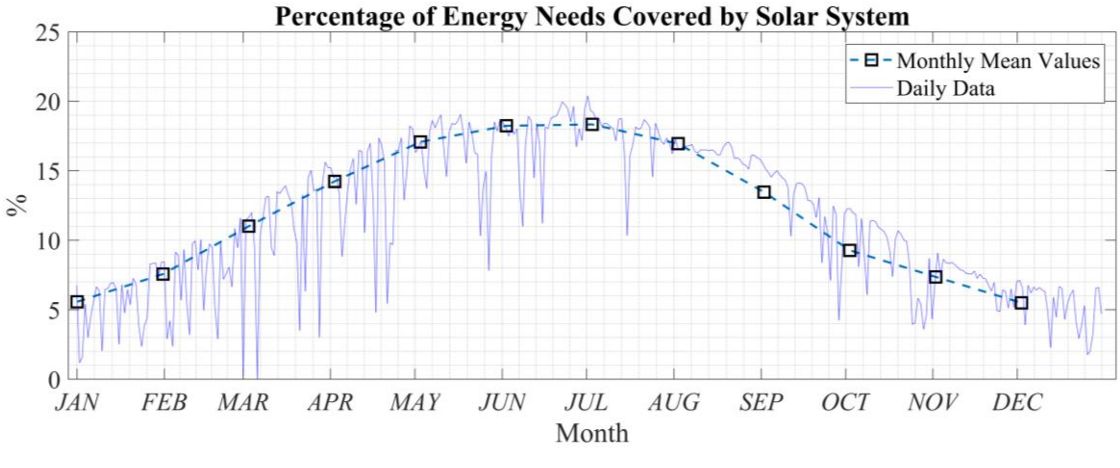

Figure 5-17. Percentage of energy needs covered by the auxiliary solar system on a daily basis and in average monthly values.

5.4. *Discussion and model extensions*

In this chapter, a novel Boundary Element Method (BEM) formulation is presented for predicting the resistance, as well as the hydrodynamic behaviour, of twin–hull vessels travelling at low speeds, aiming to quantify the benefits of integrating auxiliary solar systems onboard. The developed method is applied for a case study concerning an electric twin–hull vessel measuring 33 m in length. The BEM formulation incorporates a combination of steady and unsteady BEM models, which treat the combined effects of incident flow and waves interacting with the vessel, supporting an accurate calculation of the total resistance (including the added–wave resistance component) as well as the dynamic responses. The velocity gradient terms, involved in the (steady and unsteady) free–surface boundary conditions, are treated by a four–point upstream finite difference scheme. Furthermore, the steady model is supplemented by a mirroring technique while the unsteady BEM is used in conjunction with a Perfectly Matched Layer (PML) technique to treat conditions at infinity.

The placement of solar panels on deck is discussed and their utilization in terms of real–time energy generation is assessed, aiming to partially cover the energy needs, while also reducing carbon emissions. Numerical results are presented, verified and discussed regarding calm water resistance and added–wave resistance, as well as the wave–induced motions of the vessel. Moreover, the energy generated by the integrated solar system is quantified and combined with power demand estimates to assess the percentage of power needs covered without relying on external sources. Various operational factors are considered in predicting the power needs as well as the power production by the auxiliary solar system. Based on the selected parameters and operation conditions, the results indicate that the considered system contributes by 13.6% on average to the coverage of the total power requirements, with the latter percentage ranging from 5% to around 18.3% throughout a TMY. The direct effect of dynamics on the solar system’s energy yield is limited to rolling motion.

As mentioned in §2.3.1, the pitching motion is not expected to modify the PV system’s performance, provided that the mounted PVs are aligned with the vessel’s longitudinal axis, as is the case in the scenario considered in this chapter. In this case, the combined results of all angular responses can be incorporated into the analysis using coupled roll and yaw response time series. The latter approach ensures that the resulting phase difference between the two motions will be consistent with the predictions of the hydrodynamic model, since the responses are caused by a common incident spectrum. However, from the perspective of system theory, this highlights the importance of considering the full coupled system, as each degree of freedom influences all the others through the system’s inertia, as well as the matrices of hydrodynamic coefficients (refer to Appendix A). The latter problem can be treated as is a single–input, multiple–output (SIMO) system, where the input is the sea spectrum and the outputs are the time series of responses in the various DOFs (see e.g. [194]). The coupling must be considered to ensure accurate modelling of the system’s behaviour in the time domain, particularly as regards phase relationships.

The results of the case study presented and discussed, are derived considering the mean values of the stochastic wave parameters, corresponding to head quartering seas. In this case the transformation between absolute and encounter frequency is one–to–one. However, extension of the analysis to include following and following–quartering seas introduces additional complications. Specifically in the latter case, the transformation between absolute and encounter frequency is no longer one–to–one across the entire spectrum. This causes significant implications in the response analysis, as the multi–valued nature of the transformation creates regions where the encounter frequency is highly sensitive to variations in the wave frequency and the ship’s velocity. Figure 5-18 illustrates the resulting encounter frequency for the setup discussed in §5.3, corresponding to $Fn = 0.25$, for $\beta = 0°$ (following seas).

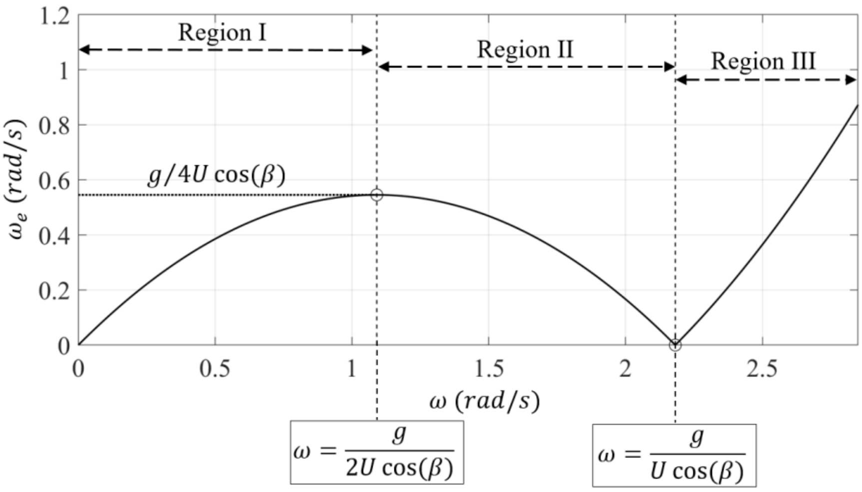

Figure 5-18. Variation of the encounter frequency with respect to the absolute frequency in the case of following seas ($\beta = 0°$). $Fn = 0.25$.

The absolute frequency $\omega = g/U\cos(\beta)$, for which $\omega_e = 0$, reflects the situation where the component of the vessel's speed in the direction of wave propagation exactly matches the wave speed [137]. For the discussed case, where $\beta = 0°$, this corresponds to $c = \omega/k = U$. Given that the analysis assumes propagation in deep water, the latter relation yields, $\omega = g/U$. In Regions I and II, as defined in. Figure 5-18, the waves move faster than the vessel, while in Region III, the vessel overtakes the waves. Within each of the regions, the transformation between the absolute and encounter frequency is one–to–one [137]. Therefore, the response spectrum has to be defined in three overlapping regions. In the overlapping areas, although the ship oscillates at the same encounter frequency, the amplitude of oscillation may vary, depending on the absolute frequency.

The same applies to added–wave resistance, since this quantity is also influenced by the absolute frequency. This is intuitively consistent, considering that in Region III, where the ship technically encounters head seas (since it overtakes following waves), an increase in added resistance is anticipated.

Other interesting extensions include the investigation of installing additional renewable energy sources on ships, such as sails or flapping–foil thrusters placed at the bow. The latter technology has been numerically and experimentally studied in Ref. [55], and the results suggest that it offers increased dynamic stability and a reduction in added–wave resistance, while also exploiting energy from dynamic motions and directly converting it to useful power. It must be noted however, that both sails and foil–thrusters significantly influence the vessel's dynamic behaviour and must therefore be modelled as coupled systems, combined with the methodology discussed earlier in this chapter. Consequently, the cumulative advantages of multiple renewable sources could accelerate the transition towards more sustainable maritime solutions.

Part III

HYDRODYNAMIC ANALYSIS AND PERFORMANCE OF WAVE ENERGY PARKS

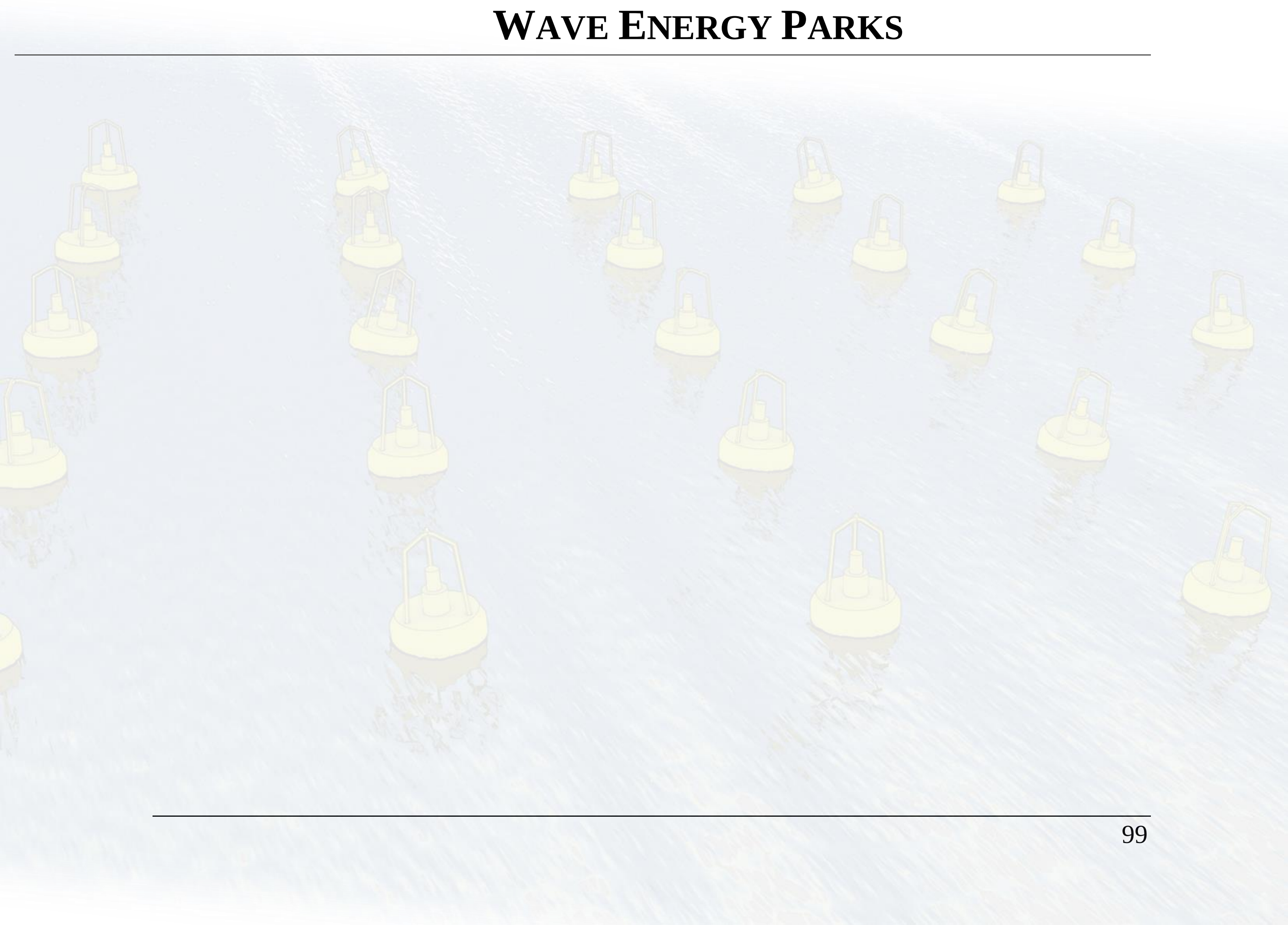

6

MODELLING OF NEARSHORE WAVE ENERGY PARKS

Marine renewables currently support the development of sustainable energy policies and the reduction in carbon emissions via several energy capturing devices that operate based on different principles, which however have not yet reached full commercialization [66]. One of the most common and commercially mature technologies for wave energy harvesting is the installation of heaving point absorber WECs (see Figure 6-1) in offshore and nearshore locations (see, e.g., [195]). Estimation of the production capacity of wave energy converter arrays (WECs) of the type of simple floaters deployed in nearshore locations highly depends on the evaluation of their performance. The latter also depends on several factors, including the dimensions and inertial characteristics of the devices, their relevant positioning and the power–take–off (PTO) system characteristics. Studying the system operation, based on the prevailing sea conditions in the region considered for deployment, can ensure that such WEC farms are sized and designed in an effective way.

Several approaches have been utilized to assess the response and power production capacity of WEC arrays, including frequency and time domain BEM approaches, as well as CFD models. A review of different modelling approaches, along with their advantages and limitations, can be found in Ref. [196]. Moreover, reduced models can be applied to obtain results in an extended frequency range with low computational cost, such as the simplified 2D Modified Mild Slope Equation (MMSE) model, proposed in Ref. [197].

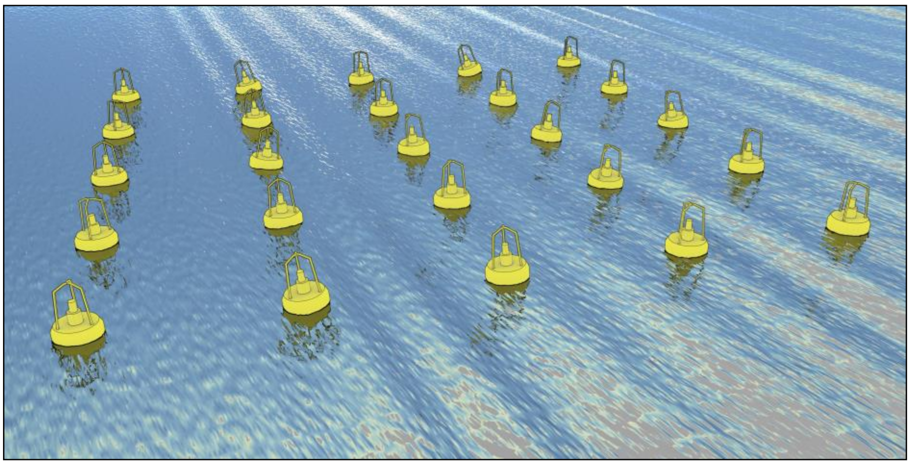

Figure 6-1. Point absorber wave park comprising twenty five (25) identical floating devices.

Gap resonance phenomena may also occur in hydrodynamic interaction problems, involving multiple floating bodies placed in close proximity [198,199]. The latter could prove to be beneficial, in the sense of enhancing the energy conversion efficiency of WECs. Recent studies indicate that viscous effects become significant during gap resonance phenomena, especially regarding the heaving motion of the structures, and should be accounted for; see Ref. [200]. The effect of viscous forces on surging wave energy converters is quantified in Refs.[201,202], where it is demonstrated that viscous phenomena are significant in terms of annual power absorption. Specifically, in Ref. [202], it is shown that the peak power absorption of surge converters can be reduced by a factor of about 35% due to viscous effects.

The identification of structural and functional features, the evaluation of power absorption capacity, and the optimal design and layout of WEC farms depend on the performance evaluation of WECs. The total power generated by an array of WECs may be augmented or decreased as compared to the corresponding power generated by an equal number of individual floating devices, due to hydrodynamic interactions between multiple bodies, also referred to as intra–array interactions [203]. In nearshore locations, the wavelength and propagation direction of incoming wave fields can be significantly impacted by wave–seabed interactions, which can alter the WECs' response pattern and ultimately the array's power output. More specifically, the presence of seabed slope, or any depth irregularity in general, can influence the power absorption capacity, especially at low frequencies, where the interaction of the flow fields with the seabed becomes significant. This effect is studied in Ref. [155], using appropriate methods. The tools proposed in the latter work can be utilized for preliminary optimization studies of WEC park designs with a low computational cost; see also [204].

In this chapter, a 3D BEM hydrodynamic model is proposed aiming to assess the energy–capturing capacity of WEC arrays, accounting for the hydrodynamic intra–array interactions among various identical floating devices, as well as the local seabed topography. The methodology is supplemented by a Coupled Mode Model (CMM) for computing the incident field propagating over varying bathymetry, thereby simulating nearshore environments in a more realistic manner, without necessitating assumptions of a flat seabed or mild seabed slopes. Additionally, a case study is conducted for a specific geographic area situated north of the coast of Ikaria Island, located in the Eastern Aegean Sea region. This area is characterized by a notably high wave potential, particularly noteworthy within the context of Mediterranean standards [57]. The case study utilizes long–term data and employs real bathymetric information, underscoring the practicality of the proposed method and demonstrating its applicability as a supporting tool to toward optimal design decisions for Wave Energy Converter (WEC) parks.

The model that is discussed in this chapter is developed on the basis of linear theory and comprises a frequency domain BEM approach, supplemented by a Consistent Coupled Mode System (CMS) that models wave propagation over irregular bathymetry. Thus, the influence of fluid viscosity is not taken into account, which could cause important deviations at specific frequencies. Nevertheless, the 3D numerical approach based on boundary integral equations allows for the modelling of any WEC shape, as opposed to reduced 2D models, and can provide useful results in an extended range of frequencies and angles of incidence. In the context of the present work, an array of single degree–of–freedom (DoF) point absorbers is considered, with each unit being free to oscillate in heave alone, leading to a simplified hydrodynamic model, as compared to the full six DoF setup. As a result, the proposed model ignores the coupling between different degrees of freedom, which could lead to underestimation or overestimation on the response of certain units of the array at particular excitation frequencies. However, it is much more efficient in terms of computational requirements, as compared to the six DoF setup. The results concerning the response of the array can be used to assess the system performance on the basis of spectral average characteristics. In the existing literature, the effect of irregular bathymetry on the operation of wave energy parks has been investigated at a preliminary stage. More specifically, Ref. [205], investigates bathymetric effects on the far field of a WEC park, with the bathymetry profile, however, being constant in the vicinity of the WEC array. Additionally, in Ref. [197], the operation of WECs is studied over irregular bathymetry by a 2D model, that makes use of the MMSE. In the latter work, the point absorbers are modelled on the free surface plane as energy absorbing circular inclusions, while the absorption parameters are calibrated by local 3D BEM formulations in constant local depth. The innovation of the present model lies in the inclusion of real bathymetric data in the modelling, along with oblique wave incidence on the WEC park, which allows for the quantification of the power absorption in site–specific cases, based on local seabed topography, combined with local wave climate data.

6.1. *Mathematical Formulation*

A WEC array of single degree–of–freedom (DoF) heaving point absorbers is considered, comprising M identical devices, operating in a nearshore area where the seabed may present arbitrary variations, while harmonic propagating incident waves stimulate the whole array. The response of each device in heave is obtained by modelling the surrounding field in the domain D (see Figure 6-2), accounting for the interaction of the field with the variable bathymetry, as well as intra–array interactions, as discussed in more detail in the sequel. In accordance with the standard hydrodynamic theory for floating structures (refer to Appendix A), the overall flow field consists of the propagating field (incident and diffracted) and M radiation fields, generated by the devices' motion. Each of the above is represented by a corresponding potential function $\Phi_0(\mathbf{x};t),\ \Phi_d(\mathbf{x};t)$, and $\Phi_m(\mathbf{x};t),\ m=1,2,\dots,M$ respectively, so that the resulting velocity fields are equal to $\mathbf{v}_m(\mathbf{x};t)=\nabla\Phi_m(\mathbf{x};t),\ m=0,d,1,2,\dots,M$.

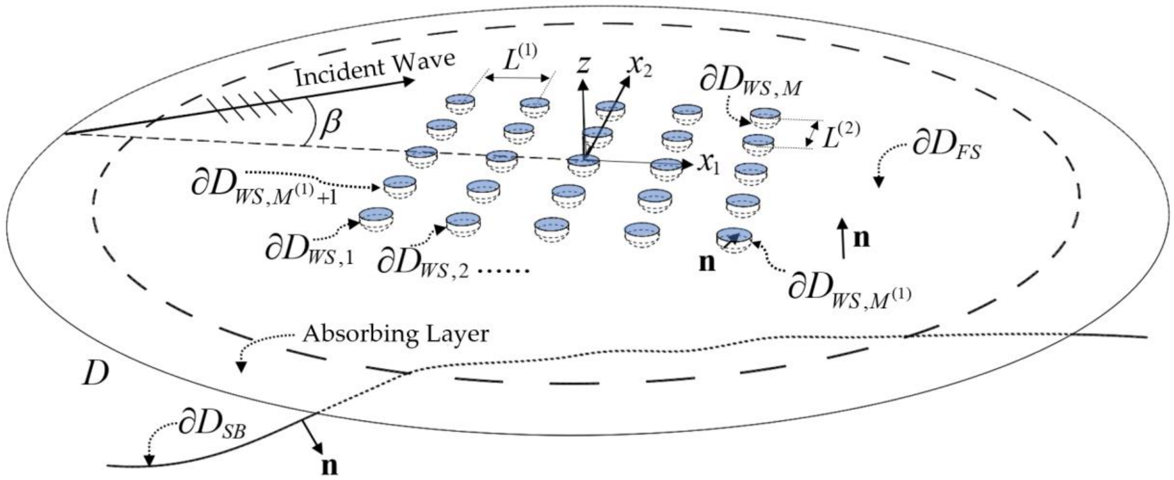

Figure 6-2. Sketch of a WEC park comprising twenty five $(M^{(1)}=M^{(2)}=5)$ floating devices, illustrating the flow Domain D and the parts of boundary ∂D, along with basic parameters.

A Cartesian coordinate system $\mathbf{x} = (\mathbf{x}_h, z) = (x_1, x_2, z)$ is defined, whose origin is placed at Still Water Level (SWL), so that the waterplanes of the whole array are symmetric with respect to the $x_1 z$ and $x_2 z$ planes (see Figure 6-2). The number of WECs in the x_1 and x_2–directions is $M^{(1)}$ and $M^{(2)}$, respectively (thus, $M = M^{(1)} M^{(2)}$). In the present work's context, the submerged volume of each WEC consists of a cylindrical buoy of radius a and draft T_C, supplemented by an oblate semi–spheroidal part, with semi–major axis equal to a and semi–minor axis equal to T_S (see Figure 6-2 and Figure 6-3), leading to a total draft of $T = T_C + T_S$. The unit vector, that is normal to the boundary ∂D and directed toward the exterior of D, is denoted by $\mathbf{n} = (n_1, n_2, n_3)$. The centers of two adjacent WECs' waterplanes are positioned $L^{(1)}$ apart in the x_1–direction and $L^{(2)}$ apart in the x_2–direction. Finally, the WEC numbering starts from the device, in the 3rd quadrant of the $z = 0$ plane, which is the farthest from the origin (see Figure 6-2). The numbering continues along the x_1–axis until the WEC $M^{(1)}$ and the next device is selected to be the one located in the next row of the park and whose waterplane's midpoint shares the same x_1–coordinate as the 1st device. The numbering is defined similarly until the M^{th} unit. Assuming that all time–dependent quantities oscillate harmonically in the form $\exp(-i\omega t)$, where ω denotes the angular frequency in (rad s^{-1}) and i is the imaginary unit, the problem is transferred to the frequency domain by employing the following representation,

$$\begin{aligned}\Phi(\mathbf{x};\beta,t) = \Phi_0(\mathbf{x};\beta,t) + \Phi_d(\mathbf{x};\beta,t) + \sum_{m=1}^{M} \frac{d\xi_m}{dt} \Phi_m(\mathbf{x};t) = \\ = \mathrm{Re}\left\{ -\frac{igH}{2\omega} \varphi(\mathbf{x};\beta) \cdot \exp(-i\omega t) \right\},\end{aligned} \tag{6.1}$$

where H stands for the incident wave height, g is the gravitational acceleration, ξ_m is the complex amplitude of the m^{th} device's response in heave, β is the angle of incidence with respect to the x_1–axis (see Figure 6-2) and $\varphi(\mathbf{x}, \beta)$ is the total complex potential, which comprises all the subfields and is defined in the frequency domain as,

$$\varphi(\mathbf{x};\beta) = -i\omega \left\{ \varphi_0(\mathbf{x};\beta) + \varphi_d(\mathbf{x};\beta) + \sum_{m=1}^{M} \xi_m \varphi_m(\mathbf{x}) \right\}. \tag{6.2}$$

In Eq. (6.2), $-i\omega\varphi_0(\mathbf{x}, \beta)$ and $-i\omega\varphi_d(\mathbf{x}, \beta)$, respectively, stand for complex amplitudes of the incident and the diffracted subfields. Finally, $\varphi_m(\mathbf{x}, \beta)$, $m = 1,2, \dots, M$ is the complex amplitude of the radiation field generated by a unit–amplitude heaving oscillation of the m^{th} WEC.

6.1.1. Formulation of the Incident Field

The potential function of the incident field $\Phi_0(\mathbf{x}; \beta, t)$ propagating over the seabed, is obtained by a consistent coupled mode model (CMS) [81], free of mild bottom slope assumptions, as extended for three–dimensional environments in Ref. [82]. In the general case, the incident potential is obtained by splitting the function that expresses the depth variation into two components: $h(\mathbf{x}_h) = h_I(x_1) + h_D(\mathbf{x}_h)$, where $h_I(x_1)$ is a parallel–contour bathymetry and $h_D(\mathbf{x}_h)$ denotes additional three–dimensional depth irregularities. The solution is accordingly split as $\varphi_0(\mathbf{x}; \beta) = \exp(ik_1 \sin(\beta)\, x_2)\, \varphi_I(x_1, z) + \varphi_D(\mathbf{x}; \beta)$. Within the scope of this work, considering that the isobaths are approximately parallel approaching the coastline, the depth function of the domain D is considered to exhibit a $1D$ variation – Figure 6-2 and Figure 6-4(b) of the form $h(\mathbf{x}_h) = h_I(x_1)$, connecting two regions of fixed but different depths, h_1 (incidence region) and h_3 (transmission region). The incident field is given by:

$$\varphi_0(\mathbf{x};\beta) = \exp\left(ik_1 \sin(\beta) x_2\right) \varphi_I(x_1, z), \tag{6.3}$$

where k_1 is the incident wavenumber at depth h_1, and β is the angle of incidence over the parallel contour bathymetry $h_I(x_1)$. Substituting Eq. (6.3) into the Laplace equation, the linear form of the free–surface boundary condition (BC) and the Neumann BC at the sea bottom, a corresponding BVP is formulated, for the unknown potential $\varphi_I(x_1, z)$, for the case of oblique–incident harmonic waves, which is supplemented by proper radiation conditions for the incidence and transmission regions [82]. This problem is solved utilizing a one–dimensional version of the CMS, where the potential $\varphi_I(x_1, z)$ accepts the local–mode representation,

$$\varphi_I(x_1, z) = \phi_{I,-1}(x_1) Z_{-1}(z; x_1) + \sum_{n=0}^{\infty} \phi_{I,n}(x_1) Z_n(z; x_1). \tag{6.4}$$

In the above expression, $\phi_{I,0}(x_1)Z_0(z;x_1)$ denotes the propagating mode, $\phi_{I,n}(x_1)Z_n(z;x_1), n \geq 1$ denote the evanescent modes, and the term $\phi_{I,-1}(x_1)Z_{-1}(z;x_1)$ is an additional term, referred to as the sloping–bottom mode, which is introduced to satisfy the homogeneous Neumann BC on the non–horizontal parts of the seabed. The eigenfunctions $Z_n, n \geq 0$, which are obtained by local vertical Sturm–Liouville problems formulated in the local vertical intervals $-h_I(x_1) \leq z \leq 0$, represent the local vertical structure of the n^{th} mode and are given by,

$$Z_n(z; x_1) = \cosh\left[k_n(x_1) \cdot \left(z + h_I(x_1)\right)\right] \cdot \left[\cosh\left(k_n(x_1) \cdot h_I(x_1)\right)\right]^{-1}, n \geq 0, \tag{6.5}$$

where the eigenvalues $k_n(x_1), n \geq 0$, involved in the above expression, are obtained as the roots of the local dispersion relations,

$$\omega^2 = k_n(x_1) g \tanh\left[k_n(x_1) h_I(x_1)\right], \ n \geq 0, \tag{6.6}$$

with $k_0(x_1)$ being the only real root and $k_n(x_1), n \geq 1$ being the infinite series of imaginary roots of Eq. (6.6). Utilizing the local–mode representation of Eq. (6.4), a coupled–mode system is formulated for the horizontal complex amplitudes $\phi_{I,n}(x_1), n \geq -1$ of the form,

$$\sum_{n=-1}^{\infty} \left\{ \begin{array}{c} a_{mn}(x_1) \dfrac{d^2 \phi_{I,n}(x_1)}{d{x_1}^2} + b_{mn}(x_1) \dfrac{d\phi_{I,n}(x_1)}{dx_1} + \\ + \left[c_{mn}(x_1) - a_{mn}(x_1) \left(k_1(x_1)\right)^2 \sin^2(\beta) \right] \phi_{I,n}(x_1) \end{array} \right\} = 0, \ m \geq -1, \tag{6.7}$$

where the definition of the coefficients $a_{mn,}$ b_{mn} and c_{mn} of the CMS is based on the vertical modes Z_n, which are spatially variable due to local depth dependence; see [82]. The system of Eq. (6.7) is supplemented by appropriate BCs, extracted by matching the unknown potential with the solutions at the two semi–infinite strips of depth h_1 and h_3, respectively. The sloping–bottom mode becomes important in cases of local topographies with steep sloping parts and considerably accelerates the convergence of the local–mode series, described by Eq. (6.4); with four to six terms in total being enough to assess the incident field in areas characterized by seabed slopes of more than 100%; see Refs. [81,82] for more details. In the special case where only

$\phi_{I,0}(x_1)Z_0(z;x_1)$ is kept in the expansion, the model reduces to the modified mild–slope equation (MMSE) derived by Massel [130] in 1993 and by Chamberlain and Porter [206] in 1995.

6.1.2. BEM Formulation for the Diffraction and Radiation Problems

Boundary value problems (BVPs), with the Laplace equation for the potential functions being the field equation, supplemented by suitable boundary conditions (BCs) at the different sections that make up the ∂D boundary of the domain, are numerically solved to evaluate the diffraction and radiation fields. The latter boundary, as illustrated in Figure 6-2, comprises the water free surface (∂D_{FS}) the wetted surface of each device ($\partial D_{WS,m}$, $m = 1, 2,\dots, M$) and the solid boundary of the seabed (∂D_{SB}). The mixed free surface boundary condition (FSBC) is used on (∂D_{FS}) and no–entrance BCs are used on the solid boundaries, resulting in the following BVPs,

$$\nabla^2\varphi_m(\mathbf{x}) = 0,\ \mathbf{x}\in D,\ m = d,1,2,\dots,M, \tag{6.8}$$

$$\frac{\partial\varphi_m(\mathbf{x})}{\partial n} - \mu(\mathbf{x}_h;\ \omega)\varphi_m(\mathbf{x}) = 0,\quad \mathbf{x}\in\partial D_{FS},\ m = d,1,2,\dots,M, \tag{6.9}$$

$$\frac{\partial\varphi_d(\mathbf{x})}{\partial n} = -\frac{\partial\varphi_0(\mathbf{x})}{\partial n},\quad \mathbf{x}\in\bigcup_{m=1}^{M}\partial D_{WS,m}, \tag{6.10}$$

$$\frac{\partial\varphi_m(\mathbf{x})}{\partial n} = \delta_{m\ell}\,n_3^{\ell}(\mathbf{x}),\ \mathbf{x}\in\partial D_{WS,\ell},\ m,\ell = 1,2,\dots,M, \tag{6.11}$$

$$\frac{\partial\varphi_m(\mathbf{x})}{\partial n} = 0,\quad \mathbf{x}\in\partial D_{SB}\ ,\ m = d,1,2,\dots,M. \tag{6.12}$$

In the above Equations, $\mathbf{n} = (n_1, n_2, n_3)$ denotes the unit normal vector on ∂D, directed toward the exterior of the domain (also shown in Figure 6-2). In Equation (6.11), $\delta_{m\ell}$ is the Kronecker delta. According to the latter equation, the m^{th} radiation field is evaluated by applying a BC which enforces a unitary heaving oscillation of the m^{th} WEC, while the rest of the devices are treated as being fixed at their mean position. The frequency parameter $\mu = \omega^2/g$ involved in the FSBC [Eq. (6.9)], is expressed as a function of the horizontal position $\mathbf{x}_h$, to account for modifications concerning the application of appropriate radiation conditions at infinity. Specifically, the wave fields computed as solutions to the above BVPs propagate undisturbed in directions $\theta = \tan^{-1}(x_2/x_1) \in [0, 2\pi)$, which implies that the flow domain extends infinitely. A perfectly matched layer (PML) technique (see Figure 6-2) is utilized to truncate the computational domain. The PML consists of an absorbing layer that is used to artificially weaken and ultimately zero–out the outgoing wave solutions, treating their radiating behaviour at far distances from the WEC park; see also Ref. [155].

The layer's thickness, which must be of the order of one local wavelength [155], determines the solution damping efficiency and the elimination of numerical reflections. In this work's context, the layer thickness is selected to be equal to one mean wavelength $\bar{\lambda} = 2\pi/\overline{k_0}$, amplified by a factor of 15% to account for longer wavelengths at the deeper regions of the domain. $\overline{k_0}$ denotes the real root of the dispersion relation, as defined at the mean depth ($\bar{h}$) of the area spanned by the WEC array. It is noted that the absorbing layer with the above characteristics was found to provide sufficient solution damping at the deeper regions of the domain for the local topography studied in this work, which is analyzed in the sequel, as well as the studied frequency range. However, the layer thickness might need readjustment for lower frequencies and for areas with greater depth changes between deep and shallow regions. The PML technique is implemented by introducing an imaginary component to the frequency parameter μ in the layer,

$$\mu(\mathbf{x};\omega)=\begin{cases}\omega^2 g^{-1}, & |\mathbf{x}|<R_{PML},\\ \omega^2 g^{-1}\left(1+ic\dfrac{\left(|\mathbf{x}|-R_{PML}\right)^n}{\bar{\lambda}^n}\right)^2, & |\mathbf{x}|\geq R_{PML},\end{cases} \tag{6.13}$$

where R_{PML} denotes the PML activation radius (see Figure 6-2). Optimum values of the parameters c and n, involved in Eq. (6.13), are selected (see Ref. [155]) to increase the efficiency of the layer, with regard to the minimization of numerical reflections in the assessed solutions.

A low–order Boundary Element Method (BEM) scheme is developed to numerically solve the BVPs, described by Eqs. (6.8)–(6.13). The method involves simple singularity distributions on 4–node quadrilateral elements, while continuity of the geometry is ensured on the boundary parts and the junctions between them. The functions $\varphi_m, m=d,1,2,\dots.M$, are represented by the boundary integral,

$$\varphi_m(\mathbf{x})=\int_{\partial D}\sigma^{(m)}(\mathbf{x}')\,\mathbf{n}\nabla G(\mathbf{x}'|\mathbf{x})\,ds(\mathbf{x}'),\quad \mathbf{x}\in D,\ \mathbf{x}'\in\partial D,\ m=d,1,2,\dots M, \tag{6.14}$$

where $G(\mathbf{x}',\mathbf{x})=|\mathbf{x}'-\mathbf{x}|^{-1}/4\pi$ is the Green's function for the Laplace equation in three dimensions and $\sigma^{(m)}(\mathbf{x}'), m=d,1,2,..,M$, are discrete (dipole) strength distributions, defined on the panels that make up the boundary ∂D. The latter strength distributions are obtained by the BEM, given that they are defined as piecewise constant. The distributions $\sigma^{(m)}$, combined with a discrete form of the integral representation [Eq. (6.14)], define the involved subfields $\varphi_m, m=d,1,2,\dots.M$. In particular, the potential functions φ_m and the velocity fields $\nabla\varphi_m$ are approximated by,

$$\varphi_m(\mathbf{x})=\sum_p \sigma_p^{(m)}\Phi_p(\mathbf{x}),\quad \nabla\varphi_m(\mathbf{x})=\sum_p \sigma_p^{(m)}\mathbf{U}_p(\mathbf{x}),\ m=d,1,2,\dots,M, \tag{6.15}$$

where the summation index (p) covers all of the panels that model ∂D and $\sigma_p^{(m)}$ is the strength of the singularity distribution, corresponding to the m^{th} subfield, on the p^{th} panel which is, in general, complex due to the non–zero imaginary part of the frequency parameter in the PML region. The induced quantities (potential and velocity) by the p^{th} element (carrying unitary distributed dipole singularity) to the point **x** in the field are, respectively, denoted by Φ_p and $\mathbf{U}_p$; see e.g., Ref. [136]. Numerical solutions are obtained by satisfying each BC at the centroids of the panels distributed across the various boundary sections, using a collocation technique. Constant normal dipole distributions are used on the panels and thus induced potential is analytically available using the solid angle; see Ref. [156]. Furthermore, induced velocity can be computed by the repetitive application of the Biot–Savart law, exploiting the equivalence of a constant dipole element to a vortex ring [156]; (refer to Appendix C for more details).

6.1.3. Mesh Generation and Evaluation of Power Output

The mesh is generated by combining matching structured meshes of the distinct boundary surfaces, ensuring continuous junctions between the different segments which, in conjunction with the 4–node panels, results in global continuity of the discretized boundary (refer to Appendix B). More specifically, the mesh of a WEC's wetted surface consists of a part that models the lateral surface of the submerged volume's cylindrical part, supplemented by a mesh of the oblate semi–spheroidal part, defined in local spherical coordinates. Furthermore, the free surface in the vicinity of each WEC is modelled by a rectangular block of dimensions $L^{(1)}$ and $L^{(2)}$, in the x_1 and x_2–directions, respectively, centered at the WEC waterplane's midpoint. The block is discretized by a radial mesh, using gradually increasing resolution while approaching the wetted surface, for obtaining better quality results. An indicative boundary mesh of a WEC, along with the corresponding free surface block mesh, is illustrated in Figure 6-3(a). The computational mesh shown in Figure 6-3(a) is replicated M times to produce the mesh of the whole WEC park, as depicted in Figure 6-3(b), for the case $M^{(1)} = M^{(2)} = 2$. Subsequently, a radial mesh is constructed around the WEC park, modelling the remainder of the free surface boundary, extending to a certain number of mean wavelengths ($\bar{\lambda}$) and thus, the total radius of the mesh as well as the activation radius of the PML are frequency–dependent. It is noted that the nodes distributed in the azimuthal direction are doubled at a specific radius, as shown in Figure 6-3(b), in order to maintain a predefined minimum of elements per wavelength (15–20) in both the angular and radial directions, at the outer part of the free surface mesh. The (x_1, x_2) coordinates of the seabed mesh in the area spanned by the park are defined by a simple rectangular mesh, while the rest of the seabed boundary mesh is defined similarly to that of the free surface. The z–coordinate can be used to model any arbitrary seabed topography.

After obtaining all of the involved subfields, the complex amplitudes of the devices' response in heave ($\xi_m, m = 1,2,\dots,M$) are obtained as solution to the following linear system,

$$\left[-\omega^2\left(\mathbf{M}+\mathbf{A}(\omega)\right)-i\omega\left(\mathbf{B}(\omega)+\mathbf{B}_{\mathrm{PTO}}\right)+\left(\mathbf{C}+\mathbf{C}_{\mathrm{PTO}}\right)\right]\cdot\boldsymbol{\xi} = \mathbf{F}_0(\omega,\beta)+\mathbf{F}_d(\omega,\beta). \tag{6.16}$$

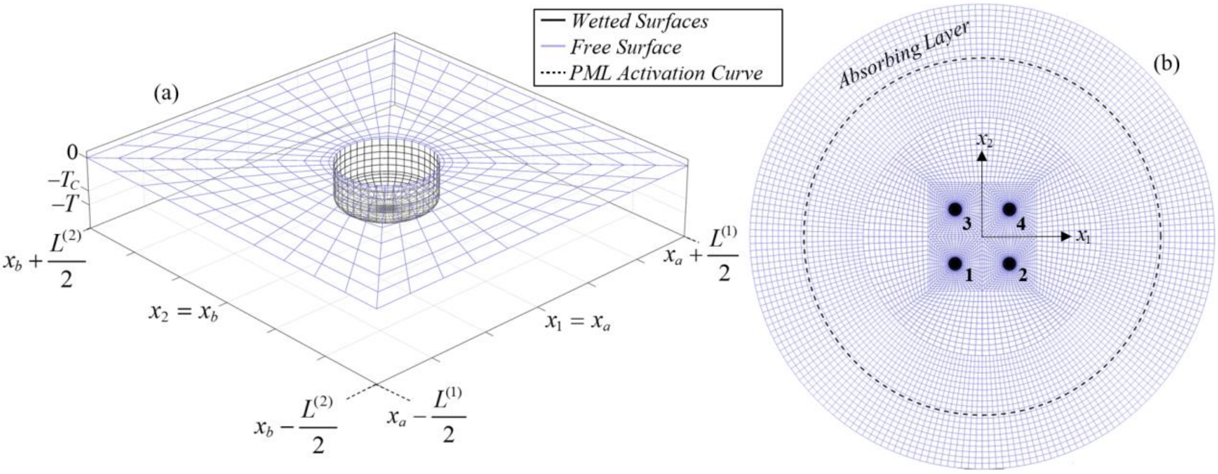

Figure 6-3. (**a**) Indicative mesh of a WEC's wetted surface, along with the corresponding free surface block's mesh. (**b**) Mesh of a WEC park comprising 4 devices (top view), illustrating the WEC numbering and the PML activation curve.

In Eq. (6.16), the diagonal matrix $\mathbf{M} = M\mathbf{I}$ models the inertia of the heaving point absorbers, with $\mathbf{I}$ being the identity matrix, $M = \rho\pi a^2(T_C + 2T_S/3)$ being the mass of each device and ρ being the density of the water. Furthermore, hydrostatic restoring forces are represented in Eq. (6.16) by the matrix $\mathbf{C} = c_{33}\mathbf{I}$, where $c_{33} = \rho g\pi\alpha^2$ is the hydrostatic restoring coefficient in heave. The energy extraction by the power–take–off (PTO) system is modelled by a damping coefficient, denoted in Eq. (6.16) by the diagonal matrix $\mathbf{B}_{\text{PTO}} = B_{PTO}\,\mathbf{I}$, and $\mathbf{C}_{\text{PTO}} = C_{PTO}\,\mathbf{I}$ is the PTO system stiffness. The added mass is modelled by an $M \times M$ matrix, whose elements $A_{m,\ell}\,(\omega)$ are defined, for a given frequency, by the component of the radiation force, induced by the ℓ^{th} radiation field on the m^{th} WEC, that is in phase with the acceleration, while the corresponding elements $B_{m,\ell}\,(\omega)$ of the $M \times M$ hydrodynamic damping matrix are evaluated by the component in phase with the velocity. The aforementioned force is computed via integration of the pressure induced by the ℓ^{th} radiation field on the m^{th} wetted surface, multiplied by the n_3 (vertical) component of the normal vector,

$$\omega^2 A_{m\ell} + i\omega B_{m\ell} = i\omega\rho \int\limits_{\partial D(WS,m)} \varphi_\ell(\mathbf{x})\cdot n_3(\mathbf{x})\,dS(\mathbf{x}), \mathbf{x}\in\partial D_{WS,m},\ m,\ell = 1,2,..,M. \qquad (6.17)$$

Furthermore, the pressure induced by the incident and the diffracted subfields, in conjunction with the vertical component of $\mathbf{n}$, is integrated on each wetted surface to determine the Froude–Krylov and the diffraction excitation forces on each WEC,

$$F_{m,\ell} = i\omega\rho \int\limits_{\partial D_{WS,m}} \varphi_\ell(\mathbf{x};\beta)\cdot n_3(\mathbf{x})\,ds(\mathbf{x}), \mathbf{x}\in\partial D_{WS,m},\ m = 1,2,....,M,\ \ell = 0,d. \qquad (6.18)$$

The mean power output by each device is subsequently defined as,

$$P_{OUT,m}(\omega,\beta;B_{PTO},C_{PTO}) = \frac{1}{2}\omega^2 B_{PTO}\left|\xi_m\right|^2, \text{ where } \xi_m = \xi_m(\omega,\beta;B_{PTO},C_{PTO}), \qquad (6.19)$$

assuming there are no losses due to the PTO system. The normalized power $\bar{P}_m$, which is evaluated taking into account the intra–array interactions as well as the local bathymetry, is defined by dividing the mean power output with the incident power flux over a cross section equal to each device's waterline diameter, evaluated at the depth of the deep region (region of incidence). The latter incident power flux is used since, in the general case, the wave amplitudes and wave numbers at the vicinity of each WEC differ due to depth variations. Considering an incident wave of height $H = 2A$ at the region of incidence, $\bar{P}_m$ equals,

$$\bar{P}_m(\omega,\beta;B_{PTO},C_{PTO}) = \frac{P_{OUT,m}(\omega,\beta;B_{PTO},C_{PTO})}{0.25\ \rho g H^2 C_g(h_1,\omega)\ a}, \qquad (6.20)$$

where $C_g(h_1,\omega)$ denotes the group velocity, calculated at the incidence region's depth.

6.2. *Case Study in the Eastern Aegean region*

In the present section, the model presented in §6.1 is implemented to simulate the operation of a WEC park consisting of twenty five (25) devices, placed in a 5 × 5 arrangement, (see Figure 6-1), operating at the north coast of the island of Ikaria, located in the Eastern Aegean Sea region, where the wave energy potential is relatively increased [57].

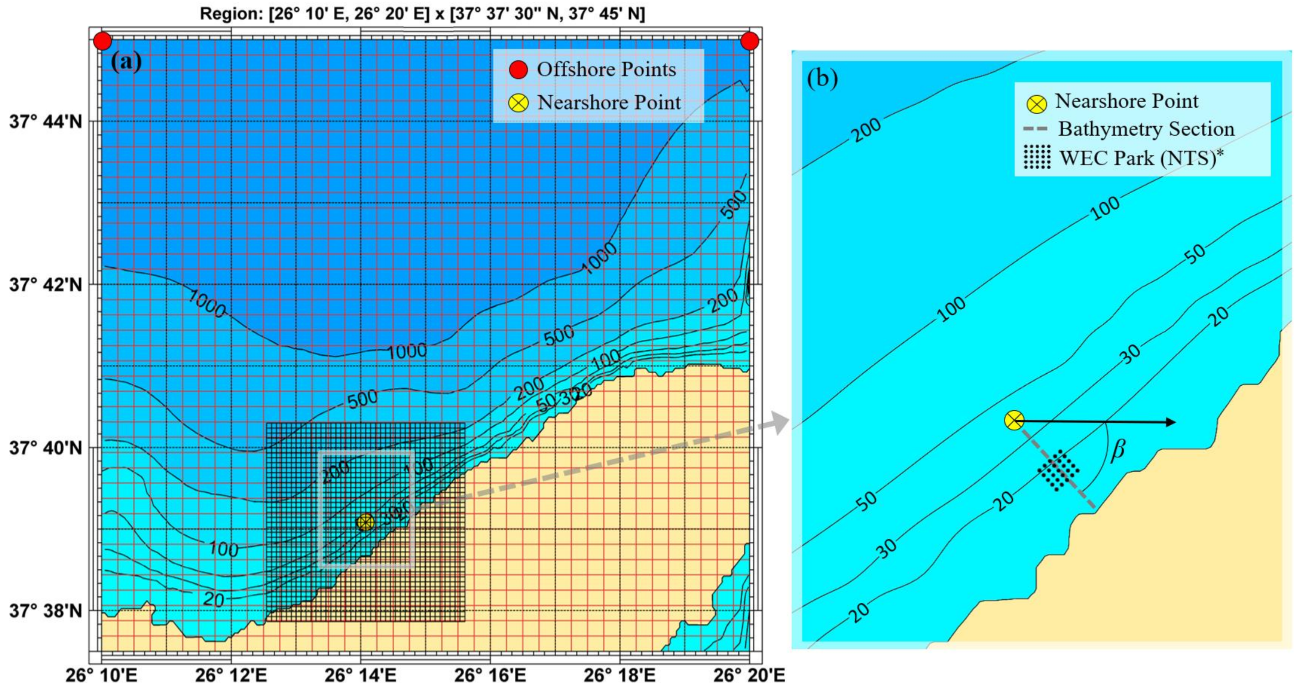

Figure 6-4. (**a**) Computational grid for the application of SWAN and (**b**) local bathymetry at the north coast of Ikaria Island, indicating the considered WEC park position and the section that defines the local bathymetry of the BEM–CMS model (* not to scale).

The wave climatology in the region is derived by a 10–year–long time series, which is obtained from the ERA5 database [149] and covers the period between the years 2013 and 2022, at the offshore points 37°45′ N, 26°10′ E and 37°45′ N, 26°20′ E; see Figure 6-4(a). The dataset includes significant wave height (H_S) and mean energy period (T_{-10}), along with mean wave direction ($\theta_m -$ measured clockwise from North), recorded at 3–hour intervals. Nearshore wave parameters at the target point 37°39′05″N, 26°14′05″E, are obtained by an offshore–to–nearshore (OtN) transformation, which utilizes the SWAN spectral model as described in Ref. [150]. The local depth at the target point is 40 m, (see Figure 6-4), which is also the maximum depth (h_1) used in the BEM–CMS model for the region of incidence; see Eq. (6.20). Known offshore conditions, defined by the parameters (H_S, T_{-10}, θ_m), at the seaward boundary are used to reconstruct directional spectra $S(f,\theta)$ using the JONSWAP spectrum in conjunction with a hyperbolic type spreading function, as analyzed in detail in Section 3.4.4 of Ref. [207].

The bathymetry used for the OtN, is obtained from GEBCO [208] and the coastline data have been extracted from the GMT–GSHHS database; see [162]. Considering that the isobath lines are approximately parallel approaching the coastline, the depth profile of the domain D is defined by a 1D section of the local bathymetry, parallel to the x_1–axis of the BEM–CMS model; see Figure 6-2 and Figure 6-4(b). Distributed offshore conditions on the seaward boundary are the main forcing of the system. The phase–averaged model SWAN is used, based on the offshore data, to assess the wave parameters within the computational grid, using adequate spatial resolution, as illustrated in Figure 6-4. The main equation applied in the SWAN model is the radiative transfer equation [209],

$$\frac{\partial}{\partial t}N+\frac{\partial}{\partial x}c_{x1}N+\frac{\partial}{\partial y}c_{x2}N+\frac{\partial}{\partial \omega}c_{\omega}N+\frac{\partial}{\partial \theta}c_{\theta}N=\frac{F}{\omega}, \tag{6.21}$$

which expresses action balance, with $N = N(\omega, \theta; x_1, x_2, t) = S(\omega, \theta; x_1, x_2, t)/\omega$ representing the wave action density, defined in terms of spectral density S and frequency ω. The components c_{x1}, c_{x2} denote propagation velocity in the physical space, while c_ω, c_θ denote corresponding components in the Fourier space. Furthermore, F represents the source terms, encompassing factors such as wind–generated wave growth, wave breaking–induced dissipation in both deep and shallow waters, and bottom friction. More details can be found in Ref. [209].

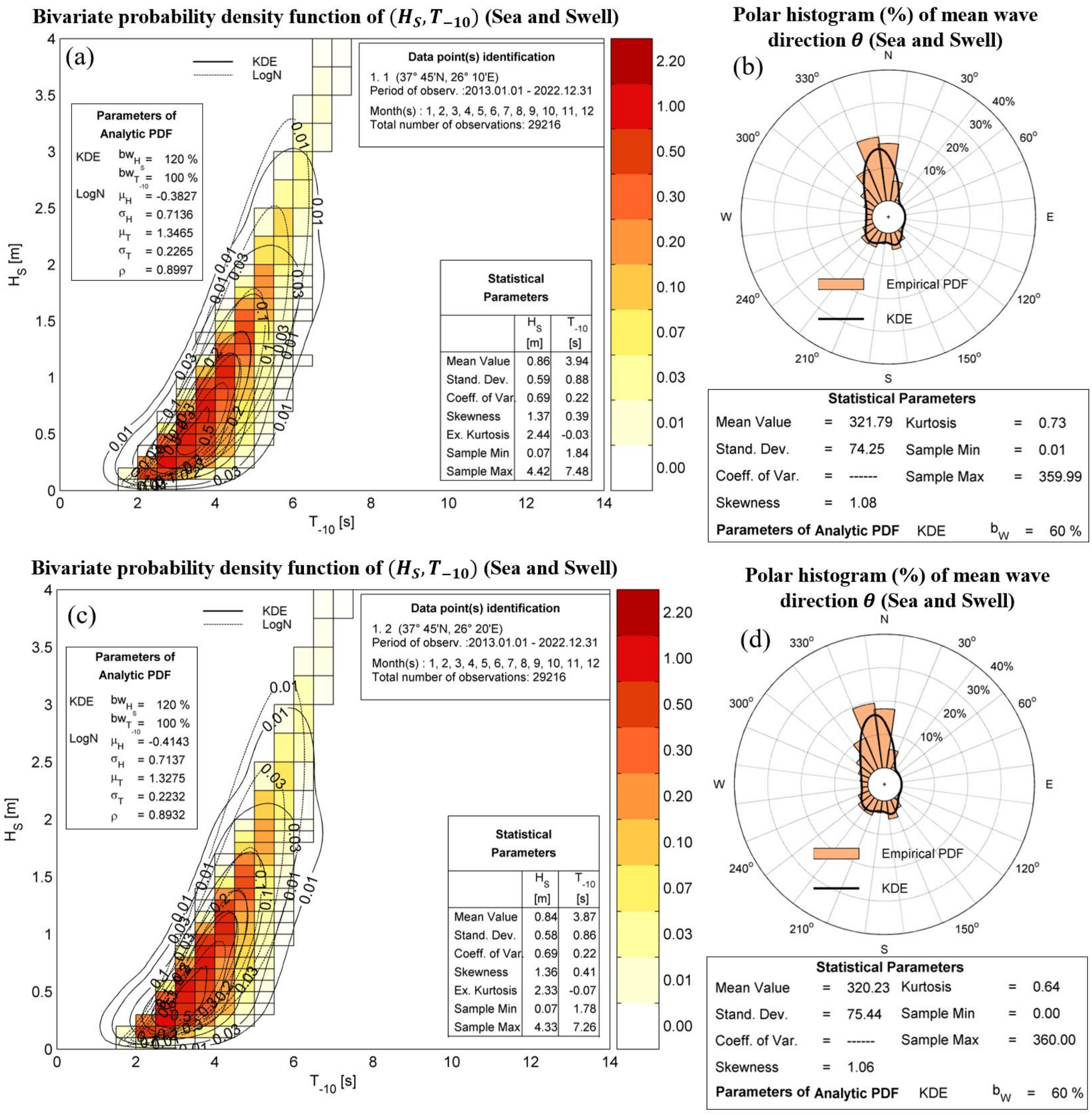

Figure 6-5. Wave climatology at the offshore points (**a**, **b**) 37°45′ N, 26°10′ E and (**c**, **d**) 37°45′ N, 26°20′ E. (**a**, **c**) $H_S - T_{-10}$ statistics and (**b**, **d**) corresponding polar histograms.

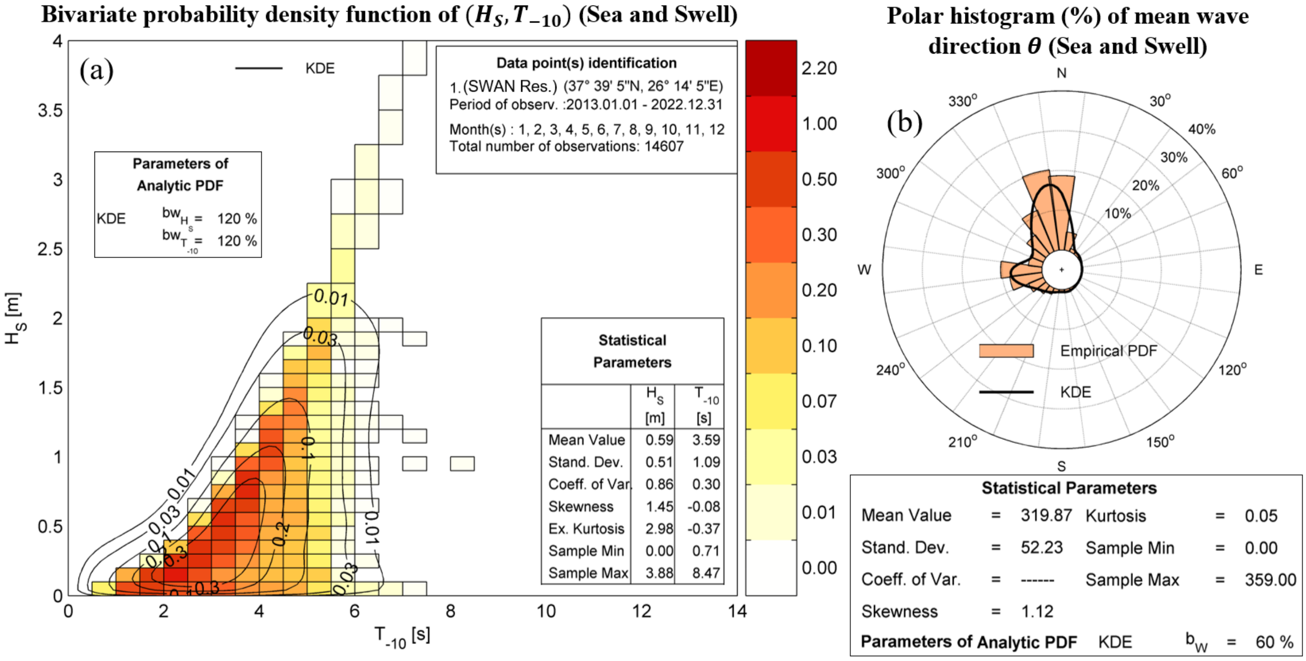

Figure 6-6. Wave data at the target point with geographical coordinates 37°39′05″ N, 26°14′05″ E and depth $h = 40$ m. (**a**) $H_S - T_{-10}$ statistics and (**b**) corresponding polar histogram.

A detailed discussion of the OtN transformation can be found in Ref. [163]. The offshore wave climatology at the two offshore points is depicted in Figure 6-5, where the distributions are represented using standard lognormal and Kernel Density Estimation (KDE) models. The corresponding nearshore wave climatology is illustrated in Figure 6-6.

6.2.1. Application of the BEM–CMS Model

In order to efficiently implement the proposed BEM–CMS model, a parallel code was developed using MATLAB R2023a, for calculating the wave fields and the responses of the WEC array for a given frequency and the direction of incidence. The acquisition of the results presented and discussed in the sequel, for the studied ranges of frequencies and incidence directions, required a computing time of the order of 72 hours on a workstation equipped with 192 GB RAM and two Intel Xeon Gold 6230R CPUs with 26 cores each. The studied frequency range corresponds to periods up to 10 s and the wavelength at the mean depth of the area spanned by the WEC array ($\bar{h} \approx 10.3$ m), ranges from 7.6 m to 93.3 m. The total number of quadrilateral elements used for the computational mesh corresponding to the lowest frequency is 53,520, of which 21,600 on the twenty five wetted surfaces, 19,920 on the free surface and the rest on the seabed boundary. For higher frequencies, although the mesh radius decreases, maintaining a minimum number of elements per wavelength on the boundary of the free surface requires finer discretization, due to the constant spacing between the devices. For the case of the minimum wave period, the model used 63,740 elements, maintaining the size of the BEM influence matrix below 61 GB to meet memory limitations.

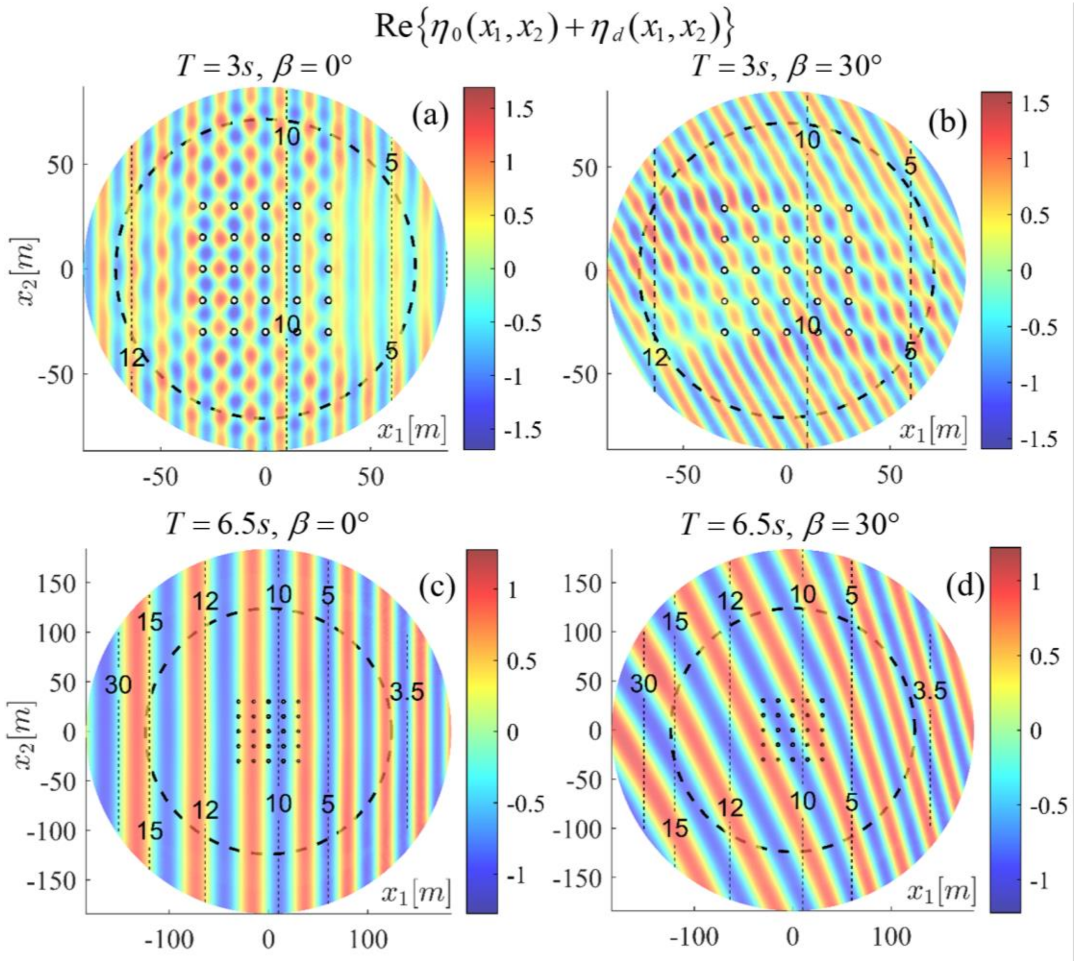

Figure 6-7. Superposition of the incident and the diffracted subfields. Incident wave period (**a**, **b**) $T = 3$ s, (**c**, **d**) $T = 6.5$ s. Angle of incidence (**a**, **c**) $\beta = 0°$, (**b**, **d**) $\beta = 30°$. Dashed lines represent isobaths. The bold dashed line denotes the PML activation curve.

Figure 6-7 illustrates the real part of the propagating field (comprising the incident and the diffracted subfields), for the array of 25 WECs of radius $a = 1.5$ m, with total draft $T = a$ and $T_C = 0.8a$, placed in a 5×5 arrangement with $L^{(1)} = L^{(2)} = 10a$. The origin of the coordinate system of the BEM–CMS model is located 190 m away from the coastline and the local depth at $x_1 = x_2 = 0$ is 10.5 m. All subsequent results in the present chapter refer to the above setup.

The color plots in Figure 6-7 provide detailed illustrations of the potential on the free surface, scaled by the factor $(i\omega/g)$ so that it represents the free surface elevation, denoted as $\eta(x_1, x_2)$. Figure 6-8 shows the real part of the free surface elevation corresponding to indicative radiation fields generated by the WECs 1 and 13. Upon examination of the results, it is evident that at lower frequencies [refer to Figure 6-7(c, d) and Figure 6-8(c, d)], the interaction of the fields with the variable bathymetry becomes significant. Conversely, for higher frequencies [refer to Figure 6-7(a, b) and Figure 6-8(a, b)] the floating devices exert a more considerable effect on both the propagating and the radiated fields, and thus the effect of intra–array interactions is more noticeable.

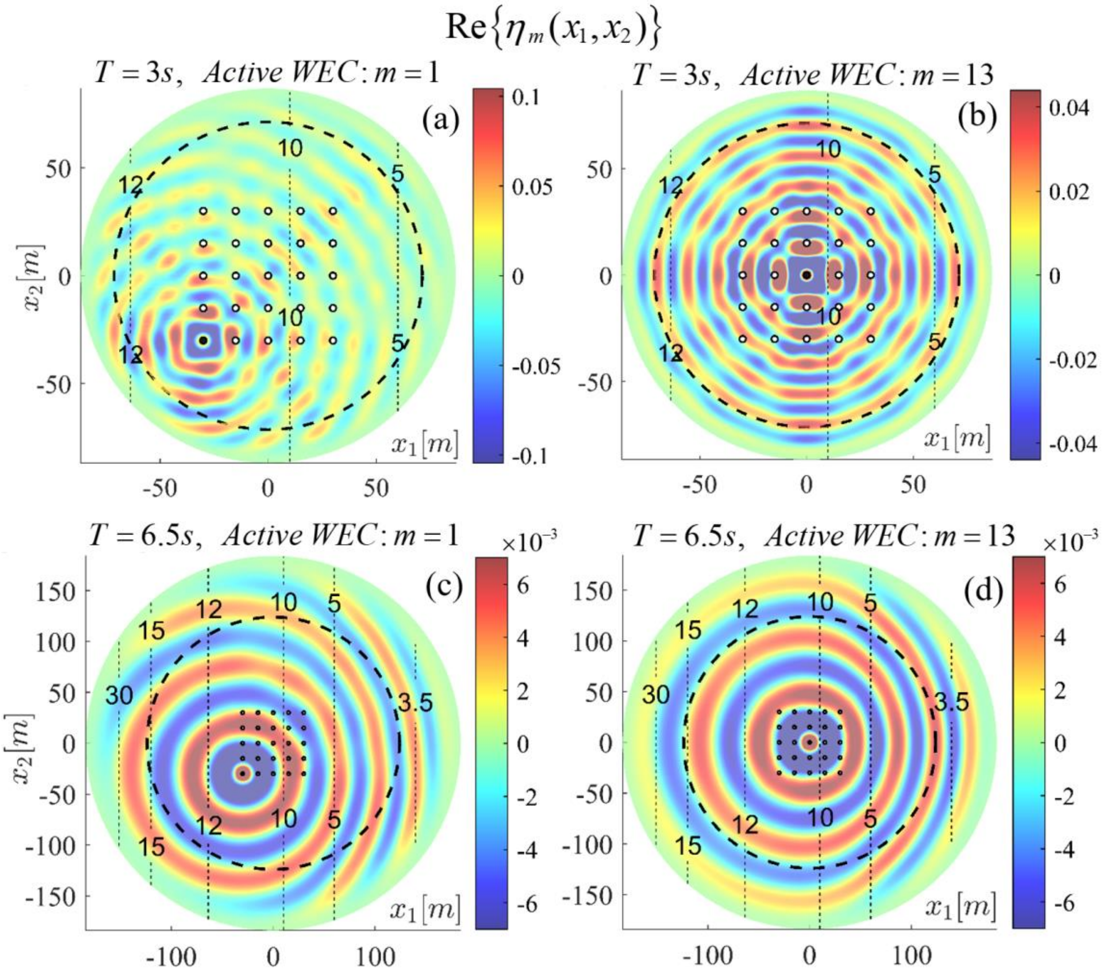

Figure 6-8. Radiation fields by the WECs (**a**, **c**) 1 and (**b**, **d**)13. Oscillation period (**a**, **b**) $T = 3$ s, (**c**, **d**) $T = 6.5$ s (equal to incident wave period). Dashed lines represent isobaths. The bold dashed line denotes the PML activation curve.

Furthermore, a notable reduction in the local wavelength is evident in Figure 6-7(c). This reduction is attributed to the decrease in phase velocity, which occurs as a result of the interaction between the wave field and the shoaling bathymetry. In the wave field shown in Figure 6-7(d), the decrease in phase velocity also leads to wave refraction. Due to oblique wave incidence, it can be observed that the wavefronts tend to align with the isobath lines, illustrating the influence of bathymetric variations on wave behaviour.

Figure 6-9 illustrates added mass contributions on WECs 1, 5, 13 and 25. For comparison purposes, the normalized added mass of an individual (isolated) WEC operating at the same region and located at $x_1 = x_2 = 0$ (position of WEC 13 in the array), is also plotted. The elements of the added mass matrix are normalized using the mass of a WEC with the considered submerged volume, which equals 9.89 m^3. Approximately 85.8% of this volume corresponds to the cylindrical part of the WEC's geometry and 14.2% corresponds to the oblate semi–spheroidal part with semi–major axis equal to a and semi–minor axis equal to $T_S = 0.2a$ $(= T - T_C)$.

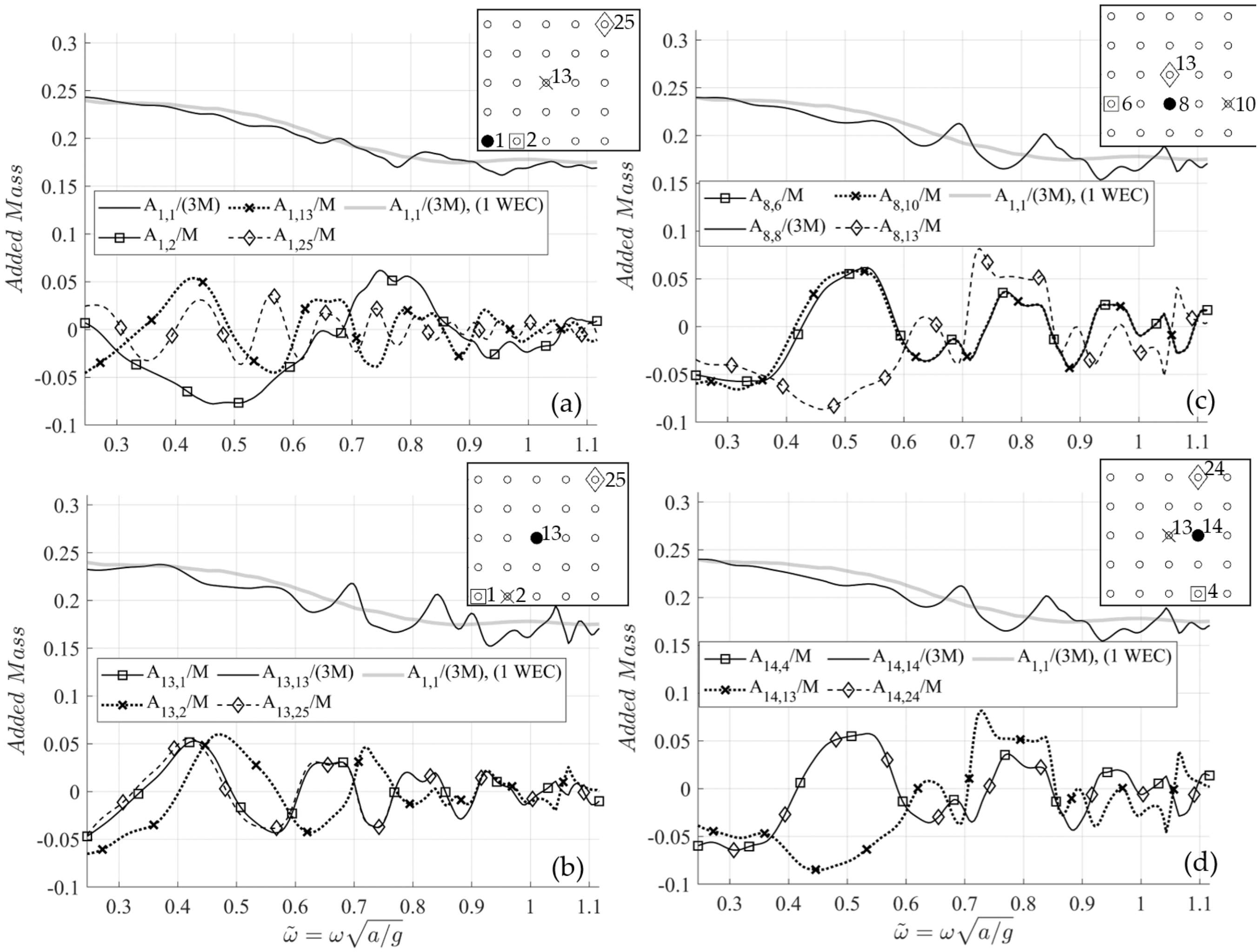

Figure 6-9. Normalized added mass contributions on WECs (**a**) 1, (**b**) 5, (**c**) 8 and (**d**) 14. The normalized added mass of an isolated WEC operating at the same region and located at $x_1 = x_2 = 0$ (position of WEC 13 in the array), is also plotted for comparison. Relative position of the WECs is illustrated in the auxiliary legend.

As it can be seen in Figure 6-9(b), the elements $A_{13,1}$ and $A_{13,25}$ of the added mass matrix present almost identical behaviour due to the symmetry of the relevant position of the corresponding devices on the x_1x_2–plane. However, minor differences are observed at the low frequency range, which are triggered by the seabed profile variations. This effect is also evident in Figure 6-9(c), as regards the added mass contributions of the WECs 6 and 10 on WEC 8. On the other hand, the elements $A_{14,4}$ and $A_{14,24}$ of the added mass matrix behave identically [refer to Figure 6-9(d)], since not only are the relevant positions of these devices symmetric on the x_1x_2–plane, but also the devices 4 and 24 are located over the same isobath line.

Corresponding results concerning the hydrodynamic damping are illustrated in Figure 6-10. The hydrodynamic damping data have been made non–dimensional by normalization with respect to the product of the mass of a WEC and the angular frequency. The bathymetry induced effects are also observable in the hydrodynamic damping data.

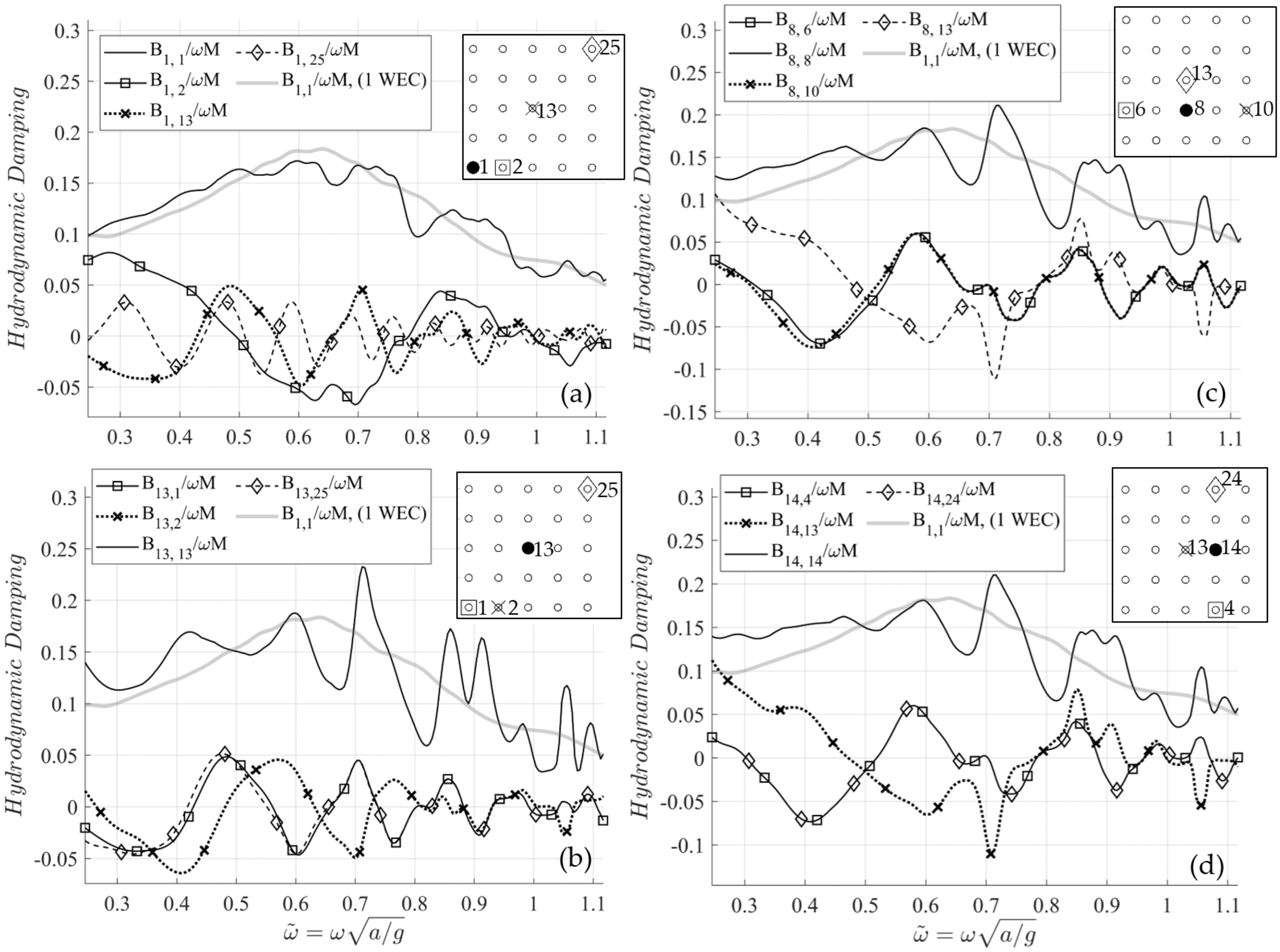

Figure 6-10. Normalized hydrodynamic damping contributions on WECs (**a**) 1, (**b**) 13, (**c**) 8 and (**d**) 14. The normalized damping of an isolated WEC operating at the same region and located at $x_1 = x_2 = 0$ (position of WEC 13 in the array), is also plotted for comparison. Relative position of the WECs is illustrated in the auxiliary legend.

Non–dimensional forces acting on WECs 1, 5, 13 and 25 (normalized by $\rho g \pi A \alpha^2$, where A is the amplitude of the incident field at the region of incidence), are shown in Figure 6-11, for wave incidence normal to the depth contours ($\beta = 0°$), and for $\beta = 30°$. The figure shows both the Froude–Krylov (FK) and diffraction forces. Corresponding results concerning an individual (isolated) WEC operating at the same region and located at $x_1 = x_2 = 0$ (position of WEC 13 in the array), are also shown for comparison. It can be observed that the FK forces acting on WEC 13 exactly match those acting on the isolated device, while the FK forces on the other WECs present minor differences, depending on the local depth where they are located. The diffraction forces present more complicated patterns due to intra–array interactions. As it can be seen in Figure 6-11(c), the diffraction forces acting on the WECs 5 and 25 are identical in the case of wave propagation normal to the depth contours, due to symmetry. This applies to any two devices positioned symmetrically, with respect to the $x_2 = 0$ plane for $\beta = 0°$.

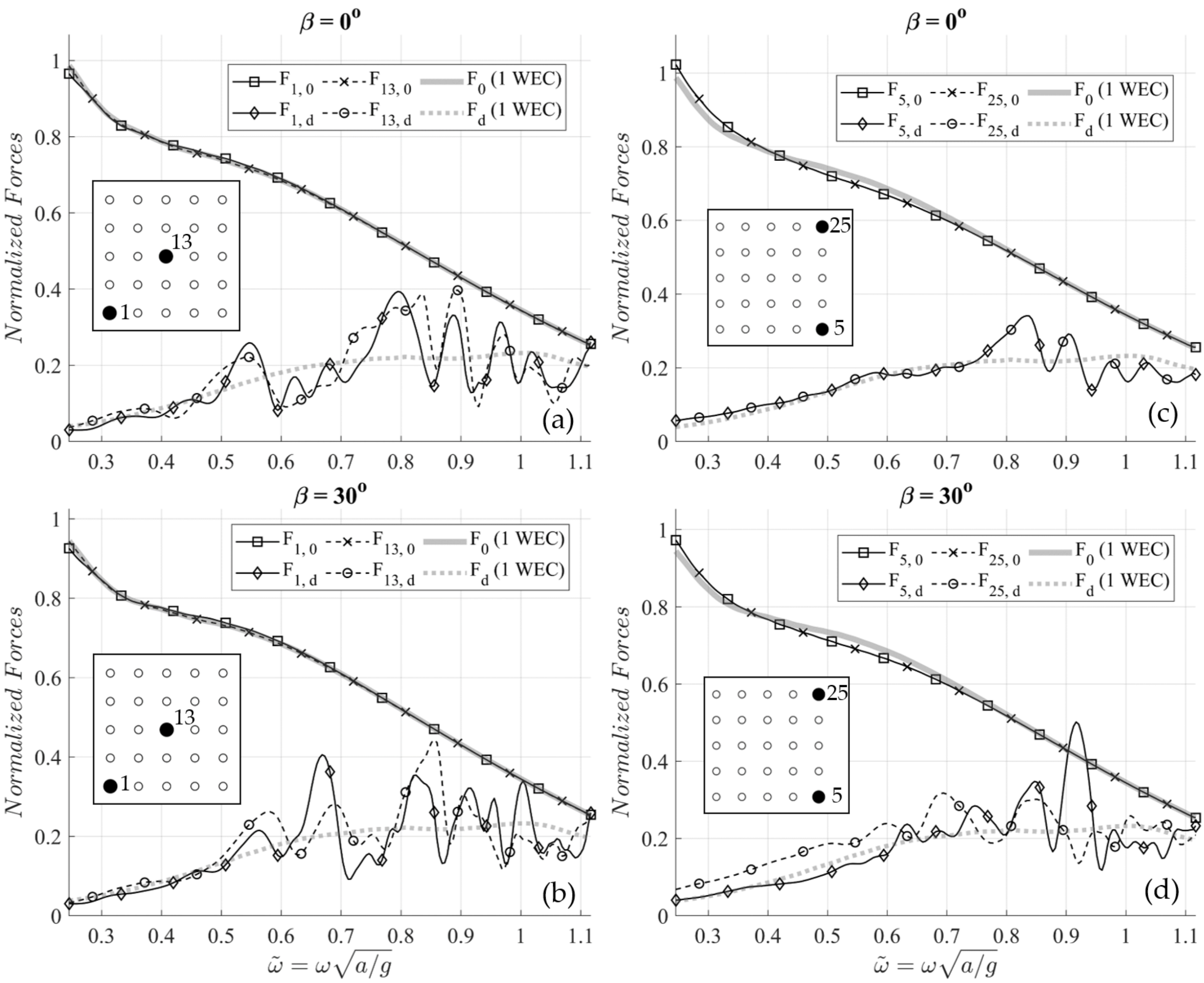

Figure 6-11. Normalized Froude–Krylov and diffraction forces on WECs (**a**, **b**) 1 and 13, (**b**, **d**) 5 and 25. Propagation direction (**a**, **c**) $\beta = 0°$ and (**b**, **d**) $\beta = 30°$. The normalized Froude–Krylov and diffraction forces acting on an individual WEC operating at the same region and located at $x_1 = x_2 = 0$ (position of WEC 13 in the array), are also plotted for comparison. Relative position of the WECs is illustrated in the auxiliary legend.

Response amplitude operators (RAOs) of the WECs 1, 13 and 25 are illustrated in Figure 6-12, as computed by Eq. (6.16) for $\beta = [0°, 15°, 30°]$. The PTO stiffness is set to 10% of the hydrostatic restoring coefficient ($C_{PTO} = 0.1\rho g \pi \alpha^2$), corresponding to magnitudes used in the literature [210] and the PTO damping is defined as $B_{PTO} = jB_{av.}^{(1\,WEC)}$, where $B_{av.}^{(1\,WEC)}$ is the mean hydrodynamic damping of an individual (isolated) WEC, operating in the under–study region (see Figure 6-10 – gray lines), and j is a multiplying factor. Based on the above, the PTO damping parameter is approximately equal to $2\,j$ kN/s. Corresponding results concerning the isolated WEC are also shown for comparison.

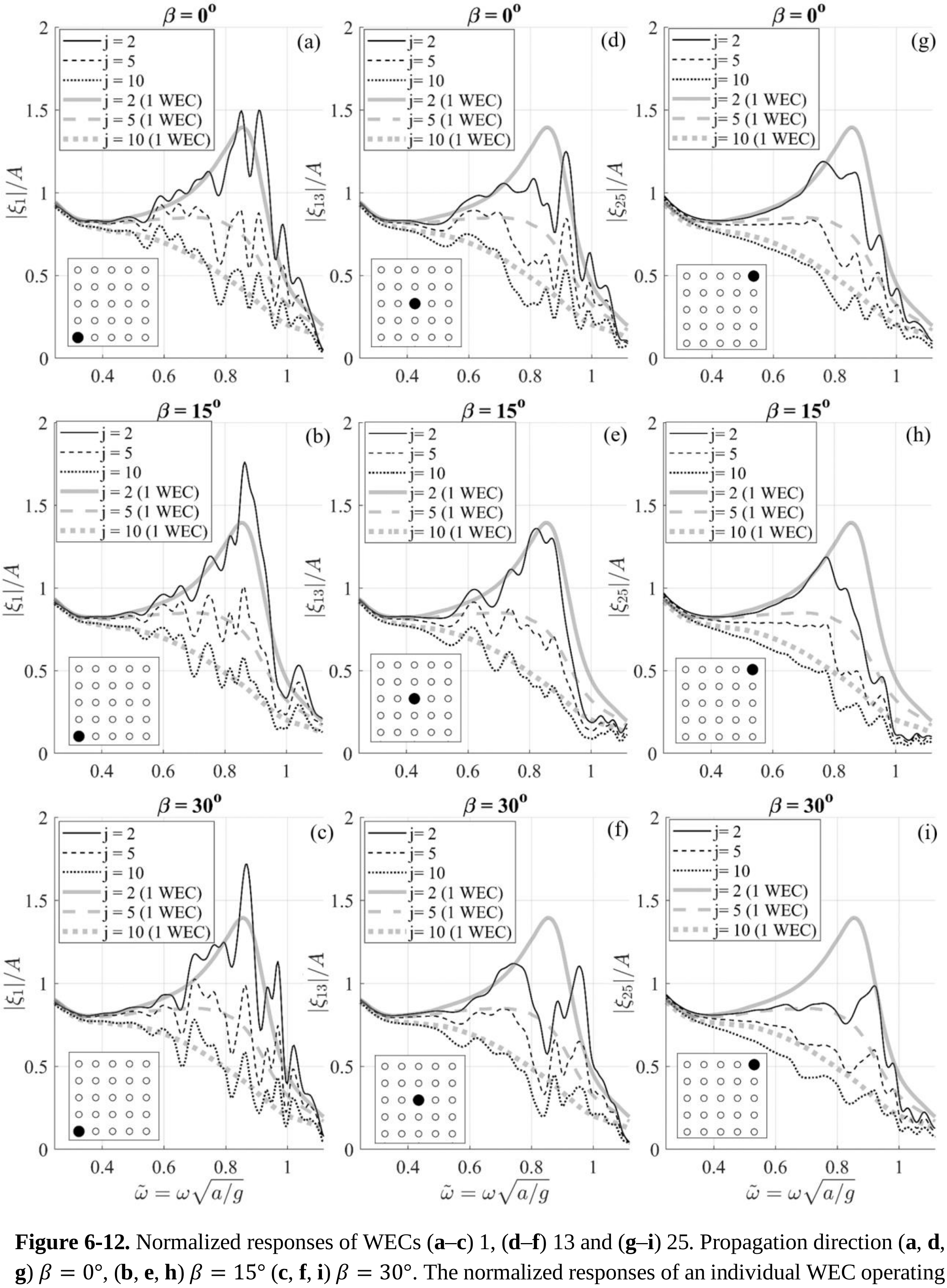

Figure 6-12. Normalized responses of WECs (**a**–**c**) 1, (**d**–**f**) 13 and (**g**–**i**) 25. Propagation direction (**a**, **d**, **g**) $\beta = 0°$, (**b**, **e**, **h**) $\beta = 15°$ (**c**, **f**, **i**) $\beta = 30°$. The normalized responses of an individual WEC operating at the same region and located at $x_1 = x_2 = 0$ (position of WEC 13 in the array) are also plotted for comparison. The relative position of the WECs is illustrated in the auxiliary legend. $C_{PTO} = 0.1\rho g \pi \alpha^2, B_{PTO} = jB_{av.}^{(1\,WEC)}$.

As it can be seen in Figure 6-12, devices with which the wavefronts interact first exhibit increased responses. This is attributed to the presence of reflected wave components generated by the other devices in the array. Conversely, the WECs located further downwave experience a shadowing effect due to the preceding devices. This results in reduced oscillation magnitudes. This disparity in response magnitude is evident when comparing the responses of WECs 1 and 25, particularly when the incident wave field propagates at an angle of $\beta = 30°$; see Figure 6-12(c, i).

Figure 6-13 depicts the normalized power output by the same WECs (1, 13 and 25) for different values of the multiplying factor j, as computed by Eq. (6.20) for $\beta = [0°, 15°, 30°]$. Results concerning the isolated WEC are also plotted for comparison. The above observation concerning the response amplitude operators also holds for the normalized power curves, since the RAO values are explicitly involved in evaluating the power output. The fact that the devices that first encounter the wavefronts benefit from intra–array interactions also agrees with the findings reported in Ref. [211]. Furthermore, as illustrated in Figure 6-13, the higher the value of PTO damping, the better the devices perform at the low–frequencies range. The complicated response patterns as well as the relationship between Power–Take–Off (PTO) damping and device efficiency, across different frequencies, highlight the intricate nature of optimizing WEC arrays for optimal energy extraction.

6.2.2. *Q–factor of the WEC park*

The q–factor is an index that quantifies the effect of hydrodynamic interactions among multiple devices on the overall power absorption of a WEC array. It was first introduced in the late 1970s [212] and it is defined as the ratio of the power generated by an array comprising M devices, to M times the power generated by an isolated device. This ratio provides insight into how the interactions within the array affect its efficiency. A q–factor less than one ($q < 1$) indicates that the average power output per WEC of the array is reduced, compared to that of an isolated WEC, operating in the same region. This suggests that the hydrodynamic interactions among the devices are detrimental, resulting in a reduction in the overall power absorption by the array. In other words, the presence of neighboring devices negatively influences each device's ability to absorb wave energy. On the contrary, a q–factor greater than one ($q > 1$) signifies that the interactions among the devices in the array act constructively [211]. In this case, the average power output per WEC within the array exceeds that of an isolated WEC, indicating that the devices benefit from their proximity to each other. This constructive interaction enhances the overall power absorption of the array.

The q–factor of the considered arrangement, defined as,

$$q(\omega,\beta;B_{PTO},C_{PTO}) = \frac{\sum_{m=1}^{M\ (=25)} \bar{P}_m(\omega,\beta;B_{PTO},C_{PTO})}{M \cdot \bar{P}_{(1\,WEC)}(\omega,\beta;B_{PTO},C_{PTO})}, \tag{6.22}$$

is shown in Figure 6-14, for different levels of the angle of incidence β and for different values of the multiplying factor j, including the value $j = 17.5$, which corresponds to PTO damping coefficient equal to $B_{PTO} = 35.14\ \mathrm{kN/s}$.

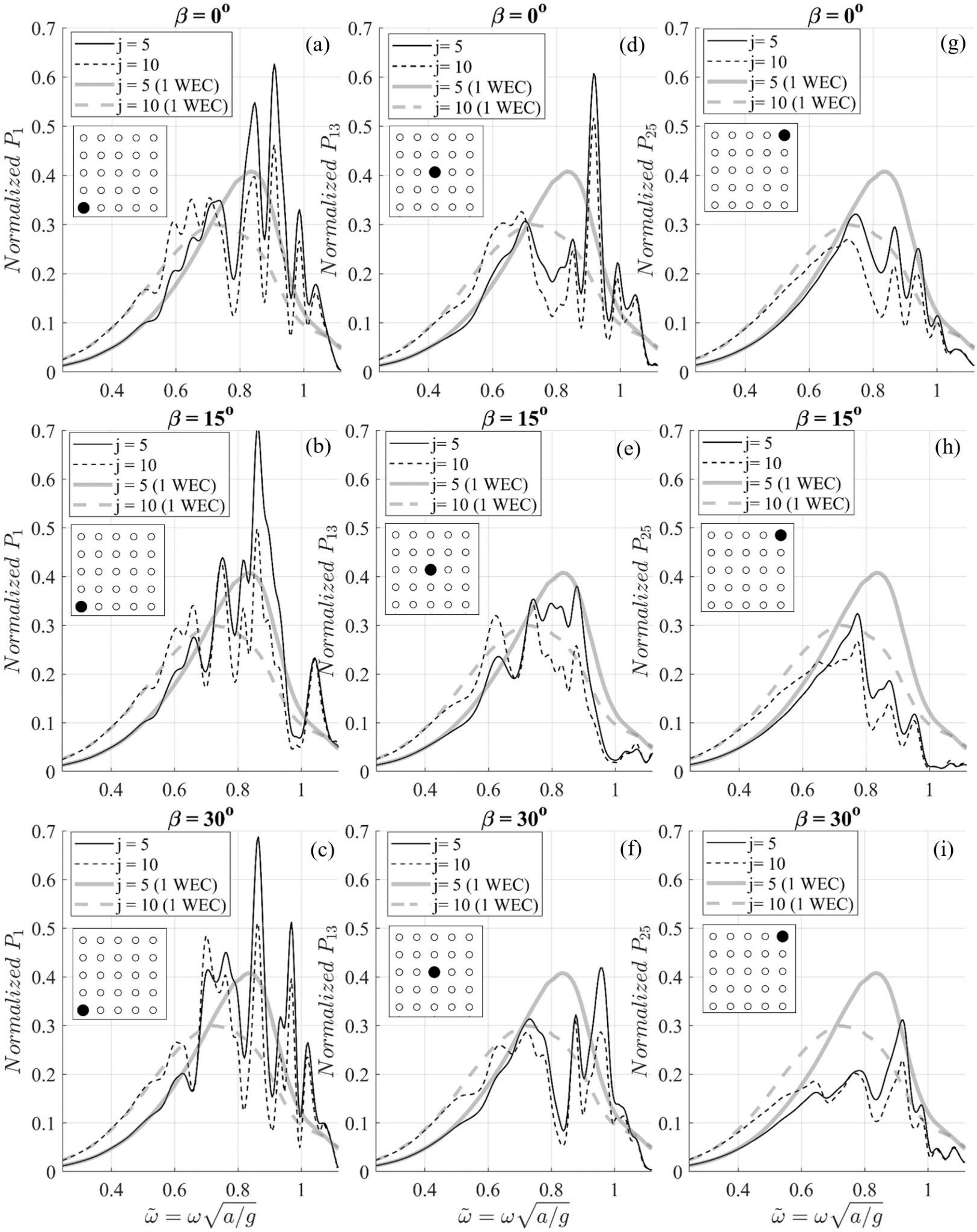

Figure 6-13. Normalized power output by the WECs (**a**–**c**) 1, (**d**–**f**) 13, and (**g**–**i**) 25. Propagation direction (**a**, **d**, **g**) $\beta = 0°$, (**b**, **e**, **h**) $\beta = 15°$, (**c**, **f**, **i**) $\beta = 30°$. The power output by an individual WEC operating at the same region and located at $x_1 = x_2 = 0$ (position of WEC 13 in the array), is also plotted for comparison. The relative position of the WECs is illustrated in the auxiliary legend. $C_{PTO} = 0.1\rho g \pi \alpha^2, B_{PTO} = jB_{av.}^{(1\,WEC)}$.

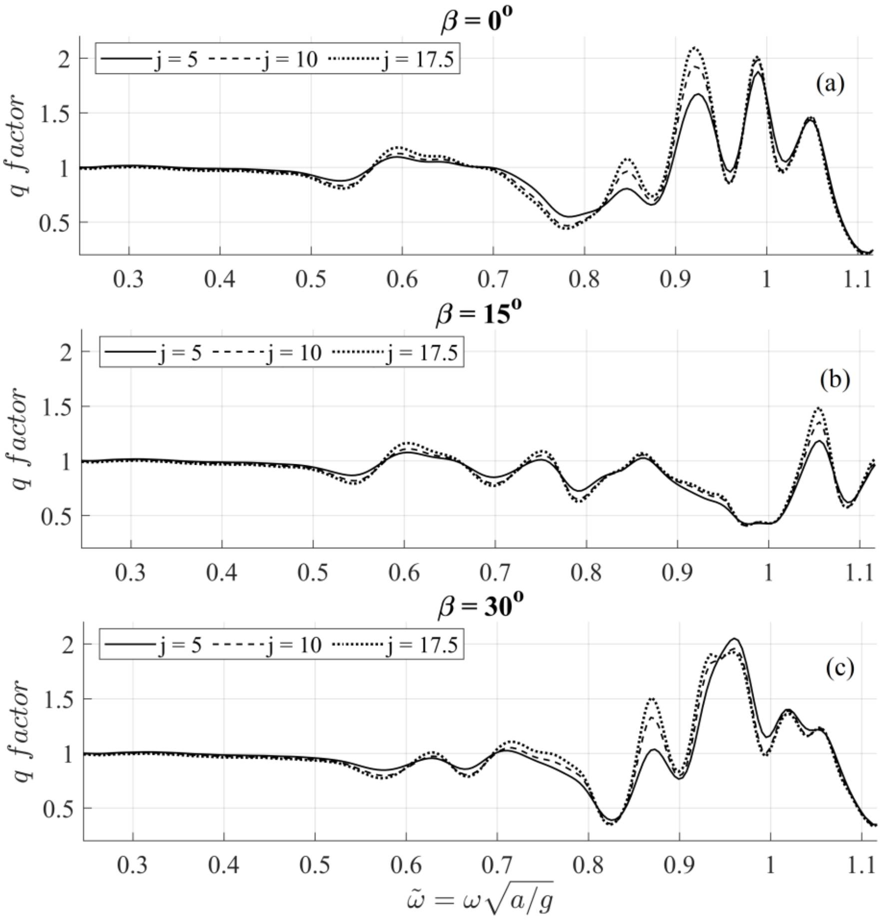

Figure 6-14. q–factor of the 5 × 5 WEC arrangement for different PTO damping values. Propagation direction (**a**) $\beta = 0°$, (**b**) $\beta = 15°$, (**c**) $\beta = 30°$, $C_{PTO} = 0.1\rho g\pi\alpha^2, B_{PTO} = jB_{av.}^{(1\,WEC)}$.

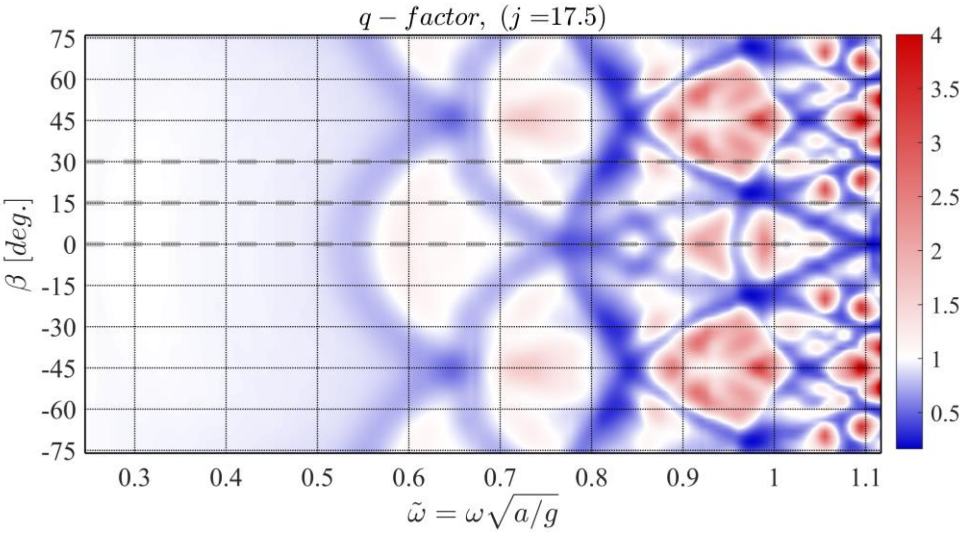

Figure 6-15. q–factor of the 5 × 5 WEC arrangement. Propagation direction $\beta \in [-76°, 76°]$, $C_{PTO} = 0.1\rho g\pi\alpha^2, B_{PTO} = jB_{av.}^{(1\,WEC)}$.

The latter value ($B_{PTO} = 35.14$ kN/s) of PTO damping was found to be the optimum, as regards the maximization of mean annual power output of this arrangement in the considered geographical region, as analyzed in more detail in the sequel. Figure 6-15 illustrates a colorplot of the considered arrangement's resulting q–factor, as function of both the frequency and the angle of incidence, with the dashed lines representing the q–factor curves shown in Figure 6-14, for $j = 17.5$.

In Eq. (6.22), $\bar{P}_m$ denotes the normalized power output by the m^{th} WEC of the 5×5 array, for the given parameters, and $\bar{P}_{(1\,WEC)}$ is the normalized power output by the isolated WEC operating at the same region and located at $x_1 = x_2 = 0$. It can be observed that in the low–frequency range, the interactions between the WECs within the array are minimal, resulting in a q–factor that is approximately one. However, at higher frequencies, the q–factor exhibits a more complex behaviour. This complexity is highly dependent on the angle of incidence. The variations in the q–factor at these frequencies suggest that the interactions among the various devices become more significant and intricate. Interestingly, the q–factor is much less sensitive to changes in the Power–Take–Off (PTO) damping parameter. However, it is important to note that PTO damping is crucial as regards the overall power absorption, as it enables the array to be tuned so that it performs better at incident wave periods that carry the highest energy content, in the region considered for deployment. The q–factor does not account for this critical aspect, since the different curves are computed using the same PTO damping value for each WEC in the array as well as for the isolated WEC. Consequently, the influence of PTO damping on the array's performance across varying wave periods is not fully reflected in the depicted q–factor curves and colorplot.

The value of B_{PTO} required to optimize the annual power output is a consequence of the selected devices’ low natural period in heave as compared to the sea states with the higher energy content in the considered region. Furthermore, the natural period is further slightly reduced by the considered PTO stiffness. Apparently, more massive devices would require less PTO damping. However, in this work’s context the studied devices were chosen to measure three meters in diameter, so that the presented results would be comparable to practical applications [213]. In the general case, a simple estimation of optimum mass and diameter values (that maximize the responses of freely floating bodies $B_{PTO} = C_{PTO} = 0$ and assuming that $H = H_S$ and $T = T_{-10}$ could be determined by adjusting the natural period of WECs in heave motion to approach the value of the period carrying the largest energy content in the region, based on the nearshore wave climate data; see Figure 6-6. The latter period is usually slightly larger than the mean wave period, due to the inherent positive correlation between the energy period and the significant wave height.

6.2.3. *Estimation of Absorbed Power*

The TMA model [214] is used to reconstruct the wave spectra based on the time series of nearshore wave data,

$$S_{TMA}\left(\omega; H_S, T_{-10}, \theta_m\right) = S_{JON}\left(\omega; H_S, T_{-10}, \theta_m\right) f\left(\omega; h\right), \tag{6.23}$$

where $S_{JON}(\omega\,; H_S, T_{-10}, \theta_m)$ is the JONSWAP spectrum and $f(\omega;\ h)$ is the TMA filter function. Every spectrum of the series, constructed by Eq. (6.23), is discretized into a large number of frequencies $\{\omega_i = i\Delta\omega, i = 1,2,3\ldots\}$, where $\Delta\omega$ is the frequency spacing, and all energy is considered to be concentrated in the mean direction θ_m. The WEC arrangement is oriented towards the northwest and specifically at 319 degrees; see Figure 6-4(b). Thus, in the case of incident fields coming from this azimuthal direction, the absorbed power by the WEC park is evaluated using the results of the BEM–CMS model for $\beta = 0°$. Given the arrangement's symmetry with respect to the x_1z–plane, the power curves for $\beta = \beta_0$, are used to estimate power absorption by indent spectra with $\theta_m = 319° \pm \beta_0$. The power output of the 25–WEC system, for each spectrum $S(\omega_i), i = 1,2, \ldots$, is estimated as follows:

$$P = \sum_{m=1}^{M=25} \sum_{i} \rho g a C_g\left(h_1, \omega_i\right) A^2\left(\omega_i\right) \bar{P}_m\left[\omega_i, \beta\left(\theta_m\right); B_{PTO}, C_{PTO}\right], \tag{6.24}$$

where $A^2(\omega_i) = 2S(\omega_i)\Delta\omega$ and $\bar{P}_m$ denotes the normalized power output by the m^{th} WEC, for the given parameters. Polar histograms of net incident and absorbed wave power are shown in Figure 6-16.

Figure 6-17 shows a 10–year–long time series of the calculated power output by the considered 5×5 WEC arrangement, operating north of the coast of Ikaria Island for $j = 17.5$, which was found to be the value that maximizes the mean power production, for the considered fixed C_{PTO} value. The system's mean power output is 15.29 kW, which translates to 134.03 MWh produced on an annual basis. The power output ranges from 0 kW to a maximum of 289.84 kW. The probability density function of the annual absorbed power is illustrated in Figure 6-18(a), while subplots (b–e) of the same Figure depict corresponding seasonal data. The data presented have been obtained using results of the BEM–CMS model with a 2–degree resolution in the angle of incidence starting from $\beta = 0°$. Thus, the normalized power curves used for spectra with $\theta_m = \bar{\theta}_m \pm 1°, \bar{\theta}_m = 0°, 2°, 4° \ldots$, are approximated by the power curves corresponding to $\bar{\theta}_m$.

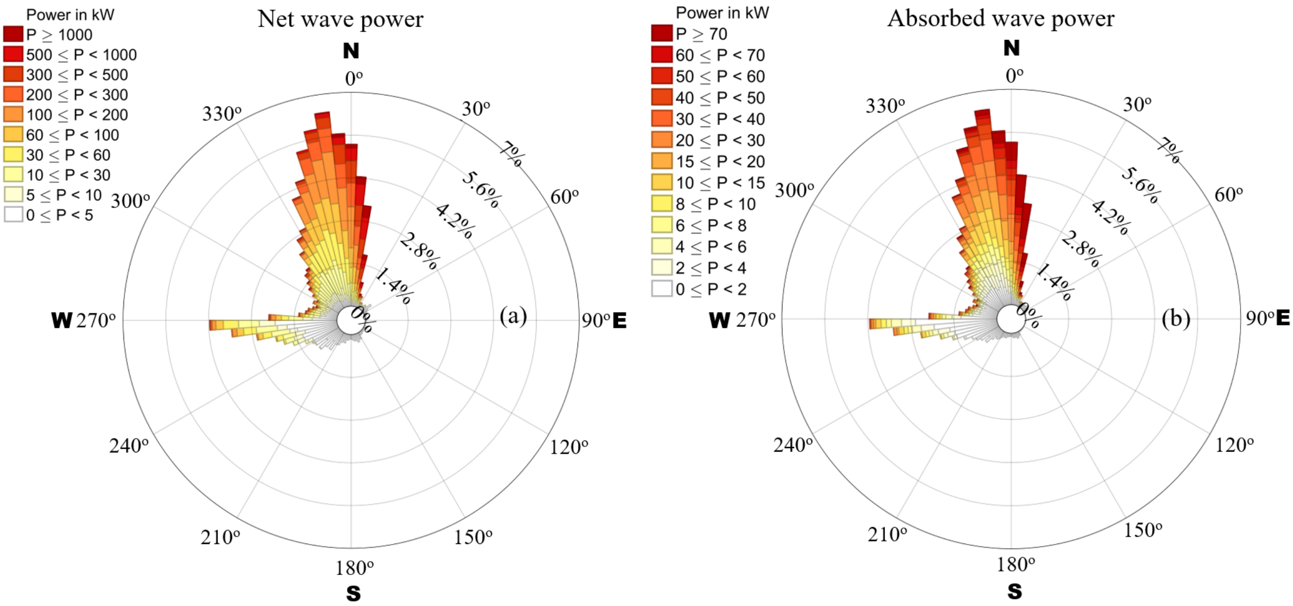

Figure 6-16. Polar histograms (%) of (**a**) net incident wave power and (**b**) absorbed wave power by the 5×5 WEC arrangement. ($C_{PTO} = 0.1\rho g \pi \alpha^2, B_{PTO} = 17.5 B_{av.}^{(1\,WEC)}$).

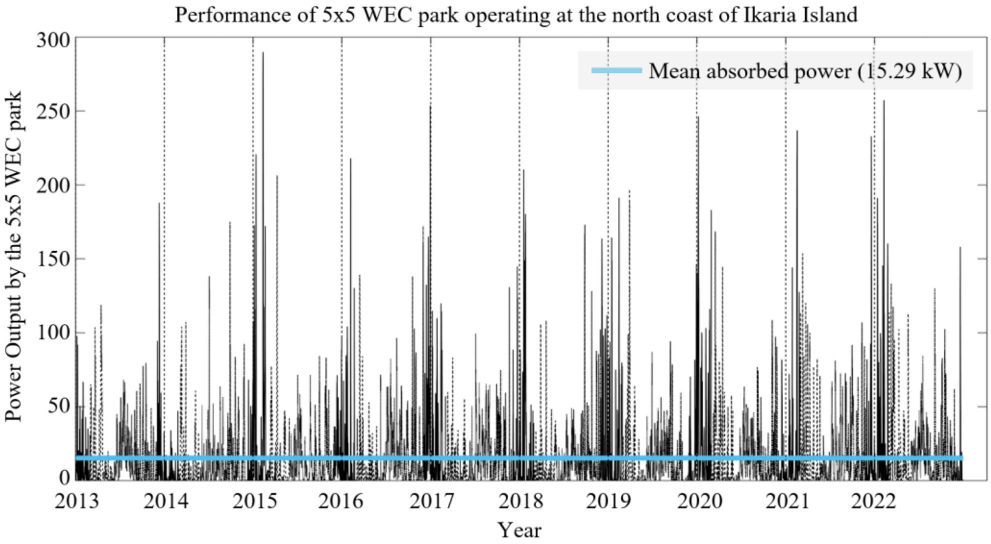

Figure 6-17. 10–year–long time series of power output (in kW) by the considered 5 × 5 WEC arrangement. ($C_{PTO} = 0.1\rho g\pi\alpha^2, B_{PTO} = 17.5B_{av.}^{(1\,WEC)}$).

6.3. *Discussion and future extensions*

This Chapter focuses on the modelling and study of WEC parks, aiming to evaluate their energy–capturing capacity and provide a supporting tool for optimization studies. Using a 3D Boundary Element Method (BEM) combined with a CMS model, various factors that influence the performance of WEC arrays, including intra–array interactions, seabed topography, PTO parameters and wave incidence angles are analyzed.

In particular, the model evaluates the forces exerted on individual WECs, which is crucial for assessing structural integrity and design, evaluates the hydrodynamic damping and added mass matrices and provides insights regarding the layout, the geometry and the PTO parameters, that could maximize power output. A case study is presented for a selected nearshore site, north of the coast of Ikaria Island, located in the Eastern Aegean Sea region, using long–term climatological data as obtained by an OtN transformation. The study illustrates the applicability of the proposed method as a tool for the optimal design of the WEC layout. In addition, indicative flow fields are presented and discussed, highlighting the effectiveness of the model in simulating refraction / diffraction phenomena. The park effect (q–factor) is also quantified and presented for the studied arrangement. Given the complex behaviour of the q–factor with respect to the frequency and propagation direction, it becomes clear that optimization of the wave park's performance is a challenging objective. The intricate behaviour of the park effect coefficient suggests that achieving optimal energy absorption requires careful consideration of a wide range of factors.

The presented results demonstrate how wave energy can play a crucial role in addressing the energy challenges faced by non–interconnected islands [85], which often depend on imported, costly fossil fuels. However, challenges remain, such as the high initial investment costs, installation and maintenance in harsh marine environments, as well as grid integration issues.

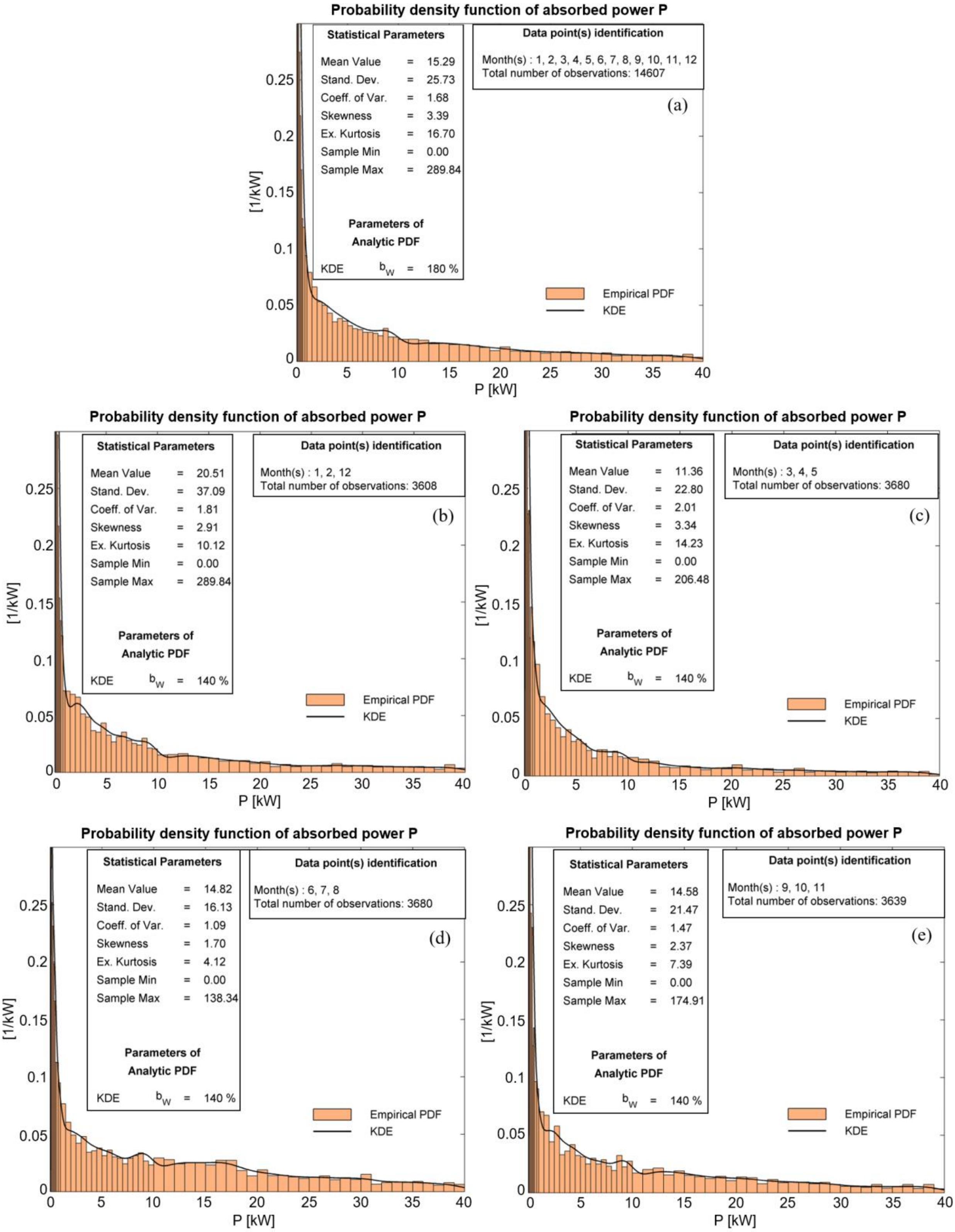

Figure 6-18. Probability density function of (**a**) annual and (**b**–**e**) seasonal absorbed wave power by the considered 5 × 5 WEC arrangement. (**b**) Winter, (**c**) Spring, (**d**) Summer, (**e**) Autumn. ($C_{PTO} = 0.1\rho g\pi\alpha^2, B_{PTO} = 17.5B_{av.}^{(1\,WEC)}$).

Recent studies have shown that installing devices with different individual dimensions within a park can improve the overall performance [215], which can be investigated using the presented methodology, along with different shapes and arrangements of the devices, aiming to maximize the power output. The performance of floating WECs could be enhanced by the consideration of additional degrees of freedom [216]. Preliminary results in this direction have been presented in Ref. [123]. In this case, the coupling between different DoFs could result in large–amplitude angular oscillations of the WECs [217], which can prove to be an additional important design parameter, as regards the survivability of the devices in harsh conditions.

It is important to highlight that theoretical modelling does not fully capture the complexities of real–world dynamics, particularly under extreme sea states. For instance, recent experimental studies have investigated the performance of scaled WECs in intermediate water depths, using extreme waves with a 50–year return period in the North Sea [218]. These experiments reveal critical factors often overlooked in numerical models, especially in models based on potential flow assumptions. The latter factors include non–linear phenomena, such as wave breaking and overtopping, which can have a substantial impact on the devices' behaviour and their ability to withstand extreme conditions. On the other hand, although experimental studies provide valuable insights, potential flow models offer a complementary approach by enabling the rapid exploration of multi–parametric spaces. Therefore, these models facilitate a preliminary estimate of optimized design parameters at a relatively low computational cost, making them a useful tool for initial system evaluations.

Given the limitations of both theoretical models and experimental setups, future studies and design methodologies should integrate both approaches, combining the predictive power of potential flow (or higher fidelity) models with the practical insights from experimental data. This integrated approach can ensure the development of robust, efficient and resilient wave energy systems.

7

INTEGRATION OF POINT ABSORBER WECS ON BREAKWATERS

The possibility of installing WEC arrays on the exposed side of breakwaters or piers has been a subject of research in the past few years. Apart from obvious benefits regarding the facilitation of installation and maintenance, this can also augment the portion of captured wave energy, due to effects of wall reflections that increase the responses; see, e.g., [219,220]. Recently, such deployments were tested in areas of increased wave potential, as in the case of the breakwater in the port of Heraklion, in the northern–central part of Crete Island, by SINN Power [221]; see Figure 7-1. Integrating WECs with breakwaters presents a dual–purpose solution, where the breakwaters serve not only as protective structures against coastal erosion but also as platforms for renewable energy generation. This approach leverages existing infrastructure to reduce costs and improve the economic feasibility of wave energy projects.

In this chapter, a variant of the 3D model presented in §6 is developed, specifically tailored for simulating WECs integrated with breakwaters. In particular, the present chapter aims to describe the modifications and enhancements to the BEM model, necessary to account for the structural interactions between the WECs and the breakwaters, examine the hydrodynamic performance of integrated WECs, including energy capturing efficiency, and provide insight as regards the performance and cost–effectiveness.

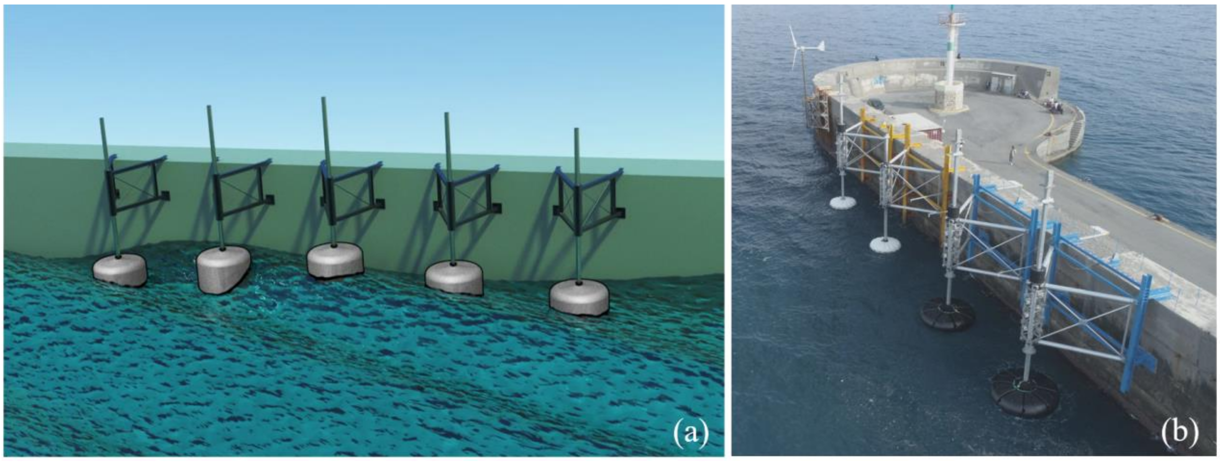

Figure 7-1. (**a**) Array of heaving–type wave energy converters (WECs) attached to a vertical wall. (**b**) Installation of WECs at the breakwater of the port of Heraklion, Crete Island, Greece, by SINN power [221].

The breakwater is modelled as a vertical wall and its reflective effects are incorporated into the evaluation of the response of the installed WECs. Additionally, hydrodynamic interactions among multiple floating devices are considered. Specifically, the reflection effects are included in the BEM solver under the assumption that an array of WEC devices is deployed on the exposed side of a breakwater, which is idealized as having infinite length for the sake of analytical simplicity. This assumption simplifies the modelling process by allowing for the consideration of uniform and consistent reflective effects along the entire length of the structure, eliminating the complexities associated with edge effects and varying boundary conditions and enabling a more straightforward application of the BEM solver.

Numerical results are presented and discussed, focusing on the forces exerted on the WECs, their responses, and power performance. The results incorporate the interactions among multiple WECs and the breakwater wall, as well as the influence of power–take–off (PTO) parameters. A significant contribution is the development and validation of a first–order model that can provide valuable data at relatively low cost for the preliminary design of complex WEC arrangements on breakwaters. The discussed model is capable of analyzing an extended range of incident wave frequencies, taking into account the long–term wave climatology of the installation site. Results obtained by the discussed methodology can play a pivotal role in determining essential parameters, such as those related to the PTO system, and in conducting preliminary assessments of both capital and operating expenses. In the context of this chapter, a case study exemplifies this approach at the port of Heraklion, in the north–central region of Crete Island in the South Aegean Sea, an area with significant wave energy potential. Utilizing long–term climatological data, the proposed method is demonstrated, showcasing its utility as a tool for supporting optimal design decisions.

In Section §7.1 of the present chapter, the mathematical formulation of diffraction and radiation problems is discussed, accounting for the complex interactions of multiple floating bodies acting as point absorber WECs in front of a vertical wall. More specifically, subsection §7.1 highlights the modifications relative to the methodology detailed in the previous chapter. In subsection §7.1.2, verification of the current model is provided, accompanied by an examination of numerical convergence.

The performance of the model is evaluated against data from the literature, confirming its reliability and accuracy in simulating complex WEC configurations. Systematic results for selected configurations are presented in §7.1.3, which includes a comprehensive analysis of the power output of various WECs within an array. In Section §7.2, an analysis of long–term performance is conducted, regarding the deployment of a WEC array at the port of Heraklion, in Crete, utilizing case–specific climatological data. Annual and seasonal power output statistics are presented, providing valuable insights into the effectiveness of such WEC installations. Section §7.3 summarizes conclusions drawn from the chapter's findings. Additionally, it presents promising areas for future research, emphasizing opportunities for advancing the effectiveness and practical application of WEC simulations in engineering contexts.

7.1. *Mathematical Formulation and 3D BEM*

Following the notation established in §6, an array of M identical single–Degree–of–Freedom (DoF) heaving point absorber WECs is considered to be deployed on the exposed side of a breakwater, operating in constant local depth h as depicted in Figure 7-3. The depth is assumed to remain constant in the vicinity of the breakwater for simplicity and cost–effectiveness of the developed methodology, as analyzed in more detail in the sequel. The array of floaters experiences harmonic wave excitation and the magnitude and phase of each floater's response in heave is determined by the total surrounding flow field within the flow domain D. The latter's boundary comprises the seabed, the free surface of the water and the wetted surfaces of all devices, but also the vertical wall that models the breakwater.

This analysis considers the hydrodynamic interactions among the WECs, along with reflection effects caused by the presence of the vertical boundary, as illustrated in Figure 7-2 and Figure 7-3. On the basis of standard hydrodynamic theory for floating bodies (refer to Appendix A), the total field is decomposed into the incident, diffracted, and M radiated subfields. The velocity field associated with each subfield is expressed by the gradient of the corresponding potential function $\Phi_0(\mathbf{x};t)$, $\Phi_d(\mathbf{x};t)$ and $\Phi_m(\mathbf{x};t)$, where m ranges from 1 to M.

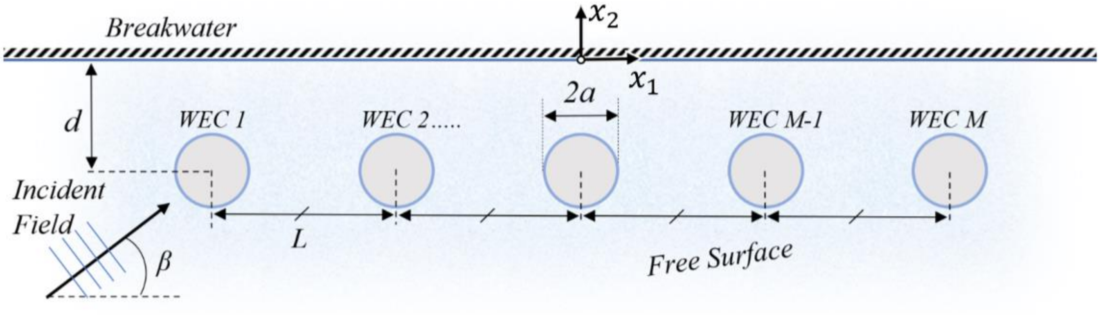

Figure 7-2. Top view of the considered configuration, illustrating basic dimensions.

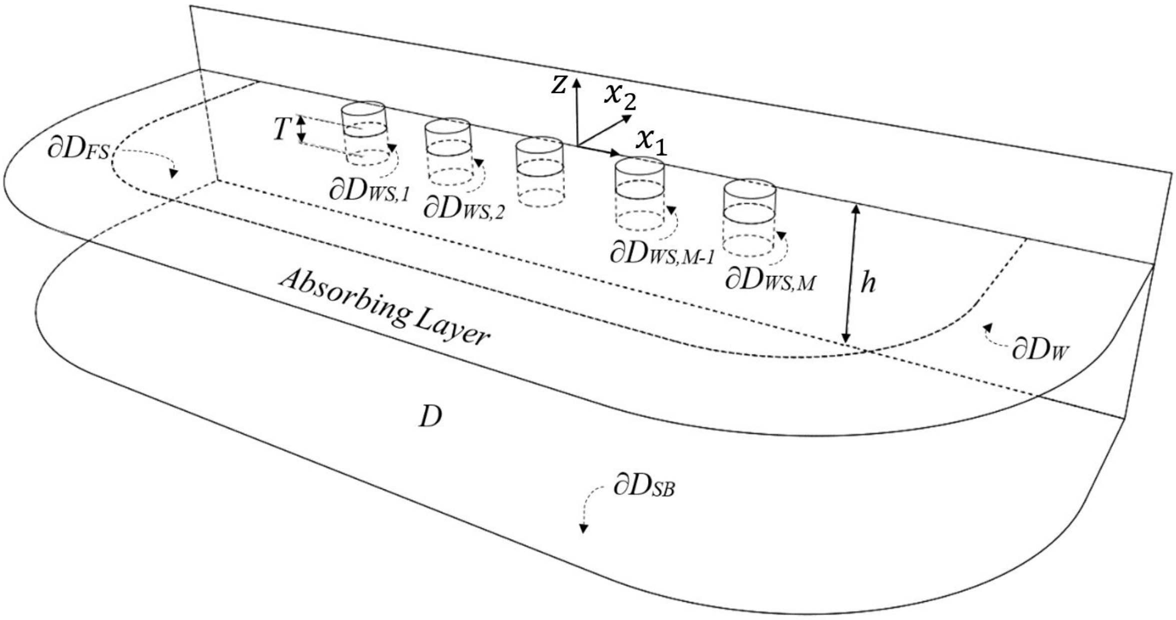

Figure 7-3. 3D sketch of the configuration, illustrating the various parts of the flow field boundary.

The coordinate system $\mathbf{x} = (x_1, x_2, z)$ is used, with the origin placed at mean water level (MWL) at the position of the vertical wall, so that the center of each WEC's waterplane area is located on the line $x_2 = -d$, parallel to the breakwater. This positioning ensures that the center of each Wave Energy Converter's waterplane area is aligned along the line $x_2 = -d$ which runs parallel to the breakwater. For the chosen origin location, the whole configuration is symmetric with respect to the $x_2 z$–plane, as schematically shown in Figure 7-2 and Figure 7-3.

In the framework of the model discussed in this chapter, cylindrical–shaped WECs are considered, characterized by a radius a and a draft T. Cylindrical geometry is chosen due to its simplicity and the ease with which it can be modelled and analyzed. Furthermore, existing literature provides data on cylindrical WECs placed in front of a vertical impermeable boundary [219], supporting the validity and reliability of using this geometry in the analysis. However, extending the presented methodology to accommodate different WEC shapes is straightforward. For example, the numerical results derived in §6 indicate that the methodology can be applied to various geometries, illustrating its flexibility and broad applicability. This applies not only as regards the WEC shape, but also the local seabed topography. Consequently, the approach remains robust and adaptable to different configurations, allowing comprehensive analyses of different layouts.

Similar to the analysis discussed in §6, the above interaction problem is treated in the frequency domain, assuming harmonic time–dependence of the form $\exp(-i\omega t)$, with ω being the angular frequency and i the imaginary unit. The resulting complex potential in the frequency domain is,

$$\varphi(\mathbf{x};\beta) = -i\omega\left\{\varphi_0(\mathbf{x};\beta) + \varphi_d(\mathbf{x};\beta) + \sum_{m=1}^{M} \xi_m \varphi_m(\mathbf{x})\right\}, \tag{7.1}$$

where the terms $-i\omega\varphi_0(\mathbf{x},\beta)$ and $-i\omega\varphi_d(\mathbf{x},\beta)$, represent the complex amplitudes of the incident and diffracted subfields, respectively, $\varphi_m(\mathbf{x},\beta), m = 1,2,\dots,M$, denotes the complex amplitude of the radiation field produced by the unit–amplitude vertical (heaving) oscillation of the m^{th} device and ξ_m is the complex amplitude of the m^{th} device's response in heave. For more details, refer to §6.1.

The complex potential of the incident field, incorporating the reflection effects due to the presence of the vertical wall, is assumed to be known, and for unit wave amplitude $(A = 1)$ is given by

$$\varphi_0(\mathbf{x},\beta) = \frac{g}{\omega^2}\frac{\cosh(k[z+h])}{\cosh(kh)} F(x_1, x_2, \beta), \text{ where} \tag{7.2}$$

$$\begin{aligned} F(x_1, x_2, \beta) = {} & \exp\big(ik(\cos(\beta)x_1 + \sin(\beta)x_2)\big) + \\ & + R\exp\big(ik(\cos(-\beta)x_1 + \sin(-\beta)x_2)\big). \end{aligned} \tag{7.3}$$

In the above equations, β is the propagation direction (also shown in Figure 7-2) and R is a reflection coefficient, which eliminates the reflection of the incident field $(R = 0)$ in case of propagation parallel to the wall ($\beta = 0°$ or $\beta = 180°$), or generates the reflected field $(R = 1)$ otherwise. Furthermore, k stands for the wavenumber, obtained by the dispersion relation, as formulated at the local depth h,

$$\omega^2 = k\, g \tanh\left(kh\right). \tag{7.4}$$

It is noted that Eqs. (7.2) and (7.3) presuppose a fully reflective vertical boundary of infinite length. The limitations of this assumption are investigated in Ref. [220] where it is shown that it leads to reduced accuracy as regards the estimation of the heave excitation forces, especially at low frequencies, compared to more realistic, finite–length breakwater cases.

The evaluation of the diffraction and the M radiation subfields is accomplished through the utilization of boundary value problems (BVPs), governed by the Laplace equation. These BVPs are supplemented by appropriate boundary conditions (BCs) enforced at the various segments of the boundary ∂D. The latter consists of the free surface of the water (∂D_{FS}), the wetted surfaces of the WECs ($\partial D_{WS,m,} m = 1,2,\dots,M$), and the impermeable boundaries of the wall (∂D_W), and the seabed (∂D_{SB}); see also Figure 7-3. The BVPs are fundamentally the same as those defined by Eqs. (6.8) to (6.12) in §6. However, significant modifications are introduced, given the presence of the vertical boundary ∂D_W. More specifically, the flow domain extents infinitely to the azimuthal directions $\theta = \tan^{-1}(x_2, x_1) \in [\pi, 2\pi]$, and is bounded by the vertical boundary at $x_2 = 0$. As a result, the description of the incident field is now expressed by Eqs. (7.2) and (7.3) which incorporate reflective effects induced by the presence of the breakwater. Moreover, an additional homogeneous Neumann boundary condition is imposed on ∂D_W, for the evaluation of the diffraction and radiation fields,

$$\frac{\partial \varphi_m\left(\mathbf{x}\right)}{\partial n} = 0, \quad \mathbf{x} \in \partial D_W,\ m = d,1,2,\dots,M. \tag{7.5}$$

Finally, given the assumption of constant local depth h, a mirroring technique is adopted to reduce the computational cost of the present model as described in more detail in the sequel. These alterations are crucial for the developed model to account for the influence of the vertical boundary and to ensure a valid analysis of diffraction and radiation phenomena in the presence of multiple devices along with the breakwater. The PML technique is numerically implemented as described in §6. However, the PML activation curve is defined by a more complex curve defined on Mean Water Level (MWL), comprising three linear segments and two 90–degree circular sectors (see Figure 7-3). Moreover, the PML thickness is set to one local wavelength, as defined by the dispersion relation for each frequency at the local depth h, since no alterations to the wavelength are expected due to interactions with the seabed.

The modified BVPs described above are treated by means of a low–order panel method, based on piecewise constant dipole singularity distributions and 4–node quadrilateral boundary elements, ensuring continuity of the geometry of the various parts of the boundary [155]. Exploiting the assumption of constant local depth, the complex potential functions $\varphi_m, m = d, 1,2, \dots . M$, are represented by,

$$\varphi_m\left(\mathbf{x}\right) = \int_{\partial \bar{D}} \sigma_m\left(\mathbf{x}'\right) \cdot \mathbf{n} \nabla \hat{G}\left(\mathbf{x}' \middle| \mathbf{x}\right) dS\left(\mathbf{x}'\right), \quad \mathbf{x} \in D, \mathbf{x}' \in \partial \bar{D},\ m = d,1,2,\dots M. \tag{7.6}$$

In Eq. (7.6), $\partial \bar{D}$ denotes the boundary of D, excluding the seabed part (∂D_{SB}), while the homogeneous Neumann BC on the latter part is accounted for by using the following Green's function for the Laplace equation in 3D in Eq. (7.6),

$$\hat{G}\left(\mathbf{x}'|\mathbf{x}\right)=G\left(\mathbf{x}'|\mathbf{x}\right)+G\left(\mathbf{x}'|\hat{\mathbf{x}}\right), \tag{7.7}$$

which involves the contribution by the mirror point $\hat{\mathbf{x}}=(x_1,x_2,-2h-z)$ with respect to the horizontal seabed plane $z=-h$. Furthermore, $\sigma^{(m)}(\mathbf{x}'), m=d,1,2,\dots,M$ are dipole strength distributions defined on the boundary $\partial\bar{D}$, which are obtained by means of the low–order panel method, under the assumption of being piecewise constant on each element. The above distributions, in conjunction with a discretized form of Equation (7.6), define the fields $\varphi_m, m=d,1,2,\dots.M$. Following the notation established in the previous chapter (§6), the potential functions and the corresponding velocity fields are approximated by:

$$\varphi\left(\mathbf{x}\right)=\sum_p \sigma_p \Phi_p\left(\mathbf{x}\right),\ \nabla\varphi\left(\mathbf{x}\right)=\sum_p \sigma_p \mathbf{U}_p\left(\mathbf{x}\right), \tag{7.8}$$

where the summation ranges over all panels that discretize the reduced boundary $\partial\bar{D}$ of the flow domain, indexed by p, and σ_p is the singularity distribution's strength on the p^{th} element. An important modification regarding the numerical implementation, as compared to §6, lies in the definition of Φ_p and $\mathbf{U}_p$. In the context of the present model, these parameters represent not only the induced potential and velocity from the p^{th} element but also from its mirrored counterpart. More specifically, the quantities Φ_p and $\mathbf{U}_p$ are evaluated as induced potential and velocity by both the actual and the mirrored elements, both carrying unit singularity distribution, contributing collectively to the field point $\mathbf{x}$; for more details see [156].

Numerical solutions are obtained using a collocation technique, satisfying each BC at the centroid of the corresponding boundary elements on the different parts of the boundary $\partial\bar{D}$. The impermeability BC on $z=-h$ is universally satisfied due to contributions by the mirrored points, while the computational boundary mesh does not need to include ∂D_{SB}, significantly reducing the computational cost. Using constant normal dipole distributions on each quadrilateral element, the induced potential matrix is analytically calculated via the solid angle. Moreover, exploiting the equivalence of a constant dipole element to a vortex ring, the calculation of induced velocity is obtained by repetitive use of the Biot–Savart law [156] (refer to Appendix C). As concerns discretization, a minimum of 15–20 elements per wavelength is applied to the discretization of the free surface boundary to eliminate numerical errors due to the damping and dispersion associated with the above numerical scheme.

7.1.1. Mesh Generation and Power Output

A crucial component of the BEM formulation involves the generation of the computational mesh. The discretization is achieved by incorporating structured meshes onto various boundary surfaces. A key feature is maintaining continuous junctions between different mesh segments so that global continuity of the discretized boundary is ensured. An illustrative example of a flow domain's boundary, comprising 12,332 quadrilateral elements and featuring 5 cylindrical Wave Energy Converters (WECs), is depicted in Figure 7-4 and Figure 7-5.

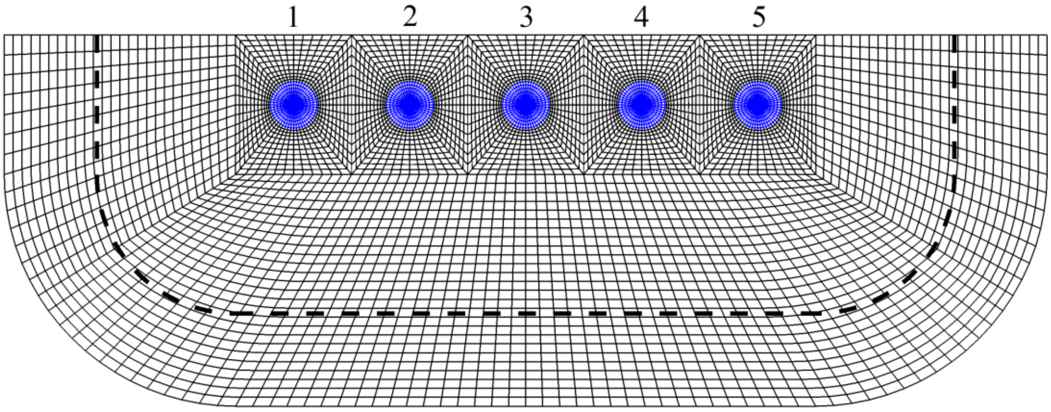

Figure 7-4. Top view of boundary mesh with the PML activation curve marked by a thick dashed line. The numbering of WECs is also indicated.

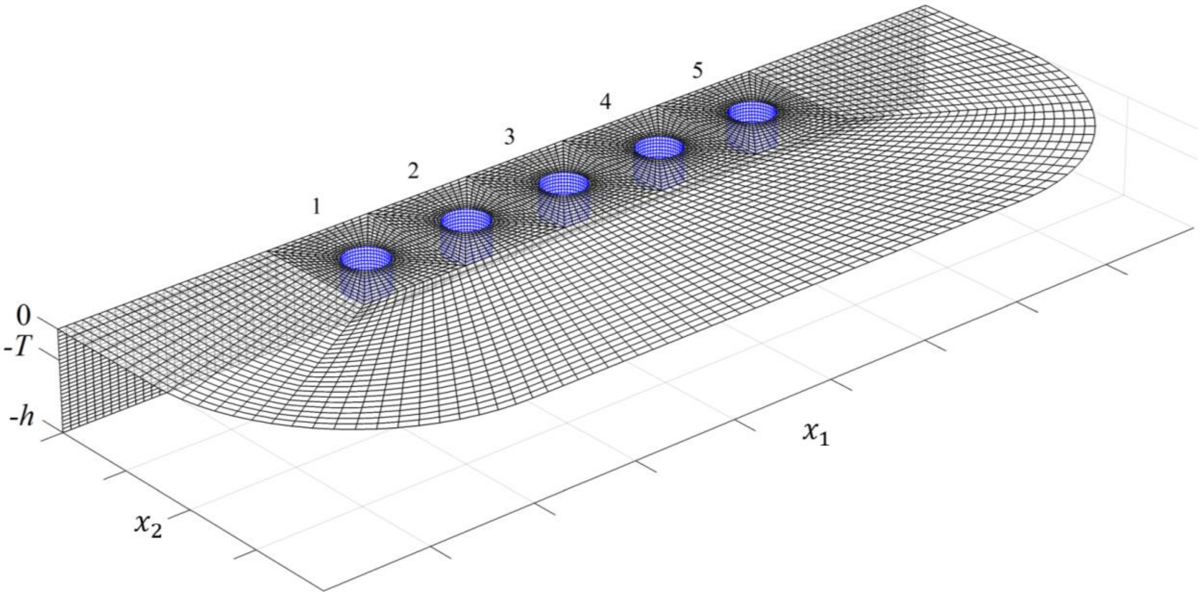

Figure 7-5. 3D view of arrangement and boundary mesh, also indicating the numbering of the WECs.

The above figures demonstrate the formation of free surface mesh sections surrounding each WEC to ensure discretization continuity. The surrounding free surface mesh extends over a certain number of wavelengths and integrates an absorbing layer. Additionally, enhanced grid resolution is applied to the near field (see Figure 7-4) and the wetted surfaces of the WECs to yield improved quality results.

Having calculated the diffracted and radiated subfields, the analysis proceeds identical to the previous chapter (refer to §6.1.3). Specifically, the heave response $\xi_m, m = 1,2, \dots, M$ of each WEC of the array is obtained by the following $M \times M$ linear system:

$$\left[-\omega^2\left(\mathbf{M}+\mathbf{A}(\omega)\right)-i\omega\left(\mathbf{B}(\omega)+\mathbf{B}_{PTO}\right)+\left(\mathbf{C}+\mathbf{C}_{PTO}\right)\right]\cdot\boldsymbol{\xi}=\mathbf{F}_0(\omega,\beta)+\mathbf{F}_d(\omega,\beta), \tag{7.9}$$

where the inertia of the WECs is modelled by the diagonal matrix $\mathbf{M} = M\mathbf{I}$, with $M = \rho\pi\alpha^2 T$, and ρ being the water density. The effects of the hydrostatic restoring forces, the PTO parameters as well as the added mass and hydrodynamic damping matrices $\mathbf{A}(\omega)$ and $\mathbf{B}(\omega)$ and the forces exerted on the devices are modelled as discussed in detail in §6.1.3 [refer to Eqs. (6.16)–(6.18)].

The mean output power of the each WEC device is subsequently evaluated as,

$$P_{OUT,m} = \frac{1}{2}\omega^2 B_{PTO} \left|\xi_m\right|^2, \tag{7.10}$$

and the normalized performance curves are defined as the ratio of the above result and the incident wave power flux over the cross section of each device, given by the WEC waterline diameter, considering a wave of height $H = 2A$,

$$P_m = \frac{P_{OUT,m}}{0.25\rho g H^2 C_g a}, \tag{7.11}$$

where C_g denotes the wave group velocity, evaluated at constant depth h.

7.1.2. Model Verification

In this section, results obtained by the present model are compared against data from previous research for verification purposes. In particular, the total Froude–Krylov (FK) and diffraction vertical forces exerted on five cylindrical WECs of an array operating in a region of water depth $h = 10$ m in front of a vertical impermeable wall are examined (see Figure 7-5). The propagation direction is $\beta = 90°$, corresponding to wave incidence normal to the wall, and thus, both the incident and diffracted fields present symmetry with respect to the central device. As a result, the total forces acting on the devices 1 and 5, as well as the ones acting on devices 2 and 4, are equal. The WECs' diameter is $a = 1.4$ m and the draft is $T = 1$ m. The distance from the wall to the midpoints of the devices' circular waterplanes is $d = 6$ m and the non–dimensional distance between two adjacent WECs is $L/a = 4$. The above configuration is studied in Ref. [220] assuming finite breakwater length.

Figure 7-6 depicts results concerning the normalized total forces $F/\rho g A \pi \alpha^2$, exerted on each WEC of the array, as functions of the angular frequency ω, in the range $[1\ \mathrm{rad/s}, 4\ \mathrm{rad/s}]$, as calculated by the present model. The data are derived from the present BEM based on two different computational grid settings, with different numbers of elements, in order to verify the convergence of the results. In particular, a medium and a fine mesh are used. In the medium mesh, the wetted surface of each cylindrical WEC is approximated by 1044 quadrilateral elements, while in the fine mesh configuration, each WEC is represented by 1584 elements. The surrounding free surface mesh spans 2.5 wavelengths and is redefined for each frequency. The latter boundary part incorporates the absorbing layer, which is activated one wavelength before the edge of the grid. In the medium mesh case, the free surface is discretized by 15 elements per wavelength and the total mesh size varies from 22,000 to 26,000 elements (for higher frequencies). The increase in the number of elements is a consequence of maintaining a minimum of 15 elements per wavelength on the free surface parts surrounding the WECs, and increased grid resolution is used in the near field; see Figure 7-4 and Figure 7-5. In the finer mesh case, the free surface is discretized by using 17 elements per wavelength and the total mesh size varies from 32,500 to 38,600 elements. As observed in Figure 7-6, the medium mesh provides convergent results for all frequencies.

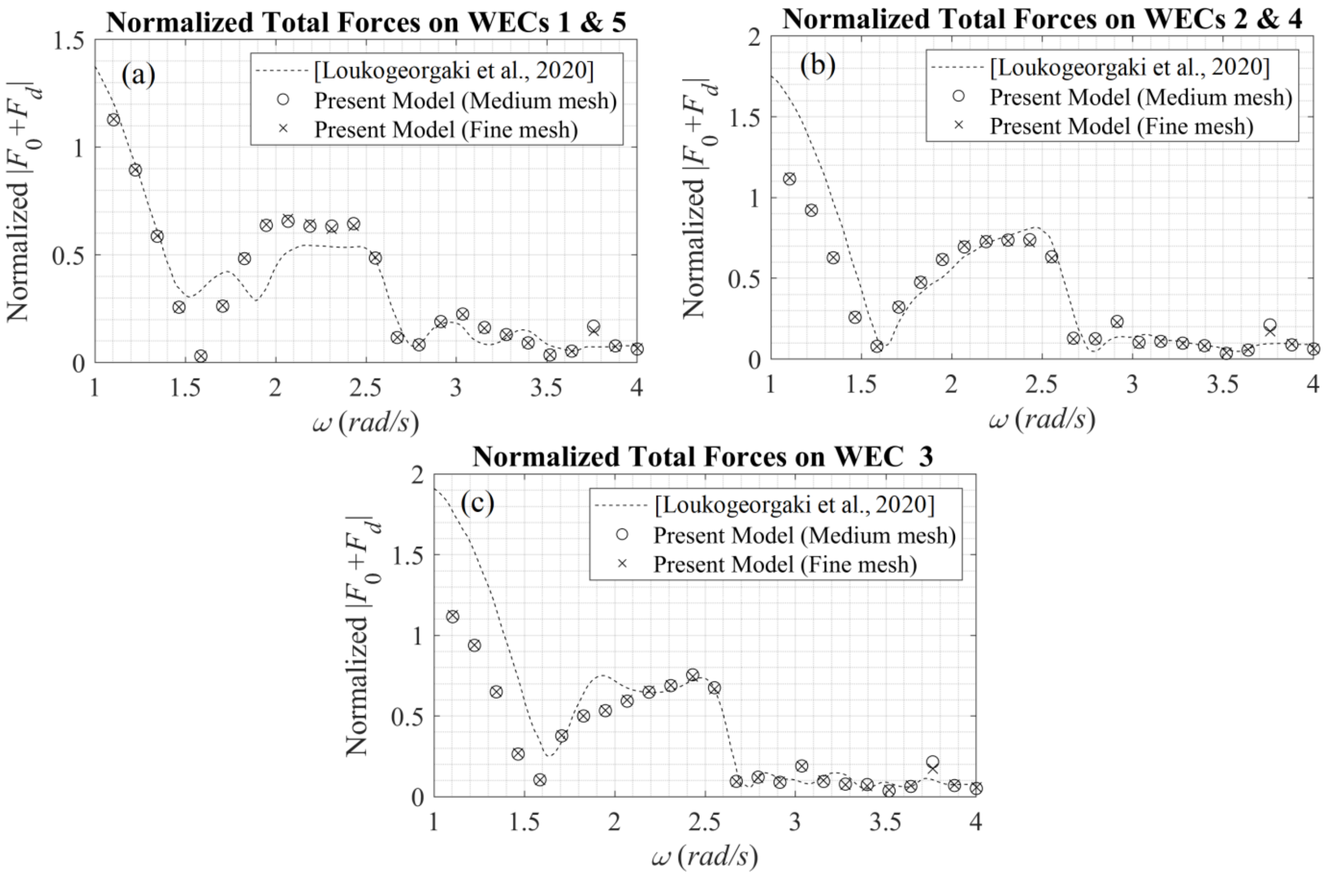

Figure 7-6. Normalized total vertical forces $F/\rho gA\pi\alpha^2$ on WECs (**a**) 1 and 5, (**b**) 2 and 4 and (**c**) 3 of the 5–WEC array; $h = 10$ m, $d = 6$ m, $L/a = 4, \beta = 90°$. (Data adapted from [220]).

Moreover, in Figure 7-6, the presented methodology's predictions are compared against numerical results from Ref. [220] which are shown by using dashed lines. As remarked above, in the latter work the breakwater wall length is finite and equal to $l_W = 18a$ and thus, the WEC array spans the whole breakwater length. On the contrary, in the discussed model, the far–field radiation condition is implemented by using an absorbing layer technique, and the results practically correspond to infinite wall length. The above remark justifies the differences observed between the two data sets. For angular frequencies lower than $1\ \mathrm{rad/s}$, due to the substantial increase in the wavelength, the consideration of the finite breakwater wall configuration of Ref. [220] results in reduced reflection effects as compared to the present method, which leads to major differences concerning the excitation forces, and therefore the responses. On the other hand, the infinite wall assumption of the present model results in full reflection of the incident field for all wavelengths, as described by Eqs. (7.2) and (7.3), and the WEC responses that will be examined in more detail in the sequel, especially for very low frequencies, are severely affected by the field generated by the superposition of the incident and reflected components.

7.1.3. Numerical Results

In this section, numerical results are derived and discussed for the case of an array consisting of five cylindrical WECs installed in an area of water depth h, with $a/h = 0.225$, $T/h = 0.3$,

$d/a = 3$ and $L/a = 6$. Moreover, following the notation established in §6, representative values for $B_{PTO} = jB_{33,av}$ are used, where $B_{33,av}$ denotes a characteristic value obtained as the frequency average of the calculated hydrodynamic damping coefficient B_{33} corresponding to the middle (third) WEC of the array, and j is a multiplying factor, defined as $j = [2, 5, 10]$. The PTO stiffness is taken to be $C_{PTO} = [0.1, 0.2]\ c_{33}$, corresponding to magnitudes used in the literature [210]. The case $B_{PTO} = C_{PTO} = 0$ is additionally considered, corresponding to an array consisting of freely floating bodies in front of the breakwater.

The Froude–Krylov (FK) vertical forces acting on the WECs, normalized with respect to $(\rho g A \pi \alpha^2)$ are depicted in Figure 7-7, as functions of the non–dimensional frequency $\widetilde{\omega} = \omega\sqrt{\alpha/g}$, showing a strong dependence on the direction of propagation of the incident field. In particular, Figure 7-7 shows the FK forces resulting from propagation at incident wave directions $30°, 60°$, and $90°$, with the $90°$ case corresponding to normal incidence on the wall. The case $\beta = 0°$, corresponding to incident wave propagation parallel to the breakwater, is also included. The position of each device only affects the phase of the FK forces, except for the case where $\beta = 90°$, in which the FK forces on all WECs share the same phase. It is observed in Figure 7-7 that in the low–frequency limit and $\beta \neq 0°$, the normalized FK forces approach 2, which is due to wall reflection effects on the wave field. On the contrary, for $\beta = 0°$ the wall reflection is zero and has no effect. However, the latter case is not expected in practice, since for breakwaters in nearshore / coastal regions, the bathymetry–induced refraction and shoaling effects on wave propagation will result in incident waves with a direction component towards the breakwater.

Normalized diffraction forces on each WEC are illustrated in Figure 7-8 and it is observed that these forces present complicated patterns as a result of the wall's presence. Furthermore, the diffraction forces on the WECs 1 and 5, as well as on the WECs 2 and 4, are equal in the case of normal incidence to the wall ($\beta = 90°$) due to symmetry of the arrangement and the resulting fields. It is noted that the magnitudes of the diffraction forces are different for each WEC in the arrangement, as opposed to the FK forces.

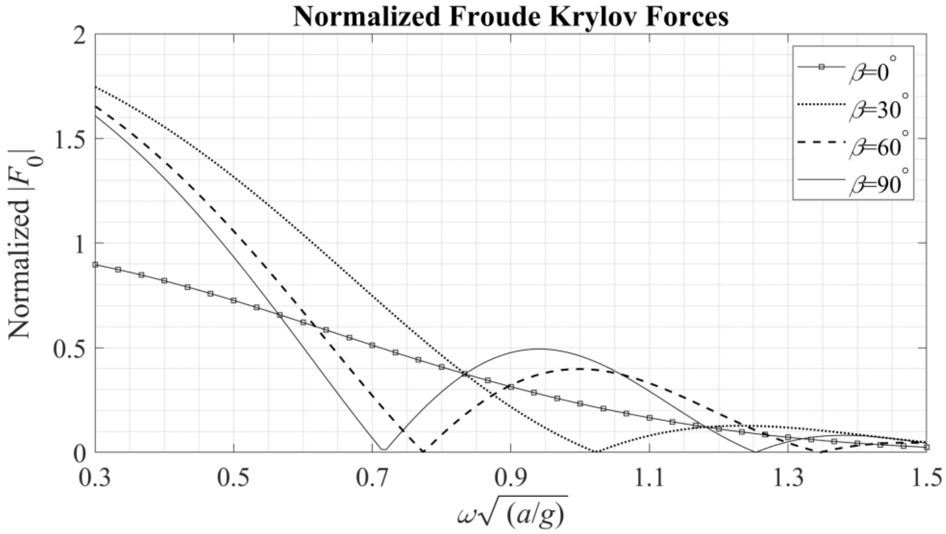

Figure 7-7. Normalized vertical Froude–Krylov forces on each cylindrical WEC, for incident wave directions $\beta = [0°, 30°, 60°, 90°]$. Geometrical parameters of the configuration, $a/h = 0.225$, $T/h = 0.3$, $d/a = 3$ and $L/a = 6$.

Data concerning the diagonal components of the added mass and the hydrodynamic damping matrices are presented in Figure 7-9. In particular, Figure 7-9(a) shows the diagonal elements of the added mass matrix **A** (normalized with respect to the mass of each WEC: $M = \rho\pi\alpha^2 T$ and Figure 7-9(b) shows the (non–dimensional) diagonal elements of the hydrodynamic damping matrix **B** as functions of the non–dimensional frequency $\omega\sqrt{a/g}$.

For comparison, non–diagonal elements of **A** and **B** matrices, corresponding to the middle (third) WEC of the array are presented in Figure 7-10.

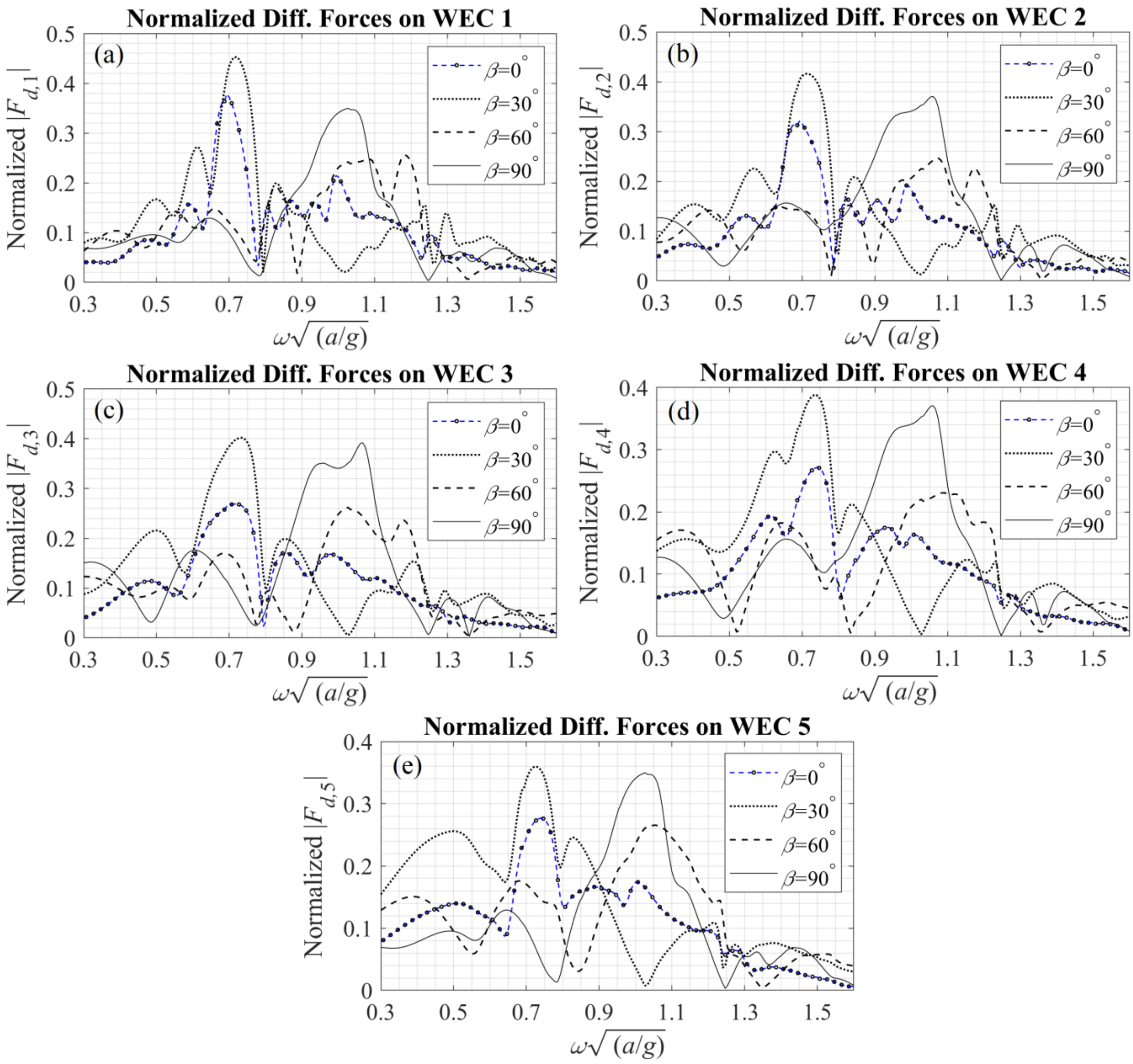

Figure 7-8. Normalized vertical diffraction forces on WECs (**a**) 1, (**b**), 2 (**c**), 3 (**d**), 4 and (**e**) 5, for incident wave directions $\beta = [0°, 30°, 60°, 90°]$. Geometrical parameters of the configuration, $a/h = 0.225$, $T/h = 0.3$, $d/a = 3$ and $L/a = 6$.

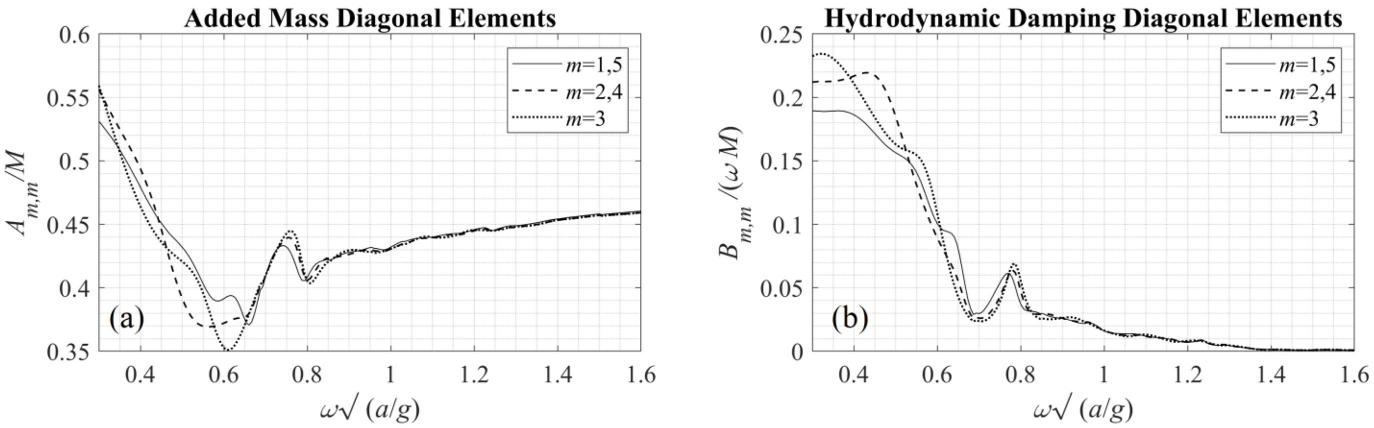

Figure 7-9. Diagonal elements of (**a**) the added mass and (**b**) the hydrodynamic damping matrices, as functions of the non–dimensional frequency, for $a/h = 0.225, T/h = 0.3, d/a = 3, L/a = 6$.

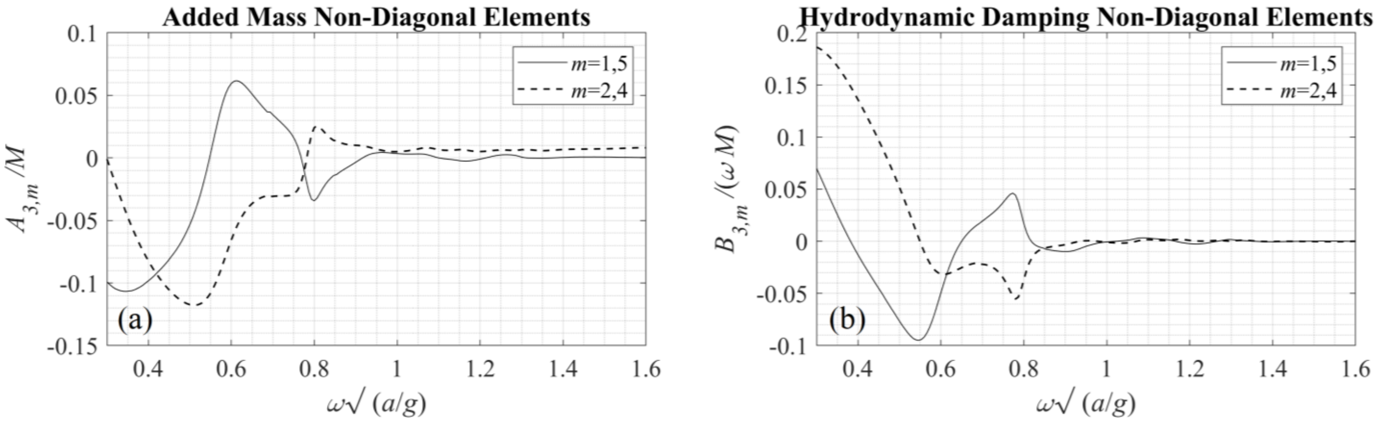

Figure 7-10. Non–diagonal elements of (**a**) the added mass and (**b**) the hydrodynamic damping matrices, as functions of the non–dimensional frequency, corresponding to the middle (third) WEC of the array, for $a/h = 0.225, T/h = 0.3, d/a = 3, L/a = 6$.

The response amplitude operators (RAOs) of each WEC are shown in Figure 7-11 for $\beta = [0°, 30°, 60°, 90°]$, as functions of the non–dimensional frequency $\omega\sqrt{a/g}$ for the case of freely floating bodies ($B_{PTO} = C_{PTO} = 0$). In this case, it is observed in Figure 7-11 that the responses become significant for frequencies near the resonance, especially for $\beta = 90°$, as illustrated in subplot (e) of Figure 7-11, which shows a zoom–in of the response of the central WEC in the band of frequencies near resonance.

It is worth noting that the responses of the WECs are highly dependent on the gap between the devices and the vertical wall. Especially in the case of normal incidence, the formation of standing waves leads to low responses when the WECs are centered on a node of the incident field, which corresponds to wavelengths of length λ such that $(2n + 1)\lambda/4 = d, n = 0,1,2 \ldots$, where d is the distance from the WEC waterplanes' midpoints to the breakwater (refer to Figure 7-2). For the considered case, this happens for wavelengths corresponding to non–dimensional frequencies $\omega\sqrt{a/g} = [0.716, 1.25, 1.61, \ldots]$ and the RAOs present a pattern similar to that of the FK forces, which vanish at these points (refer to Figure 7-7).

The effect of PTO parameters on the devices' responses is illustrated in Figure 7-12 for $\beta = 90°$. In particular, Figure 7-12(a–c) shows the responses of WECs 1 and 5, Figure 7-12(d–f) shows the responses of the WECs 2 and 4 and Figure 7-12(g–i) shows the responses of WEC 3 as functions of the non–dimensional frequency. The PTO stiffness (C_{PTO}) is set to $0 \times c_{33}$ in the first column of Figure 7-12, while in the subplots of the second and third columns, it is set to $0.1 \times c_{33}$ and $0.2 \times c_{33}$, respectively. The various subplots illustrate the responses for $B_{PTO} = [0, 2, 5, 10] \times B_{33,\,av}$. The above, for a dimensional configuration with $a = 1.5$ m, respectively correspond to the following values of the damping coefficient: $0\ \mathrm{Ns\,m^{-1}}$, $2{,}331.37\ \mathrm{Ns\,m^{-1}}$, $5{,}828.42\ \mathrm{Ns\,m^{-1}}$ and $11{,}656.85\ \mathrm{Ns\,m^{-1}}$.

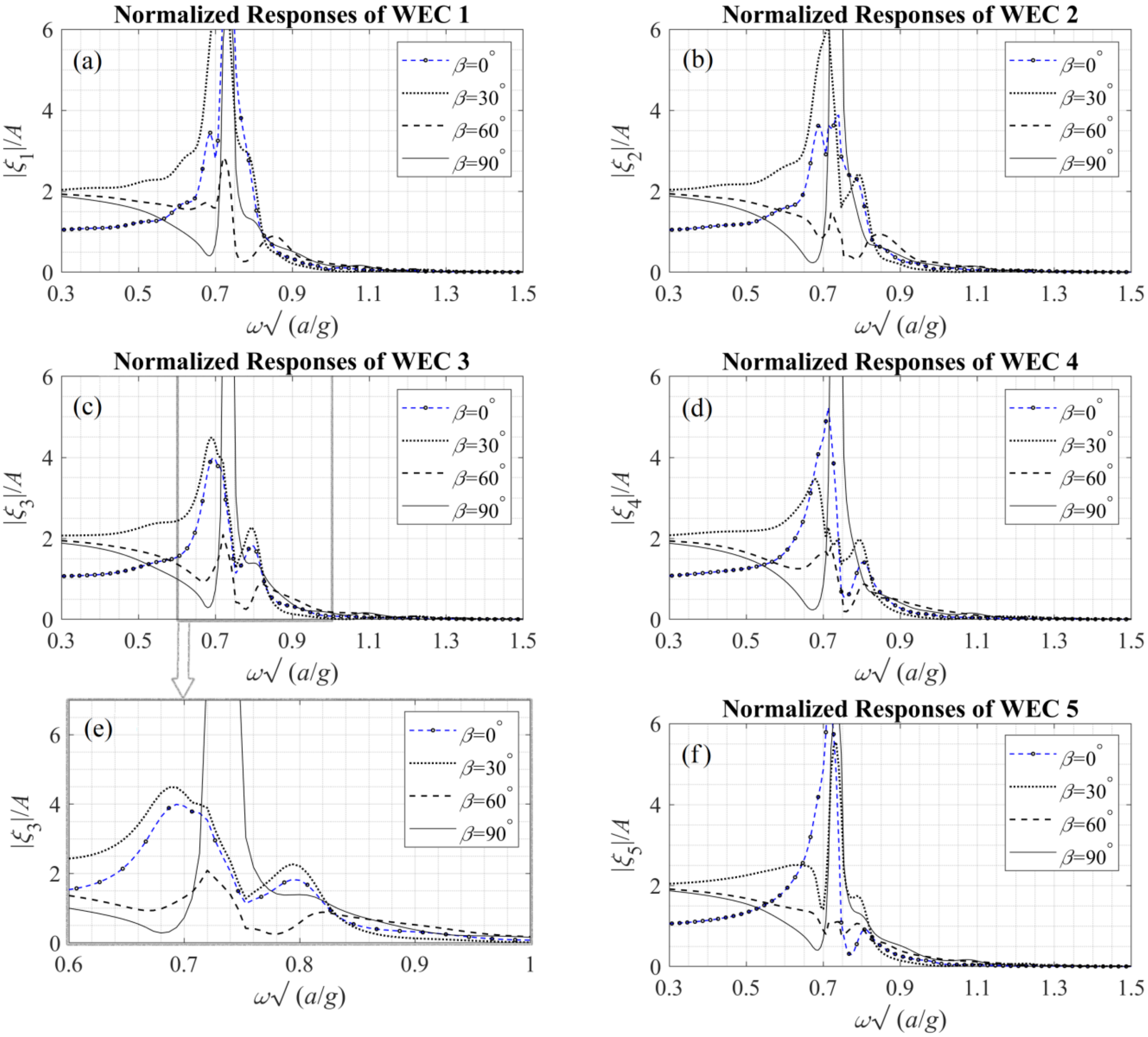

Figure 7-11. Normalized responses of WEC (**a**) 1, (**b**) 2, (**c**) 3, (**d**) 4 and (**f**) 5 for $a/h = 0.225$, $T/h = 0.3$, $d/a = 3$, $L/a = 6$ and $\beta = [0°, 30°, 60°, 90°]$. (**e**) zoom–in of the central (third) WEC's response in the band of frequencies near resonance. ($B_{PTO} = C_{PTO} = 0$).

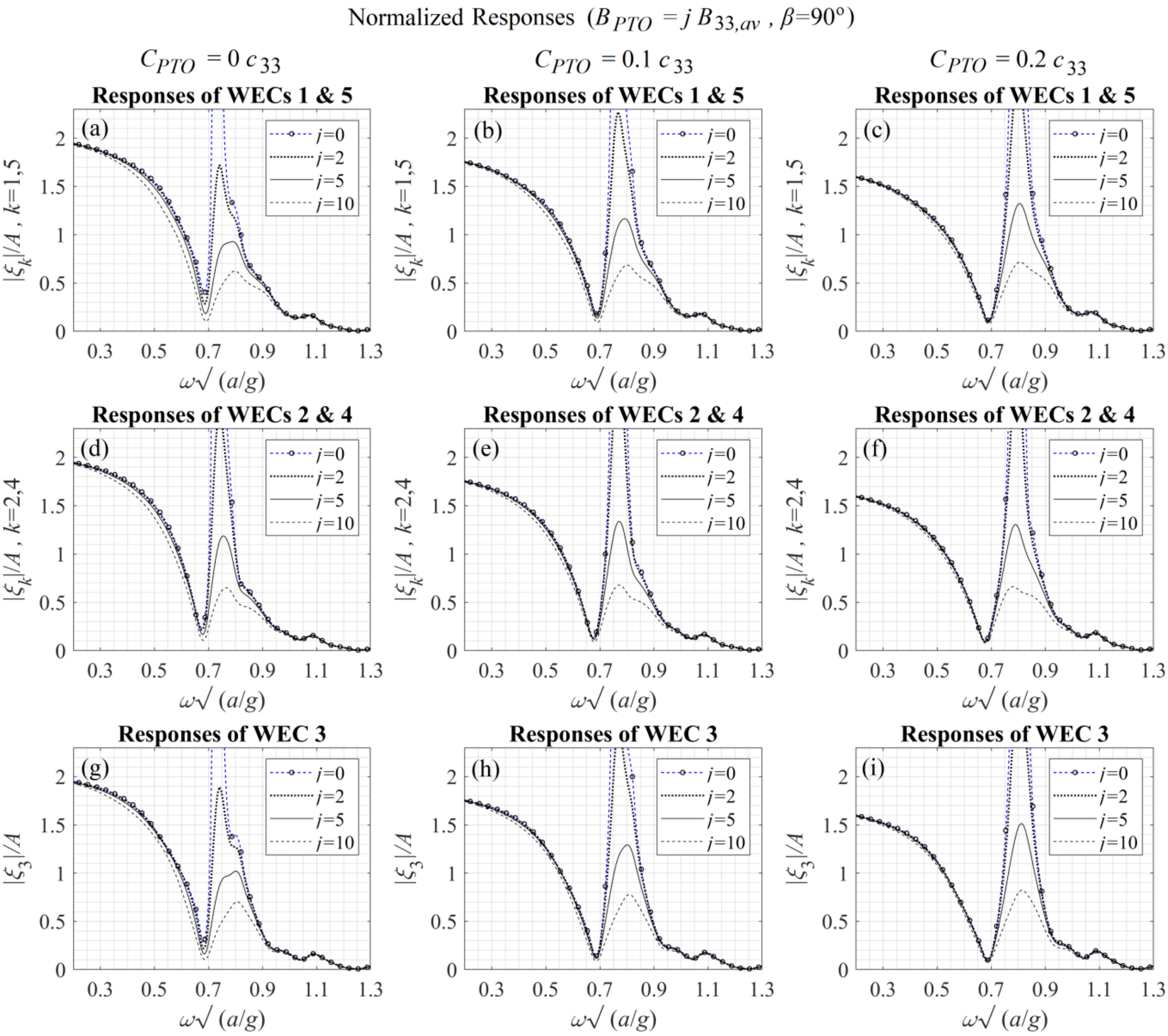

Figure 7-12. Normalized responses of each cylindrical WEC, for normally incident waves (β = 90°). PTO parameters: B_{PTO} = [0, 2, 5, 10] × $B_{33,\,av}$, (**a**, **d**, **g**) C_{PTO} = 0 × c_{33}, (**b**, **e**, **h**) C_{PTO} = 0.1 × c_{33}, (**c**, **f**, **i**) C_{PTO} = 0.2 × c_{33}. Responses of (**a**, **b**, **c**) WECs 1 and 5, (**d**, **e**, **f**) WECs 2 and 4 and (**g**, **h**, **i**) WEC 3.

The resulting performance index (normalized power output) for each WEC of the array, as evaluated by Eq. (7.11), is illustrated in Figure 7-13. Specifically, the power output for C_{PTO} = 0 × c_{33} is shown in the subplots of the first column (a, d, g). Corresponding results for C_{PTO} = 0.1 × c_{33} and C_{PTO} = 0.2 × c_{33} are presented in the subplots of the second (b, e, h) and third (c, f, i) columns. As expected, higher values of PTO damping lead to decreased peak values of heave response. However, at the same time, they result in increased power absorption at low frequencies, as shown in Figure 7-13, since the power output of the WECs' is directly related to the PTO damping, while the RAOs at frequencies below resonance are not gravely affected. As regards the PTO stiffness, it can be seen, both in Figure 7-12 and Figure 7-13 that higher values of C_{PTO}, slightly shift the natural frequency and tend to keep the responses lower at the low frequencies range (refer to Figure 7-12).

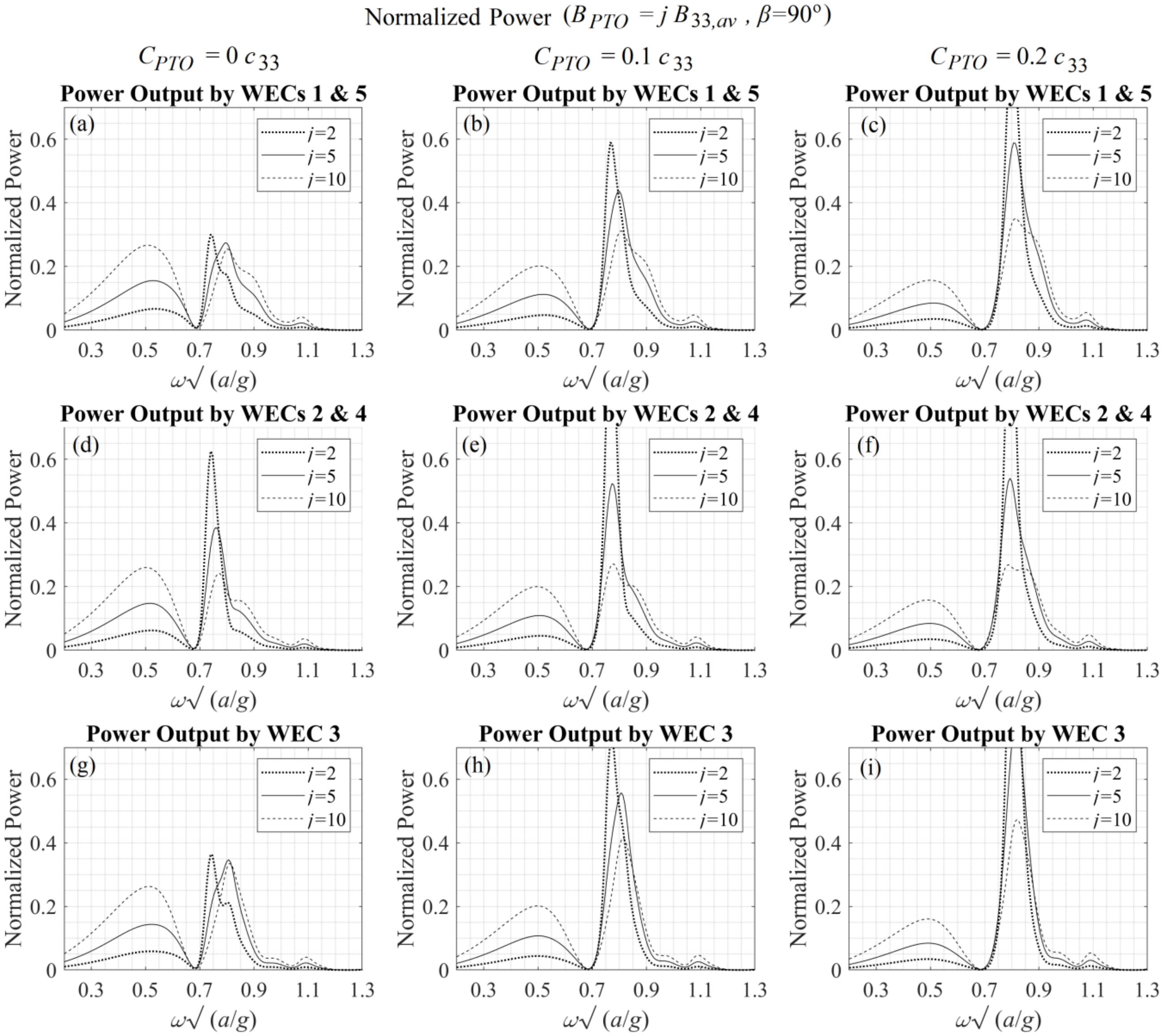

Figure 7-13. Normalized power output by each cylindrical WEC, for normally incident waves (β = 90°). PTO parameters: B_{PTO} = [2, 5, 10] × $B_{33,\ av}$, (**a**, **d**, **g**) C_{PTO} = 0 × c $_{33}$, (**b**, **e**, **h**) C_{PTO} = 0.1 × c $_{33}$, (**c**, **f**, **i**) C_{PTO} = 0.2 × c $_{33}$. Power output be (**a**, **b**, **c**) WECs 1 and 5, (**d**, **e**, **f**) WECs 2 and 4 and (**g**, **h**, **i**) WEC 3.

The discussed analysis focuses on the ideal flow case, providing preliminary estimations of the system's performance. While the results offer valuable insights into the dynamic behaviour of the system, the effects of viscosity on the responses, as well as the influence of gap resonance phenomena, have not been addressed. These parameters could be incorporated by introducing additional damping terms into the model to account for viscous losses, so that the dynamic behaviour is more accurately captured. However, the precise impact of such effects, along with their implications on the overall efficiency of the WEC array, remains an open area for further investigation.

7.2. *Case Study in the port of Heraklion*

The nearshore area at the port of Heraklion, situated on the north coast of Crete Island, in the Southern Aegean Sea, is studied as an example of the application of the developed methodology in the Greek Seas region; see Figure 7-14. The above nearshore area is characterized by relatively increased wave potential [57] and is thus considered to demonstrate the applicability of the present method, as regards the evaluation of the WEC array's power output.

The wave climatology in the studied area is based on a long–term time series, covering the 10–year period between January 2013 and December 2022, at the offshore points with geographical coordinates $35°30'00''\,\mathrm{N} - 25°00'00''\,\mathrm{E}$ and $35°30'00''\,\mathrm{N} - 25°30'00''\,\mathrm{E}$, as derived from the ERA5 database [149]. The relevant information includes significant wave height (H_s), mean energy wave period (T_{-10}), and mean wave direction (θ_m – measured clockwise from the North) with a 3–hour temporal resolution. Based on the above data, the offshore wave climatology is derived and presented in Figure 7-15. An Offshore–to–Nearshore (OtN) transformation technique is used to generate nearshore wave data at the target point located at a distance in front of the breakwater with geographical coordinates $35°21'15''\,\mathrm{N} - 25°09'00''\,\mathrm{E}$, as shown in Figure 7-16. The calculations are based on the SWAN nearshore wave spectral model [150].

Offshore wave conditions, represented by appropriate spectral parameters (significant wave height, mean wave period, and mean wave direction), are considered known all along the seaward boundary from which directional spectra $S(f,\theta)$ are reconstructed using the JONSWAP frequency spectrum, in conjunction with a hyperbolic cosine spreading function. The bathymetric data used are obtained from the General Bathymetric Chart of the Oceans (GEBCO) [208]. The coastline data utilized are sourced from the Global, Self–consistent, Hierarchical, High–resolution Shoreline Database (GMT–GSHHS), which is made available under the GNU Lesser General Public License, [162].

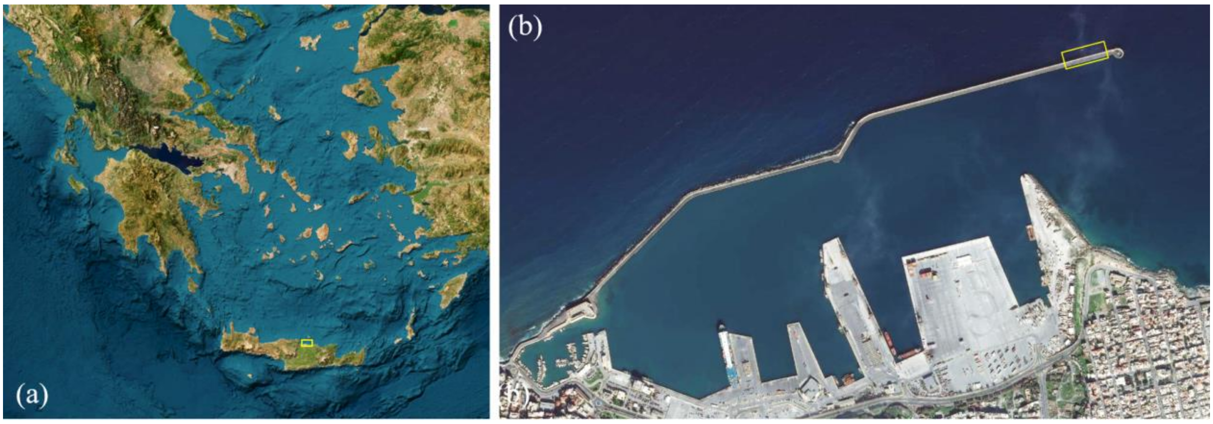

Figure 7-14. (**a**) Map of the Southern Aegean Sea and the coastal port area of Heraklion in Crete Island shown using the yellow rectangle. (**b**) Port of Heraklion and protective breakwater. The site of the WEC arrangement is indicated by the yellow rectangle. (Source: Google Earth).

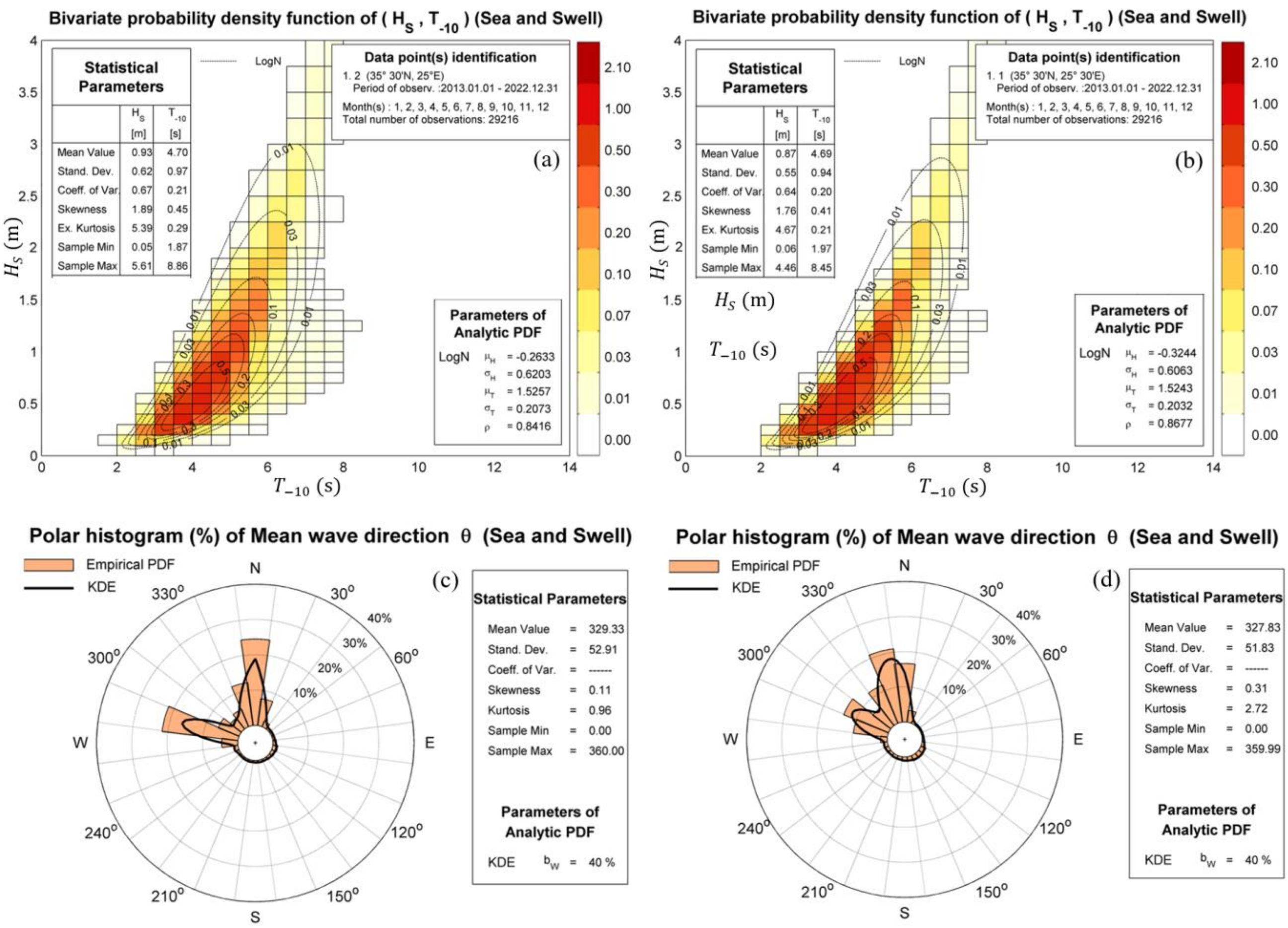

Figure 7-15. Wave climate data at the offshore points with geographical coordinates (**a**, **c**) $35°30'00''$ N– $25°00'00''$ E and (**b**, **d**) $35°30'00''$ N– $25°30'00''$ E. The bivariate $H_S – T_{-10}$ statistics are presented in subplots (**a**, **b**) and the corresponding polar histograms in subplots (**c**, **d**).

The primary driving factor of the system under investigation is the offshore wave conditions, which are uniformly distributed along the seaward boundary. Using these offshore boundary conditions, the phase–averaged model SWAN is employed to compute the wave conditions within the computational domain, ensuring adequate spatial resolution, as illustrated in Figure 7-16. The basic equation used in the model is the radiative transfer equation expressing action balance [209] (refer also to Eq. (6.21) in §6.2).

Selected results are presented in Figure 7-17 concerning the spatial distributions of the calculated significant wave height in the domain corresponding to characteristic wave conditions at the offshore boundary. It is clearly seen in this figure that the transformation of wave conditions includes refraction–diffraction and shoaling effects, as well as the sheltering effects by the small island (Dia) at the northern side of the domain. The derived nearshore wave climatology, at the target point located at a distance of about 3.5 km from the port of Heraklion breakwater and water depth $h = 15$ m, as obtained by the OtN transformation, is presented in Figure 7-18, and the corresponding basic statistics of the offshore and nearshore wave parameters are listed in Table 7-1.

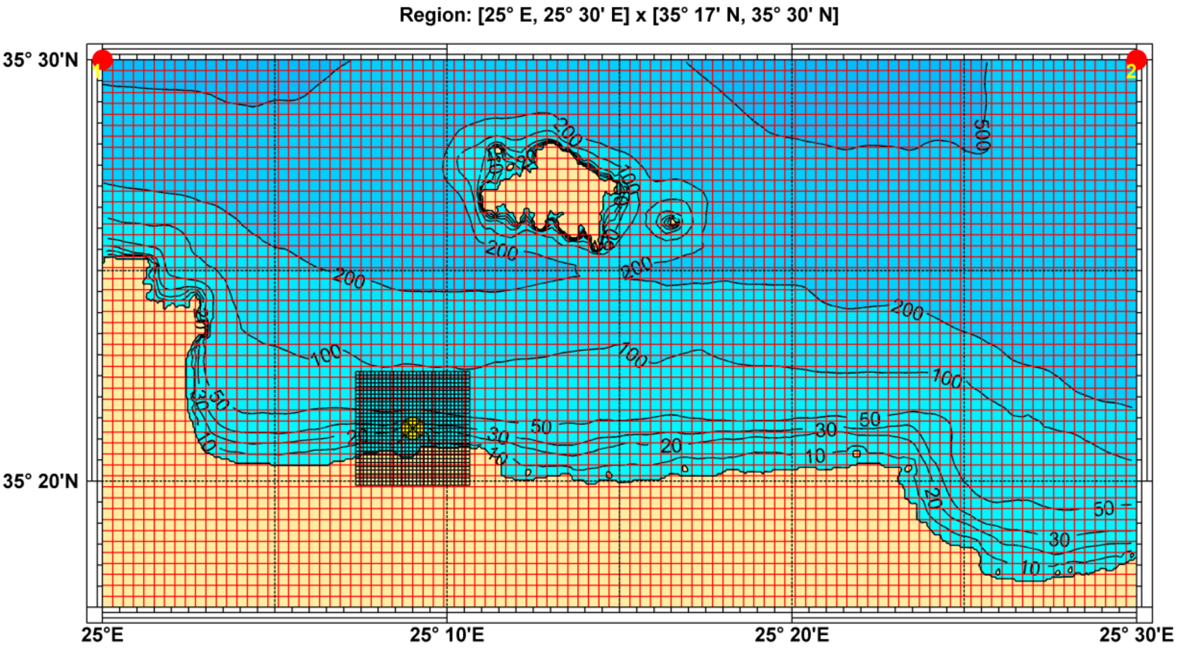

Figure 7-16. Numerical mesh for the application of the SWAN model, applied to derive the nearshore climatology at the target point in front of the Heraklion port breakwater shown by using a yellow circle. Offshore points are shown by using red circles.

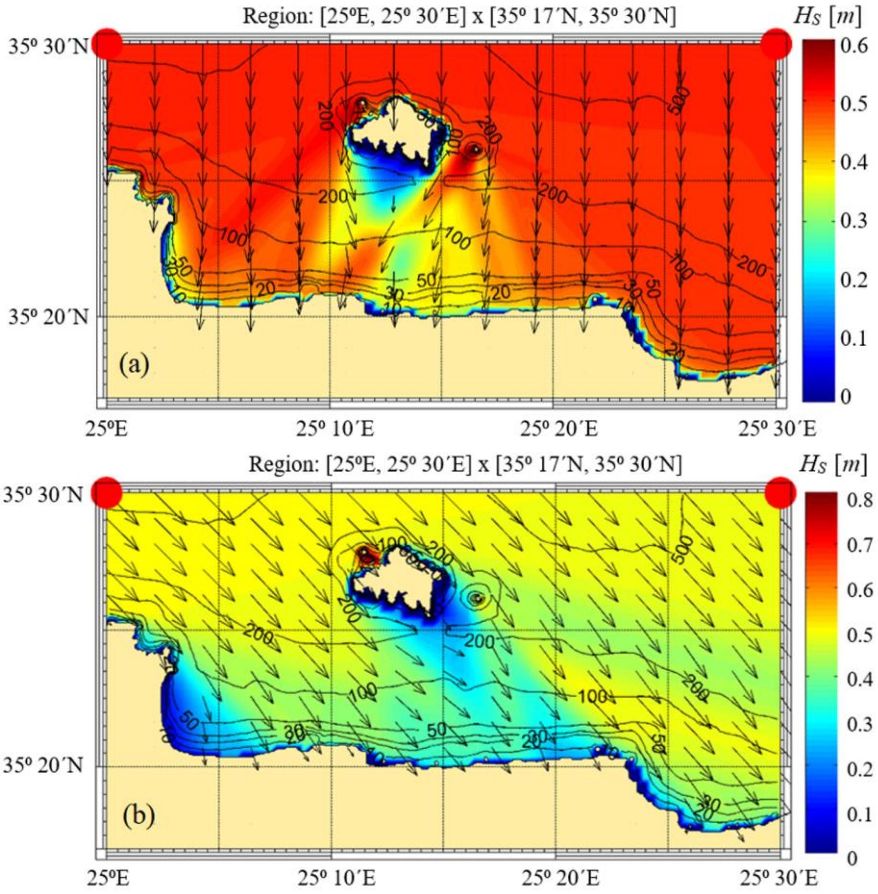

Figure 7-17. Calculated results of the OtN wave transformation technique using SWAN, in the nearshore coastal site of Heraklion in the northern–central part of Crete Island, corresponding to characteristic wave conditions at the offshore boundary. Incident waves from (**a**) North and (**b**) North–West directions.

Table 7-1. Basic statistics of wave parameters at the offshore and nearshore points.

Point	H_S(m)	T_{-10}(s)	$\theta_{Peak\ 1}$(deg)	$\theta_{Peak\ 2}$(deg)
Offshore	0.93	4.70	285	360
Target (TP)	0.67	4.38	315	345

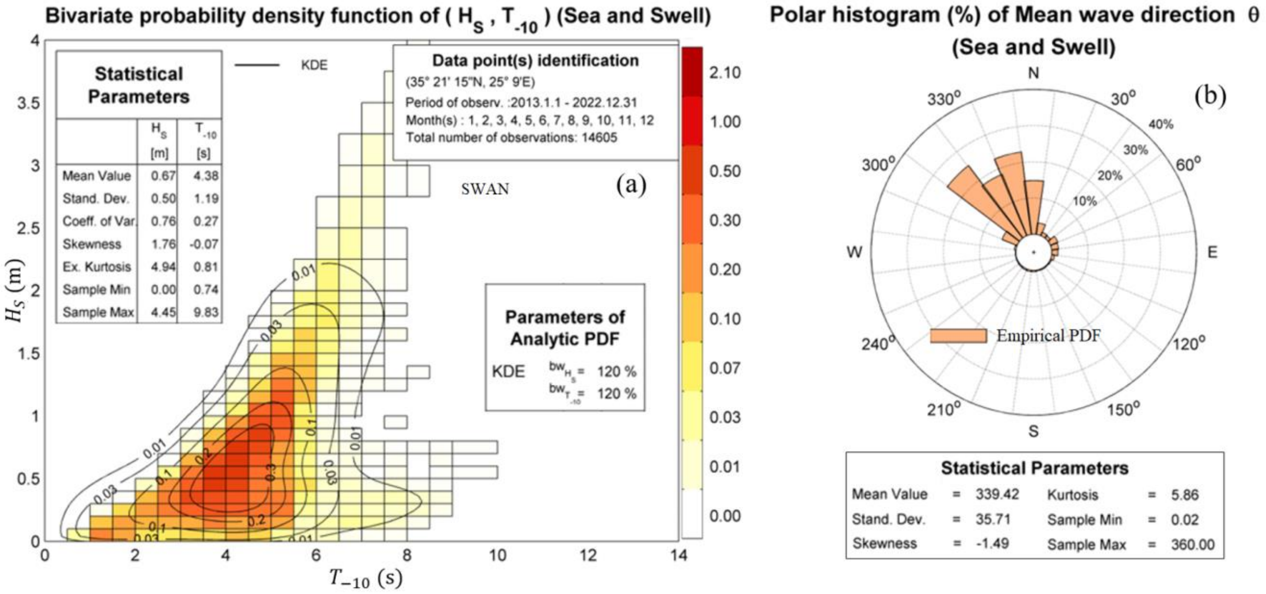

Statistical Parameters

	H_S [m]	T_{-10} [s]
Mean Value	0.67	4.38
Stand. Dev.	0.50	1.19
Coeff. of Var.	0.76	0.27
Skewness	1.76	-0.07
Ex. Kurtosis	4.94	0.81
Sample Min	0.00	0.74
Sample Max	4.45	9.83

Data point(s) identification
(35° 21' 15"N, 25° 9'E)
Period of observ. :2013.1.1 - 2022.12.31
Month(s) : 1, 2, 3, 4, 5, 6, 7, 8, 9, 10, 11, 12
Total number of observations: 14605

Parameters of Analytic PDF
KDE bw_{H_S} = 120 %
$bw_{T_{-10}}$ = 120 %

Statistical Parameters
Mean Value = 339.42
Stand. Dev. = 35.71
Skewness = -1.49
Kurtosis = 5.86
Sample Min = 0.02
Sample Max = 360.00

Figure 7-18. Nearshore wave data at the target point located at a distance of 3.5 km in front of the Heraklion breakwater and depth $h = 15$ m, as obtained by the OtN transformation.

7.2.1. Estimation of absorbed power

The power output of the examined WEC array is quantified by considering the arrangement of five cylindrical WECs at the Heraklion port breakwater, where the local depth is considered constant and equal to $h = 6.67$ m. The floater radius is 1.5 m, and a PTO system characterized by the parameters $B_{PTO} = 10\times B_{33,av}$ (corresponding to $B_{PTO} = 11{,}656.85\ \mathrm{Ns\ m^{-1}}$) and $C_{PTO} = 0.1\times c_{33}$, is considered. All incident wave energy is assumed to be concentrated in the direction normal to the breakwater. This assumption simplifies the calculations by eliminating the need to consider wave directionality. In shallow waters, wave refraction causes the wavefronts to align with the bathymetry contours (refer to Figure 6-7(d) in §6.2.1), which makes the above assumption reasonable for modelling purposes. A 10–year–long time series of nearshore wave parameters, covering the period from January 2013 to December 2022 is used to reconstruct wave spectra using the TMA model (see e.g. Ref. [214] and §6.2.3). Specifically, the output power time series of the 5–WEC system is estimated as,

$$P = \sum_{k=1}^{5}\sum_{i=1}^{N} \rho g a C_g\left(\omega_i\right) A^2\left(\omega_i\right) P_k\left(\omega_i; B_{PTO}\right) , \tag{7.12}$$

where $P_k(\omega_i;\ B_{PTO})$ denotes the normalized power output of the k^{th} WEC, at frequency ω_i and the given B_{PTO} , C_{PTO} , that is estimated using data from the power curves shown in Figure 7-13. Moreover, the coefficients $A^2(\omega_i) = 2S(\omega_i)\Delta\omega$, represent the amplitude of the spectral field at frequency $\omega_i, i = 1,2, \dots . N$, where N is the number of frequencies used to discretize the spectrum $S(\omega_i)$ and $\Delta\omega$ denotes the constant spacing.

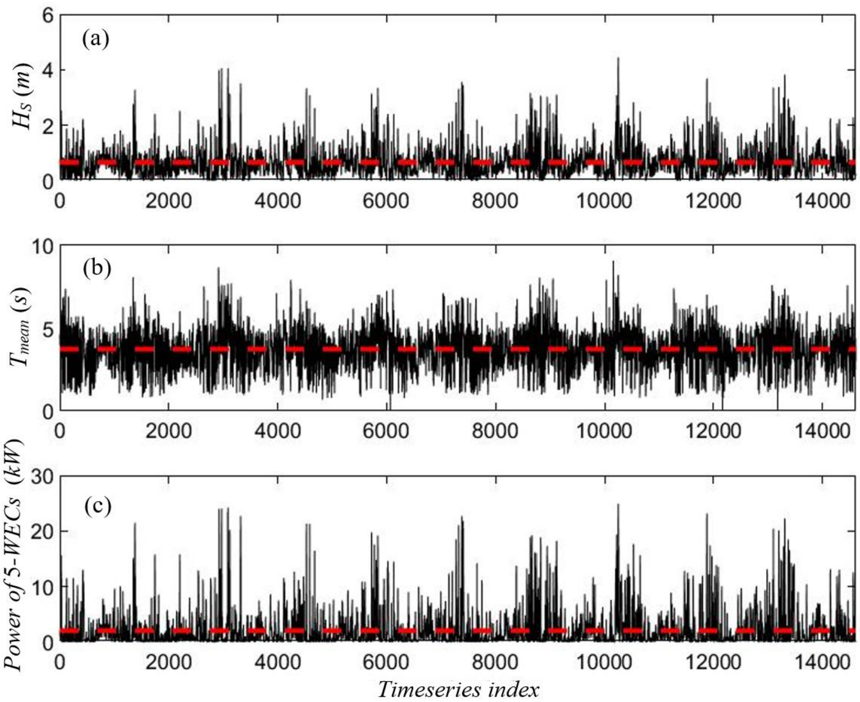

Figure 7-19. 10–year–long time series of nearshore wave data and power output by the considered 5–WEC arrangement at the breakwater. (**a**) Significant wave height H_S (m). (**b**) Mean wave period T_m (s). (**c**) Output power by the system (kW). The mean values are indicated by using dashed lines.

Figure 7-19 illustrates the calculated 10–year–long time series of nearshore wave data and power output, by the considered 5–WEC arrangement at the breakwater of Heraklion port. The annual and seasonal statistics of power production by the system are presented in Figure 7-20 and Figure 7-21, respectively, including data concerning mean values and several other statistical parameters.

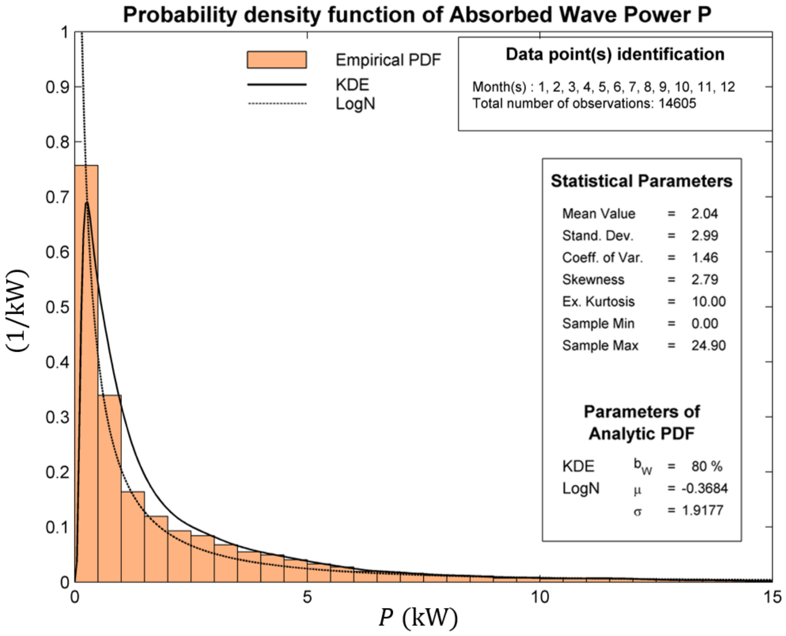

Figure 7-20. Annual statistics of power output by the considered 5–WEC system at Heraklion port breakwater.

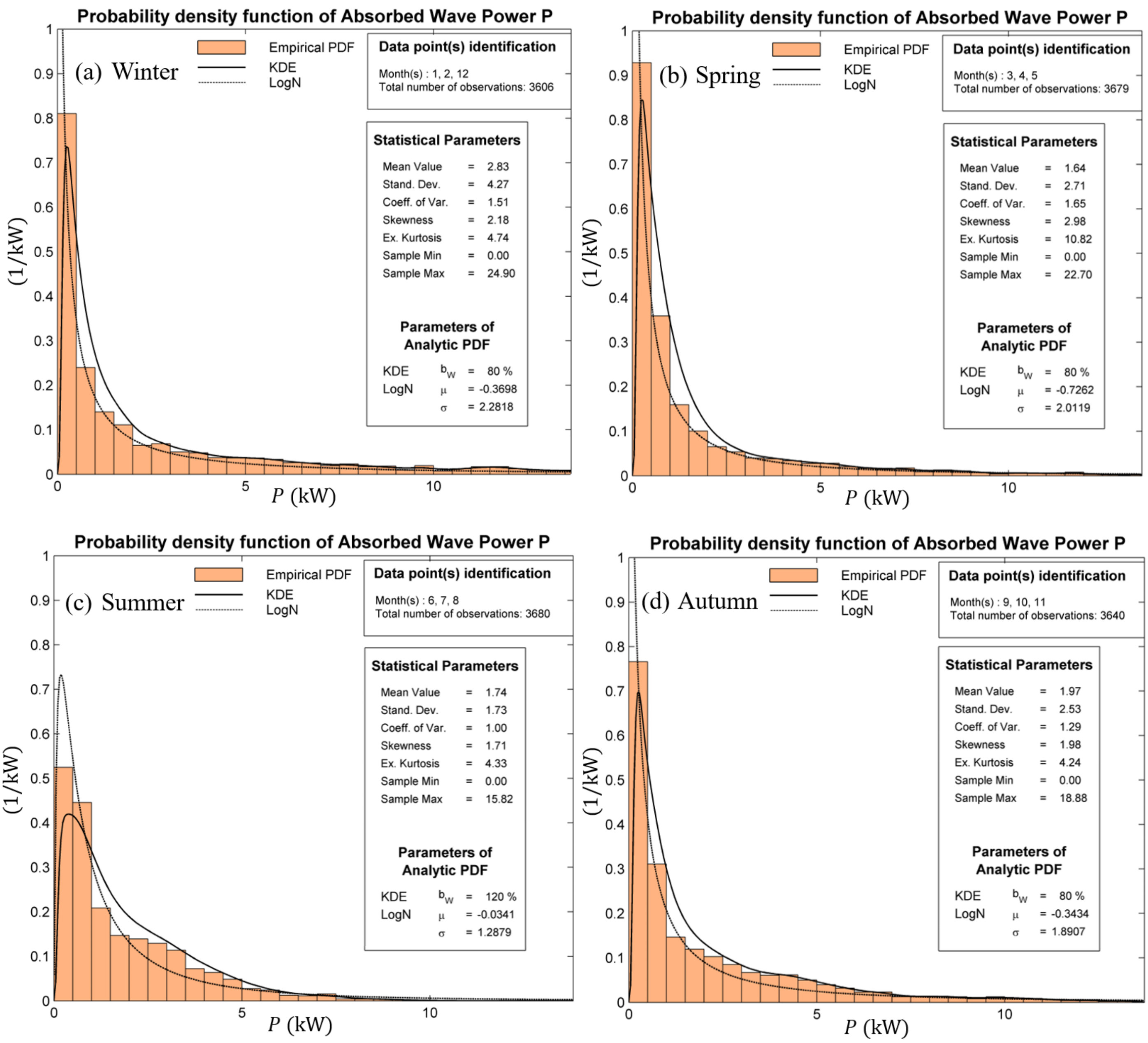

Figure 7-21. Seasonal statistics of the power output by the considered 5–WEC system at Heraklion port breakwater.

Based on the above data, the mean power output of the system is 2.04 kW, corresponding to an annual energy production of 17.7 MWh, and the power production ranges from zero to a maximum value of about 25 kW. For comparison, the corresponding output concerning the same system without the breakwater wall effects is estimated to be 2.3% lower.

7.3. *Discussion and Optimization Considerations*

In this chapter, a 3D hydrodynamic model based on the boundary element method (BEM) is presented and discussed, aiming to evaluate the performance of WEC arrays consisting of multiple heaving bodies attached to the exposed side of a breakwater, which is modelled as a vertical wall. The model accounts for the reflective effects by the wall as well as the hydrodynamic interactions among the multiple devices. Numerical results are presented, accounting for effects of various parameters on power performance, including interactions of multiple floaters, the breakwater wall, as well as the power–take–off (PTO) system parameters. Furthermore, a case study is presented based on data of the above numerical model in conjunction with wave climate data at the port of Heraklion, situated on the north coast of Crete Island, in the Southern Aegean Sea, obtained by an Offshore–to–Nearshore transformation technique.

Although the present ideal flow model does not consider the influence of viscosity, which could become significant at specific frequencies associated with gap resonances [200], it still provides useful results in an extended frequency range and could be exploited for the preliminary evaluation of the system performance and the optimal design and construction contributing to the decarbonization of energy in harbors and neighbor coastal sites. Furthermore, the present BEM method can be easily applied to investigate more general shapes of axisymmetric floaters in one or more degrees of freedom, as well as to study the effects of various control strategies, such as latching techniques that are frequently applied to maximize the power output of the device, by constraining some of the operational characteristics [222].

The energy production potential of the studied configuration could be further enhanced through optimal design improvements, refining key structural and operational aspects. Furthermore, considering additional benefits, compared to offshore installations – which include the ease of installation, the simplicity of maintenance as well as the simpler grid connection – the advantages become even more prominent. These factors not only reduce the complexity of implementation but also contribute to the long–term sustainability and cost–effectiveness of the system. Given these considerations, WEC arrays constitute a valuable contribution in supporting the transition to greener energy solutions in ports and harbors. By integrating these energy production systems, port facilities can reduce their dependence on conventional energy sources and play an active role in promoting the adoption of renewable energy. This aligns with the growing interest in port electrification [223,224], a key development in recent years aiming to reduce emissions and enhance energy efficiency within port operations, thus contributing to the broader efforts towards the reduction of the environmental impact of maritime operations and the enhancement of coastal infrastructure sustainability.

Regarding practical applications of the considered energy stations, it is evident that the selected devices’ natural period in heave can be selected or tuned to coincide with the wave period carrying the highest energy content, based on local wave climatology, in order to maximize the power production. Another critical factor in optimizing energy absorption is the distance of the floaters from the breakwater. As demonstrated by the presented numerical results, the presence of the breakwater can lead to the formation of standing waves in the area, under certain conditions. This phenomenon creates locations of nodes and antinodes, which significantly influence the energy content available for harnessing. Therefore, it is essential to carefully optimize the positioning of WECs to ensure that they are not located at a node, where the wave amplitude is minimal, but rather at an antinode, where the energy density is the highest. Of course, due to the stochastic nature of the incident wave spectra, achieving perfect alignment with the antinodes cannot be guaranteed at all times. Nonetheless, it remains crucial to consider this factor and optimize the arrangement of the floaters for specific wavelengths, taking into account local wave climate data. Further enhancements in power output can be achieved by systematically applying the developed BEM model to optimize various other system parameters, including dimensions, inertial properties and PTO parameters.

In addition to optimizing the latter parameters, a key area for improving design efficiency lies in reducing the computational cost of the simulations. The BEM model, that was developed and discussed in the present chapter, can be used to calibrate reduced–order models, such as the one presented in Ref. [197]. The latter model is based on the modified mild slope equation (MMSE) and it offers the advantage of rapidly scanning a multidimensional parameter space. These reduced models can help identify the most promising subdomains of performance, allowing for a more effective design process. Once the optimal design configurations are identified, a full 3D BEM (or higher fidelity) model can be applied in the final stage to verify and fine–tune the solution, ensuring that the most efficient parameters for energy conversion are selected. This approach can significantly accelerate the design process while also enhancing the overall accuracy of the performance predictions.

8

CONCLUSIONS AND SUGGESTIONS FOR FUTURE WORK

The present dissertation investigates how the marine environment affects the performance of offshore photovoltaic (PV) systems, mainly focusing on the hydrodynamic aspects. Offshore PV systems are examined both in the form of floating energy production units and in configurations mounted on vessels. The operation of wave energy parks comprising multiple point absorber devices is also modelled and investigated, as part of the broader objective of developing the computational tools necessary for studying hybrid wave–solar offshore energy systems. The modelling relies on BEM algorithms, combined with several complementary techniques, including absorbing layers, mirroring and Coupled Mode Systems. The hydrodynamic theory used to develop the BEM models is briefly presented in Appendix A, while details regarding numerical implementation are discussed in Appendices B and C, for completeness purposes.

As concerns FPV units, the results presented in §3 and §4 indicate that the dynamic motion of floating platforms caused by wave activity can negatively impact the performance and power output. Although the drop in power output is not excessive for sea states typically encountered in the Mediterranean, it remains an important factor to consider for optimizing the overall efficiency and long–term viability of floating photovoltaic systems. This effect could be mitigated or potentially reversed by the cooling effects posed by the marine environment, which enhance PV efficiency. A simplified method to incorporate cooling effects into the analysis is discussed in Appendix D. However, the results presented in the main body of the present work do not incorporate these factors. Thus, the modelling of floating photovoltaic systems, along with the combined effects of dynamic motion, cooling mechanisms, and grid connection challenges, remains an interesting topic for further investigation. The accurate estimation of the effects of cooling (as well as wind loads) requires high–fidelity models or experimental measurements, as air flow is highly complex and influenced by factors such as compressibility, turbulence, temperature gradients and surface roughness. Therefore, refined models are needed for more accurate predictions.

The solar ship concept is examined in §5 based on a 33–meter–long catamaran vessel. The modelling relies on a hybrid BEM formulation that incorporates a combination of steady and unsteady models, used to treat the combined effects of incident flow and waves interacting with the twin–hull vessel, supporting an accurate calculation of the total resistance (including the added–wave resistance component) along with the dynamic responses. The effects of forward vessel motion in the analysis cannot be properly accounted for by using dipole singularities in the BEM models. In this case, it is necessary to use source elements, which makes the overall modelling process more computationally demanding (refer to Appendix C). The results indicate that while the mounted PV system can significantly contribute to the vessel's energy demands, the actual contribution depends on several factors, including the vessel's operational profile and the weather conditions. Furthermore, in this case the cooling effect is expected to be significantly enhanced, due to increased apparent wind speeds resulting from the vessel's forward motion (refer to Appendix D). Although the solar PV system can reduce reliance on conventional fuel sources, it is clear that supplementary power from traditional fuels or other energy sources is still required, especially during periods of low sunlight or high energy demand. Therefore, while solar–powered maritime transport solutions are promising, they are likely to be most effective when combined with other energy systems, ensuring increased reliability and sustainability.

The hydrodynamic modelling of wave energy parks, comprising several point absorber devices, is addressed in §6 and §7. In particular, §6 discusses the operation of such parks in nearshore regions, accounting for several environmental and operational factors. These include the local wave climatology and seabed topography, as well as the WECs' shape, dimensions, spacing and PTO parameters. The results reveal a complex behaviour of the wave energy park's q–factor, showing that intra–array interactions can influence the generated power either constructively or destructively. The presented numerical results further demonstrate that the q–factor is highly sensitive to combined variations in frequency and wave propagation direction. Refraction phenomena caused by depth reduction in a selected nearshore region are also modelled, quantifying the effects that they pose both on the forces acting on the floaters and the hydrodynamic coefficients' matrices (refer to Appendix A). Chapter §7, extends the modelling to study arrays of point absorber WECs attached to port breakwaters. In this case, additional reflection phenomena due to the presence of the breakwater need to be included in the analysis. Consequently, the optimization process involves a broader set of parameters compared to WEC parks in open sea conditions, accounting for the interactions between multiple floating devices along with the breakwater. On the other hand, the proximity to shore significantly simplifies maintenance activities, reducing operational costs. Additionally, the shorter distance to the electrical grid facilitates easier and more cost–effective grid connections, enhancing the overall economic viability of the system. This synergy between renewable energy generation and port infrastructure optimization makes WECs on port breakwaters an attractive solution for advancing marine energy technologies.

An exciting prospect lies in the integration of wave and solar energy technologies (see Figure 8-1). This concept involves hybrid platforms where floating PV systems are mounted on floating structures supported by WECs, allowing the simultaneous capture of solar and wave energy. Such systems could optimize the use of marine space while leveraging shared infrastructure, providing a multifunctional solution to increase renewable energy yields. Notably, this hybrid configuration offers the added benefit of reducing the motions of the platform, as the WECs act as dampers while simultaneously generating power. Consequently, losses in solar system efficiency due to excessive platform motions can be mitigated. While the present thesis has explored the fundamentals of these technologies, further research is needed to unlock the potential of such systems.

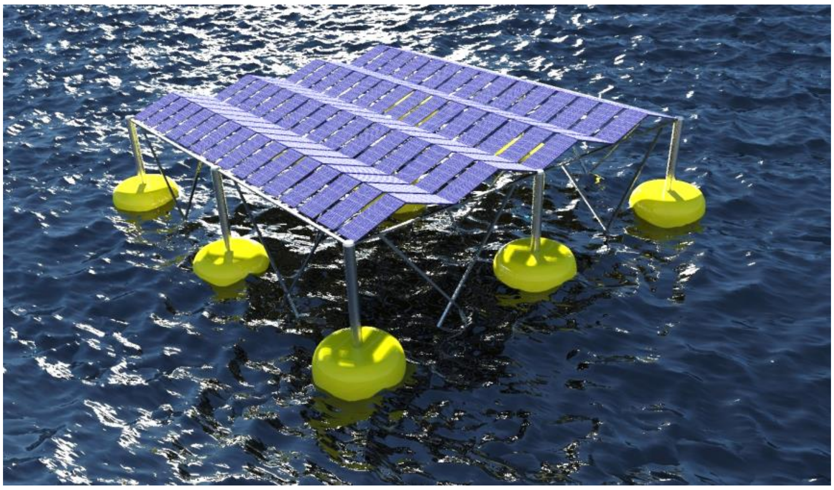

Figure 8-1. Photorealistic illustration of hybrid wave–solar floating unit.

Advanced structural designs, motion–dampening mechanisms and robust mooring systems could reduce the impact of wave–induced motion on PV output. Additionally, the durability of floating PV components under long–term exposure to saltwater needs to be further investigated. For integrated wave–solar platforms, research should evaluate the interaction between wave motion and energy generation, assessing whether wave activity can enhance WEC performance without significantly affecting PV output. Economic feasibility studies and pilot projects will be crucial to determine the viability of these hybrid systems on a larger scale. Additional challenges related to the deployment, operation, and sustainability FPV systems include improving the towing and launching processes, as well as designing robust anchoring systems for deep–sea installations, ensuring stability in remote, deep–water environments, prone to extreme weather conditions. Moreover, the development of specialized operation and maintenance vessels, appropriately equipped for harsh offshore conditions, is essential for the continuous and safe operation of these systems [225].

Another promising offshore renewable energy solution is Floating thin–film photovoltaics. This technology harnesses solar energy at sea while minimizing hydrodynamic impacts. As they are designed to operate on the waterline, these systems maintain thermal equilibrium with the water and are thus characterized by improved energy conversion efficiency. One of the main motivations for the development of the above concept was the lower hydrodynamic impacts on the mooring lines [226], which are expected to result in significantly lower mooring costs compared to other offshore renewable energy technologies.

Other important areas of research in offshore photovoltaics include the environmental and socioeconomic impacts of deploying large–scale PV or hybrid units. Understanding their effects on marine ecosystems is crucial for ensuring sustainable deployment, as the introduction of large structures into the marine environment could alter local biodiversity and affect ecosystems (see e.g., [227]). Research is being conducted to evaluate the long–term impacts on marine life and how these systems can be designed to coexist with the surrounding environment, potentially even benefiting marine ecosystems by providing artificial reefs or creating new habitats [228]. Additionally, investigating the social and economic implications of these technologies is vital for ensuring that they provide net benefits to local communities, especially in remote coastal areas or islands that are not connected to larger power grids.

Integrating energy storage solutions, such as batteries, into these systems could significantly enhance their reliability by addressing the inherent variability in energy generation from solar and wave resources. Efficient storage technologies would enable these hybrid systems to deliver uninterrupted power, even when solar or wave energy generation is minimal, thereby enhancing overall stability and energy accessibility in remote areas.

In conclusion, hybrid energy production systems that combine wave, solar, and wind energy technologies have the potential to transform the use of offshore renewable resources. This integration offers a more stable and diversified energy mix, as wave energy is often more predictable than solar power, particularly during cloudy or nighttime periods, while wind energy can boost the energy production by generating power during times of low sunlight or wave activity. By incorporating multiple renewable resources, these systems become more resilient and reliable, ensuring a consistent energy supply, despite fluctuations in individual resource availability. Such technologies represent a sustainable and efficient approach to clean energy production, contributing significantly to the global transition away from fossil fuels. The future of offshore renewable energy depends on creating integrated systems that harmonize environmental, economic, and social advantages, setting the stage for a sustainable future.

APPENDICES

Appendix A

HYDRODYNAMIC THEORY FOR FLOATING BODIES

In order to study the dynamic interaction phenomena between a floating body and the surrounding fluid, the former is often considered to be rigid. This assumption is valid for bodies of small dimensions, where the effects of deformation can be neglected without significantly impacting the accuracy of the analysis. However, for larger structures such as long ships or extensive offshore platforms, this assumption may introduce errors due to the more pronounced effects of elasticity and deformation under the action of marine loads (see e.g., [229]). Despite these limitations, the rigid body assumption remains valid within the scope of the work discussed in the present thesis, where the primary focus is on small to moderately sized floating bodies. This appendix provides a brief overview of linear hydrodynamic theory for floating bodies and ships, that is extensively used in the context of the present thesis, based on Ref. [230].

Any floating structure can freely move on the surface of the sea, and thus can move in all spatial directions. Therefore, following the above assumption, it has six Degrees of Freedom (DoFs), since it is free to move in the three–dimensional space (i.e., it can perform three linear motions and an equal number of rotations).

Loads (forces and moments) that develop on the structure are due to various causes. Apart from the hydrostatic loads, there are loads due to the prevailing sea state, the wind, joints (i.e., anchoring) etc. The coexistence of all the above, makes the accurate determination of the developed loads particularly complicated. To simplify the analysis, some of the loads are often omitted, due to a small percentage of contribution to the total acting forces and moments. Finally, the equations of motion are derived by appropriately formulating the Momentum and Angular Momentum Change Theorems.

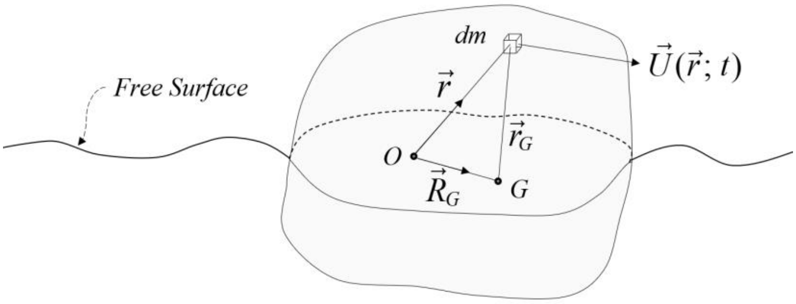

Figure A-1. Sketch of freely floating body of general shape.

Let $[B]$ be a rigid body which floats freely on the sea surface ∂D_{FS}. The center of mass is denoted by G, O is a body–fixed reference point and $\mathbf{R}_G$ stands for the vector $\overrightarrow{OG}$. Furthermore, $\mathbf{r}$ represents the vector radius from the point O to any differential mass element dm of the studied floating body and $\mathbf{r}_G$ is the vector radius from the point G to the same differential mass element dm. The (absolute) velocity $\mathbf{U}_{dm}(\boldsymbol{r};t)$ of the element $dm(\mathbf{r})$ at a given time instant t (see Figure A-1), is given by,

$$\mathbf{U}_{dm}\left(\mathbf{r},t\right)=\mathbf{U}+\mathbf{\Omega}\times\mathbf{r}\ , \tag{A.1}$$

where $\mathbf{U} = (U_1, U_2, U_3)$ is the velocity of the reference point O and $\mathbf{\Omega} = (\Omega_1, \Omega_2, \Omega_3)$ is the angular velocity of the body at the same time instant in 3D space. The momentum of the element dm is then given by the product $(\mathbf{U} + \mathbf{\Omega} \times \mathbf{r})dm$, while the angular momentum of the same element with respect to the point O is expressed by the product $\mathbf{r} \times (\mathbf{U} + \mathbf{\Omega} \times \mathbf{r})dm$. Consequently, the total momentum and angular momentum are respectively given by integration of the above relations over the volume,

$$\lim_{dm\to 0} \sum_{dm} \left(\mathbf{U}+\mathbf{\Omega}\times\mathbf{r}\right) dm = \int_{V_B} \rho_{\mathrm{B}} \left(\mathbf{U}+\mathbf{\Omega}\times\mathbf{r}\right) dV_B \,, \tag{A.2}$$

$$\lim_{dm\to 0} \sum_{dm} \mathbf{r}\times\left(\mathbf{U}+\mathbf{\Omega}\times\mathbf{r}\right) dm = \int_{V_B} \rho_{\mathrm{B}} \mathbf{r}\times\left(\mathbf{U}+\mathbf{\Omega}\times\mathbf{r}\right) dV_B \,, \tag{A.3}$$

where ρ_B is the floating body's density, V_B is the total volume of the body and dV_B is the differential volume element $(dm = \rho_B \, dV_B)$. It must be noted that, for the case of a floating body with forward speed (e.g., ship), the body–fixed reference point O is not stationary, but moves along with the body, at speed $\mathbf{U}_G$. Therefore, the Angular Momentum [Eq. (A.3)] refers to a moving center. This fact must be taken into account for the correct formulation of the Angular Momentum Change Theorem. Based on the above, the theorems of momentum and angular momentum change are expressed as,

$$\frac{d}{dt}\left[\int_{V_B} \rho_B \left(\mathbf{U}+\mathbf{\Omega}\times\mathbf{r}\right) dV_B\right] = \mathbf{F} \,, \tag{A.4}$$

$$\frac{d}{dt}\left[\int_{V_B} \rho_B \mathbf{r}\times\left(\mathbf{U}+\mathbf{\Omega}\times\mathbf{r}\right) dV_B\right] + M\mathbf{U}\times\mathbf{U}_G = \mathbf{K} \,, \tag{A.5}$$

where $\mathbf{F}, \mathbf{K}$ are the total exerted loads (forces, and moments with respect to the point O, respectively) and the term $M\mathbf{U} \times \mathbf{U}_G$ on the left–hand side of Eq. (A.5), is due to the fact that the reference point O moves at speed $\mathbf{U}_G$.

The above equations are a first general form of equations of motion of a freely floating solid body (e.g., ship). Eqs. (A.4) and (A.5) are vector differential equations, which, broken down into components, correspond to six differential equations, which involve two unknown vector functions of time: the velocities $\mathbf{U}(t)$ and the angular velocities $\mathbf{\Omega}(t)$. These functions can be expressed by means of six position functions, i.e., the six degrees of freedom of the solid body. Thus, under the hypothesis of a completely non–deformable solid body, it seems that the system formed by Eqs. (A.4) and (A.5) is "closed" (six equations, six unknown functions), and may thus be solved so that the velocities and motions of the body can be determined. However, this is not the case, due to effects of the surrounding fluid. Specifically, the right–hand side terms of the motion equations, i.e., the loads **F** and **K**, include effects of the surrounding fluid, which are functions of the position and velocity of the solid body (since any movement of the floating structure, whether triggered by wave loads or by any other cause, creates outgoing wave fields which affect the surrounding flow field). Thus, the right–hand terms of the equations of motion [Eqs. (A.4) and (A.5)] contain not only known quantities, but also quantities that depend on (unknown) functions of the left–hand side. Consequently, the loads **F** and **K** must be understood as operators which depend not only on the geometry of the entire hydromechanical system, including the geometry of the floating structure as well as the seabed topography that may be characterized by local irregularities, but also on the unknown functions $\mathbf{U}(t)$ and $\boldsymbol{\Omega}(t)$.

A.1. Reference Frames (Coordinate Systems)

To analyze the kinematic and dynamic quantities involved in the equations of motion of a freely floating rigid body, various coordinate systems can be employed. The most significant of these are a stationary reference frame relative to the Earth's surface, which will be briefly referred to as S.S., and a body–fixed system, briefly referred to as B.S., which is firmly attached to the floating body and tracks all its movements (this coordinate system is also called stability system). In certain situations, moving reference frames that are not body–fixed are also employed. One such instance is the study of the dynamic behaviour of a ship moving with a non–zero average speed while simultaneously performing oscillatory motions around its mean position, due to the influence of waves. In such cases, in addition to the two systems (S.S. and B.S) mentioned above, a moving system is also employed, briefly referred to as M.S., which follows the ship's mean motion. This system can be inertial (if the ship moves at a constant mean speed and zero mean angular velocity) or non–inertial in the general case (for instance, when the ship maneuvers). Another interesting situation, in which a moving non–body–fixed system must be employed, is the study of the dynamic behaviour of two (or more) floating bodies. In this case, the motion is usually referred to a body–fixed system on one body, which is moving, non–inertial and non–body–fixed relative to the other. The three systems (S.S., B.S. and M.S.), with their corresponding notations for the unit vectors and the position vector in space, are presented in Table A-1.

Table A-1. Reference frames used in the study of dynamic behaviour of floating bodies.

Coordinate System	Notation	
Stationary System (S.S),	x_{10}, x_{20}, x_{30} $\mathbf{i}_{10}$, $\mathbf{i}_{20}$, $\mathbf{i}_{30}$ $\mathbf{r}_0$	The plane $x_{10}x_{20}$ coincides with the undisturbed free surface of the water. The x_3–axis is positive above the free surface.
Moving System (M.S)	x_1, x_2, x_3 $\mathbf{i}_1$, $\mathbf{i}_2$, $\mathbf{i}_3$ $\mathbf{r}$	System moving with the mean horizontal velocity of the floating body. If the mean velocity is zero, the M.S. coincides with the S.S.
Body–fixed System (B.S.) (Stability system)	x_{1B}, x_{2B}, x_{3B} $\mathbf{i}_{1B}$, $\mathbf{i}_{2B}$, $\mathbf{i}_{3B}$ $\mathbf{r}_B$	System firmly attached to the floating body, tracking all its movements. In the case where the floating body has planes of symmetry (e.g., ship), the planes of the axes are chosen to coincide with the planes of symmetry.

A.2. Degrees of Freedom

A floating solid body, like any other rigid body moving freely in space, has six Degrees of Freedom (DoFs). That is, its position in space is fully determined by means of six independent generalized coordinates. The first three generalized coordinates (ξ_1, ξ_2, ξ_3) are selected to be the Cartesian coordinates of a reference point O with respect to a stationary (space–fixed)

Coordinate System. For this purpose, a Cartesian coordinate system $\mathbf{x} = (x_1, x_2, x_3)$ is introduced, with the origin placed at the mean water level, coinciding with the structure's center of flotation[1], with the x_3–axis pointing upwards.

The rest of the generalized coordinates, $(\theta_1, \theta_2, \theta_3)$, are chosen to be the angles of rotation about the axes Ox_1, Ox_2 and Ox_3 respectively. Therefore, the generalized coordinates are defined as follows:

ξ_1, ξ_2, ξ_3: Cartesian coordinates of the body–fixed reference point O, relative to the coordinate system moving at the body's average speed.

$\theta_1, \theta_2, \theta_3$: Rotations around the body–fixed axes Ox_{1B}, Ox_{2B} and Ox_{3B}, which, in the first order, are identical to the corresponding rotations around the three axes Ox_1, Ox_2 and Ox_3 of the Coordinate System moving at the average velocity $\mathbf{U}_G$.

The rotations $\theta_1, \theta_2, \theta_3$ will hereafter be denoted as: $\theta_1 = \xi_4$, $\theta_2 = \xi_5$, $\theta_3 = \xi_6$, defining the response vector $\xi_k(t), k = 1,..,6$ which, in the context of linear wave theory, fully describes the dynamic behaviour of the floating body. The first and second derivatives of $\xi_k(t)$ with respect to time define the velocities and accelerations in the corresponding generalized direction. In the case of ships and floating structures (as well as other 6–DoF rigid bodies) the motions have specific names, which are presented in Figure A-2.

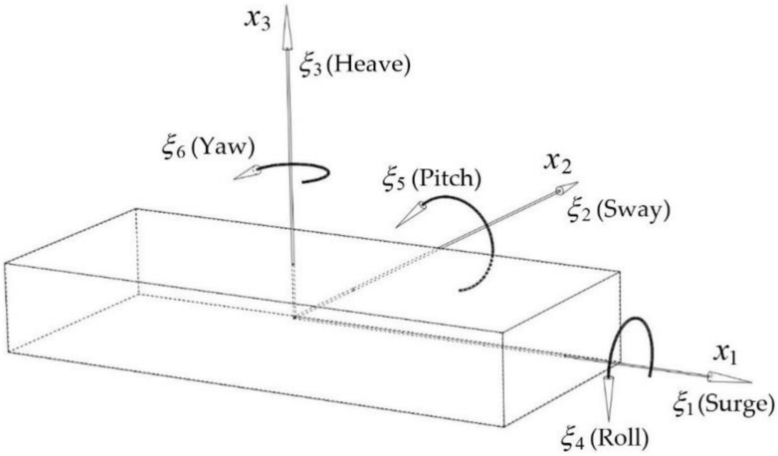

Figure A-2. Nomenclature of ship (or floating body) motions.

A.3. Equations of motion of a floating solid body

To analyze the vector equations of motion for a freely floating solid structure, an appropriate coordinate system (C.S.) must be selected. Using the latter C.S. the vector differential equations are converted to six differential equations expressed in terms of the components of linear and angular velocity.

Using a stationary coordinate system presents significant disadvantages:

---

[1] The geometric center of a floating body's waterplane. The structure rotates about this point if subjected to an external force.

- The body's geometric and inertial characteristics with respect to a stationary system become time–dependent and intricately linked to the unknown velocities.
- Most measurements are taken using accelerometers fixed to the body, providing direct components of inertial accelerations in body–defined directions.

Therefore, a body–fixed reference system is preferable. The origin is chosen to coincide with the body–fixed reference point O, aligning the angular velocity of the coordinate system with that of the floating body. This maintains the geometric and inertial characteristics constant over time, relative to the body–fixed coordinates,

$$\frac{d}{dt}\left(\int_{V_B} \rho_{\mathrm{B}}\left(\mathbf{U}+\mathbf{\Omega}\times\mathbf{r}_B\right)dV_B\right)=\int_{V_B}\rho_{\mathrm{B}}\frac{d}{dt}\left(\mathbf{U}+\mathbf{\Omega}\times\mathbf{r}_B\right)dV_B\,, \tag{A.6}$$

$$\frac{d}{dt}\left(\int_{V_B} \rho_{\mathrm{B}}\mathbf{r}_B\times\left(\mathbf{U}+\mathbf{\Omega}\times\mathbf{r}_B\right)dV_B\right)=\int_{V_B}\rho_{\mathrm{B}}\frac{d}{dt}\left\{\mathbf{r}_B\left(\mathbf{U}+\mathbf{\Omega}\times\mathbf{r}_B\right)\right\}dV_B\,, \tag{A.7}$$

where $\mathbf{r}_B$ is the position vector defined in the body–fixed reference frame. Therefore, the analysis of the left–hand–side members of the equations of motion of the freely floating body in components with respect to the body–fixed coordinate system, requires analysis in components, with respect to the same system, of the inertial derivatives

$$\frac{d}{dt}\left(\mathbf{U}+\mathbf{\Omega}\times\mathbf{r}_B\right)\ \text{and}\ \frac{d}{dt}\left\{\mathbf{r}_B\left(\mathbf{U}+\mathbf{\Omega}\times\mathbf{r}_B\right)\right\}. \tag{A.8}$$

The analysis of the above derivatives with respect to the body–fixed system is achieved by applying the following equation, which states that the time derivative of any arbitrary (inertial) vector $\mathbf{a}(t)$ is equal to its time derivative in the rotating frame $S(t)$, which rotates at angular velocity $\mathbf{\Omega}(t)$, plus the cross product of the angular velocity $\mathbf{\Omega}(t)$ and the vector $\mathbf{a}(t)$,

$$\frac{d\mathbf{a}(t)}{dt}=\partial_t\mathbf{a}(t)\Big|_{S(t)}+\mathbf{\Omega}(t)\times\mathbf{a}(t)\,. \tag{A.9}$$

Using Eq. (A.9), the inertial derivatives involved in the theorems of momentum and angular momentum change are expanded as follows,

$$\frac{d}{dt}\left(\mathbf{U}+\mathbf{\Omega}\times\mathbf{r}_B\right)=\underbrace{\partial_t\mathbf{U}-\mathbf{r}_B\times\partial_t\mathbf{\Omega}}_{Linear\ Terms}+\underbrace{\mathbf{\Omega}\times\mathbf{U}+\mathbf{\Omega}\left(\mathbf{\Omega}\cdot\mathbf{r}_B\right)-\mathbf{r}_B\left(\mathbf{\Omega}\cdot\mathbf{\Omega}\right)}_{Non\text{-}Linear\ Terms} \tag{A.10}$$

$$\begin{aligned}\frac{d}{dt}\left\{\mathbf{r}_B\left(\mathbf{U}+\mathbf{\Omega}\times\mathbf{r}_B\right)\right\}=&\underbrace{\mathbf{r}_B\times\partial_t\mathbf{U}+\left(\mathbf{r}_B\cdot\mathbf{r}_B\right)\partial_t\mathbf{\Omega}-\mathbf{r}_B\left(\mathbf{r}_B\cdot\partial_t\mathbf{\Omega}\right)}_{Linear\ Terms}+\\&\underbrace{\mathbf{r}_B\left(\mathbf{U}\cdot\mathbf{\Omega}\right)-\ \mathbf{U}\left(\mathbf{r}_B\cdot\mathbf{\Omega}\right)+\left(\mathbf{r}_B\times\mathbf{\Omega}\right)\left(\mathbf{r}_B\cdot\mathbf{\Omega}\right)}_{Non\ Linear\ Terms}.\end{aligned} \tag{A.11}$$

The noted linearity / non–linearity in Eqs. (A.10) and (A.11) refers to velocities $\mathbf{U}(t)$ and $\mathbf{\Omega}(t)$. That is, the terms noted as non–linear are terms that contain products of the velocity components of the form $U_k\Omega_m$ or $\Omega_k\Omega_m$.

A.3.1. Linearization

Assuming that all components $U_k(t), \Omega_k(t),\ k = 1,2,3$, are "small", implying that all non–linear terms are of second order and can be neglected, and by using the following nomenclature for "small" quantities,

$$U_k(t) = u_k(t),\ \ \Omega_k(t) = \omega_k(t),\ \ k = 1,2,3, \tag{A.12}$$

the derivatives involved in the theorems of momentum and angular momentum change [Eqs. (A.10) and (A.11)] are simplified as,

$$\frac{d}{dt}(\mathbf{U}+\mathbf{\Omega}\times\mathbf{r}_B) = \partial_t\mathbf{u}-\mathbf{r}_B\times\partial_t\boldsymbol{\omega}, \tag{A.13}$$

$$\frac{d}{dt}\{\mathbf{r}_B(\mathbf{U}+\mathbf{\Omega}\times\mathbf{r}_B)\} = \mathbf{r}_B\times\partial_t\mathbf{u}+(\mathbf{r}_B\cdot\mathbf{r}_B)\partial_t\boldsymbol{\omega}-\mathbf{r}_B(\mathbf{r}_B\cdot\partial_t\boldsymbol{\omega}). \tag{A.14}$$

By substituting the above expressions in the equations of motion [Eqs. (A.4) and (A.5)] and neglecting the non–linear term $M\mathbf{U}\times\mathbf{U}_G$ involved in Eq. (A.5), the following linearized form of the equations of motion is obtained,

$$\left(\int_{V_B}\rho_B dV_B\right)\partial_t\mathbf{u}-\left(\int_{V_B}\rho_B\mathbf{r}dV_B\right)\times\partial_t\boldsymbol{\omega}=\mathbf{F}, \tag{A.15}$$

$$\left(\int_{V_B}\rho_B\mathbf{r}_B dV_B\right)\times\partial_t\mathbf{u}+\underbrace{\int_{V_B}\rho_B\{(\mathbf{r}_B\cdot\mathbf{r}_B)\partial_t\boldsymbol{\omega}-\mathbf{r}_B(\mathbf{r}_B\cdot\partial_t\boldsymbol{\omega})\}dV_B}_{*}=\mathbf{K}. \tag{A.16}$$

These equations, transcribed in matrix form, are extensively used in the scope of the present thesis. Below is the necessary nomenclature that allows the expression of the inertial characteristics of the body [left–hand members of Eqs.(A.15) and (A.16)] in matrix form,

$$\int_{V_B}\rho_B dV_B = M = \text{Mass of the body}, \tag{A.17}$$

$$\int_{V_B}\rho_B\mathbf{r}_B dV_B = \mathbf{J} = (j_1, j_2, j_3) = M\mathbf{R}_G = M(R_{G1}, R_{G2}, R_{G3}). \tag{A.18}$$

The second term of the left–hand side of Eq. (A.16) is rather complicated and requires further attention. If $\mathbf{r}_B = (r_1, r_2, r_3)$ and $\partial_t\omega = (\dot\omega_1, \dot\omega_2, \dot\omega_3)$, then the term becomes,

$$\begin{aligned}
&\int_{V_B}\rho_B\{(\mathbf{r}_B\cdot\mathbf{r}_B)\partial_t\boldsymbol{\omega}-\mathbf{r}_B(\mathbf{r}_B\cdot\partial_t\boldsymbol{\omega})\}dV_B = \\
&\quad=\int_{V_B}\rho_B\left\{\sum_{k=1}^{3}r_k{}^2\sum_{m=1}^{3}\dot\omega_m\mathbf{i}_m-\sum_{k=1}^{3}r_k\mathbf{i}_k\sum_{m=1}^{3}r_m\dot\omega_m\right\}dV_B = \\
&\qquad=\int_{V_B}\rho_B\{(r_2^2+r_3^2)\dot\omega_1-r_1r_2\dot\omega_2-r_1r_3\dot\omega_3\}dV_B\cdot\mathbf{i}_1+ \\
&\qquad\ +\int_{V_B}\rho_B\{-r_2r_1\dot\omega_1+(r_1^2+r_3^2)\dot\omega_2-r_2r_3\dot\omega_3\}dV_B\cdot\mathbf{i}_2+ \\
&\qquad\ +\int_{V_B}\rho_B\{-r_3r_1\dot\omega_1-r_3r_2\dot\omega_2+(r_1^2+r_2^2)\dot\omega_3\}dV_B\cdot\mathbf{i}_3= \\
&\qquad\qquad=\left(\sum_{k=1}^{3}\mathrm{I}_{1k}\dot\omega_k\right)\mathbf{i}_1+\left(\sum_{k=1}^{3}\mathrm{I}_{2k}\dot\omega_k\right)\mathbf{i}_2+\left(\sum_{k=1}^{3}\mathrm{I}_{3k}\dot\omega_k\right)\mathbf{i}_3.
\end{aligned} \tag{A.19}$$

In Eq. (A.19), **I** is the inertial tensor of the body with respect to the axes of the body–fixed system, defined as,

$$I_{kk} = \int_{V_B} \rho_{\mathrm{B}} \left(\sum_{m=1}^{3} r_m^2 - r_k^2 \right) dV_B, \qquad k = 1,2,3, \tag{A.20}$$

$$I_{km} = -\int_{V_B} \rho_{\mathrm{B}} r_k r_m dV_B, \qquad k \neq m, \;\; k,m = 1,2,3. \tag{A.21}$$

The terms $I_{kk}, k = 1,2,3$ are the moments of inertia and the terms $I_{km}, k,m = 1,2,3,\; k \neq m$ are products of inertia (cross–inertia) of the examined body in relation to the body–fixed coordinate system. Using the Eqs. (A.17), … ,(A.21) and analysing in components with respect to the axes of the body–fixed system, Eqs (A.15) and (A.16) are transformed into the following six differential equations,

$$\begin{array}{ccccccccccccc}
M\dot{u}_1 & + & 0 & + & 0 & + & 0 & + & J_3\dot{\omega}_2 & - & J_2\dot{\omega}_3 & = & F_1 \\
0 & + & M\dot{u}_2 & + & 0 & - & J_3\dot{\omega}_1 & + & 0 & + & J_1\dot{\omega}_3 & = & F_2 \\
0 & + & 0 & + & M\dot{u}_3 & + & J_2\dot{\omega}_1 & - & J_1\dot{\omega}_2 & + & 0 & = & F_3 \\
0 & - & J_3\dot{u}_2 & + & J_2\dot{u}_3 & + & I_{11}\dot{\omega}_1 & + & I_{12}\dot{\omega}_2 & + & I_{13}\dot{\omega}_3 & = & K_1 \\
J_3\dot{u}_1 & + & 0 & - & J_1\dot{u}_3 & + & I_{21}\dot{\omega}_1 & + & I_{22}\dot{\omega}_2 & + & I_{23}\dot{\omega}_3 & = & K_2 \\
-J_2\dot{u}_1 & + & J_1\dot{u}_2 & + & 0 & + & I_{31}\dot{\omega}_1 & + & I_{32}\dot{\omega}_2 & + & I_{33}\dot{\omega}_3 & = & K_3
\end{array}, \tag{A.22}$$

where

$\dot{u}_1, \dot{u}_2, \dot{u}_3$	are the rates of change of the inertial velocity **u**, with respect to the body–fixed system (components of $\partial_t \mathbf{u}$),
$\dot{\omega}_1, \dot{\omega}_2, \dot{\omega}_3$	are the rates of change of the angular inertial velocity **ω**, with respect to the body–fixed system (components of $\partial_t \boldsymbol{\omega}$),
F_1, F_2, F_3	are the components of the force **F** and
K_1, K_2, K_3	are the components of the moment **K**.

The six equations contained in Eq. (A.22) can easily be written in matrix form. Grouping these equations into the three "equations of forces" (first three equations), and the three "equations of moments", they can be written in the form,

$$\mathbf{M}_{F\dot{u}} \underline{\dot{u}} + \mathbf{M}_{F\dot{\omega}} \underline{\dot{\omega}} = \underline{F}, \tag{A.23}$$

$$\mathbf{M}_{K\dot{u}} \underline{\dot{u}} + \mathbf{M}_{K\dot{\omega}} \underline{\dot{\omega}} = \underline{K}, \tag{A.24}$$

where $\underline{\dot{u}}, \underline{\dot{\omega}}, \underline{F}, \underline{K}$ are 3 × 1 matrix representations of the vectors $\partial_t \mathbf{u}, \partial_t \boldsymbol{\omega}, \mathbf{F}, \mathbf{K}$, respectively,

$$\underline{\dot{u}} = \begin{pmatrix} \dot{u}_1 \\ \dot{u}_2 \\ \dot{u}_3 \end{pmatrix}, \; \underline{\dot{\omega}} = \begin{pmatrix} \dot{\omega}_1 \\ \dot{\omega}_2 \\ \dot{\omega}_3 \end{pmatrix}, \; \underline{F} = \begin{pmatrix} F_1 \\ F_2 \\ F_3 \end{pmatrix}, \; \underline{K} = \begin{pmatrix} K_1 \\ K_2 \\ K_3 \end{pmatrix}, \tag{A.25}$$

and $\mathbf{M}_{F\dot{u}}, \mathbf{M}_{F\dot{\omega}}, \mathbf{M}_{K\dot{u}}, \mathbf{M}_{K\dot{\omega}}$ are 3 × 3 matrix representations of the inertia characteristics, which according to Eq. (A.22) are equal to,

$$\mathbf{M}_{F\dot{u}} = \begin{pmatrix} M & 0 & 0 \\ 0 & M & 0 \\ 0 & 0 & M \end{pmatrix}, \ \mathbf{M}_{K\dot{\omega}} = \begin{pmatrix} I_{11} & I_{12} & I_{13} \\ I_{21} & I_{22} & I_{23} \\ I_{31} & I_{32} & I_{33} \end{pmatrix},$$
$$\mathbf{M}_{F\dot{\omega}} = -\mathbf{M}_{K\dot{u}} = \begin{pmatrix} 0 & J_3 & -J_2 \\ -J_3 & 0 & J_1 \\ J_2 & -J_1 & 0 \end{pmatrix}. \tag{A.26}$$

As observed in Eq. (A.23), the "equation of forces" includes not only linear accelerations $\underline{\dot{u}}$ but also angular accelerations $\underline{\dot{\omega}}$. Similarly, the "equation of moments" includes both angular accelerations $\underline{\dot{\omega}}$ and linear accelerations $\underline{\dot{u}}$. Therefore, the equations of forces and moments are coupled and the coupling depends on the tables $\mathbf{M}_{F\dot{\omega}}$ and $\mathbf{M}_{K\dot{u}}$, which are functions of the quantity $\mathbf{J} = M\mathbf{R}_G = M\overrightarrow{OG}$. Hence, in the case of a freely floating body, the equations of forces [Eq. (A.23)] are decoupled from the equations of the moments [Eq. (A.24)], if the reference point of the velocities (O) coincides with the center of mass (G). In this case, the equations reduce to

$$\mathbf{M}_{F\dot{u}}\underline{\dot{u}} = \underline{F} \ \text{and} \tag{A.27}$$

$$\mathbf{M}_{K\dot{\omega}}\underline{\dot{\omega}} = \underline{K}. \tag{A.28}$$

An equivalent matrix representation of Eqs. (A.23)–(A.24), which is used extensively in the present thesis is the following,

$$\mathbf{M}\underline{\dot{u}} = \underline{F}, \ \text{or} \ \sum_{m=1}^{6} M_{km}\dot{u}_m = F_k, \quad k = 1,....,6, \tag{A.29}$$

where

$$\mathbf{M} = \begin{pmatrix} \mathbf{M}_{F\dot{u}} & \mathbf{M}_{F\dot{\omega}} \\ \mathbf{M}_{K\dot{u}} & \mathbf{M}_{K\dot{\omega}} \end{pmatrix} = \left(\begin{array}{ccc|ccc} M & 0 & 0 & 0 & J_3 & -J_2 \\ 0 & M & 0 & -J_3 & 0 & J_1 \\ 0 & 0 & M & J_2 & -J_1 & 0 \\ \hline 0 & -J_3 & J_2 & I_{11} & I_{12} & I_{13} \\ J_3 & 0 & -J_1 & I_{21} & I_{22} & I_{23} \\ -J_2 & J_1 & 0 & I_{31} & I_{32} & I_{33} \end{array}\right) \tag{A.30}$$

is the generalized inertial tensor of the body and $\underline{\dot{u}}$, $\underline{F}$ are 6 × 1 matrices (6–dimensional vectors) defined as,

$$\underline{\dot{u}} =^{def} \begin{pmatrix} \dot{u}_1 \\ \dot{u}_2 \\ \dot{u}_3 \\ \dot{u}_4 \\ \dot{u}_5 \\ \dot{u}_6 \end{pmatrix} = \begin{pmatrix} \dot{u}_1 \\ \dot{u}_2 \\ \dot{u}_3 \\ \dot{\omega}_1 \\ \dot{\omega}_2 \\ \dot{\omega}_3 \end{pmatrix}, \ \underline{F} =^{def} \begin{pmatrix} F_1 \\ F_2 \\ F_3 \\ F_4 \\ F_5 \\ F_6 \end{pmatrix} = \begin{pmatrix} F_1 \\ F_2 \\ F_3 \\ K_1 \\ K_2 \\ K_3 \end{pmatrix}, \tag{A.31}$$

where $\underline{\dot{u}}_{k+3} = \underline{\dot{\omega}}_k, k = 1,2,3$ and $\underline{F}_{k+3} = \underline{K}_k, k = 1,2,3$. The 6–dimensional vector $\underline{F}$, which includes the vectors of forces and moments exerted on the body, is also called the generalized load vector. Respectively, the 6–dimensional vector $\underline{\dot{u}}$, which includes the components of the linear and angular accelerations of the body with respect to the body–fixed coordinate system (i.e., the vectors $\partial_t \mathbf{u}$ and $\partial_t \boldsymbol{\omega}$) is also called generalized acceleration. Finally, given that $\underline{\dot{u}} = \underline{\ddot{\xi}}$,

$$\mathbf{M}\underline{\ddot{\xi}} = \underline{F}\,, \text{ or } \sum_{m=1}^{6} M_{km}\ddot{\xi}_m = F_k, \quad k = 1,....,6\,. \tag{A.32}$$

A.3.2. Linearization in the case of a floating body with forward speed

In the case where the floating body (ship) moves at a “high” average speed $\mathbf{U}_G = (U, 0,0)$ along the x_1–axis, while simultaneously performing “small” oscillatory motions with respect to all its degrees of freedom, it can be assumed that,

$$U_1 = U + u_1(t), \quad U_k = u_k(t), \; k = 2,3 \text{ and} \tag{A.33}$$

$$\Omega_k = \omega_k(t) = u_{k+3}(t), \; k = 1,2,3. \tag{A.34}$$

In this case, the products $u_k u_\ell, k, \ell = 1,2..,6$ can be considered negligible (second order) compared to the linear terms and can thus be omitted. However, the products of the form Uu_k are comparable to the linear terms and cannot be ignored. Based on the above, the non–linear terms on the right–hand sides of Eqs. (A.10) and (A.11) are linearized as follows,

$$\boldsymbol{\Omega}\times\mathbf{U} = U\omega_3\mathbf{i}_2 - U\omega_2\mathbf{i}_3 + O(u_k\omega_1)\,, \tag{A.35}$$

$$\boldsymbol{\Omega}(\boldsymbol{\Omega}\cdot\mathbf{r}_B) - \mathbf{r}_B(\boldsymbol{\Omega}\cdot\boldsymbol{\Omega}) = O(\omega_k\omega_1)\,, \tag{A.36}$$

$$\mathbf{r}_B(\mathbf{U}\cdot\boldsymbol{\Omega}) = U\omega_1\mathbf{r}_B + O(u_k\omega_1)\,, \tag{A.37}$$

$$-\mathbf{U}(\mathbf{r}_B\cdot\boldsymbol{\Omega}) = -U(\mathbf{r}_B\cdot\boldsymbol{\omega})\mathbf{i}_1 + O(u_k\omega_1)\,, \tag{A.38}$$

$$(\mathbf{r}_B\times\boldsymbol{\Omega})(\mathbf{r}_B\cdot\boldsymbol{\Omega}) = O(\omega_k\omega_1)\,. \tag{A.39}$$

Moreover, linearization of the term $M\mathbf{U}\times\mathbf{U}_G$ results in,

$$M\mathbf{U}\times\mathbf{U}_G = U(J_1\omega_2 - J_2\omega_1)\mathbf{i}_2 + U(J_1\omega_3 - J_3\omega_1)\mathbf{i}_3 + O(u_k\omega_1). \tag{A.40}$$

Inserting the above relations [Eqs. (A.35)–(A.40)] into the equations of motion [Eqs. (A.4),(A.5)], and writing the latter in matrix form yields,

$$\mathbf{M}_{F\dot{u}}\underline{\dot{u}} + \mathbf{M}_{F\dot{\omega}}\underline{\dot{\omega}} + U\mathbf{M}_{F\omega}\underline{\omega} = \underline{F}, \tag{A.41}$$

$$\mathbf{M}_{K\dot{u}}\underline{\dot{u}} + \mathbf{M}_{K\dot{\omega}}\underline{\dot{\omega}} + U\mathbf{M}_{K\omega}\underline{\omega} = \underline{K}, \tag{A.42}$$

where the new matrices $\mathbf{M}_{F\omega}$ and $\mathbf{M}_{K\omega}$ are equal to,

$$\mathbf{M}_{Fu} = \begin{pmatrix} 0 & 0 & 0 \\ 0 & 0 & M \\ 0 & -M & 0 \end{pmatrix}, \quad \mathbf{M}_{K\omega} = \begin{pmatrix} 0 & -J_2 & -J_3 \\ 0 & J_1 & 0 \\ 0 & 0 & J_1 \end{pmatrix}. \tag{A.43}$$

Eqs. (A.41) and (A.42) can also be expressed in unified matrix form – analogous to Eq. (A.29) – as follows,

$$\mathbf{M}\underline{\dot{u}} + U\,\mathbf{N}\underline{u} = \underline{F}\,, \tag{A.44}$$

where

$$\mathbf{N} = (N_{km})_{6\times 6} = \begin{pmatrix} 0 & \mathbf{M}_{F\omega} \\ 0 & \mathbf{M}_{K\omega} \end{pmatrix} = \begin{pmatrix} 0 & 0 & 0 & 0 & 0 & 0 \\ 0 & 0 & 0 & 0 & 0 & M \\ 0 & 0 & 0 & 0 & -M & 0 \\ 0 & 0 & 0 & 0 & -J_2 & -J_3 \\ 0 & 0 & 0 & 0 & J_1 & 0 \\ 0 & 0 & 0 & 0 & 0 & J_1 \end{pmatrix}. \tag{A.45}$$

Finally, taking into account that the generalized acceleration equals $\underline{\dot{u}} = \underline{\ddot{\xi}}$, Eq. (A.44) becomes,

$$\mathbf{M}\underline{\ddot{\xi}} + U\mathbf{N}\underline{\dot{\xi}} = \underline{F}\,, \text{ or } \sum_{m=1}^{6} M_{km}\ddot{\xi}_m + UN_{km}\dot{\xi}_m = F_k\,. \tag{A.46}$$

A.3.3. Hydrostatic Loads

To maintain simplicity in the analysis, the zero–speed case is considered hereafter. The total (constant) forces and moments (relative to a reference center) that develop due to the permanent part of the hydrostatic pressure, are balanced by the body’s weight. However, when a floating body performs small motions around a position of stable hydrostatic equilibrium, additional hydrostatic loads develop. The right–hand–side of Eq. (A.32) represents the total loads acting on a floating structure, which in the general case include hydrodynamic, hydrostatic and external components. By isolating the hydrostatic components, their individual contributions to the overall loading condition can be better understood. The additional hydrostatic loads act as restoring forces (and moments) and are defined as,

$$\underline{F}^{(hydrostatic)} = -\mathbf{C}\cdot\underline{\xi}\,, \tag{A.47}$$

where $\mathbf{C}$ is a 6×6 matrix of the form:

$$\mathbf{C} = \begin{pmatrix} 0 & 0 & 0 & 0 & 0 & 0 \\ 0 & 0 & 0 & 0 & 0 & 0 \\ 0 & 0 & C_{33} & C_{34}\big|^{2} & C_{35}\big|^{1} & 0 \\ 0 & 0 & C_{43}\big|^{2} & C_{44} & C_{45}\big|^{1,2} & 0 \\ 0 & 0 & C_{53}\big|^{1} & C_{54}\big|^{1,2} & C_{55} & 0 \\ 0 & 0 & 0 & 0 & 0 & 0 \end{pmatrix}, \tag{A.48}$$

where

$$C_{33} = \rho g A\,, \tag{A.49}$$

$$C_{34} = C_{43} = \rho g A_2\,, \tag{A.50}$$

$$C_{35} = C_{53} = \rho g A_1\,, \tag{A.51}$$

$$C_{44} = Mg\overline{GB} + \rho g A_{22}\,, \tag{A.52}$$

$$C_{45} = C_{54} = -\rho g A_{12}, \tag{A.53}$$

$$C_{55} = Mg\overline{GB} + \rho g A_{11}. \tag{A.54}$$

In the above equations, M is the mass of the floating body, A is the waterplane area and A_k, A_{km} are the first and second moments of inertia of the waterplane area, respectively, defined as,

$$A_k = \int_A x_k \, dA, \quad A_{km} = \int_A x_k x_m dA. \tag{A.55}$$

Furthermore, $\overline{GB}$ is the vertical distance between the center of gravity G and the center of buoyancy B of the floating body, considered positive when B is higher than G. The elements of **C** define the hydrostatic coefficients of the floating body. The notations $C_{km}|^{\,i}$ (respectively $C_{km}|^{\,i,j}$) is used to state that the corresponding hydrostatic coefficients are zero when the plane $x_{iB} = 0$ (respectively the planes $x_{iB} = 0$ and $x_{jB} = 0$) is a symmetry plane of the geometry.

The form of the Matrix **C**, and specifically the fact that its first, second and sixth lines (that correspond to surge, sway and yaw motions) are zero, reflects the natural fact that horizontal motions (that is motions on the horizontal plane – lacking a vertical component), do not induce hydrostatic reactions.

Based on the above, the equations of motion [see Eq. (A.29)] of a body oscillating around a position of stable hydrostatic equilibrium becomes,

$$\mathbf{M}\ddot{\underline{\xi}} + \mathbf{C}\underline{\xi} = \underline{F}^{(ext)} + \underline{F}^{(HD)}. \tag{A.56}$$

A.3.4. Hydrodynamic Loads

Ignoring viscosity and assuming irrotational flow (potential flow) the velocity field $\mathbf{v}(\mathbf{x}, t)$ is expressed by a velocity potential $\Phi(\mathbf{x}, t)$ via the relation,

$$\mathbf{v}(\mathbf{x},t) = \nabla\Phi(\mathbf{x},t), \ \mathbf{x} \in D, \tag{A.57}$$

where D is the geometric domain occupied by the fluid. If $p^{(HD)} = p^{(HD)}(\mathbf{x}, t)$ is the hydrodynamic pressure exerted on the wetted surface area, the developing hydrodynamic loads (forces and moments) are given by the following equations,

$$F^{(HD)} = \iint_{\partial D_B} p^{(HD)}(\mathbf{x},t)\mathbf{n}\partial S_B, \tag{A.58}$$

$$K^{(HD)} = \iint_{\partial D_B} p^{(HD)}(\mathbf{x},t)\mathbf{r}\times\mathbf{n}\partial S_B. \tag{A.59}$$

The above two relations can be written in a unified form with the aid of the generalized (six–dimensional) "normal" vector $\underline{n} = n_k, k = 1,..,6$, which is defined as follows: n_1, n_2, n_3 are the three components of the (usual) normal vector, and n_4, n_5, n_6 are the three components of the vector $\mathbf{r} \times \mathbf{n}$, that is,

$$\begin{cases} n_4 = r_2 n_3 - r_3 n_2 \\ n_5 = r_3 n_1 - r_1 n_3 \\ n_6 = r_1 n_2 - r_2 n_1 \end{cases} . \tag{A.60}$$

Based on the above, Eqs. (A.58) and (A.59) can be expressed as,

$$F^{(HD)} = \iint_{\partial D_B} p^{(HD)}(\mathbf{x},t) n_k \partial S_B, \quad k = 1, 2, \ldots\ldots, 6. \tag{A.61}$$

Furthermore, since the motions and velocities of all points of the hydromechanical system are assumed to be small, the hydrodynamic equations can be linearized, in accordance with the corresponding linearization of solid body motion equations. Under these conditions, the hydrodynamic pressure $p^{(HD)}$ is expressed by the velocity potential via the relation,

$$p^{(HD)}(\mathbf{x},t) = -\rho \frac{\partial \Phi(\mathbf{x},t)}{\partial t} \equiv -\rho\, \dot{\Phi}(\mathbf{x},t). \tag{A.62}$$

Therefore, the hydrodynamic loads [Eq. (A.61)], which are exerted on the floating body by the surrounding fluid, are given by,

$$F^{(HD)} = -\rho \iint_{\partial D_B} \frac{\partial \Phi(\mathbf{x},t)}{\partial t}(\mathbf{x},t) n_k \partial S_B, \quad k = 1, 2, \ldots\ldots, 6, \tag{A.63}$$

where, due to linearization, ∂D_B now denotes the mean position of the body's wetted surface.

A.4. The General Hydrodynamic Problem

The discussed hydrodynamic problem involves two unknown fields, namely the velocity potential $\Phi(\mathbf{x},t)$ and the free surface elevation $\eta(x_1,x_2,t)$, which plays the role of a time dependent (unknown) upper boundary of the flow domain D. The unknown positions and velocities of the body are also involved in the formulation. The two unknown fields $\Phi(\mathbf{x},t)$ and $\eta(x_1,x_2,t)$ must satisfy the following equations and conditions:

- In the interior of the flow field $D = D(\eta)$, the potential $\Phi(\mathbf{x},t)$ must satisfy the Laplace equation, which expresses continuity (conservation of mass) and the irrotationality of the flow field,

$$\nabla^2 \Phi(\mathbf{x},\, t) = 0, \;\; \mathbf{x} \in D. \tag{A.64}$$

- The condition that applies on the body's wetted surface imposes continuity of the normal velocities of the fluid and the solid body (impermeability condition),

$$\frac{\partial \Phi(\mathbf{x},t)}{\partial \mathbf{n}} = (\mathbf{u} + \boldsymbol{\omega} \times \mathbf{r})\mathbf{n} = \mathbf{u}\cdot\mathbf{n} + \boldsymbol{\omega}\cdot(\mathbf{r}\times\mathbf{n}) = \sum_{k=1}^{6} \dot{\xi}_k n_k, \;\; \mathbf{x} \in \partial D_{\mathrm{B}}. \tag{A.65}$$

- On the free surface ∂D_{FS}, two Boundary Conditions (BCs) apply, namely the dynamic condition (pressure = constant), which after linearization is written in the form,

$$\frac{\partial \Phi(x_1,x_2,t)}{\partial t}+g\eta(x_1,x_2,t)=0,\quad \mathbf{x}\in\partial D_{FS}\xrightarrow{Linearization}(\mathrm{x}_3=0),\tag{A.66}$$

and the kinematic condition (vertical velocity of the surface = vertical velocity of surface elements of the fluid), which after linearization becomes,

$$\frac{\partial \Phi(x_1,x_2,t)}{\partial x_3}=\frac{\partial \eta(x_1,x_2,t)}{\partial t},\qquad \mathbf{x}\in\partial D_{FS}\xrightarrow{Linearization}(\mathrm{x}_3=0).\tag{A.67}$$

Eliminating the unknown field $\eta(x_1,x_2,t)$, which expresses the free surface elevation from Eqs. (A.66) and (A.67) results in the following (mixed) condition for $\Phi(\mathbf{x},t)$,

$$\frac{\partial^2 \Phi(x_1,x_2,t)}{\partial t^2}+g\frac{\partial \Phi(x_1,x_2,t)}{\partial x_3}=0,\ \mathrm{x}_3=0.\tag{A.68}$$

- At the seabed (in cases of shallow or intermediate water depth, where there is interaction of the flow field with the seabed), the potential function must satisfy the impermeability condition,

$$\frac{\partial \Phi(\mathbf{x},t)}{\partial \mathbf{n}}=0,\quad \mathbf{x}\in\partial D_{SB}.\tag{A.69}$$

- The above conditions must be supplemented by an appropriate “infinity condition”, which describes the behaviour of the potential, in large distances from the body, i.e., when $|\mathbf{x}|\to\infty$. Such conditions can be implemented in several ways. In this dissertation’s context, the treatment of the flow fields’ behaviour at infinity is treated by perfectly matched layers (absorbing layers) or Dirichlet–to–Neumann (DtN) operators that match the computed solutions to known analytical relations that apply outside of the computational domains. Another way to treat the “radiating” behaviour of the computed fields is the Sommerfeld’s radiation condition, see e.g., [152].

Assuming that the whole hydromechanical system is characterized by time–harmonic behaviour with frequency ω, it holds that,

$$\Phi(\mathbf{x},t)=\mathrm{Re}\{\varphi(\mathbf{x})\exp(i\omega t)\},\tag{A.70}$$

where $\varphi(\mathbf{x})$ plays the role of the complex amplitude of the time–harmonic quantity $\Phi(\mathbf{x},t)$. Similar representations, involving complex amplitudes, can be defined for every quantity that changes harmoniously with time, e.g., the free surface elevation, or the studied structure’s response in the k^{th} generalized direction,

$$\xi_k(t)=\mathrm{Re}\{\tilde{\xi}_k\exp(i\omega t)\},k=1,2,\ldots,6,\tag{A.71}$$

$$\eta(x_1,x_2,t)=\mathrm{Re}\{\tilde{\eta}(x_1,x_2)\exp(i\omega t)\},\tag{A.72}$$

where the tilde is introduced to denote complex amplitudes. An equivalent representation for Eqs. (A.70)–(A.72), can be derived by considering harmonic time dependence of the form $\exp(-i\omega t)$. In the present work’s framework, both the above formulations are used.

Replacing the above representations in the BVP described by Eqs. (A.64)–(A.69), results in the following,

$$\nabla^2\varphi(\mathbf{x}) = 0,\ \mathbf{x}\in D, \tag{A.73}$$

$$\frac{\partial\varphi(\mathbf{x})}{\partial n} = \sum_{k=1}^{6} i\omega\tilde{\xi}_k n_k,\ \mathbf{x}\in\partial D_B, \tag{A.74}$$

$$\frac{\omega^2}{g}\varphi(\mathbf{x}) + \frac{\partial\varphi(\mathbf{x})}{\partial x_3} = 0,\ \mathbf{x}\in\partial D_{FS}, \tag{A.75}$$

$$\frac{\partial\varphi(\mathbf{x})}{\partial n} = 0,\ \mathbf{x}\in\partial D_{SB}. \tag{A.76}$$

From Eq. (A.74) it is evident that the potential of the total field is coupled to the motions of the floating body. Moreover, the dynamic equations of motion [Eq. (A.56)] which, using the representations of complex amplitudes [Eqs. (A.70)–(A.72)] become,

$$\left[(i\omega)^2\mathbf{M} + \mathbf{C}\right]\underline{\tilde{\xi}} = \underline{\tilde{F}}^{(ext)} + \underline{\tilde{F}}^{(HD)}, \tag{A.77}$$

are coupled to the field's potential by the expression of the hydrodynamic forces [Eq. (A.63)].

Eqs. (A.73)–(A.77) form a complete system of coupled equations in terms of the potential and the body's responses, which can be used to determine the harmonically oscillating behaviour of the hydromechanical system. Prior to that however, the body's equations of motion must be uncoupled from the hydrodynamic equations. This is achieved by introducing an appropriate linear decomposition of the potential function which allows for the hydrodynamic interaction to be expressed via hydrodynamic coefficients, that are independent of body motion.

A.4.1. Decomposition of the flow field

The linearity of Eqs. (A.73)–(A.76) allows for the introduction of the following linear decomposition for the complex potential,

$$\varphi(\mathbf{x}) = \varphi_0(\mathbf{x}) + \varphi_d(\mathbf{x}) + \sum_{k=1}^{6} i\omega\tilde{\xi}_k\varphi_k(\mathbf{x}). \tag{A.78}$$

In Eq. (A.78), φ_0 denotes the complex amplitude of the incident field while φ_d stands for the diffraction (or scattering) potential. This potential describes the "modification" imposed on the incident field due to the presence of the floating body, with the latter being maintained stationary at its mean position. In cases where the water depth is constant or the water is deep, φ_0 is analytically available. Otherwise, it must be evaluated by appropriate numerical schemes; see e.g. [81,82]. Furthermore, φ_d can be evaluated as solution to the BVP described by Eqs. (A.73), (A.75) and (A.76) (for $\varphi = \varphi_d$) using the following boundary condition on the wetted surface,

$$\frac{\partial\varphi_d(\mathbf{x})}{\partial n} = -\frac{\partial\varphi_0(\mathbf{x})}{\partial n},\ \mathbf{x}\in\partial D_B, \tag{A.79}$$

which leads to the superposition of the incident and diffracted fields to satisfy a no–entrance condition on ∂D_B.

Assuming that the floating body performs forced oscillations of frequency ω and (complex) amplitude $\tilde{\xi}_k, k = 1,2, \ldots 6$, and that enough time has passed following the initiation of body motion, (and therefore the transient effects have died out), the surrounding fluid will be performing an oscillating motion of the same frequency ω (due to linearity). The total potential of the resulting flow (stimulated exclusively by the motion of the body) will then be a time–harmonic function of the form,

$$\Phi_R(\mathbf{x},t) = \mathrm{Re}\{\varphi_R(\mathbf{x})\exp(i\omega t)\}, \tag{A.80}$$

which must also satisfy Eqs. (A.73)–(A.76). The form of the impermeability condition on the wetted surface [Eq. (A.74)], combined with the assumption that the fluid is not stimulated by any other cause, other than the oscillation of the body, lead to the following linear decomposition for the radiation potential,

$$\varphi_R(\mathbf{x}) = \sum_{k=1}^{6} i\omega\xi_k\varphi_k(\mathbf{x}). \tag{A.81}$$

Substituting the above equation in Eq. (A.74), results in,

$$\sum_{k=1}^{6} i\omega\tilde{\xi}_k\left(\frac{\partial\varphi_k(\mathbf{x})}{\partial n}\right) = \sum_{k=1}^{6} i\omega\tilde{\xi}_k n_k,\ \mathbf{x}\in\partial D_B \Rightarrow \tag{A.82}$$

$$\sum_{k=1}^{6} \tilde{\xi}_k\left(\frac{\partial\varphi_k(\mathbf{x})}{\partial n} - n_k\right) = 0,\ \mathbf{x}\in\partial D_B. \tag{A.83}$$

Applying Eq. (A.83) for $\tilde{\xi}_k = 1$ leads to,

$$\frac{\partial\varphi_k(\mathbf{x})}{\partial n} = n_k,\ \mathrm{k}=1,2,\ldots,6,\ \mathbf{x}\in\partial D_B. \tag{A.84}$$

Therefore, the (radiation) potential of the flow induced by unitary oscillation of the body towards the k^{th} generalized direction can be evaluated as solution to the BVP defined by Eqs. (A.73), (A.75) and (A.76) (for $\varphi = \varphi_k$) supplemented by Eq. (A.84).

A.4.2. Decomposition of the hydrodynamic loads

Based on the decomposition of the complex potential, as it is described in the previous subsection, the loads exerted on the floating body are equal to [see Eq. (A.63)],

$$\begin{aligned} F_k^{(HD)} &= -(i\omega)^2\rho\left[A\iint_{\partial D_B}\varphi_0 n_k\partial S_B + A\iint_{\partial D_B}\varphi_d n_k\partial S_B + \rho\sum_{\ell=1}^{6}\tilde{\xi}_\ell\iint_{\partial D_B}\Phi_\ell n_k\partial S_B\right] \equiv \\ &\equiv F_{0k} + F_{dk} + \sum_{\ell=1}^{6}F_{\ell k}. \end{aligned} \tag{A.85}$$

In the above equation, an incident field of amplitude A has been considered, which leads to a diffraction field scaled by the same factor. Additionally, the potential functions of the incident and diffracted fields have been multiplied (and divided) by $(i\omega)$ so that this term can be factored out from the entire set of expressions that define the total potential. It should be noted that an additional term $(i\omega)$ was already present in the equation due to differentiation with respect to time; [see Eq. (A.63)]. Therefore, the total hydrodynamic loads comprise the following individual terms:

- The Froude–Krylov loads (forces and moments)

  $$F_{0k} = -(i\omega)^2 \rho A \iint_{\partial D_B} \varphi_0 n_k \partial S_B \,, \tag{A.86}$$

  which are solely due to the undisturbed incident wave field. They can be calculated directly (without solving the hydrodynamic problem), by integrating the pressure of the undisturbed incident flow field (multiplied by the corresponding component of the generalized normal vector) on the wetted surface.

- The diffraction loads (forces and moments)

  $$F_{dk} = -(i\omega)^2 \rho A \iint_{\partial D_B} \varphi_d n_k \partial S_B \,, \tag{A.87}$$

  that are due to the dynamic pressure induced by the diffraction potential. For their calculation, it is first required to solve for the diffracted field.

- The radiation loads (forces and moments)

  $$F_{\ell k} = -(i\omega)^2 \rho \tilde{\xi}_\ell \iint_{\partial D_B} \varphi_\ell n_k \partial S_B, \; k = 1, 2, \ldots\ldots, 6 \,, \tag{A.88}$$

  that are due to the pressure fields “radiated” by the oscillating body. These loads result from integration of the pressure field that is produced by the body, when the latter performs forced oscillations of unitary amplitude towards the k^{th} (generalized) direction, on the undisturbed – by any other reason – free surface.

A.4.3. Hydrodynamic coefficients

By setting

$$\Pi_{\ell k} = \rho \iint_{\partial D_B} \varphi_\ell n_k \partial S_B \,, \tag{A.89}$$

the expression of the radiation loads becomes,

$$F_{\ell k} = -(i\omega)^2 \xi_\ell \Pi_{\ell k} \,. \tag{A.90}$$

The quantities $\Pi_{\ell k}$ depend not only on the geometry of the floating body (and of the whole field, in general), but also on the frequency of motion, since the radiation potentials depend on both the geometry and the frequency [via the free surface BC – Eq. (A.68)]. Furthermore, the existence of a free surface and a fluid extending to infinity (in all horizontal directions) lead the potential (and therefore the quantities $\Pi_{\ell k}$) to take complex values. Based on the above, $\Pi_{\ell k}$ equals

$$\Pi_{\ell k} = \Pi_{\ell k}(\omega) = A_{\ell k}(\omega) + \frac{1}{i\omega} B_{\ell k}(\omega), \tag{A.91}$$

where $A_{\ell k}(\omega)$ and $B_{\ell k}(\omega)$ are real numbers. Introducing the above equation in Eq. (A.90) results in,

$$F_{\ell k} = F_{\ell k}(\omega) = -(i\omega)^2 \tilde{\xi}_\ell A_{\ell k}(\omega) - i\omega \tilde{\xi}_\ell B_{\ell k}(\omega) \,. \tag{A.92}$$

Thus, the radiation loads in the frequency domain, are split in two parts (per frequency):

- one proportional to the acceleration $[\ddot{\xi}_\ell = (i\omega)^2\tilde{\xi}_\ell]$ of the floating body, with ratio coefficient $A_{\ell k}(\omega)$ which is called added inertial coefficient (added mass or added moment of inertia, depending on its units), and
- one proportional to the velocity $[\dot{\xi}_\ell = (i\omega)\tilde{\xi}_\ell]$ of the body, with ratio coefficient $B_{\ell k}(\omega)$, called radiation damping coefficient.

Based on the above analysis the equations of motion of the floating body [expressed in the frequency domain; see Eq. (A.77)], assuming that there are no external forces, become,

$$(i\omega)^2\left(\mathbf{M}+\mathbf{A}(\omega)\right)\tilde{\xi}+(i\omega)\mathbf{B}(\omega)\cdot\tilde{\xi}+\mathbf{C}\cdot\tilde{\xi}=\mathbf{F}_0(\omega)+\mathbf{F}_d(\omega). \tag{A.93}$$

A.5. Numerical Implementation

Solutions of potential flow problems in hydrodynamics, that are governed by the Laplace equation – such as the one discussed here – can be obtained by distributing elementary solutions (of the governing equation) of continuously varying strength on the flow domain's boundary. This property derives from the ability to reformulate the problem and express it as a boundary integral equation (see e.g., [133]), and it also applies to problems governed by other linear differential equations (e.g., Helmholtz, Poisson's equation, etc.), for which the superposition principle holds. The latter principle states that a linear system's response to a set of inputs equals the sum of responses to each individual input.

The first order BEM (Boundary element method) formulation is built on the basis of the assumption that the singularity strengths are piecewise constant on a discretized version of the studied domain's boundary and thus, the solution is reduced to computing a finite vector that defines the (constant) strength of the singularity distribution on each of the "pieces" (panels or boundary elements). The elements can be linear segments in the case of a formulation in two dimensions, or 2D panels in three–dimensional analysis. More specifically, in three–dimensional analysis the panels can take many different shapes, such as triangular or rectangular. Although the former shape offers more flexibility in the modelling, rectangular (4–node) elements facilitate the definition of structured meshes, due to simpler connectivity relationships to adjacent elements. (Higher order BEM formulations also utilize 8 or more nodes on each panel; see e.g., [231,232]).

The potential and velocity at any specific point inside the domain (or on its boundary surface) is evaluated as the summation of contributions by the complete set of boundary elements, each scaled by the corresponding (unknown) strength. Furthermore, the governing equation is inherently satisfied by any arbitrary strength distribution, due to linearity. The method's application involves setting an influence matrix that quantifies the boundary conditions' expressions on a set of points on the boundary, evaluated as the sum of contributions by all the elements carrying unit singularity strength. A linear system is then established to determine the strength distribution that satisfies the boundary conditions at the selected set of points. Consequently, the boundary conditions are not universally satisfied over the corresponding surfaces, but only at the selected set of points (collocation points, see e.g. [233]).

The 3D numerical models developed and discussed in this dissertation's framework utilize 4–node quadrilateral elements, carrying constant dipole or source distributions. For completeness purposes, the 4–node quadrilateral element is presented and analyzed in Appendix B. Additionally, the calculation of induced quantities (potential and velocity), by a quadrilateral element carrying dipole and source distributions is included in Appendix C.

Appendix B

THE QUADRILATERAL ELEMENT

Considering a quadrilateral element placed on a 3D domain's boundary, a parametric coordinate system (ξ_1, ξ_2) is introduced, bounded in $[-1, 1]$, as shown in Figure B-1. Consequently, by using isoparametric coordinate transformation, the rectangle $[-1, 1]^2$, which is defined in the parametric space (ξ_1, ξ_2) is transformed to the 3D surface S of the quadrilateral element, defined in the physical space, as

$$\mathbf{x}(\xi_1,\xi_2)=\left[x_1(\xi_1,\xi_2),x_2(\xi_1,\xi_2),x_3(\xi_1,\xi_2)\right]=\sum_{k=1}^{4}\mathbf{x}_k N_k(\xi_1,\xi_2),\ \mathbf{x}\in S\,, \tag{B.1}$$

where $\mathbf{x} = (x_1, x_2, x_3)$ are the Cartesian coordinates of a point with intrinsic coordinates (ξ_1, ξ_2) and $\mathbf{x}_k$ are the coordinates of the element's corner nodes $k = 1,2,3,4$, numbered as illustrated in Figure B-1.

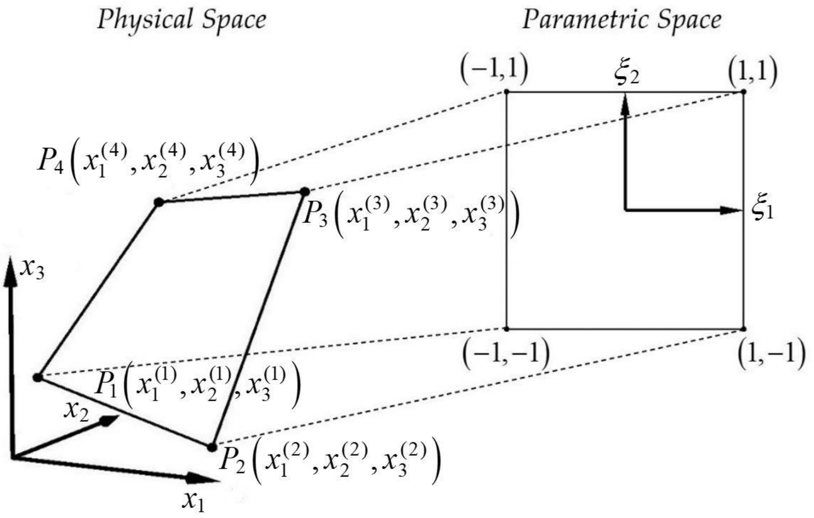

Figure B-1. Mapping of a 4–node quadrilateral element from the Physical Space ($\mathbb{R}^3$) to the Parametric Space (ξ_1, ξ_2).

The general expression of the shape functions, with respect to the node numbering introduced in Figure B-1 is,

$$N_k=\left(\frac{1+\xi_1^{(k)}\xi_1}{2}\right)\left(\frac{1+\xi_2^{(k)}\xi_2}{2}\right),\ k=1,2,3,4, \tag{B.2}$$

where $(\xi_1^{(k)}, \xi_2^{(k)})$ are the local coordinates of the k^{th} corner node (see Figure B-1). The individual shape function for each node is given in Eqs (B.3)–(B.6); see Figure B-2.

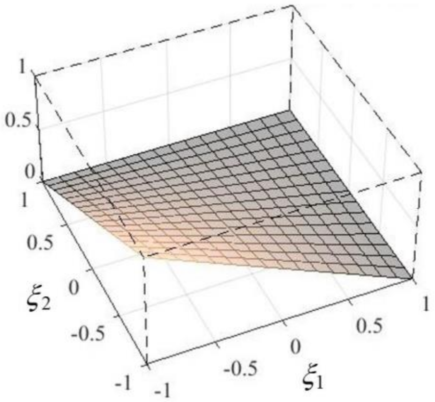

$$\mathrm{N}_1(\xi_1,\xi_2)=\left(\frac{1-\xi_1}{2}\right)\left(\frac{1-\xi_2}{2}\right) \tag{B.3}$$

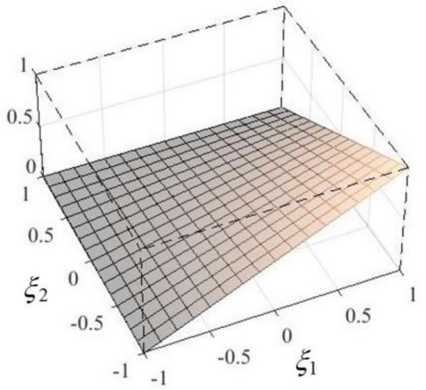

$$\mathrm{N}_2(\xi_1,\xi_2)=\left(\frac{1+\xi_1}{2}\right)\left(\frac{1-\xi_2}{2}\right) \tag{B.4}$$

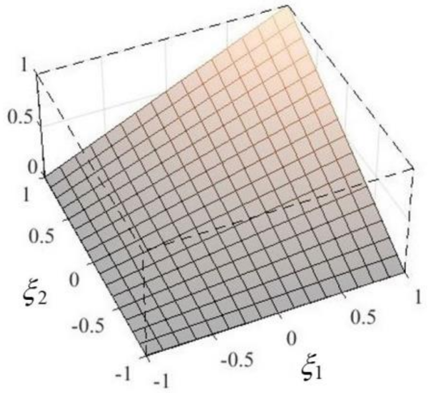

$$\mathrm{N}_3(\xi_1,\xi_2)=\left(\frac{1+\xi_1}{2}\right)\left(\frac{1+\xi_2}{2}\right) \tag{B.5}$$

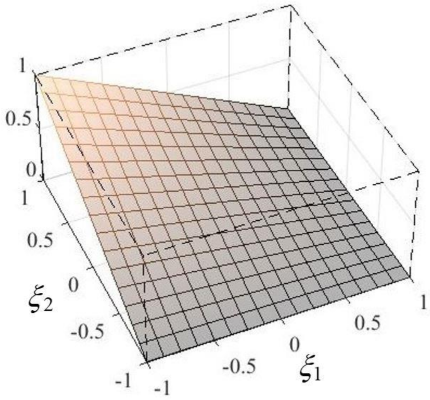

$$\mathrm{N}_4(\xi_1,\xi_2)=\left(\frac{1+\xi_1}{2}\right)\left(\frac{1-\xi_2}{2}\right) \tag{B.6}$$

Figure B-2. Individual shape functions for each node of a quadrilateral element.

The tangent vectors, parallel to the ξ_1 and ξ_2 directions can be evaluated as,

$$\begin{aligned}\mathbf{e}_{\xi 1}=\frac{\partial \mathbf{x}}{\partial \xi_1}=\sum_{k=1}^{4}\frac{\partial N_k(\xi_1,\xi_2)}{\partial \xi_1}\mathbf{x}_k= \\ =\left(\frac{\xi_2-1}{4}\right)\mathbf{x}_1+\left(\frac{1-\xi_2}{4}\right)\mathbf{x}_2+\left(\frac{1+\xi_2}{4}\right)\mathbf{x}_3+\left(\frac{-1-\xi_2}{4}\right)\mathbf{x}_4\end{aligned} \tag{B.7}$$

$$\begin{aligned}\mathbf{e}_{\xi 2}=\frac{\partial \mathbf{x}}{\partial \xi_2}=\sum_{k=1}^{4}\frac{\partial N_k(\xi_1,\xi_2)}{\partial \xi_2}\mathbf{x}_k= \\ =\left(\frac{\xi_1-1}{4}\right)\mathbf{x}_1+\left(\frac{-1-\xi_1}{4}\right)\mathbf{x}_2+\left(\frac{1+\xi_1}{4}\right)\mathbf{x}_3+\left(\frac{1-\xi_1}{4}\right)\mathbf{x}_4\end{aligned} \tag{B.8}$$

and the Jacobian determinant of the transformation is,

$$\sqrt{a}=\left\|\mathbf{e}_{\xi 1}\times\mathbf{e}_{\xi 2}\right\|. \tag{B.9}$$

Any function $f(\mathbf{x}), \mathbf{x} \in S$ can be integrated on the surface S of the quadrilateral element by integration in the unit square defined in the parametric space (ξ_1, ξ_2), multiplied by the local value of the Jacobian determinant,

$$\iint_S f(\mathbf{x})\,dS = \int_{-1}^{1}\int_{-1}^{1} f\left(\mathbf{x}(\xi_1,\xi_2)\right)\sqrt{\alpha(\xi_1,\xi_2)}\,d\xi_1\,d\xi_2 . \tag{B.10}$$

Furthermore, the unit normal vector on any point on S is equal to $\hat{\mathbf{n}} = \dfrac{\mathbf{e}_{\xi 1}\times\mathbf{e}_{\xi 2}}{\left\|\mathbf{e}_{\xi 1}\times\mathbf{e}_{\xi 2}\right\|}$. (B.11)

Integration of the unit function on the surface S results in the area of the surface. This can be achieved, among other ways, by using the Simpson integration rule for the directions ξ_1 and ξ_2. Specifically, by defining a square grid of size $(M \times M)$ in the parametric space (ξ_1, ξ_2) the Jacobian determinant can be evaluated at each point of the grid as defined above. The tangent vectors, parallel to the ξ_1 and ξ_2 directions are evaluated, at each point as,

$$\mathbf{e}_{\xi 1(i,j)} = \left.\frac{\partial \mathbf{x}}{\partial \xi_1}\right|_{\substack{\xi_1=\xi_{1i}\\ \xi_2=\xi_{2j}}} = \left.\begin{pmatrix} \dfrac{\partial x_1}{\partial \xi_1} \\ \dfrac{\partial x_2}{\partial \xi_1} \\ \dfrac{\partial x_3}{\partial \xi_1} \end{pmatrix}\right|_{\substack{\xi_1=\xi_{1i}\\ \xi_2=\xi_{2j}}} = \left.\begin{pmatrix} \sum\limits_{k=1}^{4} x_1^{(k)} \dfrac{\partial N_k(\xi_1,\xi_2)}{\partial \xi_1} \\ \sum\limits_{k=1}^{4} x_2^{(k)} \dfrac{\partial N_k(\xi_1,\xi_2)}{\partial \xi_1} \\ \sum\limits_{k=1}^{4} x_3^{(k)} \dfrac{\partial N_k(\xi_1,\xi_2)}{\partial \xi_1} \end{pmatrix}\right|_{\substack{\xi_1=\xi_{1i}\\ \xi_2=\xi_{2j}}} ,\ i,j = 1,2,\ldots\ldots,M , \tag{B.12}$$

$$\mathbf{e}_{\xi 2(i,j)} = \left.\frac{\partial \mathbf{x}}{\partial \xi_2}\right|_{\substack{\xi_1=\xi_{1i}\\ \xi_2=\xi_{2j}}} = \left.\begin{pmatrix} \dfrac{\partial x_1}{\partial \xi_2} \\ \dfrac{\partial x_2}{\partial \xi_2} \\ \dfrac{\partial x_3}{\partial \xi_2} \end{pmatrix}\right|_{\substack{\xi_1=\xi_{1i}\\ \xi_2=\xi_{2j}}} = \left.\begin{pmatrix} \sum\limits_{k=1}^{4} x_1^{(k)} \dfrac{\partial N_k(\xi_1,\xi_2)}{\partial \xi_2} \\ \sum\limits_{k=1}^{4} x_2^{(k)} \dfrac{\partial N_k(\xi_1,\xi_2)}{\partial \xi_2} \\ \sum\limits_{k=1}^{4} x_3^{(k)} \dfrac{\partial N_k(\xi_1,\xi_2)}{\partial \xi_2} \end{pmatrix}\right|_{\substack{\xi_1=\xi_{1i}\\ \xi_2=\xi_{2j}}} ,\ i,j = 1,2,\ldots\ldots,M , \tag{B.13}$$

and therefore,

$$\iint_S dS = \int_{-1}^{1}\int_{-1}^{1}\sqrt{\alpha(\xi_1,\xi_2)}\,d\xi_1\,d\xi_2 = \frac{\Delta\xi_1}{3}\sum_{i=1}^{M} C_i\left[\frac{\Delta\xi_2}{3}\sum_{j=1}^{M} C_j\sqrt{a_{(i,j)}}\right], \tag{B.14}$$

where,

$$\Delta\xi_1 = \Delta\xi_2 = \frac{1-(-1)}{M-1} = \frac{2}{M-1} \text{ and } C_i = \begin{cases} 3+(-1)^i, & i = 2,3,\ldots\ldots,M-1, \\ 1 \quad , & i = 1, M. \end{cases} \tag{B.15}$$

For example, the area of the quadrilateral element defined by the nodes: $P_1(1,0,0), P_2(1,0,2), P_3(3,0,2), P_4(4,0,0)$ can be defined using Eq. (B.14). The numerical integration results in an area of 5 square units, which can easily be verified as the sum of areas of a square and a right triangle with areas of 4 and 1 square units, respectively.

The tangent vectors $\mathbf{e}_{\xi 1}$ and $\mathbf{e}_{\xi 2}$ parallel to the ξ_1 and ξ_2 directions, as well as the vector $\mathbf{e}_{\xi 1} \times \mathbf{e}_{\xi 2}$ whose length defines the Jacobian determinant of the transformation from the physical to the parametric space, are shown in Figure B-3, for a 5×5 grid of (ξ_1, ξ_2) in $[-1, 1]^2$.

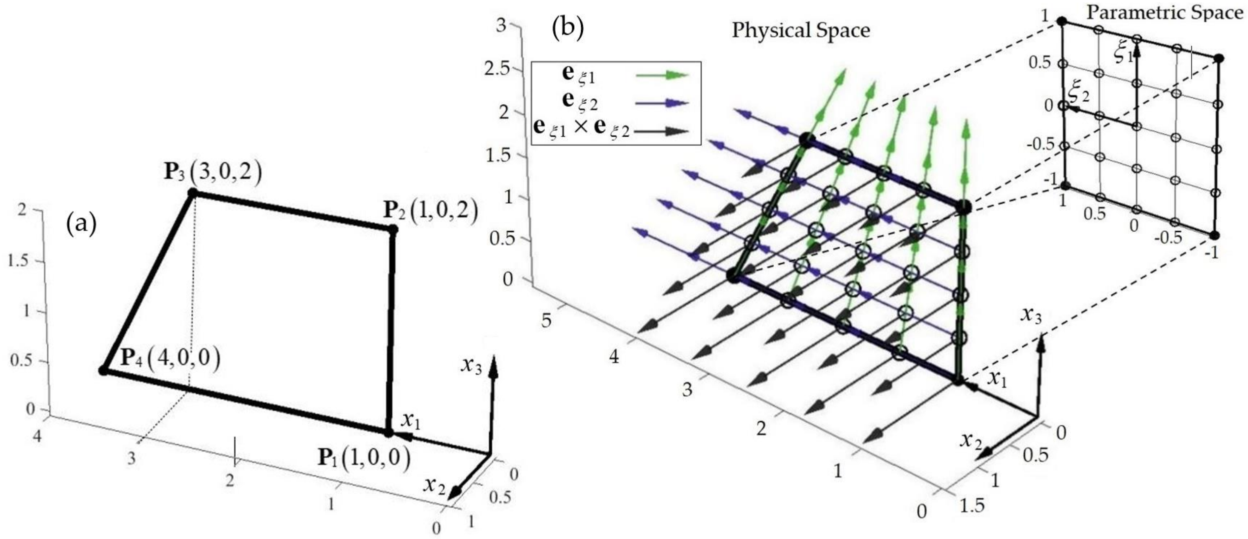

Figure B-3. (**a**) Quadrilateral element defined by the nodes: P_1, P_2, P_3, P_4. (**b**) Tangent vectors $\mathbf{e}_{\xi 1}$ and $\mathbf{e}_{\xi 2}$, and $\mathbf{e}_{\xi 1} \times \mathbf{e}_{\xi 2}$.

Appendix C

EVALUATION OF INDUCED POTENTIAL AND VELOCITY

C.1. Potential and velocity induced from doublet element

Assuming a constant doublet distribution of strength μ on a quadrilateral element, and using the coordinate system $\mathbf{x} = (x_1, x_2, x_3)$, the evaluation of induced potential at any point P of 3D space located at $\mathbf{x}^{(P)} = (x_1^{(P)}, x_2^{(P)}, x_3^{(P)})$, is given by,

$$\Phi(\mathbf{x}^{(P)}) = -\mu \int_S \mathbf{n} \nabla G(\mathbf{x} | \mathbf{x}^{(P)})\, dS, \tag{C.1}$$

where

$$G(\mathbf{x} | \mathbf{x}^{(P)}) = -\frac{1}{4\pi}\left[\left(x_1^{(P)} - x_1\right)^2 + \left(x_2^{(P)} - x_2\right)^2 + \left(x_3^{(P)} - x_3\right)^2\right]^{-1/2}. \tag{C.2}$$

Without loss of generality, the element is considered to be positioned on the plane $x_3 = 0$, as this assumption allows for simplification of the analysis using local coordinates. (The results can subsequently be transferred to the global coordinate system to ensure consistency with the overall framework of the studied problems). In this case, Eq. (C.1) becomes,

$$\Phi(\mathbf{x}^{(P)}) = -\frac{\mu}{4\pi}\int_S \frac{x_3^{(P)}\, dS}{r^3} \quad \text{where } r = \sqrt{\left(x_1^{(P)} - x_1\right)^2 + \left(x_2^{(P)} - x_2\right)^2 + \left(x_3^{(P)}\right)^2}. \tag{C.3}$$

Therefore, the resulting velocity equals,

$$\mathbf{v}(\mathbf{x}^{(P)}) = -\frac{\mu}{4\pi}\int_S \nabla \frac{x_3^{(P)}}{r^3} dS = \frac{\mu}{4\pi}\int_S \left[\mathbf{i}\frac{\partial}{\partial x_1}\frac{x_3^{(P)}}{r^3} + \mathbf{j}\frac{\partial}{\partial x_2}\frac{x_3^{(P)}}{r^3} + \mathbf{k}\left(\frac{1}{r^3} - \frac{3x_3^{(P)}}{r^5}\right)\right] dS, \tag{C.4}$$

where the following relations have been used

$$\frac{\partial}{\partial x_1^{(P)}}\frac{1}{r^3} = -\frac{\partial}{\partial x_1}\frac{1}{r^3}, \quad \frac{\partial}{\partial x_2^{(P)}}\frac{1}{r^3} = -\frac{\partial}{\partial x_2}\frac{1}{r^3}. \tag{C.5}$$

If C represents the curve that bounds the panel and a vortex filament of circulation Γ is positioned along C (see Figure C-1), then the velocity due to the filament can be obtained by applying the Biot–Savart law [156],

$$\mathbf{v} = \frac{\Gamma}{4\pi}\oint_C \frac{d\,\mathbf{l} \times \mathbf{r}}{r^3}. \tag{C.6}$$

For $d\mathbf{l} = (dx_1, dx_2)$ and $\mathbf{r} = (x_1^{(P)} - x_1,\ x_2^{(P)} - x_2,\ x_3^{(P)})$, Eq. (C.6) becomes

$$\mathbf{v}(\mathbf{x}^{(P)}) = \frac{\Gamma}{4\pi}\int_S \left\{\mathbf{i}\frac{x_3^{(P)}}{r^3} dx_2 - \mathbf{j}\frac{x_3^{(P)}}{r^3} dx_1 + \mathbf{k}\left[\left(x_2^{(P)} - x_2\right)\partial x_1 - \left(x_1^{(P)} - x_1\right)\partial x_2\right]\right\} dS. \tag{C.7}$$

Stokes theorem for the vector $\mathbf{q}$ states that

$$\oint_C \mathbf{q}\, d\,\mathbf{l} = \int_S \mathbf{n} \cdot \nabla \mathbf{q}\, dS. \tag{C.8}$$

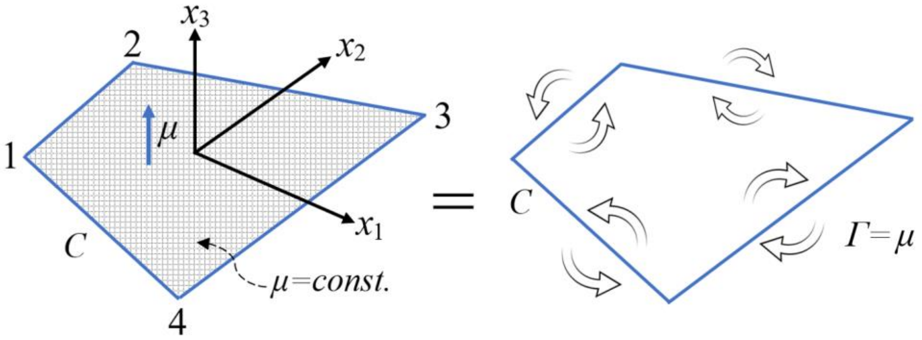

Figure C-1. Doublet singularity on quadrilateral element and equivalence to a vortex ring.

Using the above relation for the velocity [Eq. (C.7)], for $\mathbf{n}=\mathbf{k}$ results in the following,

$$\mathbf{v}(\mathbf{x}^{(P)})=\frac{\Gamma}{4\pi}\int_S\left[\mathbf{i}\frac{\partial}{\partial x_1}\frac{x_3^{(P)}}{r^3}+\mathbf{j}\frac{\partial}{\partial x_2}\frac{x_3^{(P)}}{r^3}-\mathbf{k}\left(\frac{\partial}{\partial x_1}\frac{x_1^{(P)}-x_1}{r^3}+\frac{\partial}{\partial x_2}\frac{x_2^{(P)}-x_2}{r^3}\right)\right]dS. \tag{C.9}$$

By comparing Eqs. (C.4) and (C.9) it can be observed that induced velocity from the doublet singularity on the panel is equivalent to that from the vortex filament when $\Gamma=\mu$ (see Figure C-1).

Considering a segment along one of the edges of the element and an arbitrary point P, as illustrated in Figure C-2. The induced velocity in this case is

$$\mathbf{v}(\mathbf{x}^{(P)})=\frac{\Gamma}{4\pi}.\frac{d\mathbf{l}\times\mathbf{r}}{r^3}. \tag{C.10}$$

If the vortex segment points from point 1 to point 2 (see Figure C-2), then the velocity at P can be evaluated as

$$\mathbf{v}(\mathbf{x}^{(P)})=\frac{\Gamma}{4\pi}\frac{\mathbf{r}_1\times\mathbf{r}_2}{\left|\mathbf{r}_1\times\mathbf{r}_2\right|^2}\mathbf{r}_0\cdot\left(\frac{\mathbf{r}_1}{\left|\mathbf{r}_1\right|}-\frac{\mathbf{r}_2}{\left|\mathbf{r}_2\right|}\right), \tag{C.11}$$

where

$$\mathbf{r}_1=(x_1^{(P)}-x_1^{(1)},\ x_2^{(P)}-x_2^{(1)},\ x_3^{(P)}-x_3^{(1)}), \tag{C.12}$$

$$\mathbf{r}_2=(x_1^{(P)}-x_1^{(2)},\ x_2^{(P)}-x_2^{(2)},\ x_3^{(P)}-x_3^{(2)})\ \text{and} \tag{C.13}$$

$$\mathbf{r}_0=(x_1^{(2)}-x_1^{(1)},\ x_2^{(2)}-x_2^{(1)},\ x_3^{(2)}-x_3^{(1)}). \tag{C.14}$$

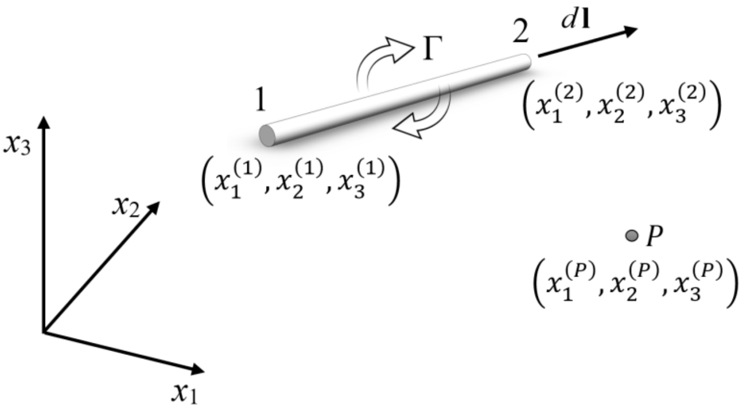

Figure C-2. Impact of a linear segment with circulation Γ to a point P.

The resulting velocity components are

$$v_i(\mathbf{x}^{(P)}) = K\left(\mathbf{r}_1 \times \mathbf{r}_2\right)_i, \; i = 1,2,3, \text{ where} \tag{C.15}$$

$$K = \frac{\Gamma}{4\pi\left|\mathbf{r}_1 \times \mathbf{r}_2\right|^2}\left(\frac{\mathbf{r}_0 \cdot \mathbf{r}_1}{|\mathbf{r}_1|} - \frac{\mathbf{r}_0 \cdot \mathbf{r}_2}{|\mathbf{r}_2|}\right). \tag{C.16}$$

The steps for the analytical derivation of the above results can be found in Ref. [156].

Considering, for simplicity, a constant doublet distribution of strength $\mu = 1$, by reciprocity the expression of induced potential [Eq. (C.1)] relates to the flux through the panel due to a point source of strength $\sigma = -4\pi$ located at P [234]. This implies that the value of the integral equals the solid angle of the panel as viewed from this point, with the algebraic convention that the sign of the solid angle is the same as that of x_3. Therefore, following Gauss–Bonnet theorem in differential geometry (see e.g. [235]), which states that if the quadrilateral panel is projected onto the unit sphere, centered at P, the area circumscribed by the panel's boundary contour (solid angle) equals [234],

$$a = 2\pi - \sum_{k=1}^{4} \theta_k = \Phi(\mathbf{x}^{(P)}), \tag{C.17}$$

where θ_k stands for the angle formed by two consecutive nodes and the point P. The same result can be derived by splitting the 4–node element into two 3–node elements and evaluating the solid angle for each. Then the induced potential from the 4–node element to the field point P is

$$\Phi(\mathbf{x}^{(P)}) = a_1 + a_2 = \sum_{m=1}^{2}\left(\pi - \sum_{k=1}^{3} \theta_k^{(m)}\right), \tag{C.18}$$

where $\theta_k^{(m)}$ denotes the angle formed by two consecutive nodes of the m^{th} 3–node element and the point P, as shown in Figure C-3(c). Validation examples of this approach can be found in Ref. [236]. An indicative field generated by a unitary strength dipole distribution on a quadrilateral element defined by the nodes $(-1,-1,0)$, $(1,-1,0)$, $(1,1,0)$ and $(-1,1,0)$ is shown in Figure C-4, using equipotential surfaces. The resulting velocity vector field will consequently be oriented normally to these surfaces, moving towards the direction of decreasing potential.

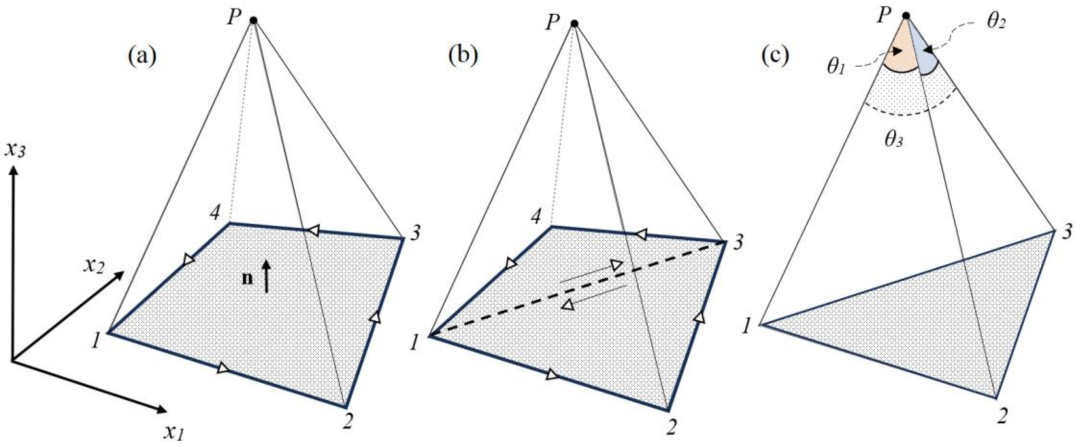

Figure C-3. (**a**) 4–node quadrilateral element and field point P. (**b**) Separation of quadrilateral element to two 3–node elements and (**c**) Tetrahedron defined by the nodes 1,2,3 and P.

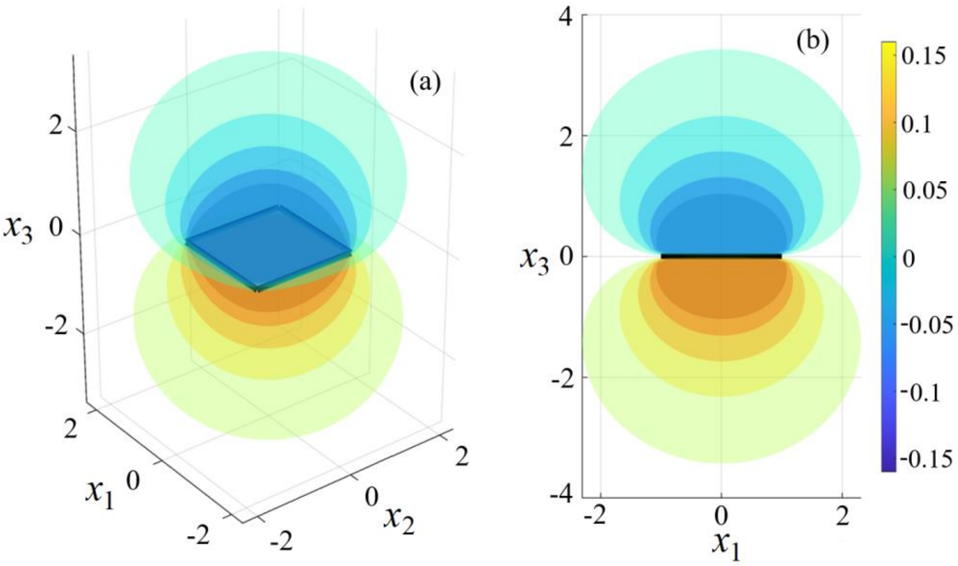

Figure C-4 Equipotential surfaces of field induced by a unitary strength dipole distribution on a quadrilateral element defined by the nodes $(-1,-1{,}0),(1,-1{,}0),(1{,}1{,}0)$ and $(-1{,}1{,}0)$. (**a**) 3D view and (**b**) side view.

C.2. Potential and velocity induced from source element

The induced velocity from a distribution of source singularity of constant strength σ on a 4–node element with surface S to the field point P equals,

$$\mathbf{v}(\mathbf{x}^{(P)}) = -\frac{\sigma}{4\pi}\int_S \frac{\mathbf{r}}{|\mathbf{r}|^3} dS\,. \tag{C.19}$$

Following the analysis of Appendix B, the above integral can be evaluated as [see Eq. (B.10)],

$$\mathbf{v}(\mathbf{x}^{(P)}) = -\frac{\sigma}{4\pi}\int_{\xi 1=-1}^{1}\left(\int_{\xi 2=-1}^{1}\frac{\mathbf{r}}{|\mathbf{r}|^3}\sqrt{\alpha}\,d\xi_2\right)d\xi_1\,, \tag{C.20}$$

where $\sqrt{a}$ is the Jacobian determinant of the isoparametric coordinate transformation used to project the 4–node element to a rectangle bounded in $[-1,1]$ in the parametric space (ξ_1,ξ_2). The above integral can be evaluated using a numerical integration rule as discussed in Appendix B. Similarly, the corresponding potential at P can be evaluated as,

$$\Phi(\mathbf{x}^{(P)}) = -\frac{\sigma}{4\pi}\int_{\xi 1=-1}^{1}\left(\int_{\xi 2=-1}^{1}\frac{1}{|\mathbf{r}|}\sqrt{\alpha}\,d\xi_2\right)d\xi_1\,. \tag{C.21}$$

Equipotential surfaces of an indicative field generated by a unit–strength source distribution on a quadrilateral element defined by the nodes $(-1,-1{,}0),(1,-1{,}0),(1{,}1{,}0)$ and $(-1{,}1{,}0)$ is shown in Figure C-5. The resulting velocity vector field will be aligned normally to these surfaces, directed toward decreasing potential regions.

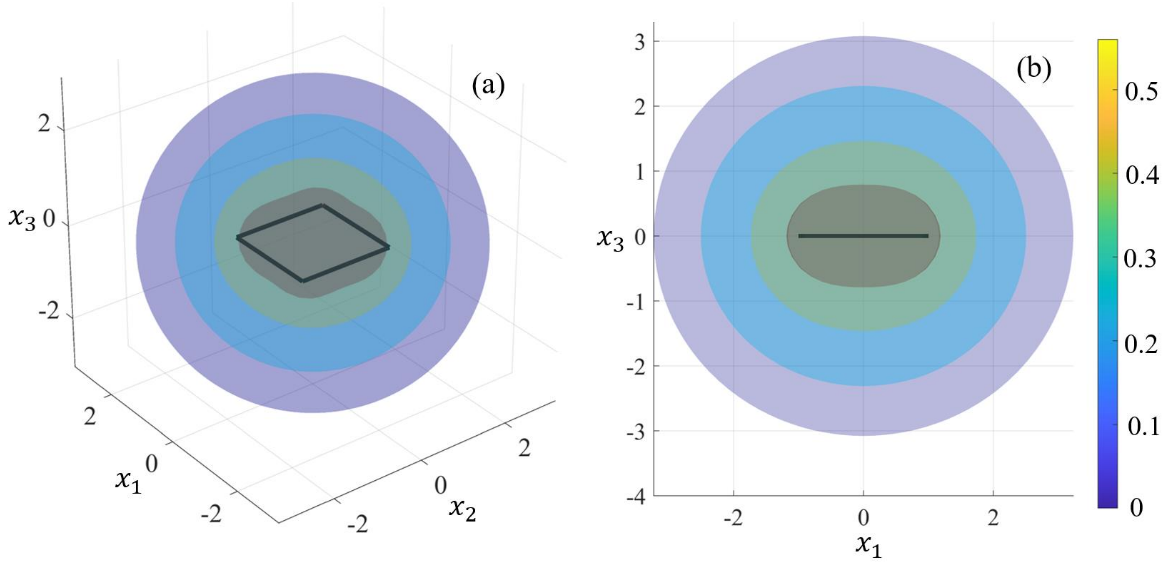

Figure C-5. Equipotential surfaces of field induced by a unitary strength source distribution on a quadrilateral element defined by the nodes $(-1,-1,0)$, $(1,-1,0)$, $(1,1,0)$ and $(-1,1,0)$. (**a**) 3D view and (**b**) side view.

Although the evaluation of induced potential and velocities from a distribution of source singularity is more computationally demanding, as compared to dipole singularity, source elements are essential in scenarios involving forward motion, such as moving ships or ocean currents, within the framework discussed in the present work. The necessity for such singularity elements arises from the fact that dipole singularities do not induce potential or velocity at coplanar points (see Figure C-4). Consequently, the four–point upstream finite difference scheme [179], presented and discussed in §5 of the present work, cannot be effectively implemented in such cases (refer to Figure 5-4), without employing source elements.

Appendix D

ESTIMATION OF WIND LOADS AND COOLING EFFECT

Parts I and II of the present thesis investigate the hydrodynamic effects of the marine environment on floating photovoltaic systems and solar ships. However, to further refine the modelling and better capture the overall performance of such systems, it is important to consider additional environmental factors, such as cooling effects and wind loads. Some simplified approaches to incorporate these phenomena are discussed hereafter. The discussed methods can be used to enhance and extend the methodologies presented in the main body of the thesis, providing a more comprehensive framework for quantifying the performance of floating PV units and solar ships.

Estimation of the wind loads can be achieved by evaluating the pressure distribution on a panel, which can then be integrated to determine the total force exerted by the wind. The evaluation of the velocity field can be achieved at a preliminary level using a simple 2D BEM approach (see e.g. §3.2 of the present work), which approximates the velocity along the panel's surface by considering a source–sink singularity distribution. The singularity distribution is evaluated such that the total flow field, comprising a uniform air flow and a disturbance, satisfies a no–entrance condition on the panel.

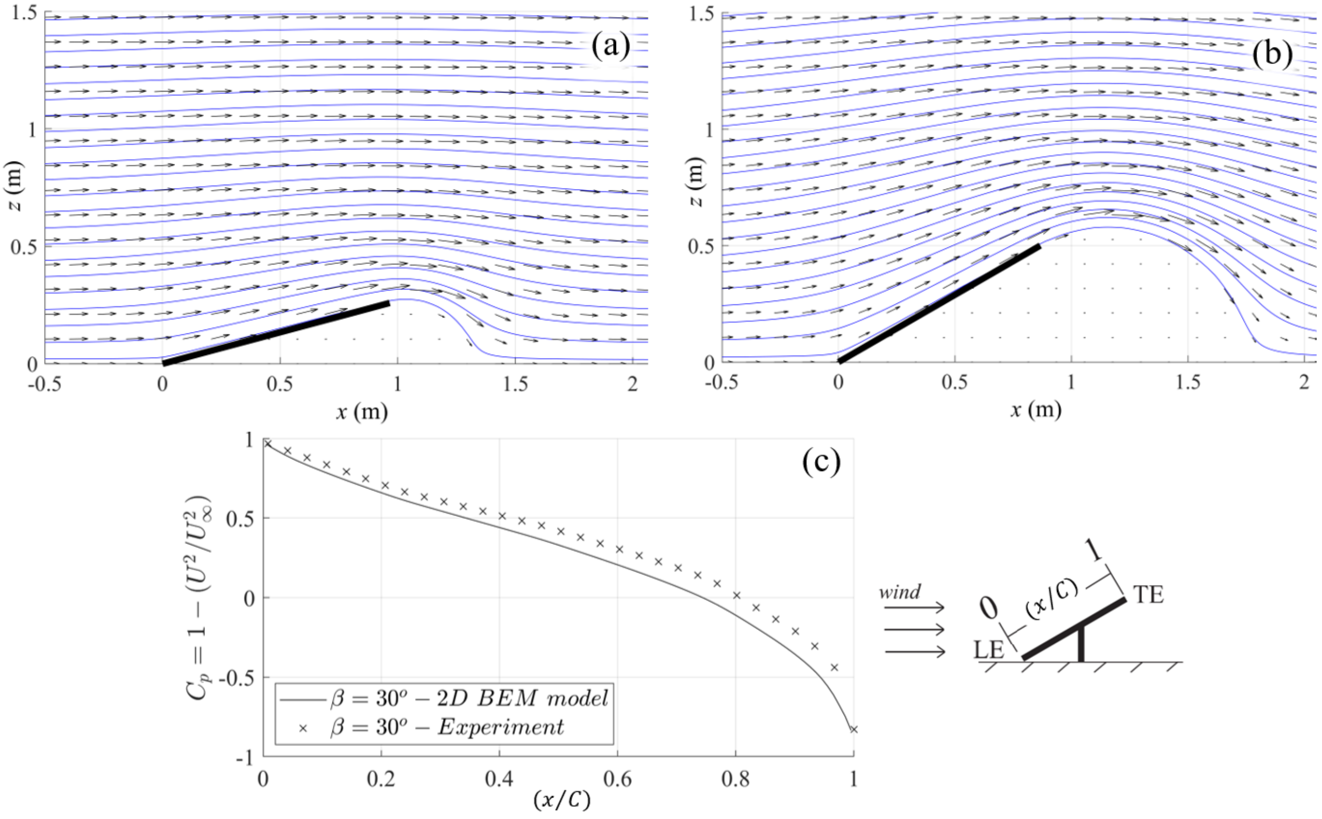

Figure D-1. Flow field generated by the interaction of a uniform airflow of velocity $U_\infty = 1\ \mathrm{m/s}$ and a tilted panel at angles (**a**) $\beta = 15°$ and (**b**) $\beta = 30°$. (**c**) Pressure coefficient on the panel's surface and comparison with experimental data. (Experimental data adapted from [237]).

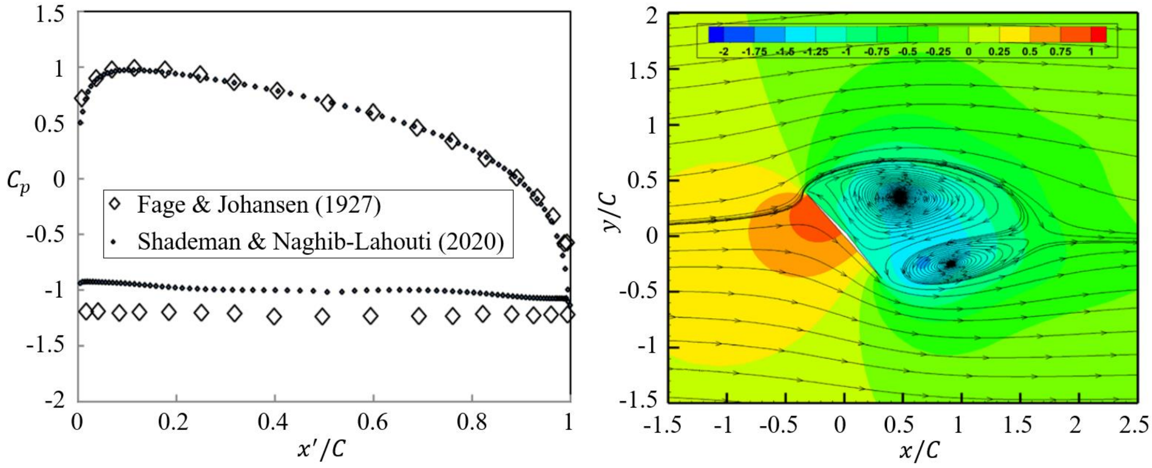

Figure D-2. (**a**) Mean pressure coefficient [238,239] and (**b**) sectional streamlines at the mid–span. (Adapted from [239]).

The potential flow solver cannot adequately address scenarios involving tilt angles greater than 20–30 degrees, as flow separation and recirculation effects become particularly important in such cases, as shown in Figure D-2 for an angle of 50°. The incorporation of such phenomena requires experimental investigation [237] or models that account for viscous effects, boundary layer behaviour and turbulence (see e.g., [239,240]). To address these limitations, an artificial surface can be introduced in the model, representing the boundary layer, and exclude the regions of viscous flow from the domain that is modelled by the potential solver. Indicative airflow fields resulting from the interaction of a uniform flow of velocity $U_\infty = 1\,\mathrm{m}/s$ with a tilted panel are shown in Figure D-1(a, b) for tilt angles equal to $\beta = 15°$ and $\beta = 30°$. The pressure on the lower surface cannot be defined by the simple methodology discussed. The resulting pressure coefficient on the upper surface, for $\beta = 30°$, is shown in Figure D-1(c), where it is compared against experimental data from the work by Abiola–Ogedengbe et al. [237]. The latter work's findings reveal that the inter–panel gaps play a critical role in large PV arrangements, indicating that the influence of 3D effects must be accounted for when assessing the overall pressure field. This, however, is beyond the scope of the present work. As it can be observed in Figure D-1(c), the potential flow model slightly underestimates the pressure coefficient. However, the overall trend aligns well with the experimental results. This indicates that, despite the underestimation, the model provides a reasonable approximation. Notably, the presence of both positive and negative values of the pressure coefficient suggests that this underestimation could lead to scenarios where the computed net force is zero, even when there is a non–zero aerodynamic force acting on the surface. Therefore, while the model can be effectively used for preliminary estimates at low wind speeds, the results should be interpreted with caution, particularly in cases where the balance of forces is critical.

Using the calculated velocity field, the temperature field can be estimated using the conservation of energy for incompressible flows ($\rho = const$). It is important to note that in the latter case, the equation that describes conservation of energy is decoupled from the ones expressing conservation of mass and momentum [241], thus justifying that the velocity field has been previously calculated without accounting for temperature variations. Under these conditions, the heat transfer equation governing the temperature field is [241],

$$\rho c_p \left[\frac{\partial T(\mathbf{x};t)}{\partial t} + \mathbf{U}(\mathbf{x}) \nabla T(\mathbf{x};t) \right] = \mu \nabla^2 T(\mathbf{x};t) + S(\mathbf{x}), \tag{D.1}$$

where ρ is the air's density, c_p is the air's specific heat capacity and $T(\mathbf{x};t)$ is the temperature field. Furthermore, $\mathbf{U}(\mathbf{x})$; where $\mathbf{x} = (x, z)$, is the velocity vector field $[\mathbf{U} = (u, v)]$ that models the airflow, μ represents the thermal conductivity and S stands for source terms, modelling energy inputs that affect the temperature field. Eq. (D.1) can be rearranged and expressed as,

$$\frac{\partial T(\mathbf{x};t)}{\partial t} = \frac{\mu}{\rho c_p} \nabla^2 T(\mathbf{x};t) - \mathbf{U}(\mathbf{x}) \nabla T(\mathbf{x};t) + \frac{S(\mathbf{x})}{\rho c_p}. \tag{D.2}$$

The above equation can be solved using a Forward–Time Centered–Space (FTCS) explicit finite difference (FD) scheme [242], in order to derive preliminary estimates as regards the temperature drop on the panel's surface (see e.g., [243]). Consequently, by considering the discrete form of the left–hand side of Eq. (D.2):

$$\frac{\partial T(\mathbf{x};t)}{\partial t} \approx \frac{T_{i,j}^{(n+1)} - T_{i,j}^{(n)}}{\Delta t}, \tag{D.3}$$

the temperature at a given field point can be evaluated as

$$T_{i,j}^{(n+1)} = T_{i,j}^{(n)} + \frac{\Delta t}{\rho c_p} \left(\mu \nabla^2 T_{i,j}^{(n)} - \rho c_p U_{i,j} \nabla T_{i,j}^{(n)} + S_{i,j} \right), \tag{D.4}$$

where $T_{i.j}^{(n)}$ is the local value of the temperature at the spatial location defined by the coordinates (x_i, z_j), at the n^{th} timestep and Δt represents the time interval between successive steps (see Figure D-3).

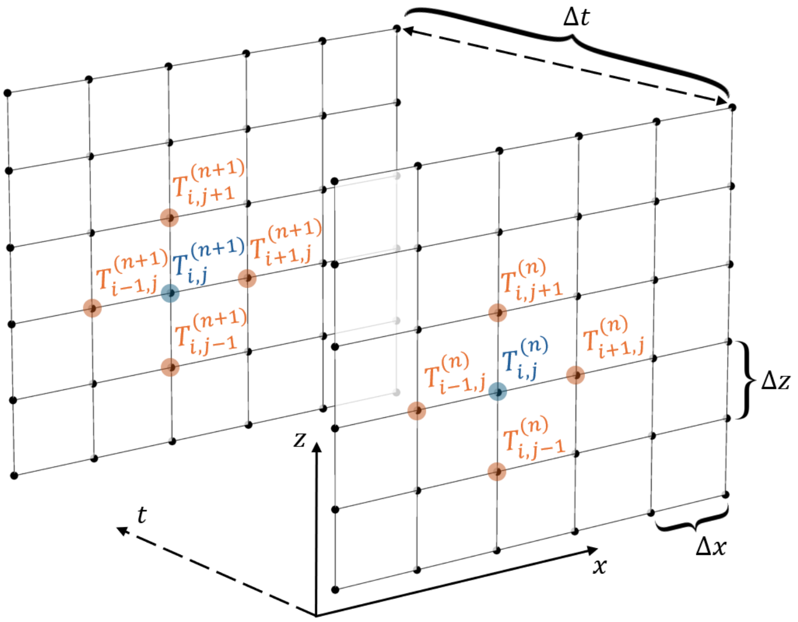

Figure D-3. Illustration of a 2D grid highlighting the stencil used in the numerical scheme around the point (x_i, z_j) at time $t = t_n$ (front grid) and at time $t = t_{n+1}$ (back grid), separated by a time step Δt.

In the simple model discussed, the convection term is approximated in the discrete scheme as,

$$\rho c_p U_{i,j} \nabla T_{i,j}^{(n)} \approx \rho c_p \left(U_{i,j}^{(x)} \frac{T_{i+1,j}^{(n)} - T_{i-1,j}^{(n)}}{2\Delta x} + U_{i,j}^{(z)} \frac{T_{i,j+1}^{(n)} - T_{i,j-1}^{(n)}}{2\Delta z} \right), \tag{D.5}$$

while the diffusion term is evaluated as,

$$\mu \nabla^2 T_{i,j}^{(n)} \approx \mu \left(\frac{T_{i+1,j}^{(n)} - 2T_{i,j}^{(n)} + T_{i-1,j}^{(n)}}{\Delta x^2} + \frac{T_{i,j+1}^{(n)} - 2T_{i,j}^{(n)} + T_{i,j-1}^{(n)}}{\Delta z^2} \right), \tag{D.6}$$

where Δx and Δz denote the grid points spacing in the horizontal and vertical directions, respectively; (see Figure D-3). In order for the above FD scheme to remain stable, it is necessary to satisfy a combined stability criterion that accounts for both diffusion and convection effects (see e.g., [244]). In particular, the grid spacing must satisfy the following inequality [245],

$$\Delta x < \frac{2\mu}{U \rho c_p}. \tag{D.7}$$

The above condition ensures that the spatial resolution is fine enough to accurately capture the effects of convection relative to the diffusion process. Additionally, the time step must be chosen such that [245],

$$\frac{\mu}{\rho c_p} \frac{\Delta t}{\Delta x^2} < \frac{1}{2} \;\rightarrow\; \Delta t < \frac{\rho c_p \Delta x^2}{2\mu}. \tag{D.8}$$

The latter condition arises from the requirement that the temporal discretization remains fine enough to properly model the diffusion process without causing numerical instability. The above conditions combined ensure that the numerical scheme can accurately represent both diffusion and convection phenomena, preventing instabilities that could lead to divergence.

In order to quantify the effect of wind on the panel temperature, the following assumptions are also made. The panel radiates heat due to the incidence of solar irradiance, which varies across its surface, reflecting the natural distribution of absorbed energy. This heat radiation is incorporated in the modelling via the source terms [refer to Eq. (D.1)], which represent generated heat. Furthermore, the intensity of the source terms is defined so as to follow a quadratic form, with the peak value at the center of the panel and a gradual reduction towards the edges. This reflects the natural temperature gradient that forms on the panel, where heat dissipation is more efficient at the edges, which are in direct contact with the surrounding environment, while the center is insulated by the surrounding heated surface.

The intensity of the source terms is calibrated so that the mean value of temperature on the panel reaches a steady–state value of $50°\mathrm{C}$ at ambient temperature $T_A = 25°\mathrm{C}$, in the absence of airflow; (refer to Eq. (2.18) in §2.3). The latter calibration ensures that the model accurately simulates a specific thermal behaviour of the panel under solar exposure, and therefore the calculated source intensity can be used in conjunction with wind velocity data to quantify the effects of wind on panel temperature. Finally, the thermal conductivity is assumed to be constant and is evaluated at the ambient temperature.

The temperature conditions on the panel are evaluated by defining a profile adjacent to the panel's surface, and the temperature field values along this profile are interpolated to obtain a detailed representation of the temperature distribution. The temperature drop can then be measured by comparing the mean values of the latter distribution at different wind speeds. Figure D-4 shows the resulting temperature field for wind speeds of $0, 1,$ and $2\,\mathrm{m/s}$, along with the temperature distribution on the profile and the corresponding mean values. The mean temperature drops for $U = 1\,\mathrm{m/s}$ and $U = 2\,\mathrm{m/s}$ and 5.8% and 14% respectively, suggesting that higher wind speeds contribute to a more pronounced cooling effect on the panel.

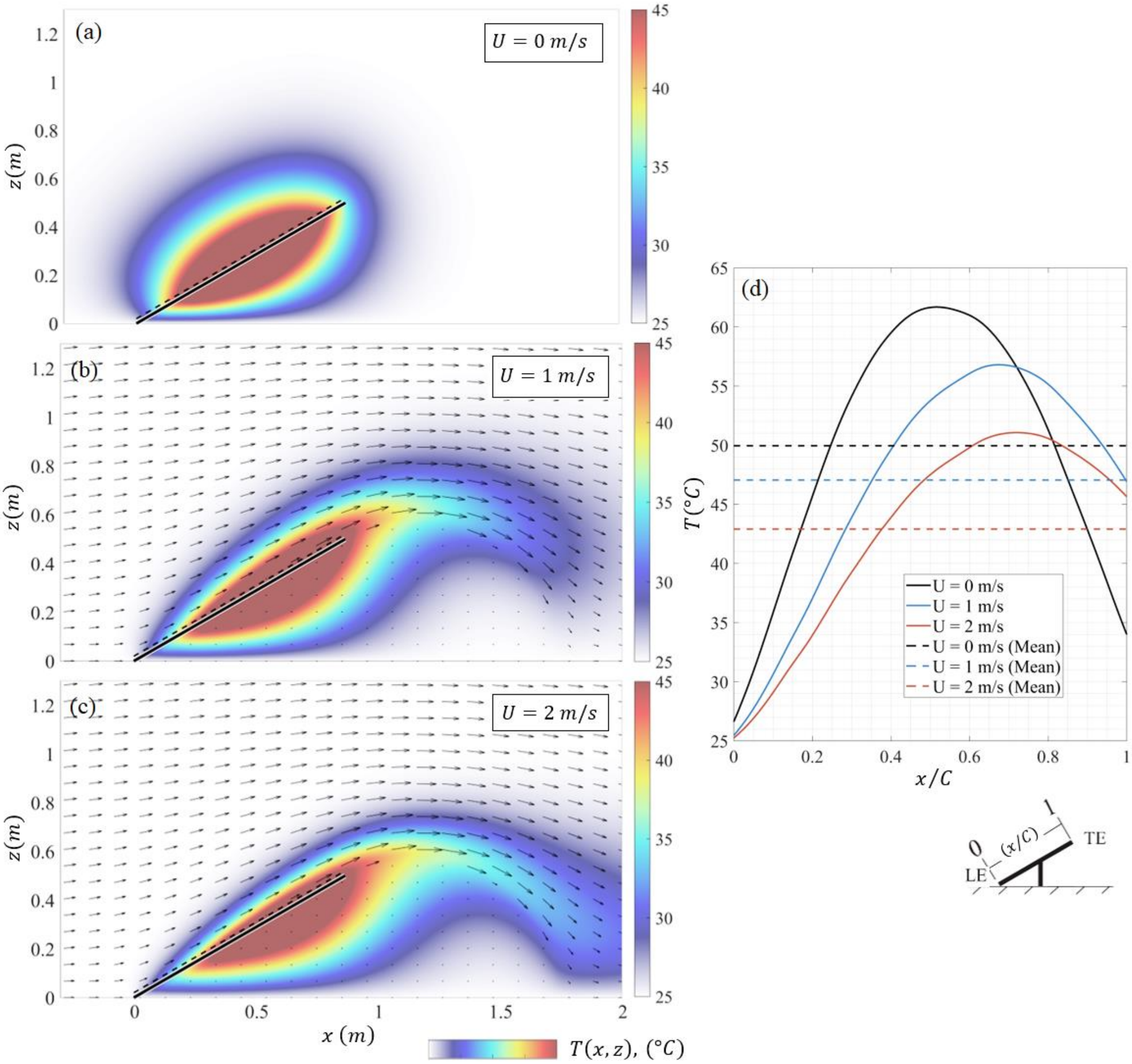

Figure D-4. (**a**–**c**) Temperature fields for wind speeds of $0, 1,$ and $2\,\mathrm{m/s}$. (**d**) Temperature distribution on the profile (dashed line in subplots a–c) and mean values. The source terms are calibrated to achieve a mean steady state temperature of $50°\mathrm{C}$ in the absence of wind.

REFERENCES

1. Fink, A.M.; Stulz, R.J. 2000 W society: a sustainable energy vision for the future. *Proceedings of the Institution of Civil Engineers - Engineering Sustainability* **2012**, *165*, 255-260, doi:10.1680/ensu.10.00059.
2. European; Commission. *European green deal – Delivering on our targets*; Publications Office of the European Union: 2021.
3. *European Court of Auditors (ECA). Offshore renewable energy in the EU. Ambitious plans for growth but sustainability remains a challenge*; 2023.
4. Giuntoli, J. *Final Recast Renewable Energy Directive for 2021–2030 in the European Union*; Washington, DC, USA, 2018.
5. Directive (EU) 2023/2413 of the European Parliament and of the Council. *Official Journal of the European Union* **2023**.
6. *European, Commission Directorate. Energy – Roadmap 2050*; Publications Office: 2012.
7. Botelho, A.; Arezes, P.; Bernardo, C.; Dias, H.; Pinto, L.M.C. Effect of Wind Farm Noise on Local Residents' Decision to Adopt Mitigation Measures. *International Journal of Environmental Research and Public Health* **2017**, *14*, doi:10.3390/ijerph14070753.
8. Lizet Ramírez; Daniel Fraile; Brindley, G. *Offshore Wind in Europe; Key trends and statistics 2020*; 2021.
9. Rtimi, R.; Sottolichio, A.; Tassi, P. The Rance tidal power station: Toward a better understanding of sediment dynamics in response to power generation. *Renewable Energy* **2022**, *201*, 323-343, doi:https://doi.org/10.1016/j.renene.2022.10.061.
10. Meegahapola, L.; Udawatta, L.; Witharana, S. The Ocean Thermal Energy Conversion strategies and analysis of current challenges. In Proceedings of the *2007 International Conference on Industrial and Information Systems*, 9-11 Aug. 2007, 2007; pp. 123-128.
11. Islam Rony, Z.; Rasul, M.G.; Jahirul, M.I.; Mofijur, M. Harnessing marine biomass for sustainable fuel production through pyrolysis to support United Nations' Sustainable Development Goals. *Fuel* **2024**, *358*, 130099, doi:https://doi.org/10.1016/j.fuel.2023.130099.
12. Melikoglu, M. Current status and future of ocean energy sources: A global review. *Ocean Engineering* **2018**, *148*, 563-573, doi:https://doi.org/10.1016/j.oceaneng.2017.11.045.
13. Abdelal, Q. Floating PV; an assessment of water quality and evaporation reduction in semi-arid regions. *International Journal of Low-Carbon Technologies* **2021**, *16*, 732-739, doi:10.1093/ijlct/ctab001.

14. Lozano, I.L.; Alados, I.; Foyo-Moreno, I. Analysis of the solar radiation/atmosphere interaction at a Mediterranean site: The role of clouds. *Atmospheric Research* **2023**, *296*, 107072, doi:https://doi.org/10.1016/j.atmosres.2023.107072.
15. SolarPower; Europe. *Global Market Outlook For Solar Power 2023 - 2027*; 2023.
16. TotalEnergies. *Qatar: TotalEnergies announces the startup of Al Kharsaah (800 MWp), one of the largest solar power plants in the Middle East*; 2022.
17. Santos, B. TotalEnergies, Marubeni switch on 800 MW of solar in Qatar. Available online: https://www.pv-magazine.com/2022/10/19/totalenergies-marubeni-switch-on-800-mw-of-solar-in-qatar/
18. IRENA. *Future of Solar Photovoltaic: Deployment, investment, technology, grid integration and socio-economic aspects (A Global Energy Transformation: paper),*; Abu Dhabi, 2019.
19. Pourasl, H.H.; Barenji, R.V.; Khojastehnezhad, V.M. Solar energy status in the world: A comprehensive review. *Energy Reports* **2023**, *10*, 3474-3493, doi:10.1016/j.egyr.2023.10.022.
20. Huang, G.; Tang, Y.; Chen, X.; Chen, M.; Jiang, Y. A Comprehensive Review of Floating Solar Plants and Potentials for Offshore Applications. *Journal of Marine Science and Engineering* **2023**, *11*, doi:10.3390/jmse11112064.
21. Kaplani, E.; Kaplanis, S. PV Module Temperature Prediction at Any Environmental Conditions and Mounting Configurations. In *Renewable Energy and Sustainable Buildings: Selected Papers from the World Renewable Energy Congress WREC 2018*, Sayigh, A., Ed.; Springer International Publishing: Cham, 2020; pp. 921-933.
22. Silalahi, D.F.; Blakers, A. Global Atlas of Marine Floating Solar PV Potential. *Solar* **2023**, *3*, 416-433, doi:10.3390/solar3030023.
23. Kennedy, R. Floating PV could reach 4.8 GW globally by 2026. Available online: https://www.pv-magazine.com/2022/01/19/floating-pv-could-reach-4-8-gw-globally-by-2026/
24. Elshafei, M.; Ibrahim, A.; Helmy, A.; Abdallah, M.; Eldeib, A.; Badawy, M.; AbdelRazek, S. Study of massive floating solar panels over Lake Nasser. *J. Energy* **2021**, *2021*, 1-17, doi:10.1155/2021/6674091.
25. Lightsourcebp. Queen Elizabeth II Reservoir solar. Available online: https://lightsourcebp.com/project/queen-elizabeth-ii-reservoir-solar/
26. Al-Widyan, M.; Khasawneh, M.; Abu-Dalo, M. Potential of Floating Photovoltaic Technology and Their Effects on Energy Output, Water Quality and Supply in Jordan. *Energies* **2021**, *14*, doi:10.3390/en14248417.
27. Helfer, F.; Lemckert, C.; Zhang, H. Impacts of climate change on temperature and evaporation from a large reservoir in Australia. *Journal of Hydrology* **2012**, *475*, 365-378, doi:https://doi.org/10.1016/j.jhydrol.2012.10.008.
28. Colthorpe, A. Renewable retail plans from Japanese utility TEPCO include home battery rollout. Available online: https://www.energy-storage.news/renewable-retail-plans-from-japanese-utility-tepco-include-home-battery-rollout/

29. Pfeifroth, U.K., Steffen; Drücke, Jaqueline; Trentmann, Jörg; Schröder, Marc; Selbach, Nathalie; Hollmann, Rainer. Surface Radiation Data Set - Heliosat (SARAH) - Edition 3. **2023**, doi:https://doi.org/10.5676/EUM_SAF_CM/SARAH/V003.
30. Diendorfer, C.; Haider, M.; Lauermann, M. Performance Analysis of Offshore Solar Power Plants. *Energy Procedia* **2014**, *49*, 2462-2471, doi:10.1016/j.egypro.2014.03.261.
31. IRENA. *Renewable Power Generation Costs in 2022*; Abu Dhabi, 2023.
32. Rosa-Clot, M.; Marco Tina, G. *Submerged and Floating Photovoltaic Systems : Modelling, Design and Case Studies*; Elsevier Science & Technology: Saint Louis, 2017.
33. Seme, S.; Štumberger, B.; Hadžiselimović, M.; Sredenšek, K. Solar Photovoltaic Tracking Systems for Electricity Generation: A Review. *Energies* **2020**, *13*, doi:10.3390/en13164224.
34. Shi, W.; Yan, C.; Ren, Z.; Yuan, Z.; Liu, Y.; Zheng, S.; Li, X.; Han, X. Review on the development of marine floating photovoltaic systems. *Ocean Engineering* **2023**, *286*, 115560, doi:https://doi.org/10.1016/j.oceaneng.2023.115560.
35. Sukarso, A.P.; Kim, K.N. Cooling Effect on the Floating Solar PV: Performance and Economic Analysis on the Case of West Java Province in Indonesia. *Energies* **2020**, *13*, doi:10.3390/en13092126.
36. DNV. *DNV-RP-0584 Design, development and operation of floating solar photovoltaic systems. Recommended practice*; 2021.
37. Muscat, M. A study of floating PV module efficiency. L-Università ta' Malta, 2014.
38. Mohit, A.; Sarvesh, D. *Floating Solar Photovoltaic (FSPV): A Third Pillar to Solar PV Sector?, TERI Discussion Paper: Output of the ETC India Project*; (New Delhi: The Energy and Resources Institute): 2019.
39. Abdullah-Al-Mahbub, M.; Towfiqul Islam, A.R.M.; Alam, E.; Asha, M.R. Sustainable solar energy potential on marine passenger ships of Bay of Bengal: A way of reducing carbon dioxide emissions and disaster risk reduction. *Energy Exploration & Exploitation* **2023**, *41*, 1697-1723, doi:10.1177/01445987231173097.
40. Verma, J.; Kumar, D. Retracted Article: Recent developments in energy storage systems for marine environment. *Materials Advances* **2021**, *2*, 6800-6815, doi:10.1039/D1MA00746G.
41. Monkelbaan, J. Interactions between Trade and Climate Governance; Exploring the Potential of Climate Clubs. *The Global Trade and Customs Journal (GTCJ)* **2021**, doi:10.54648/GTCJ2021037.
42. Deng, S.; Mi, Z. A review on carbon emissions of global shipping. *Marine Development* **2023**, *1*, 4, doi:10.1007/s44312-023-00001-2.
43. Chukwuemeka, N.K.; Ulusow, A.H.; Sylvanus, O.M. Climate change, causes, economic impact and mitigation. *International Journal of Scientific Research Updates (IJSRU)* **2024**, *08*, 001-008, doi:https://doi.org/10.53430/ijsru.2024.8.1.0043.
44. Minak, G. Solar Energy-Powered Boats: State of the Art and Perspectives. *Journal of Marine Science and Engineering* **2023**, *11*, doi:10.3390/jmse11081519.
45. Leung, C.P.; Cheng, K.W.E. Zero emission solar-powered boat development. In Proceedings of the *2017 7th International Conference on Power Electronics Systems and Applications - Smart Mobility, Power Transfer & Security (PESA)*, 12-14 Dec. 2017, 2017; pp. 1-6.

46. EcoMarinePower. Hybrid Marine Power; Low Emission and Cost Effective Solutions for Shipping. Available online: https://www.ecomarinepower.com/en/products/8-products-services-and-consulting/14-hybrid-marine-power

47. Ajlif, M.A.; Joseph, S.C.; Chacko, R.V.; Joseph, A.; Jayan, P.; Raghavan, D.P. LVDC Architecture for Energy Efficient House Boat Hotel Load System. In Proceedings of the *2019 National Power Electronics Conference (NPEC)*, 13-15 Dec. 2019, 2019; pp. 1-5.

48. Tercan, Ş.H.; Eid, B.; Heidenreich, M.; Kogler, K.; Akyürek, Ö. Financial and Technical Analyses of Solar Boats as A Means of Sustainable Transportation. *Sustainable Production and Consumption* **2021**, *25*, 404-412, doi:https://doi.org/10.1016/j.spc.2020.11.014.

49. Gürsu, H.M. Solar And Wind Powered Concept Boats: The Example Of Volitan. *Metu Journal of The Faculty of Architecture* **2014**, *31*, doi:10.4305/METU.JFA.2014.2.6.

50. Özden, Y.A.; Dogrul, A.; Çelik, F.; Alkan, A.D. Energy Efficient Hull Form Design for A Pleasure Boat Powered by A Solar-Hydrogen Energy System. In Proceedings of the *IX International Symposium on High Speed Marine Vehicles (HSMV)*, Naples, Italy, 2011.

51. Grozdanic, L. Tûranor PlanetSolar: World's Largest Solar-Powered Boat Sets Transatlantic Speed Record. Available online: https://inhabitat.com/turanor-planetsolar-worlds-largest-solar-powered-boat-sets-transatlantic-speed-record/

52. Hasan, T.; Jamaludin, S.; Nik, W.W.; Rajib, M.H. Study and analysis of a solar electric boat with dynamic design strategy in efficient way. In Proceedings of the *13th International Conference on Marine Technology (MARTEC 2022)*, May 12, 2023.

53. Spagnolo, G.S.; Papalillo, D.; Martocchia, A.; Makary, G. Solar-Electric Boat. *Journal of Transportation Technologies* **2012**, *2*, 144-149.

54. Seatech. Pursuing greater fuel efficiency and lower emissions. Available online: https://seatech2020.eu/publications/

55. Belibassakis, K.; Filippas, E.; Papadakis, G. Numerical and Experimental Investigation of the Performance of Dynamic Wing for Augmenting Ship Propulsion in Head and Quartering Seas. *Journal of Marine Science and Engineering* **2022**, *10*, doi:10.3390/jmse10010024.

56. Belibassakis, K. Augmenting ship propulsion in waves by flapping-foil thrusters. In Proceedings of the *the 8th International Symposium on Ship Operations, Management & Economics (SOME)*, Athens, Greece, 7-8 March 2023, 2023.

57. Soukissian, T.; Gizari, N.; Chatzinaki, M. Wave potential of the Greek seas. In Proceedings of the *Energy and Sustainability III*, 2011/4/11, 2011.

58. Falcão, A.F.O. 8.02 - Historical Aspects of Wave Energy Conversion. In *Comprehensive Renewable Energy*, Sayigh, A., Ed.; Elsevier: Oxford, 2012; pp. 7-9.

59. Gunn, K.; Stock-Williams, C. Quantifying the global wave power resource. *Renewable Energy* **2012**, *44*, 296-304.

60. Barua, A.; Salauddin Rasel, M. Advances and challenges in ocean wave energy harvesting. *Sustainable Energy Technologies and Assessments* **2024**, *61*, 103599, doi:https://doi.org/10.1016/j.seta.2023.103599.

61. Magagna, D.; Uihlein, A. Ocean Energy Development in Europe: current status and future perspectives. *International Journal of Marine Energy* **2015**, *11*, 84-104, doi:10.1016/j.ijome.2015.05.001.
62. Hansen, R.H. Design and Control of the PowerTake-Off System for a Wave Energy Converter with Multiple Absorbers. PhD thesis, Department of Energy Technology, Aalborg University, 2013.
63. Bozzi, S.; Miquel, A.M.; Antonini, A.; Passoni, G.; Archetti, R. Modeling of a Point Absorber for Energy Conversion in Italian Seas. *Energies* **2013**, *6*, 3033-3051, doi:10.3390/en6063033.
64. Farrok, O.; Ahmed, K.; Tahlil, A.D.; Farah, M.M.; Kiran, M.R.; Islam, M.R. Electrical Power Generation from the Oceanic Wave for Sustainable Advancement in Renewable Energy Technologies. *Sustainability* **2020**, *12*, doi:10.3390/su12062178.
65. Cruz, J. *Ocean Wave Energy; Current Status and Future Prespectives*, 1 ed.; Springer Berlin, Heidelberg: Bristol, UK, 2007; p. 431.
66. Guo, B.; Ringwood, J.V. A review of wave energy technology from a research and commercial perspective. *IET Renewable Power Generation* **2021**, *15*, 3065-3090, doi:https://doi.org/10.1049/rpg2.12302.
67. Pérez-Collazo, C.; Astariz, S.; Abanades, J.; Greaves, D.; Iglesias, G. Co-located wave and offshore wind farms: a preliminary case study of an hybrid array. In Proceedings of the *International Conference in Coastal Engineering (ICCE)*, Seoul, Korea, 15-20 June 2014, 2014.
68. Bonovas, M. WECs over general bathymetry: A novel approach for performance evaluation and optimization. National Technological University of Athens, 2019, doi:10.26240/HEAL.NTUA.9198.
69. Gerostathis, T.; Magkouris, A.; Belibassakis, K. A 3D BEM-Coupled Mode Model for the Performance Analysis of Wave Energy Converter Parks in Nearshore-Coastal Regions. *Journal of Marine Science and Engineering* **2024**, *12*, doi:10.3390/jmse12020212.
70. Mei, C.C. *The Applied Dynamics of Ocean Surface Waves*; World Scientific: 1989.
71. Kuznetsov, N.; Maz'ya, V.; Vainberg, B. Introduction: Basic Theory of Surface Waves. In *Linear Water Waves: A Mathematical Approach*; Cambridge University Press: Cambridge, 2002; pp. 1-18.
72. Ohyama, T.; Tsuchida, M. Expanded mild-slope equations for the analysis of wave-induced ship motion in a harbor. *Coastal Engineering* **1997**, *30*, 77-103, doi:https://doi.org/10.1016/S0378-3839(96)00037-3.
73. Noblesse, F. Alternative integral representations for the Green function of the theory of ship wave resistance. *Journal of Engineering Mathematics* **1981**, *15*, 241-265, doi:10.1007/BF00042923.
74. Liu, Y.J.; Mukherjee, S.; Nishimura, N.; Schanz, M.; Ye, W.; Sutradhar, A.; Pan, E.; Dumont, A.; Frangi, A.; Saez, A. Recent Advances and Emerging Applications of the Boundary Element Method. *Applied Mechanics Reviews* **2011**, *64*, doi:10.1115/1.4005491.
75. Jaswon, M.A. Integral equation methods in potential theory. I. *Proc. R. Soc. Lond.* **1963**, *275*, 23-32, doi:10.1098/rspa.1963.0152.

76. Magkouris, A.; Belibassakis, K. Performance of photovoltaic systems supported by twin-hull floating structures in offshore and coastal regions. In Proceedings of the *XII International Conference on Structural Dynamics (EURODYN 2023)*, Delft, The Netherlands, 2023.

77. Magkouris, A.; Bonovas, M.; Gerostathis, T.; Belibassakis, K. A 3D BEM Model for the Hydrodynamic Analysis and Design of Heaving WEC Arrays Attached to a Breakwater. *Sustainability* **2023**, *15*, doi:10.3390/su151712777.

78. Kegkeroglou, A. A nonlinear boundary element method for the ship wave-resistance problem in calm water. **2020**, doi:10.26240/HEAL.NTUA.19659.

79. Magkouris, A.; Belibassakis, K. A Novel BEM for the Hydrodynamic Analysis of Twin-Hull Vessels with Application to Solar Ships. *Journal of Marine Science and Engineering* **2024**, *12*, doi:10.3390/jmse12101776.

80. Turkel, E.; Yefet, A. Absorbing PML boundary layers for wave-like equations. *Applied Numerical Mathematics* **1998**, *27*, 533-557, doi:https://doi.org/10.1016/S0168-9274(98)00026-9.

81. Athanassoulis, G.A.; Belibassakis, K.A. A consistent coupled-mode theory for the propagation of small-amplitude water waves over variable bathymetry regions. *Journal of Fluid Mechanics* **1999**, *389*, 275-301, doi:10.1017/S0022112099004978.

82. Belibassakis, K.A.; Athanassoulis, G.A.; Gerostathis, T.P. A coupled-mode model for the refraction–diffraction of linear waves over steep three-dimensional bathymetry. *Applied Ocean Research* **2001**, *23*, 319-336, doi:https://doi.org/10.1016/S0141-1187(02)00004-4.

83. Yfanti, S.; Sakkas, N. Technology Readiness Levels (TRLs) in the Era of Co-Creation. *Applied System Innovation* **2024**, *7*, doi:10.3390/asi7020032.

84. Gadzanku, S.; Mirletz, H.; Lee, N.; Daw, J.; Warren, A. Benefits and Critical Knowledge Gaps in Determining the Role of Floating Photovoltaics in the Energy-Water-Food Nexus. *Sustainability* **2021**, *13*, doi:10.3390/su13084317.

85. Kougias, I.; Szabó, S.; Nikitas, A.; Theodossiou, N. Sustainable energy modelling of non-interconnected Mediterranean islands. *Renewable Energy* **2019**, *133*, 930-940, doi:https://doi.org/10.1016/j.renene.2018.10.090.

86. Kanellopoulou, A.; Zaraphonitis, G.; Grigoropoulos, G.; Liarokapis, D. Extensive hullform optimization studies for a series of small electric catamaran ferries. In Proceedings of the *8th International Symposium on Ship Operations, Management & Economics (SOME)*, Athens GR, 2023.

87. Chandra, A.; Anderson, G.; Melkote, S.; Gao, W.; Haitjema, H.; Wegener, K. Role of surfaces and interfaces in solar cell manufacturing. *CIRP Annals* **2014**, *63*, 797-819, doi:https://doi.org/10.1016/j.cirp.2014.05.008.

88. Beddiaf, Z. Introductory Chapter: Introduction to Photovoltaic Effect. In *Solar Panels and Photovoltaic Materials*, Beddiaf, Z., Ed.; IntechOpen: Rijeka, 2018; p. Ch. 1.

89. Vimala, M.; Ramadas, G.; Perarasi, M.; Manokar, A.M.; Sathyamurthy, R. A Review of Different Types of Solar Cell Materials Employed in Bifacial Solar Photovoltaic Panel. *Energies* **2023**, *16*, doi:10.3390/en16083605.

90. Rahman, M.A. A Review on Semiconductors Including Applications and Temperature Effects in Semiconductors. *American Scientific Research Journal for Engineering, Technology, and Sciences* **2014**, *7*, 50-70.

91. Bailey, S.; Raffaelle, R. Chapter II-4-B - Operation of Solar Cells in a Space Environment. In *McEvoy's Handbook of Photovoltaics (Third Edition)*, Kalogirou, S.A., Ed.; Academic Press: 2012; pp. 987-1003.

92. Schön, J.; Abdollahinia, A.; Müller, R.; Benick, J.; Hermle, M.; Warta, W.; Schubert, M.C. Predictive Simulation of Doping Processes for Silicon Solar Cells. *Energy Procedia* **2013**, *38*, 312-320, doi:https://doi.org/10.1016/j.egypro.2013.07.283.

93. Aly, S.P. Numerical models development for simulating optical, thermal and electrical performance, as well as structural degradation of PV modules. Hamad Bin Khalifa, 2019, doi:10.13140/RG.2.2.35817.11361.

94. Al-Ezzi, A.S.; Ansari, M.N.M. Photovoltaic Solar Cells: A Review. *Applied System Innovation* **2022**, *5*, doi:10.3390/asi5040067.

95. Shukir, S. Solar System Inverters Types. **2022**.

96. Paudyal, B.R.; Imenes, A.G. Investigation of temperature coefficients of PV modules through field measured data. *Solar Energy* **2021**, *224*, 425-439, doi:https://doi.org/10.1016/j.solener.2021.06.013.

97. Dubey, S.; Sarvaiya, J.N.; Seshadri, B. Temperature Dependent Photovoltaic (PV) Efficiency and Its Effect on PV Production in the World – A Review. *Energy Procedia* **2013**, *33*, 311-321, doi:https://doi.org/10.1016/j.egypro.2013.05.072.

98. Darhmaoui, H.; Lahjouji, D. Latitude Based Model for Tilt Angle Optimization for Solar Collectors in the Mediterranean Region. *Energy Procedia* **2013**, *42*, 426-435, doi:https://doi.org/10.1016/j.egypro.2013.11.043.

99. Barbón, A.; Bayón-Cueli, C.; Bayón, L.; Rodríguez-Suanzes, C. Analysis of the tilt and azimuth angles of photovoltaic systems in non-ideal positions for urban applications. *Applied Energy* **2022**, *305*, 117802, doi:https://doi.org/10.1016/j.apenergy.2021.117802.

100. Mehleri, E.D.; Zervas, P.L.; Sarimveis, H.; Palyvos, J.A.; Markatos, N.C. Determination of the optimal tilt angle and orientation for solar photovoltaic arrays. *Renewable Energy* **2010**, *35*, 2468-2475, doi:https://doi.org/10.1016/j.renene.2010.03.006.

101. Stanciu, C.; Stanciu, D. Optimum tilt angle for flat plate collectors all over the World - A declination dependence formula and comparisons of three solar radiation models. *Energy Conversion and Management* **2014**, *81*, 133–143, doi:10.1016/j.enconman.2014.02.016.

102. El Mghouchi, Y.; El Bouardi, A.; Choulli, Z.; Ajzoul, T. Models for obtaining the daily direct, diffuse and global solar radiations. *Renewable and Sustainable Energy Reviews* **2016**, *56*, 87-99, doi:https://doi.org/10.1016/j.rser.2015.11.044.

103. Cooper, P.I. The absorption of radiation in solar stills. *Solar Energy* **1969**, *12*, 333-346, doi:https://doi.org/10.1016/0038-092X(69)90047-4.

104. Honsberg, C.B.; Bowden, S.G. Photovoltaics Education Website. Available online: www.pveducation.org

105. Rueda, J.A.; Ramírez, S.; Sánchez, M.A.; Guerrero, J.D. Sun Declination and Distribution of Natural Beam Irradiance on Earth. *Atmosphere* **2024**, *15*, doi:10.3390/atmos15081003.

106. Hafez, A.Z.; Soliman, A.; El-Metwally, K.A.; Ismail, I.M. Tilt and azimuth angles in solar energy applications – A review. *Renewable and Sustainable Energy Reviews* **2017**, *77*, 147-168, doi:https://doi.org/10.1016/j.rser.2017.03.131.

107. Kavya Santhoshi, B.; Mohana Sundaram, K.; Padmanaban, S.; Holm-Nielsen, J.B.; K. K, P. Critical Review of PV Grid-Tied Inverters. *Energies* **2019**, *12*, doi:10.3390/en12101921.

108. Jathar, L.D.; Ganesan, S.; Awasarmol, U.; Nikam, K.; Shahapurkar, K.; Soudagar, M.E.M.; Fayaz, H.; El-Shafay, A.S.; Kalam, M.A.; Bouadila, S.; et al. Comprehensive review of environmental factors influencing the performance of photovoltaic panels: Concern over emissions at various phases throughout the lifecycle. *Environmental Pollution* **2023**, *326*, 121474, doi:https://doi.org/10.1016/j.envpol.2023.121474.

109. Dörenkämper, M.; Wahed, A.; Kumar, A.; de Jong, M.; Kroon, J.; Reindl, T. The cooling effect of floating PV in two different climate zones: A comparison of field test data from the Netherlands and Singapore. *Solar Energy* **2021**, *214*, 239-247, doi:https://doi.org/10.1016/j.solener.2020.11.029.

110. Abreu, E.F.M.; Canhoto, P.; Costa, M.J. Prediction of diffuse horizontal irradiance using a new climate zone model. *Renewable and Sustainable Energy Reviews* **2019**, *110*, 28-42, doi:https://doi.org/10.1016/j.rser.2019.04.055.

111. Dincer, I. Comprehensive energy systems. Volume 1, Part A, Energy fundamentals. **2018**.

112. Ahsan, M.; Ahmad, N.; Badar, H.M. *Simulation of Solar angles for maximizing Efficiency of Solar Thermal Collectors*; 2019; pp. 1-5.

113. Camuffo, D.; della Valle, A.; Becherini, F. From time frames to temperature bias in temperature series. *Climatic Change* **2021**, *165*, 38, doi:10.1007/s10584-021-03065-5.

114. Boutahir, M.K.; Farhaoui, Y.; Azrour, M.; Zeroual, I.; Allaoui, A. Effect of Feature Selection on the Prediction of Direct Normal Irradiance. *Big Data Mining and Analytics* **2022**, *5*, 309-317, doi:10.26599/BDMA.2022.9020003.

115. Basílio, S.d.C.A.; Saporetti, C.M.; Yaseen, Z.M.; Goliatt, L. Global horizontal irradiance modeling from environmental inputs using machine learning with automatic model selection. *Environmental Development* **2022**, *44*, 100766, doi:https://doi.org/10.1016/j.envdev.2022.100766.

116. Paulescu, E.; Paulescu, M. Minute-Scale Models for the Diffuse Fraction of Global Solar Radiation Balanced between Accuracy and Accessibility. *Applied Sciences* **2023**, *13*, doi:10.3390/app13116558.

117. Chen, Y.; Wang, S.; Yang, A.X.; Fan, Y.; Ge, J.; Li, Y. Temporal variation of wall flow and its influences on energy balance of the building wall. *City and Built Environment* **2023**, *1*, 3, doi:10.1007/s44213-022-00003-8.

118. Varamesh, S.; Mohtaram Anbaran, S.; Shirmohammadi, B.; Al-Ansari, N.; Shabani, S.; Jaafari, A. How Do Different Land Uses/Covers Contribute to Land Surface Temperature and Albedo? *Sustainability* **2022**, *14*, doi:10.3390/su142416963.

119. Jacobs, S.J.P., A.B.; Barras, V.; Bye, J.; Vihma, T. An analysis of the meteorological variables leading to apparent temperature in Australia Present climate, trends, and global

warming simulations. *Global and Planetary Change* **2013**, *107*, 145-156, doi:10.1016/j.gloplacha.2013.05.009.

120. Shakespeare, C.J.; Roderick, M.L. What controls near-surface relative humidity over the ocean? *J. Adv. Model. Earth Syst.* **2024**, *16*, doi:10.1029/2023ms004168.

121. SandiaCorporation. PV_LIB Toolbox. Available online: https://pvpmc.sandia.gov/tools/pv_lib-toolbox/

122. Tina, G.M.; Bontempo Scavo, F. Energy performance analysis of tracking floating photovoltaic systems. *Heliyon* **2022**, *8*, e10088, doi:https://doi.org/10.1016/j.heliyon.2022.e10088.

123. Bonovas, M.; Belibassakis, K.; Rusu, E. Multi-DOF WEC Performance in Variable Bathymetry Regions Using a Hybrid 3D BEM and Optimization. *Energies* **2019**, *12*, doi:10.3390/en12112108.

124. Yeung, R.W. A hybrid integral equation method for time harmonic free surface flow. In Proceedings of the *1st Intenational Conference on Numerical Ship Hydrodynamics*, Gaithersburg, MD, 1975.

125. Nestegard, A.; Sclavounos, P.D. A Numerical Solution of Two-Dimensional Deep Water Wave-Body Problems. *Journal of Ship Research* **1984**, *28*, 48-54, doi:10.5957/jsr.1984.28.1.48.

126. Drimer, N.; Agnon, Y. A hybrid boundary element method for second-order wave-body interaction. *Applied Ocean Research* **1994**, *16*, 27-45, doi:https://doi.org/10.1016/0141-1187(94)90012-4.

127. Wehausen, J., V,; Laitone, E.V. Surface Waves. In *Encyclopedia of Physics*, Online Ed. 2002 ed.; Springer Verlag: 1960; Volume IX, pp. 446-778.

128. Wehausen, J.V. The Motion of Floating Bodies. *Annual Review of Fluid Mechanics* **1971**, *3*, 237-268, doi:https://doi.org/10.1146/annurev.fl.03.010171.001321.

129. Newman, J.N. *Marine Hydrodynamics*; MIT Press: Cambridge, 1977.

130. Massel, S.R. Extended refraction-diffraction equation for surface waves. *Coastal Engineering* **1993**, *19*, 97-126, doi:https://doi.org/10.1016/0378-3839(93)90020-9.

131. Coddington, A.; Levinson, N. *Theory of Ordinary Differential Equations*; McGraw-Hill: 1955.

132. Givoli, D. Non-reflecting boundary conditions. *Journal of Computational Physics* **1991**, *94*, 1-29, doi:https://doi.org/10.1016/0021-9991(91)90135-8.

133. Wehausen, J.V. *Methods for Boundary-Value Problems in Free-Surface Flows. The Third David W. Taylor Lecture, 27 August through 19 September 1974*; 4622; Bethesda, MD, 1974.

134. Kress, R. *Linear Integral Equations*; Springer-Verlag Berlin and Heidelberg GmbH & Co. K: 1989.

135. Belibassakis, K.A. A boundary element method for the hydrodynamic analysis of floating bodies in variable bathymetry regions. *Engineering Analysis with Boundary Elements* **2008**, *32*, 796-810, doi:https://doi.org/10.1016/j.enganabound.2008.02.003.

136. Katz, J.; Plotkin, A. Numerical (Panel) Methods. In *Low-Speed Aerodynamics*, 2 ed.; Cambridge Aerospace Series; Cambridge University Press: Cambridge, 2001; pp. 206-229.

137. Lewis, E.V. *Principles of naval architecture : Motions in waves and controllability*, 2 ed.; Society of Naval Architects and Marine Enginee: Jersey City, NJ, 1990; p. 3.

138. Drimer, N.; Agnon, Y.; Stiassnie, M. A simplified analytical model for a floating breakwater in water of finite depth. *Applied Ocean Research* **1992**, *14*, 33-41, doi:https://doi.org/10.1016/0141-1187(92)90005-5.

139. Ohkusu, M. *On the heaving motion of two circular cylinders on the surface of a fluid*; 1969.

140. Rhee, K.P. Investigation of the Effect of Water Depths on Two-dimensional Hydrodynamic Coefficients for Twin-Hull Sections. *J. Soc. Nav. Archit. Korea* **1982**, *19*, 39-45.

141. Dabssi, N.; Chagdali, M.; Hémon, A. Hydrodynamic coefficients and forces on multihulls in shallow water with constant or variable depth. *Transport* **2008**, *23*, 245-252, doi:https://doi.org/10.3846/1648-4142.2008.23.245-252.

142. Piskopos, D. Study & Design of Floating Photovoltaic Devices with Emphasis on Installations at Inshore & Marine Environments. Technical University of Crete, 2021.

143. Goda, Y. Random Seas and Design of Maritime Structures. *Advanced Series on Ocean Engineering* **2000**, *33*, doi:10.1142/3587.

144. Ochi, M.K. Spectral analysis. In *Ocean Waves: The Stochastic Approach*; Cambridge Ocean Technology Series; Cambridge University Press: Cambridge, 1998; pp. 13-57.

145. Soukissian, T.H.; Denaxa, D.; Karathanasi, F.; Prospathopoulos, A.; Sarantakos, K.; Iona, A.; Georgantas, K.; Mavrakos, S. Marine Renewable Energy in the Mediterranean Sea: Status and Perspectives. *Energies* **2017**, *10*, doi:10.3390/en10101512.

146. Ramanan, C.J.; Hann, L.K.; Candra, K.J.; Sukanta, R.; Jyoti, B.B.; Jyoti, M.B. Towards sustainable power generation: Recent advancements in floating photovoltaic technologies. *Renewable and Sustainable Energy Reviews* **2024**, *194*, 114322, doi:https://doi.org/10.1016/j.rser.2024.114322.

147. Nisar, H.; Kashif Janjua, A.; Hafeez, H.; shakir, S.; Shahzad, N.; Waqas, A. Thermal and electrical performance of solar floating PV system compared to on-ground PV system-an experimental investigation. *Solar Energy* **2022**, *241*, 231-247, doi:https://doi.org/10.1016/j.solener.2022.05.062.

148. Semeskandeh, S.; Hojjat, M.; Hosseini Abardeh, M. Techno–economic–environmental comparison of floating photovoltaic plant with conventional solar photovoltaic plant in northern Iran. *Clean Energy* **2022**, *6*, 353-361, doi:10.1093/ce/zkac019.

149. Dee, D.P.; Uppala, S.M.; Simmons, A.J.; Berrisford, P.; Poli, P.; Kobayashi, S.; Andrae, U.; Balmaseda, M.A.; Balsamo, G.; Bauer, P.; et al. The ERA-Interim reanalysis: configuration and performance of the data assimilation system. *Q. J. R. Meteorol. Soc.* **2011**, *137*, 553-597, doi:10.1002/qj.828.

150. Booij, N.; Ris, R.C.; Holthuijsen, L.H. A third-generation wave model for coastal regions: 1. Model description and validation. *J. Geophys. Res.* **1999**, *104*, 7649-7666, doi:10.1029/98jc02622.

151. Ris, R.C.; Holthuijsen, L.H.; Booij, N. A third-generation wave model for coastal regions: 2. Verification. *Journal of Geophysical Research* **1999**, *104*, 7667-7681, doi:10.1029/1998JC900123.

152. Schot, S.H. Eighty years of Sommerfeld's radiation condition. *Historia Mathematica* **1992**, *19*, 385-401, doi:https://doi.org/10.1016/0315-0860(92)90004-U.

153. Magkouris, A.; Belibassakis, K.; Rusu, E. Hydrodynamic Analysis of Twin-Hull Structures Supporting Floating PV Systems in Offshore and Coastal Regions. *Energies* **2021**, *14*, doi:10.3390/en14185979.

154. Olmez, A.; Cakici, F.; Sahoo, P. Validation of Strip Theory Based Frequency-Domain Ship Motion Code. In Proceedings of the *15th International Symposium on Practical Design of Ships and Other Floating Structures (PRADS 2022)*, Dubrovnik, Croatia 9 - 13 October, 2022.

155. Belibassakis, K.; Bonovas, M.; Rusu, E. A Novel Method for Estimating Wave Energy Converter Performance in Variable Bathymetry Regions and Applications. *Energies* **2018**, *11*, doi:10.3390/en11082092.

156. Katz, J.; Plotkin, A. Singularity Elements and Influence Coefficients. In *Low-Speed Aerodynamics*, 2 ed.; Cambridge Aerospace Series; Cambridge University Press: Cambridge, 2001; pp. 230-261.

157. Pinkster, J.A.; Van Oortmerssen, G. Computation of the first and second order wave forces on oscillating bodies in regular waves. In Proceedings of the *2nd International Conference on Numerical Ship Hydrodynamics*, Berkeley, California, USA, 1978.

158. Kusumawinahyu, W.M.; Karjanto, N.; Klopman, G. Linear theory for single and double flap wavemakers. *arXiv [physics.flu-dyn]* **2017**, doi:10.48550/ARXIV.1703.09445.

159. Krogstad, H.E.; F. Barstow, S. Satellite wave measurements for coastal engineering applications. *Coastal Engineering* **1999**, *37*, 283-307, doi:https://doi.org/10.1016/S0378-3839(99)00030-7.

160. Nguyen, Q.T.; Mao, M.; Xia, M. Numerical Modeling of Nearshore Wave Transformation and Breaking Processes in the Yellow River Delta with FUNWAVE-TVD Wave Model. *Journal of Marine Science and Engineering* **2023**, *11*, doi:10.3390/jmse11071380.

161. EMODnetBathymetry Consortium. EMODnet Digital Bathymetry (DTM 2016). **2016**, doi:10.12770/C7B53704-999D-4721-B1A3-04EC60C87238.

162. Wessel, P.; Smith, W.H.F. A global, self-consistent, hierarchical, high-resolution shoreline database. *J. Geophys. Res.* **1996**, *101*, 8741-8743, doi:10.1029/96jb00104.

163. Athanassoulis, G.A.; Belibassakis, K.A.; Gerostathis, T.P. The POSEIDON nearshore wave model and its application to the prediction of the wave conditions in the nearshore/coastal region of the Greek seas. *J. Atmos. Ocean Sci.* **2002**, *8*, 201-217, doi:10.1080/10236730290004085.

164. Lee, U.-J.; Jeong, W.-M.; Cho, H.-Y. Estimation and Analysis of JONSWAP Spectrum Parameter Using Observed Data around Korean Coast. *Journal of Marine Science and Engineering* **2022**, *10*, doi:10.3390/jmse10050578.

165. De La Torre, D.; Luyo, J.; Ortega, A. On the Estimation of the Wave Energy Period and a Kernel Proposal for the Peru Basin. *Journal of Marine Science and Engineering* **2023**, *11*, doi:10.3390/jmse11061100.

166. Gherbi, A.; Belgasmia, M. Chapter 21 - Stochastic analysis basics and application of statistical linearization technique on a controlled system with nonlinear viscous dampers. In

Handbook of Probabilistic Models, Samui, P., Tien Bui, D., Chakraborty, S., Deo, R.C., Eds.; Butterworth-Heinemann: 2020; pp. 505-525.

167. Müllerová, J.; Šutta, P.; Holá, M. Optical Absorption in Si:H Thin Films: Revisiting the Role of the Refractive Index and the Absorption Coefficient. *Coatings* **2021**, *11*, doi:10.3390/coatings11091081.

168. Poulek, V.; Šafránková, J.; Černá, L.; Libra, M.; Beránek, V.; Finsterle, T.; Hrzina, P. PV Panel and PV Inverter Damages Caused by Combination of Edge Delamination, Water Penetration, and High String Voltage in Moderate Climate. *IEEE Journal of Photovoltaics* **2021**, *11*, 561-565.

169. Song, J.; Imani, H.; Yue, J.; Yang, S. Hydrodynamic Characteristics of Floating Photovoltaic Systems under Ocean Loads. *Journal of Marine Science and Engineering* **2023**, *11*, doi:10.3390/jmse11091813.

170. Peters, I.M.; Nobre, A.M. Deciphering the thermal behavior of floating photovoltaic installations. *Solar Energy Advances* **2022**, *2*, 100007, doi:https://doi.org/10.1016/j.seja.2021.100007.

171. Nguyen, N.-H.; Le, B.-C.; Nguyen, L.-N.; Bui, T.-T. Technical Analysis of the Large Capacity Grid-Connected Floating Photovoltaic System on the Hydropower Reservoir. *Energies* **2023**, *16*, doi:10.3390/en16093780.

172. Kambezidis, H.D.; Mimidis, K.; Kavadias, K.A. The Solar Energy Potential of Greece for Flat-Plate Solar Panels Mounted on Double-Axis Systems. *Energies* **2023**, *16*, doi:10.3390/en16135067.

173. Yousefi, R.; Shafaghat, R.; Shakeri, M. Hydrodynamic analysis techniques for high-speed planing hulls. *Applied Ocean Research* **2013**, *42*, 105-113, doi:https://doi.org/10.1016/j.apor.2013.05.004.

174. ITTC. Recommended Procedures and Guidelines, Testing and Data Analysis Resistance Test. **2008**.

175. Wang, H.; Zhu, R.; Gu, M.; Gu, X. Numerical investigation on steady wave of high-speed ship with transom stern by potential flow and CFD methods. *Ocean Engineering* **2022**, *247*, 110714, doi:https://doi.org/10.1016/j.oceaneng.2022.110714.

176. Couser, P., R; Wellicome, J., F; Molland, A., F. An Improved Method for the Theoretical Prediction of the Wave Resistance of Transom-Stern Hulls Using a Slender Body Approach. In Proceedings of the *Int. Shipbuild. Prog.*, 1999; pp. 331–349.

177. Doctors, L.J. A Numerical Study of the Resistance of Transom-Stern Monohulls. *Ship Technology Research* **2015**, *54*, 134-144, doi:10.1179/str.2007.54.3.005.

178. Sinha, S.N.; Gupta, A.K.; Oberai, M.M. Laminar Separating Flow over Backsteps and Cavities Part I: Backsteps. *AIAA Journal* **1981**, *19*, 1527-1530, doi:https://doi.org/10.2514/3.7885.

179. Dawson, C. A practical computer method for solving ship-wave problems. In Proceedings of the *2nd International Conference on Numerical Ship Hydrodynamics*, USA, 1977; pp. 30-38.

180. Molland, A.F.; Turnock, S.R.; Hudson, D.A. *Ship resistance and propulsion: practical estimation of ship propulsive power*; Cambridge University Press: 2011; p. 544.

181. Ohkusu, M. *Advances in Marine Hydrodynamics*; Computational Mechanics Publications: 1996.

182. Lewandowski, E.M. *The Dynamics of Marine Craft: Maneuvering and Seakeeping*; Singapore, 2004.

183. Liu, S.; Papanikolaou, A.; Zaraphonitis, G. Prediction of added resistance of ships in waves. *Ocean Engineering* **2011**, *38*, 641-650, doi:https://doi.org/10.1016/j.oceaneng.2010.12.007.

184. Liu, S.; Papanikolaou, A. On the prediction of the added resistance of large ships in representative seaways. *Ships and Offshore Structures* **2017**, *12*, 690-696, doi:10.1080/17445302.2016.1200452.

185. Kim, S.W.; Jang, H.K.; Cha, Y.J.; Yu, H.S.; Lee, S.J.; Yu, D.H.; Lee, A.R.; Jin, E.J. Development of a ship route decision-making algorithm based on a real number grid method. *Applied Ocean Research* **2020**, *101*, 102230, doi:https://doi.org/10.1016/j.apor.2020.102230.

186. Lee, J.-H.; Kim, Y. Study on steady flow approximation in turning simulation of ship in waves. *Ocean Engineering* **2020**, *195*, 106645, doi:https://doi.org/10.1016/j.oceaneng.2019.106645.

187. Lee, J.H.; Kim, B.S.; Kim, Y. Study on Steady Flow Effects in Numerical Computation of Added Resistance of Ship in Waves. *Journal of Advanced Research in Ocean Engineering* **2017**, *3*, 193-203, doi:10.5574/JAROE.2017.3.4.193.

188. Amrollahi Biyouki, Z.; Zaman, A.; Marinova, D.; Minunno, R.; Askari Shayegan, M. Solar Photovoltaics Value Chain and End-of-Life Management Practices: A Systematic Literature Review. *Sustainability* **2024**, *16*, doi:10.3390/su16167038.

189. Copernicus. Europe's eyes on Earth. Access data. Available online: https://www.copernicus.eu/en/access-data

190. Prendergast, J.; Li, M.; Sheng, W. A Study on the Effects of Wave Spectra on Wave Energy Conversions. *IEEE Journal of Oceanic Engineering* **2020**, *45*, 271-283, doi:10.1109/JOE.2018.2869636.

191. Magkouris, A.; Rusu, E.; Rusu, L.; Belibassakis, K. Floating Solar Systems with Application to Nearshore Sites in the Greek Sea Region. *Journal of Marine Science and Engineering* **2023**, *11*, doi:10.3390/jmse11040722.

192. Margaronis, P.; Kanellopoulou, A.; Silionis, N.; Liarokapis, D.; Sofras, E.; Prousalidis, J. Holistic Design of a Twin-Hull Short-Sea Shipping Vessel With Hybrid-Electric Propulsion. In Proceedings of the *2023 IEEE International Conference on Electrical Systems for Aircraft, Railway, Ship Propulsion and Road Vehicles & International Transportation Electrification Conference (ESARS-ITEC)*, 29-31 March 2023, 2023; pp. 1-6.

193. Ma, T.; Li, Z.; Zhao, J. Photovoltaic panel integrated with phase change materials (PV-PCM): technology overview and materials selection. *Renewable and Sustainable Energy Reviews* **2019**, *116*, 109406, doi:https://doi.org/10.1016/j.rser.2019.109406.

194. Price, W.G.; Bishop, R.E.D. *Probabilistic Theory of Ship Dynamics*; Chapman and Hall: 1974.

195. Babarit, A. *Ocean Wave Energy Conversion, Resource, Technologies and Performance*, 1st ed.; ISTE Press - Elsevier: 2017.

196. Amini, E.; Asadi, R.; Golbaz, D.; Nasiri, M.; Naeeni, S.T.O.; Nezhad, M.M.; Piras, G.; Neshat, M. Comparative Study of Oscillating Surge Wave Energy Converter Performance: A Case Study for Southern Coasts of the Caspian Sea. *Sustainability* **2021**, *13*, 1-21.

197. Bonovas, M.; Magkouris, A.; Belibassakis, K. A Modified Mild-Slope Model for the Hydrodynamic Analysis of Arrays of Heaving WECs in Variable Bathymetry Regions. *Fluids* **2022**, *7*, doi:10.3390/fluids7060183.

198. Gao, J.; Zang, J.; Chen, L.; Chen, Q.; Ding, H.; Liu, Y. On hydrodynamic characteristics of gap resonance between two fixed bodies in close proximity. *Ocean Engineering* **2019**, *173*, 28-44, doi:10.1016/j.oceaneng.2018.12.052.

199. Gao, J.; He, Z.; Huang, X.; Liu, Q.; Zang, J.; Wang, G. Effects of free heave motion on wave resonance inside a narrow gap between two boxes under wave actions. *Ocean Engineering* **2021**, *224*, 108753, doi:https://doi.org/10.1016/j.oceaneng.2021.108753.

200. Gao, J.; Gong, S.; He, Z.; Shi, H.; Zang, J.; Zou, T.; Bai, X. Study on Wave Loads during Steady-State Gap Resonance with Free Heave Motion of Floating Structure. *Journal of Marine Science and Engineering* **2023**, *11*, doi:10.3390/jmse11020448.

201. Bhinder, M.; Babarit, A.; Gentaz, L.; Ferrant, P. Effect of viscous forces on the performance of a surging wave energy converter. In Proceedings of the *22nd International Conference on Ocean, Offshore and Artic Engineering (ISOPE2012)*, Rhodes, Greece, 2012.

202. Bhinder, M.; Babarit, A.; Gentaz, L.; Ferrant, P. Potential Time Domain Model with Viscous Correction and CFD Analysis of a Generic Surging Floating Wave Energy Converter. *International Journal of Marine Energy* **2015**, *10*, 70-96, doi:10.1016/j.ijome.2015.01.005.

203. Stratigaki, V.; Troch, P.; Stallard, T.; Forehand, D.; Kofoed, J.P.; Folley, M.; Benoit, M.; Babarit, A.; Kirkegaard, J. Wave Basin Experiments with Large Wave Energy Converter Arrays to Study Interactions between the Converters and Effects on Other Users in the Sea and the Coastal Area. *Energies* **2014**, *7*, 701-734, doi:10.3390/en7020701.

204. Charrayre, F.; Peyrard, C.; Benoit, M.; Babarit, A. A Coupled Methodology for Wave-Body Interactions at the Scale of a Farm of Wave Energy Converters Including Irregular Bathymetry. In Proceedings of the *33rd Intern Conference on Offshore Mechanics and Arctic Engineering (OMAE2014)*, San Francisco, CA, USA, 2014.

205. Verao Fernandez, G.; Balitsky, P.; Stratigaki, V.; Troch, P. Coupling Methodology for Studying the Far Field Effects of Wave Energy Converter Arrays over a Varying Bathymetry. *Energies* **2018**, *11*, doi:10.3390/en11112899.

206. Chamberlain, P.G.; Porter, D. The modified mild-slope equation. *Journal of Fluid Mechanics* **1995**, *291*, 393-407, doi:10.1017/S0022112095002758.

207. Massel, S.R. *Ocean surface waves: Their physics and prediction (2nd edition)*, 2 ed.; World Scientific Publishing: Singapore, Singapore, 2013; p. 692.

208. Gebco Bathymetric Compilation Group. The GEBCO_2023 Grid - a continuous terrain model of the global oceans and land. **2023**, doi:10.5285/F98B053B-0CBC-6C23-E053-6C86ABC0AF7B.

209. Karathanasi, F.; Karperaki, A.; Gerostathis, T.; Belibassakis, K. Offshore-to-Nearshore Transformation of Wave Conditions and Directional Extremes with Application to Port Resonances in the Bay of Sitia-Crete. *Atmosphere* **2020**, *11*, doi:10.3390/atmos11030280.

210. Anderlini, E.; Forehand, D.I.M.; Bannon, E.; Xiao, Q.; Abusara, M. Reactive control of a two-body point absorber using reinforcement learning. *Ocean Engineering* **2018**, *148*, 650-658, doi:https://doi.org/10.1016/j.oceaneng.2017.08.017.

211. Babarit, A. On the park effect in arrays of oscillating wave energy converters. *Renewable Energy* **2013**, *58*, 68-78, doi:https://doi.org/10.1016/j.renene.2013.03.008.

212. Budal, K. Theory for Absorption of Wave Power by a System of Interacting Bodies. *Journal of Ship Research* **1977**, *21*, 248-254, doi:10.5957/jsr.1977.21.4.248.

213. Jouybari, M.B.; Xing, Y. A practical design procedure for initial sizing of heaving point absorber wave energy converters. *IOP Conf. Ser. Mater. Sci. Eng.* **2021**, *1201*, 012018, doi:10.1088/1757-899x/1201/1/012018.

214. Massel, S.R. *Hydrodynamics of Coastal Zones*; Elsevier Science: 1989.

215. Göteman, M.; Giassi, M.; Engström, J.; Isberg, J. Advances and challenges in wave energy park optimization—A review. *Front. Energy Res.* **2020**, *8*, doi:10.3389/fenrg.2020.00026.

216. Falnes, J.; Kurniawan, A. *Ocean waves and oscillating systems*; Cambridge University Press: UK, 2020; Volume 8.

217. Tarrant, K.; Meskell, C. Investigation on parametrically excited motions of point absorbers in regular waves. *Ocean Engineering* **2016**, *111*, 67-81, doi:https://doi.org/10.1016/j.oceaneng.2015.10.041.

218. Shahroozi, Z.; Göteman, M.; Engström, J. Experimental investigation of a point-absorber wave energy converter response in different wave-type representations of extreme sea states. *Ocean Engineering* **2022**, *248*, 110693, doi:https://doi.org/10.1016/j.oceaneng.2022.110693.

219. Loukogeorgaki, E.; Chatjigeorgiou, I.K. Hydrodynamic performance of an array of truncated cylinders in front of a vertical wall. *Ocean Engineering* **2019**, *189*, 106407, doi:https://doi.org/10.1016/j.oceaneng.2019.106407.

220. Loukogeorgaki, E.; Boufidi, I.; Chatjigeorgiou, I.K. Performance of an Array of Oblate Spheroidal Heaving Wave Energy Converters in Front of a Wall. *Water* **2020**, *12*, doi:10.3390/w12010188.

221. SinnPower. We customize renewables. Available online: https://www.sinnpower.com/en

222. Bonovas, M.; Magkouris, A.; Belibassakis, K. Effects of control strategies on the performance of floating WEC point absorbers operating attached to a breakwater by time-domain simulator. In Proceedings of the *15th European Wave and Tidal Energy Conference (EWTEC 2023)*, 2023.

223. Gore, K.; Rigot-Müller, P.; Coughlan, J. Cost-benefit assessment of shore side electricity: An Irish perspective. *Journal of Environmental Management* **2023**, *326*, 116755, doi:https://doi.org/10.1016/j.jenvman.2022.116755.

224. Manos, A.; Lyridis, D.; Prousalidis, J. Establishing a Framework of the Open Maritime Electric Energy Market. *Energies* **2023**, *16*, doi:10.3390/en16145276.

225. Huang, G.; Tang, Y.; Chen, X.; Chen, M.; Jiang, Y. A Comprehensive Review of Floating Solar Plants and Potentials for Offshore Applications. *Journal of Marine Science and Engineering* **2023**, *11*, doi:10.3390/jmse11112064.

226. Trapani, K.; Millar, D. Hydrodynamic Overview Of Flexible Floating Thin Film PV Arrays. In Proceedings of the *7th Offshore Energy & Storage Symposium*, Malta, 2016.

227. Wang, P.; Zhou, J.; Jin, X.; Shi, J.; Chan, N.W.; Tan, M.L.; Lin, X.; Ma, X.; Lin, X.; Zheng, K.; et al. The Impact of Offshore Photovoltaic Utilization on Resources and Environment Using Spatial Information Technology. *Journal of Marine Science and Engineering* **2024**, *12*, doi:10.3390/jmse12050837.

228. Han, C.; Liu, K.; Kinoshita, T.; Guo, B.; Zhao, Y.; Ye, Y.; Liu, Y.; Yamashita, O.; Zheng, D.; Wang, W.; et al. Assessing the Attractive Effects of Floating Artificial Reefs and Combination Reefs on Six Local Marine Species. *Fishes* **2023**, *8*, doi:10.3390/fishes8050248.

229. Karperaki, A.E.; Belibassakis, K.A.; Papathanasiou, T.K. Time-domain, shallow-water hydroelastic analysis of VLFS elastically connected to the seabed. *Marine Structures* **2016**, *48*, 33-51, doi:https://doi.org/10.1016/j.marstruc.2016.04.002.

230. Athanassoulis, G.A.; Belibassakis, K.A. Ship dynamics. Lecture notes [in Greek]. National Technical University of Athens, School of Naval Architecture and Marine Engineering: Athens, 2012.

231. Duan, W.Y.; Chen, J.K.; Zhao, B.B. Second-order Taylor expansion boundary element method for the second-order wave radiation problem. *Applied Ocean Research* **2015**, *52*, 12-26, doi:https://doi.org/10.1016/j.apor.2015.04.011.

232. Bishay, P.L.; Atluri, S.N. High-Performance 3D Hybrid/Mixed, and Simple 3D Voronoi Cell Finite Elements, for Macro- \& Micro-mechanical Modeling of Solids, Without Using Multi-field Variational Principles. *Computer Modeling in Engineering \& Sciences* **2012**, *84*, doi:10.3970/cmes.2012.084.041.

233. Jiang, W.; Gao, X. Review of Collocation Methods and Applications in Solving Science and Engineering Problems. *Computer Modeling in Engineering \& Sciences* **2024**, *140*, doi:10.32604/cmes.2024.048313.

234. Newman, J.N. Distributions of sources and normal dipoles over a quadrilateral panel. *Journal of Engineering Mathematics* **1986**, *20*, 113-126, doi:10.1007/BF00042771.

235. Cruden, B.A. Analytical formulae for the projected solid angle and differential configuration factor of arbitrary polygons. *International Communications in Heat and Mass Transfer* **2023**, *142*, 106656, doi:https://doi.org/10.1016/j.icheatmasstransfer.2023.106656.

236. Thermos, L. A Boundary Element Method for the hydrodynamic analysis of floating bodies in variable bathymetry regions. National Technical University of Athens, Athens, 2017, doi:http://dx.doi.org/10.26240/heal.ntua.15622.

237. Abiola-Ogedengbe, A.; Hangan, H.; Siddiqui, K. Experimental investigation of wind effects on a standalone photovoltaic (PV) module. *Renewable Energy* **2015**, *78*, 657-665, doi:https://doi.org/10.1016/j.renene.2015.01.037.

238. Fage, A.; Johansen, F.C. On the flow of air behind an inclined flat plate of infinite span. *Proc. R. Soc. Lond. A Math. Phys. Sci.* **1927**, *116*, 170-197, doi:10.1098/rspa.1927.0130.

239. Shademan, M.; Naghib-Lahouti, A. Effects of aspect ratio and inclination angle on aerodynamic loads of a flat plate. *Advances in Aerodynamics* **2020**, *2*, 14, doi:10.1186/s42774-020-00038-7.

240. Shenouda, R.; Abd-Elhady, M.S.; Kandil, H.A.; Dagher, M.M. Numerical investigation of the effect of dust shields on accumulation of dust over PV panels. *Environmental Science and Pollution Research* **2023**, *30*, 62905-62923, doi:10.1007/s11356-023-26502-7.

241. Sert, C. Lecture Notes for ME 582 Finite Element Analysis in Thermofluids; Chapter 1 - Governing Equations of Fluid Flow and Heat Transfer. Middle East Technical University, Department of Mechanical Engineering.

242. Eso, R.; Napirah, M.; Usman, I.; Safiuddin, L.O.; Arman; Tahir; Aba, L.; Alfat, S.; Husein; Hamimu, L.; et al. The Two-Dimensional Conduction Heat Transfer Equation on a Square Plate: Explicit vs. Crank-Nicolson Method in MS Excel Spreadsheet. *Journal of Physics: Conference Series* **2024**, *2734*, 012050, doi:10.1088/1742-6596/2734/1/012050.

243. Hindmarsh, A.C.; Gresho, P.M.; Griffiths, D.F. The stability of explicit Euler time-integration for certain finite difference approximations of the multi-dimensional advection–diffusion equation. *Int. J. Numer. Methods Fluids* **1984**, *4*, 853-897, doi:10.1002/fld.1650040905.

244. Milton, J.L.; Goss, W.P. Stability criteria for explicit finite difference solutions of the parabolic diffusion equation with non-linear boundary conditions. *International Journal for Numerical Methods in Engineering* **1973**, *7*, 57-67, doi:https://doi.org/10.1002/nme.1620070105.

245. Majchrzak, E.; Turchan, Ł. The Finite Difference Method for transient convection-diffusion problems. *Sci. Res. Inst. Math. Comput. Sci.* **2012**, *11*, 63-72, doi:10.17512/jamcm.2012.1.07.